Title
Exploration of Chemical Functionality of Self-Assembled Carborane Derivatives

Author
Avery, Erin Michele

Publication Date
2021

Peer reviewed|Thesis/dissertation

UNIVERSITY OF CALIFORNIA

Los Angeles

Exploration of Chemical Functionality of Self-Assembled Carborane Derivatives

A dissertation submitted in partial satisfaction of the requirements for the degree of Doctor of Philosophy in Chemistry

by

Erin Michele Avery

2021

ABSTRACT OF THE DISSERTATION

Exploration of Chemical Functionality of

Self-Assembled Carborane Derivatives

by

Erin Michele Avery

Doctor of Philosophy in Chemistry

University of California, Los Angeles, 2021

Professor Paul S. Weiss, Chair

Understanding the correlations between nanoscale architecture and its macroscopic function provides incredible insight to the development of next-generation electronic and photonic devices. Integration of functional molecular materials into structured devices requires in-depth understanding of the structure, reactivity, and acid-base properties of the adsorbed molecules on the surface. Self-assembled monolayers (SAMs) have been used extensively to probe and to tune the properties of these interfaces. Here, we examine different SAMs of diverse carborane derivatives. Due to the high axial symmetry and robust nature of these molecules, many of the common defects observed in *n*-alkanethiolate monolayers are eliminated, enabling controlled platforms to study the properties at substrate/environment interfaces. In addition to the presentation of relatively pristine and defect free monolayers, the carborane scaffold offers many synthetic

opportunities to alter other physical and chemical characteristics. These characteristics include but are not limited to dipole magnitude and direction, a multiplicity of additional functionalization, and diversity among anchoring groups. Therefore, we tested these three properties and the effects conferred on the substrate/monolayer interface, the interaction between adsorbate molecules, and lastly the interactivity between the monolayer and environmental interface.

This thesis describes several examples of carborane surface assembly and how they can be used to explore different facets of self-assembly. Working from the top-down and first exploring the adsorbate-environment interface we use a carboranethiol with a laterally positioned carboxylic acid. The addition of the carboxylic acid introduces changes within the monolayer such as an increased nearest neighbor spacing to maximize hydrogen-bonding interactions. Despite the lateral positioning of the carboxylic acid, the functional group still partakes in environment interactions that shift the pK_a approximately two pH units less acidic in comparison to the molecule in free solution. This shift was attributed to several factors including the change in dielectric environment that the functional group experiences, the proximity of the carboxyl to the substrate, and partial desolvation.

To examine effects of adsorbate-adsorbate interactions within the monolayer we looked at monolayers composed of two *o*-carboranedithiol isomers. By orienting the two thiol groups on the carbon vertices or directly across from them, we demonstrate a controlled system of heterogeneously mixed oppositely oriented neighboring dipoles and analyze how they interact and assemble under ambient conditions.

To alter the interactions at the substrate-monolayer interface, switching the attachment functionality can be used as a method to directly probe differences in surface attachment behavior. In comparison to thiol anchoring groups, other chalcogens such as selenols, are great candidates

to make this correlation. Carboraneselenol SAMs exhibit similar packing density when compared side by side to their carboranethiol counterparts, however, they also exhibit a dynamic double lattice. This double lattice demonstrates stochastic switching between molecules of high and low conductance states which has been observed in other cage molecule selenolate SAMs.

By utilizing an array of techniques such as scanning tunneling microscopy (STM), X-ray photoelectron spectroscopy (XPS), and contact angle goniometry, we elucidate the roles of monolayer, substrate and environmental conditions, and their effects on the underlying mechanisms of self-assembly yet, many questions remain unanswered. These unanswered questions serve as useful outlets to pursue further routes of investigation on self-assembly and the characteristics and properties that have the potential to greatly further the field of interfacial electronic design and application.

This dissertation of Erin Michele Avery is approved.

Gerard C.L. Wong

Alex M. Spokoyny

Yu Huang

Paul S. Weiss, Committee Chair

University of California, Los Angeles

2021

For my incredibly supportive family, friends, and mentors

Table of Contents

List of Abbreviations….....x

Acknowledgments.....xiii

Vita.....xv

List of Publications.....xvi

Chapter 1

Introduction to Self-Assembly and Carborane-Based Monolayers……...1

1.1 Bottom-Up Assembly for Nanoscale Fabrication……....2

1.2 Molecular Self-Assembled Monolayers……...3

1.3 Carboranes…….... 3

1.4 Characterization and Techniques.....8

1.5 Thesis Motivation and Overview ……..10

1.6 References.....13

Chapter 2

Influence of Terminal Carboxyl Group on Structure and Reactivity of Functionalized *m*-Carboranethiolate Self-Assembled Monolayers.....17

2.1 Introduction.....18

2.2 Results and Discussion.....20

2.2.1 Intrinsic Properties and Characteristics of Carboxylated *meta*-Carboranes.....20

2.2.2 Characterization of Self-Assembled Monolayers *via* Scanning Tunneling Microscopy.....23

2.2.3 Computational Analysis of the Self-Assembled Monolayer Structure.....26

2.2.4 Interaction with the Au{111} Substrate.....30

2.2.5 Carboxylic Acid at the Exposed Interface.....30

2.3 Conclusions and Prospects.....40

2.4 Materials and Methods.....42

2.4.1 Chemicals……...……42

2.4.2 Synthesis……43

2.4.3 NMR Spectroscopic Characterization……..……...45
2.4.4 X-Ray Structural Analysis…..…….....45
2.4.5 Crystallography……..45
2.4.6 Acid-base Titration…….....47
2.4.7 Mass Spectrometry Analysis……..47
2.4.8 Infrared Spectra of M1-COOH and M9-COOH…….48
2.4.9 Geometric Structural Analysis…….....……...48
2.4.10 Conformational Analysis……...49
2.4.11 Scanning Tunneling Microscopy Analysis……49
2.4.12 Simulated Scanning Tunneling Microscopy Analysis……50
2.4.13 Contact Angle Measurements……50
2.4.14 Computational Modeling of pK_a……51
2.4.15 X-Ray Photoelectron Spectroscopy……..……52
2.5 Additional Figures and Tables.....55
2.6 References.....145

Chapter 3

Isomeric Molecule Mapping within Mixed Carboranedithiol Self-Assembled Monolayers…….....152
3.1 Introduction.....153
3.2 Results and Discussion.....155
3.3 Conclusions and Prospects.....163
3.4 Materials and Methods.....163
3.5 Additional Figures…….....166
3.6 References.....170

Chapter 4

Temperature-Dependent Deposition in Carboraneselenolate Self-Assembled Monolayers.....172
4.1 Introduction.....173

4.2 Results and Discussion.....175
4.3 Conclusions and Prospects.....181
4.4 Materials and Methods.....182
4.5 References.....183

Chapter 5

Prospects and Future Directions 186
5.1 Conclusion.....187
5.2 Prospects and Future Direction 189
5.2.1 Different Factors and Their Effects on Surface pK_a……..……..189
5.2.2 Position, Number, and Dilution of ω-Functionality…….....……...190
5.2.3 Surface Curvature……192
5.3 References.....194

List of Abbreviations

Acronyms and Symbols

AFM	atomic force microscopy
BE	bonding energy
n-BuLi	*n*-butyllithium
DFT	density functional theory
E_F	Fermi energy
ESI	electrospray ionization
Fcc	face-centered cubic
FTIR	Fourier transform infrared spectroscopy
FWHM	full width at half maximum
Hcp	hexagonal close-packed
I_t	tunneling current
I_{tunnel}	tunneling current
IR	infrared spectroscopy
KE	kinetic energy
LBH	local barrier height spectroscopy
M1	*m*-1-carboranethiol
M9	*m*-9-carboranethiol
M1-COOH	carboxylic acid functionalized *m*-1-carboranethiol
M9-COOH	carboxylic acid functionalized *m*-9-carboranethiol
M1Sel	*m*-1-carboraneselenol
M9Sel	*m*-9-carboraneselenol
Me1,2O9,12	$(Me)_2$-1,2-$(SH)_2$-9,12-carboranedithiol
NMR	nuclear magnetic resonance
O1,2	1,2-carboranedithiol
O9,12	9,12-carboranedithiol
P1	*p*-carboranethiol
P1-COOH	carboxylic acid functionalized *p*-carboranethiol

PDOS	predicted density of states
PE	photoelectron
Ppm	parts per million
SAM	self-assembled monolayer
STM	scanning tunneling microscopy
STS	scanning tunneling spectroscopy
T	temperature
UPS	ultraviolet photoelectron spectroscopy
UV	ultraviolet
V_s	sample voltage bias
V_{sample}	sample voltage bias
XPS	X-ray photoelectron spectroscopy

Units

Å	Ångstroms
a.u.	arbitrary units
°C	degrees Celsius
cm^{-1}	inverse centimeters
D	Debye
deg	degree
eV	electron volt
g	gram
h	hour
Hz	Hertz
K	Kelvin
kcal	kilocalorie
kHz	kilohertz
kJ	kilojoule
kV	kilovolt
m	meter

mA	milliampere
min	minutes
mL	milliliter
mM	millimolarity
mmol	millimole
mol	mole
ms	milliseconds
mV	millivolt
N	Newton
nm	nanometer
nN	nanonewton
pA	picoampere
sec	second
μm	micrometer
V	volt

Acknowledgments

First, I would like to thank my thesis advisor, Paul S. Weiss, for his helpful mentorship and guidance throughout my journey in graduate school. I am grateful for the time I was able to spend in his lab growing as a scientist and the freedom I was able to experience in my choice in research projects. During my time in his group I was able to learn valuable skills like time management, perseverance in the lab, and better communication of my research that helped me develop into the researcher and teacher I am today. I would also like to thank the other members of my thesis committee, Prof. Gerard C.L. Wong, Prof. Alex M. Spokoyny, and Prof. Yu Huang for their support and guidance throughout my PhD.

I would like to give a special thank you to collaborator Prof. Tomáš Baše, who has been an incredibly influential part of my journey as a scientist. It has been my pleasure to work with him over the years and I immensely appreciate his support and guidance.

I would also like to thank my fellow group members of the Weiss lab for their continual feedback, engagement and troubleshooting of projects, along with their comradery that expanded beyond the lab. Dr. Dominic Goronzy for his mentorship, accountability, and advice when I first joined the group and knew nothing about grad school. Katie White, for being an amazing mentee and keeping the projects alive and going as I transition on. Gail Vinnacombe for being a great peer and friend throughout my degree. Liv Heidenreich, for also being a great friend and roommate. And Dr. Kevin Cheung for his assistance and advice throughout my time in the lab.

I gratefully acknowledge the funding sources that supported this work, the Czech Academy of Sciences (grant #M200321201) for support of the synthetic aspects of this work, the Scientific and Technological Research Council of Turkey (grant #116F174) and the NSF-CAREER award (grant #CHE-1351968) for support of the computational modeling and analyses.

Last but not least, I would like to thank my family for their unconditional love and support in my decision to move to the other side of the country and pursue my dream of becoming the first PhD in my family. From a very young age they always fostered my love for science and taught me that I could do absolutely anything in this world that I set my mind to.

Vita

I received my Bachelor of Science in Chemistry from the State University of New York College at Oneonta. During my undergraduate degree, I pursued research with Prof. Heike Geisler at the Albany NanoTech Complex and participated in two National Science Foundation Research Experiences for Undergraduates (NSF REU) program, one in the lab of Prof. Jeffrey Mativetsky at Binghamton University and another in the lab of Prof. James Batteas at Texas A&M University. In Prof. Geislers's lab, I worked on chemical vapor deposition of graphene on different substrates in ultra-high vacuum conditions using low-energy electron diffraction for analysis. In the lab of Prof. Mativetsky, my summer research project involved synthesis and characterization of organic semiconducting solar cells. In the lab of Prof. James Batteas, my love for surface science was cultivated during the work I did with Dr. Alison Pawlicki as my mentor using atomic force microscopy and scanning tunneling microscopy to explore directed surface assembly on the nanoscale.

In 2016, I began my graduate studies at the University of California, Los Angeles and joined the research group of Professor Paul S. Weiss in the Department of Chemistry and Biochemistry, further pursuing my passion for materials chemistry. During my time in the Paul Weiss lab, I studied self-assembled monolayers of a diverse array of carborane derivatives, by continuing to sharpen my skills using scanning tunneling microscopy at both ambient and ultra-high vacuum conditions. These techniques were used to explore properties and characteristics of self-assembly at the substrate-monolayer interface, interactions between adsorbates and at the exposed monolayer-environment interface. During my time at UCLA, I was also able to explore my passion of teaching through a variety of teaching assistant positions in various chemistry

courses over the years. In 2019, I was a recipient of the Hanson-Dow award for excellence in teaching.

List of Publications

1. Pawlicki, A.; Avery, E.; Jurow, M.; Ewers, B.; Vilan, A.; Drain C. M.; Batteas, J. Studies of the Structure and Phase Transitions of Nano-Confined Pentanedithiol and its Application in Directing Hierarchical Molecular Assemblies on Au {111}. *J. Condens. Matter Phys.* **2016**, 28, 94013–94018.

2. Goronzy, D. P.; Staněk, J.; Avery, E.; Guo, H.; Bastl, Z.; Dušek, M.; Gallup, N. M.; Gün, S.; Kučeráková, M.; Levandowski, B. J.; Macháček, J.; Šícha, V.; Thomas, J. C.; Yavuz, A.; Houk, K. N.; Danlşman, M. F.; Mete, E.; Alexandrova, A. N.; Baše, T.; Weiss, P. S. Influence of Terminal Carboxyl Groups on the Structure and Reactivity of Functionalized *m*-Carboranethiolate Self-Assembled Monolayers. *Chem. Mater.* **2020**, *32*, 6800–6809.

Chapter 1: Introduction to Self-Assembly and Carborane-Based Monolayers

1.1 Bottom-Up Assembly for Nanoscale Fabrication

As the push expands for devices to become electronically and spatially higher in density, new technologies must be developed for nanoscale fabrication. Typically, nanoscale fabrication is conducted one of two ways, with top-down or bottom-up methodologies. In top-down fabrication, a bulk material is used as the starting material.[1] With the use of various instruments, we carve away and perform chemical reactions on the bulk material and a nanoscale pattern is gradually produced in a series of steps. The advantages of this method are that the techniques are well studied and highly streamlined due to the long history and high availability of current silicon technology.[2] The disadvantages are that the pattern is typically limited by the precision and accuracy of the instrument, the fabrication requires pristine lab conditions, and it is typically a very expensive process.[2] The alternative comes from the bottom-up methodologies where desired properties of individual molecules are utilized to build nanoscale architecture from the ground up. Since molecular self-assembly is employed, this method is not necessarily limited by the precision of instrumentation. The main drawback with this method is its limits in designing molecules with desired characteristics and properties and furthermore understanding the interplay between fundamental interactions and how they transfer over to macroscale function.[1–4] Therefore the control and design of new nanoscale constructs requires increased understanding of the fundamentals of self-assembly and the relationship between molecular and macroscale patterning.

1.2 Molecular Self-Assembled Monolayers

An ideal construct for detailed study of the fundamentals of molecular self-assembly lies in the technology of molecular self-assembled monolayers (SAMs). Self-assembled monolayers involve the thermodynamically spontaneous assembly of molecules into ordered patterns on a substrate. There are several key areas of interest for study of fundamental interactions in self-assembled monolayers ranging from substrate-molecule interactions, adsorbate-adsorbate interactions, and monolayer-environment interface interactions that can all be controllably studied. One of the most commonly studied class of molecules for this application is *n*-alkanethiolates assembled on metal substrates. However, due to the large conformational flexibility of the alkyl chain, many defects such as gauche defects, tilt domain boundaries, and substrate vacancy islands, arise which convolutes the study of the individual interface categories, as described above.[5,6]

1.3 Carboranes

Promising alternatives to alkanethiols as the main component in self-assembled monolayers are dicarba-*closo*-dodecaboranethiols, commonly referred to as carboranethiols, on which this thesis will be focused. Carboranes first appeared in 1963 as synthesized by Heying et al. via the reaction of decaborane with acetylenic compounds.[7] Since then, they have been widely studied and used for a variety of applications such as small-molecule reversible capture, nanoparticle ligands for electron pools and ion traps, integration into biologically relevant molecules, and active components in boron neutron capture therapy.[8–13] Carboranes are boron clusters with a central scaffold component of $C_2B_{10}H_{12}$. The carborane is cage is icosahedral in shape consisting of 10 boron vertices and 2 carbon vertices with one hydrogen atom attached to each. The hexacoordinate

bonding that takes place in the cage creates a high degree of electron deficiency at the carbon vertices. This topology leads to multicenter bond creation where the optimal geometry is a body pronounced in all three dimensions (*closo*-cage). The regular polygons are hollow and *sp*-hybrid orbitals from B-H groups are shared in the middle forming "internal bonding orbitals".

Together with the less-symmetric combinations of *sp*-hybrid orbitals, the boronic *p*-orbitals tangential to the B-H bond create several degenerate molecular orbital manifolds spread across the cage surface with a large gap between highest molecular orbital (MO) of bonding and lowest MO of anti-bonding character. As long as e' = 2n+2, the Wade-Mingos-Williams rule is fulfilled, where e' is the electron count and n is the number of vertices in the cluster, the former is the highest occupied molecular orbital (HOMO), the latter is the lowest unoccupied molecular orbital (LUMO), and the electronic structure is stable.[14,15]

The electronic structure described above resembles the electronic structure of aromatic hydrocarbons, with delocalization of frontier orbitals, degeneracy, and high HOMO-LUMO gaps, but is realized in all three dimensions. Terms such as "pseudo-aromaticity" or "three-dimensional aromaticity" can be used to describe the aforementioned phenomena.

In addition to pseudo-aromaticity, the high axial isotropy and spatial requirements of the carborane cages lead to ideal characteristics for use as molecular components of self-assembled monolayers. In comparison to widely used alkanethiols, due to the bulky steric demands of the cage, when attached to metal substrates, many of the defects observed in alkanethiol monolayers from the high conformational flexibility are mitigated. Defects such as tilt domains and substrate vacancy islands are not present in carboranethiol monolayers (Figure 1.1).[16,17]

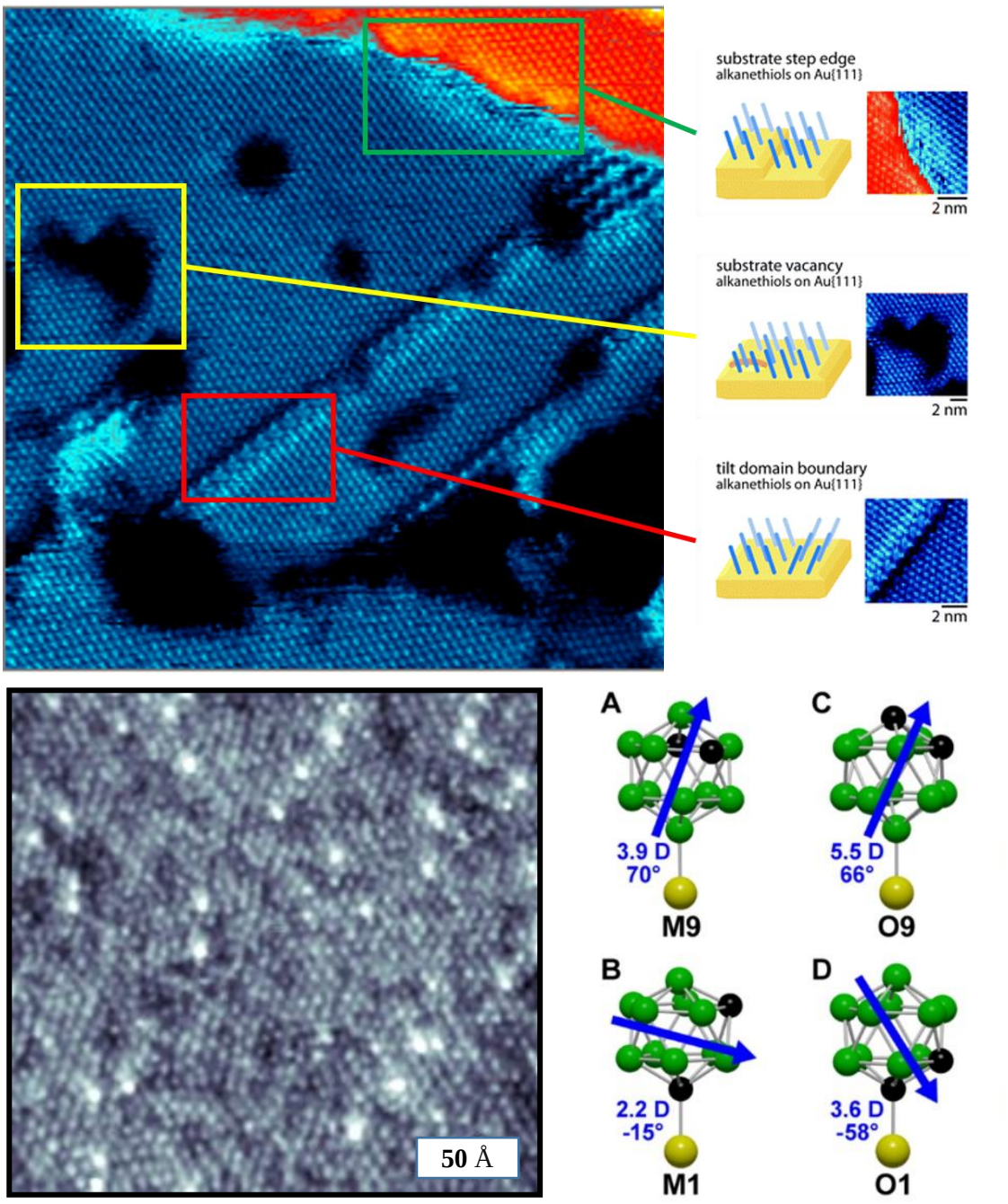

Figure 1.1 (A) A scanning tunneling microscopy image of a dodecanethiolate self-assembled monolayer of a Au{111} substrate, V_s = -1.0 V and I_t = 1.0 pA. This image demonstrates common monolayer defects including a substrate step edge (green), a substrate vacancy (yellow), and a tilt domain boundary (red). Adapted with permission from References 1 and 14. Copyrights 2013 Royal Society of Chemistry and 2008 American Chemical Society. (B) A scanning tunneling microscopy image of a *m*-9-carboxylcarboranethiolate monolayer. (C) Models of four different carboranethiol isomers, each denoted with the orientation and magnitude of their dipole moment. Adapted with permission from References 5, 16, 17, and 24. Copyrights 2016 American Chemical Society, and 2020 American Chemical Society.

In addition to pristine monolayers, the carborane cage itself offers a high degree of tailorablilty in terms of the dipole magnitude and direction. The positions of the electron- deficient carbon vertices around the carborane cage directly correlate to the dipole strength and direction. Hart and Lipscomb at Harvard University demonstrated in 1967 that upon different thermal annealing conditions, the carbon vertices could be controllably changed from the *ortho* position, to *meta* or *para* at 395-425 °C and 500-620 °C respectively.[18] By changing the positions of the carbons from *ortho* to *meta* to *para*, the dipole magnitude changes up to 5.5 D and can be changed even further with different functionalization along the cage.[17] Controlling the dipole magnitude and direction, yet keeping steric demands and spatial requirements essentially identical, has led to many interesting studies. An example is the work done by Schwartz et al. where the normal component of the molecular dipole of different carboranethiol SAMs was found to determine the in-plane liquid crystal director orientation relative to the anisotropy axis of the surface.[17]

An important feature presented by carboranes in addition to the ability to control of the carbon position in the cage is the ability to functionalize the carborane's exterior at controlled positions around the cage. Synthesis of carboranes functionalized with a thiol group has been demonstrated at electron-poor carbon vertices and also electron-rich boron vertices.[12] This variation changes the potential of the dipole to be oriented in different directions when anchored on substrates and also alters the chemical properties of the functionality. These exchanges were highlighted by the differences in pK_a values and reactivity of the acidic thiol moiety as its proximity to the carbon vertices was changed.[12,19] By adding this additional level of control to the synthesis of carboranes, work on SAMs of M1 and M9 carboranethiol isomers was done, which sheds light on the roles of dipole-dipole interactions within monolayers of each species where both monolayers exhibit the same nearest neighbor spacing and are indistinguishable *via* STM

measurements yet differences in robustness of the monolayer arise from long-range dipole-dipole interactions.[20] This contrast was shown with the M1 isomer, which has a larger dipole component in plane in comparison to the M9 isomer.[20]

Lastly, the ability of the carborane to be functionalized not only at controlled positions around the cage but also with a diverse array of functionalities or even several matching or different functionalities on the same carborane molecule further supports the potential of the carboranes to be used as platforms of study for surface science and self-assembly. Chemical functionality ranging from carboxylic acids, to alcohols, to amines, to halogens, and many more have been used as further building blocks with carboranes.[7]

The synthetic opportunities presented through carboranes to design desired building blocks makes them advantageous for the advance of surface control. The work presented in this thesis will explore three different aspects of self-assembly, yet only scratches the surface of what is possible.

1.4 Characterization and Techniques

To study the details of molecular self-assembly, we employ a variety different surface-sensitive techniques. These techniques typically fall into two categories. Chemical ensemble measurements average information and we gain knowledge about the bulk material. Some examples of methods that fall into this category from my work include X-ray photoelectron spectroscopy (XPS), Fourier transform infrared radiation spectroscopy (FTIR), and contact angle goniometry. X-ray photoelectron spectroscopy provides detailed information on the elemental composition of the surface along with insight into the oxidation states of the elements. Binding energies of electrons in individual elements within the monolayer are measured and inferences as

to the interactions within the monolayer can be drawn. Fourier transform infrared spectroscopy is a tool used to study the functional groups present on the surface. These measurements can present information testing the presence of specific functional groups along with different interactions they may have within the self-assembled lattice. Contact angle goniometry is a method where a water droplet is administered to the surface of interest and the resulting angle of contact is measured. This method can provide information on the degree of hydrophilicity/hydrophobicity along with the reactivity of the substrate towards different solvents or solution pH.

The second type of method this work used is the sub-Ångstrom precision of scanning tunneling microscopy where an atomically sharp tip is brought within a tunneling current distance of 1-10 Å of the surface, the current is stabilized through a feedback loop, and the probe is rastered across the surface, presenting a corresponding micrograph of the substrate with sub-Ångstrom precision.[22] (Figure 1.2) Since the resulting image is a product of real-space measurements, it is not an averaging technique, but rather provides detailed information about the surface and potential individual defect/lattice arrangement information.

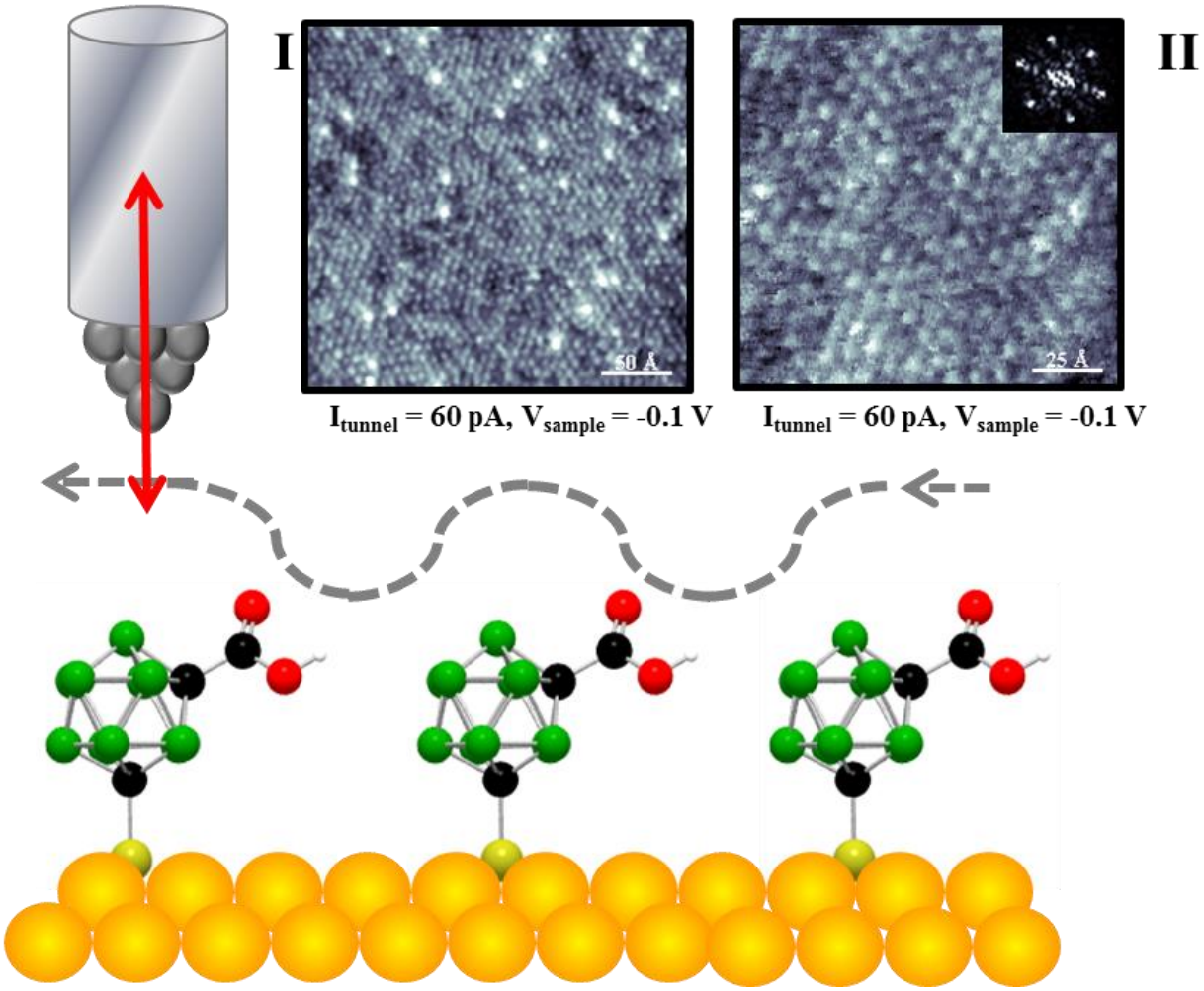

Figure 1.2 Schematic of scanning tunneling microscope rastering across a self-assembled monolayer of a *m*-1-carboxylcarboranethiol monolayer. Insets I and II depict scanning tunneling micrographs of the self-assembled monolayer where bright spots indicate areas of higher conductance and/or topographic height and darker spots indicate depressions. Adapted with permission from Reference 16. Copyright 2020 American Chemical Society.

Since the initial publication in 1981 by Binnig and Rohrer at IBM,[22] the history and development of STM has become incredibly rich employing a variety of methods in conjunction with the original instrument to extract simultaneous data at the atomic level, such as its combination with scanning tunneling spectroscopy, FTIR, photonic excitation, polarization measurements using AC-STM, measurements in liquid, ultra-high vacuum, cryogenic

temperatures, and many more.[23] The work in this thesis will only present STM data recorded under ambient conditions, but will discuss other experiments run in conjunction with the aforementioned techniques.

1.5 Thesis Motivation and Overview

Three important areas of exploration in self-assembled monolayers are the substrate-adsorbate interface, adsorbate-adsorbate interactions, and the adsorbate-environment interface. All three of these areas will be addressed in different chapters of this thesis.

Chapter 1 introduces the advantages of exploring and studying self-assembled monolayers along with the rich history of carborane chemistry and why it is advantageous to use them as scaffolds for this study.

The substrate-adsorbate interface considers the interactions between the surface and the attached adsorbates. To achieve spontaneous formation, the molecules involved in the self-assembly process typically have high affinities to the surface and form strong bonds. In the case of the most commonly studied pair, Au(111) substrates and *n*-alkanethiols, the thiolate-gold bond strength is typically ~45 kcal/mol.[6,24,25] However, studies of self-assembly involve a wide range of substrates varying from metals such as Ag,[26–29] Cu,[27,28,30] Pt,[28] and others along with a few examples of semiconductors including Ge.[31,32] In addition to changing the type of substrate, the anchoring group can also widely vary, such as -Se groups,[26,33–35] -CN,[36] -COOH,[37,38] and –NH_3,[39,40] which alters the chemistry and behavior of the adsorbate attached. Both the anchoring groups and substrates play roles in the organization of self-assembled monolayers. Due to the presence of many chemically nonequivalent binding sites on the substrate, the surface sometimes reconstructs to minimize surface energy. In addition to reconstruction, the anchoring group, which

serves as the electronic connection to the surface, also plays a large role in how the molecules assemble. Hybridization of the adsorbate orbitals influences the angle at which the molecule connects to the surface.[24] It has also been shown that the anchoring group-metal interaction can remove individual substrate atoms, *e.g.*, in the case of thiol-gold interactions the thiol lifts individual Au adatoms from the surface.[41] In the case of selenol binding in comparison to thiol, the higher bonding promiscuity results in the formation of moiré patterns of the surface.[26] The work described in Chapter 4 will explore the differences in carborane monolayers that use selenide attachment groups as compared to a thiol attachment groups and how surface arrangements vary under different annealing conditions.

Interactions between adsorbates have many important effects on the formation of self-assembled patterns in monolayers. van der Waals interactions, dipole-dipole interactions, steric demands, and symmetry of the molecular backbone can all affect the order observed on the surface.[24] The work in Chapter 3 elaborates on the roles of differing carborane dipole-dipole interactions and their effect on monolayer formation and characterization.

Lastly, an important area of study is the interaction between the monolayer and its surrounding environment. Depending on the functional group exposed at the surface, many interesting effects can arise, such as control of hydrophilicity, dipole effects, and integration into click chemistry systems for further architectural modifications. Chapter 2 describes our group's published work on exploring the reactivity of exposed carboxylic acid group on a carboranethiol monolayer and how it changes when moved from a free 3D system in solution to confinement into a 2D lattice. Chapter 2 has been modified with permission from the following publication: Goronzy, D. P.; Staněk, J.; Avery, E.; Guo, H.; Bastl, Z.; Dušek, M.; Gallup, N. M.; Gün, S.; Kučeráková, M.; Levandowski, B. J.; Macháček, J.; Šícha, V.; Thomas, J. C.; Yavuz, A.; Houk,

K. N.; Danlşman, M. F.; Mete, E.; Alexandrova, A. N.; Baše, T.; Weiss, P. S. Influence of Terminal Carboxyl Groups on the Structure and Reactivity of Functionalized *M*-Carboranethiolate Self-Assembled Monolayers. *Chem. Mater.* **2020**, *32* (15), 6800–6809. Copyright 2020 American Chemical Society. Chapter 5 will conclude and summarize the work in my thesis along with provide insight into future directions for this field of study.

1.6 References

(1) Biswas, A.; Bayer, I. S.; Biris, A. S.; Wang, T.; Dervishi, E.; Faupel, F. Advances in Top–down and Bottom–up Surface Nanofabrication: Techniques , Applications & Future Prospects. *Adv. Colloid Interface Sci.* **2012**, *170*, 2–27.

(2) Berbezier, I.; Crescenzi, M. De. Self-Assembly of Nanostructures and Nanomaterials. *J. Nanotechnol*. **2015**, *6*, 1397–1398.

(3) Gates, B. D.; Xu, Q.; Stewart, M.; Ryan, D.; Willson, C. G.; Whitesides, G. M. New Approaches to Nanofabrication : Molding , Printing , and Other Techniques. *Chem. Rev.* **2005**, *105*, 1171-1196.

(4) Ariga, K.; Hill, J. P.; Lee, M. V; Vinu, A.; Acharya, S.; Ariga, K.; Hill, J. P.; Lee, M. V; Vinu, A.; Charvet, R.; Acharya, S. Challenges and Breakthroughs in Recent Research on Self-Assembly. *Sci. Technol. Adv. Mater*. **2008**, *9*, 1-96.

(5) Weiss, P. S. Functional Molecules and Assemblies in Controlled Environments: Formation and Measurements. *Acc. Chem. Res.* **2008**, *41*, 1772–1781.

(6) Love, J. C.; Estroff, L. A.; Kriebel, J. K.; Nuzzo, R. G.; Whitesides, G. M. Self-Assembled Monolayers of Thiolates on Metals as a Form of Nanotechnology. *Chem. Rev*. **2005**, *105*, 1103-1169.

(7) Heying, T. L.; Ager, J. W.; Clark, S. L.; Mangold, D. J.; Goldstein, H. L.; Hillman, M.; Polak, R. J.; Szymanski, J. W. A New Series of Organoboranes. I. Carboranes from the Reaction of Decaborane with Acetylenic Compounds. *Inorg. Chem.* **1963**, *2*, 1089–1092.

(8) Cioran, A. M.; Musteti, A. D.; Teixidor, F.; Krpetić, Ẑeljka; Prior, I. A.; He, Q.; Kiely, C. J.; Brust, M.; Viñas, C. Mercaptocarborane-Capped Gold Nanoparticles: Electron Pools and Ion Traps with Switchable Hydrophilicity. *J. Am. Chem. Soc.* **2012**, *134*, 212–221.

(9) Valliant, J. F.; Guenther, K. J.; King, A. S.; Morel, P.; Schaffer, P.; Sogbein, O. O.; Stephenson, K. A. The Medicinal Chemistry of Carboranes. *Coord. Chem. Rev.* **2002**, *232*, 173–230.

(10) Worm, D. J.; Hoppenz, P.; Els-Heindl, S.; Kellert, M.; Kuhnert, R.; Saretz, S.; Köbberling, J.; Riedl, B.; Hey-Hawkins, E.; Beck-Sickinger, A. G. Selective Neuropeptide y Conjugates with Maximized Carborane Loading as Promising Boron Delivery Agents for Boron Neutron Capture Therapy. *J. Med. Chem.* **2020**, *63*, 2358–2371.

(11) Spokoyny, A. M.; MacHan, C. W.; Clingerman, D. J.; Rosen, M. S.; Wiester, M. J.; Kennedy, R. D.; Stern, C. L.; Sarjeant, A. A.; Mirkin, C. A. A Coordination Chemistry Dichotomy for Icosahedral Carborane-Based Ligands. *Nat. Chem.* **2011**, *3*, 590–596.

(12) Grimes, R. *Carboranes*; Academic Press: New York, **1970**.

(13) Bould, J.; Baše, T.; Londesborough, M. G. S.; Oro, L. A.; MacÍas, R.; Kennedy, J. D.; Kubát, P.; Fuciman, M.; Polívka, T.; Lang, K. Reversible Capture of Small Molecules on Bimetallaborane Clusters: Synthesis, Structural Characterization, and Photophysical Aspects. *Inorg. Chem.* **2011**, *50*, 7511–7523.

(14) Greenwood, N. N.; Earnshaw, A. *Chemistry of the Elements*; Elsevier, **2012**.

(15) Cotton, F. A.; Wikison, G.; Murillo, C. A.; Bochmann, M.; Grimes, R. *Advanced Inorganic Chemistry*, 6th ed.; Wiley: New York, **1988**.

(16) Goronzy, D. P.; Staněk, J.; Avery, E.; Guo, H.; Bastl, Z.; Dušek, M.; Gallup, N. M.; Gün, S.; Kučeráková, M.; Levandowski, B. J.; Macháček, J.; Šícha, V.; Thomas, J. C.; Yavuz, A.; Houk, K. N.; Danlşman, M. F.; Mete, E.; Alexandrova, A. N.; Baše, T.; Weiss, P. S. Influence of Terminal Carboxyl Groups on the Structure and Reactivity of Functionalized *m*-Carboranethiolate Self-Assembled Monolayers. *Chem. Mater.* **2020**, *32*, 6800–6809.

(17) Schwartz, J. J.; Mendoza, A. M.; Wattanatorn, N.; Zhao, Y.; Nguyen, V. T.; Spokoyny, A. M.; Mirkin, C. A.; Baše, T.; Weiss, P. S. Surface Dipole Control of Liquid Crystal Alignment. *J. Am. Chem. Soc.* **2016**, *138*, 5957–5967.

(18) Hart, H. V.; Lipscomb, W. N. Rearangements of Icosahedral Monohalo-*m*-Carboranes. *J. Am. Chem. Soc* **1967**, *729*, 3–4.

(19) Baše, T.; Bastl, Z.; Slouf, M.; Klementova, M.; Jan, S.; Vetushka, A.; Ledinsky, M.; Macha, J.; Carr, M. J.; Londesborough, M. G. S. Gold Micrometer Crystals Modified with Carboranethiol Derivatives. *J. Phys. Chem. C* **2008**, *112*, 14446–14455.

(20) Hohman, J. N.; Zhang, P.; Morin, E. I.; Han, P.; Kim, M.; Kurland, A. R.; McClanahan, P. D.; Balema, V. P.; Weiss, P. S. Self-Assembly of Carboranethiol Isomers on Au{111}: Intermolecular Interactions Determined by Molecular Dipole Orientations. *ACS Nano* **2009**, *3*, 527–536.

(21) Grimes, R. N. *Carboranes*, 3rd ed.; Academic Press: Oxford, **2016**.

(22) Binnig, G.; Rohrer, H.; Gerber, C.; Weibel, E. Surface Studies by Scanning Tunneling Microscopy. *Phys. Rev.* **1982**, *49*, 57-61.

(23) Bonnell, D. A.; Basov, D. N.; Bode, M.; Diebold, U.; Kalinin, S. V.; Madhavan, V.; Novotny, L.; Salmeron, M.; Schwarz, U. D.; Weiss, P. S. Imaging Physical Phenomena with Local Probes: From Electrons to Photons. *Rev. Mod. Phys.* **2012**, *84*, 1343–1381.

(24) Claridge, S. A.; Liao, W. S.; Thomas, J. C.; Zhao, Y.; Cao, H. H.; Cheunkar, S.; Serino, A. C.; Andrews, A. M.; Weiss, P. S. From the Bottom up: Dimensional Control and Characterization in Molecular Monolayers. *Chem. Soc. Rev.* **2013**, *42*, 2725–2745.

(25) Nuzzo, R. G.; Zegarski, B. R.; DuBois, L. H. Fundamental Studies of the Chemisorption of Organosulfur Compounds on Au(111). Implications for Molecular Self-Assembly on Gold Surfaces. *J. Am. Chem. Soc.* **1987**, *109*, 733–740.

(26) Shaporenko, A.; Ulman, A.; Terfort, A.; Zharnikov, M. Self-Assembled Monolayers of Alkaneselenolates on (111) Gold and Silver. *J. Phys. Chem. B* **2005**, *109*, 3898–3906.

(27) Laibinis, P. E.; Whitesides, G. M.; Aliara, D. L.; Tao, Y. T.; Parikh, A. N.; Nuzzo, R. G. Comparison of the Structures and Wetting Properties of Self-Assembled Monolayers of *n*-Alkanethiols on the Coinage Metal Surfaces, Cu, Ag, Au. *J. Am. Chem. Soc.* **1991**, *113*, 7152–7167.

(28) Zangmeister, C. D.; Picraux, L. B.; van Zee, R. D.; Yao, Y.; Tour, J. M. Energy-Level Alignment and Work Function Shifts for Thiol-Bound Monolayers of Conjugated Molecules Self-Assembled on Ag, Cu, Au, and Pt. *Chem. Phys. Lett.* **2007**, *442*, 390–393.

(29) Ulman, A. Formation and Structure of Self-Assembled Monolayers. *Chem. Rev*. **1996**, 96, 1533-1554.

(30) Azzaroni, O.; Vela, M. E.; Fonticelli, M.; Benítez, G.; Carro, P.; Blum, B.; Salvarezza, R. C. Electrodesorption Potentials of Self-Assembled Alkanethiolate Monolayers on Copper Electrodes. An Experimental and Theoretical Study. *J. Phys. Chem. B* **2003**, *107*, 13446–13454.

(31) Bent, S. F. Organic Functionalization of Group IV Semiconductor Surfaces: Principles, Examples, Applications, and Prospects. *Surf. Sci.* **2002**, *500*, 879–903.

(32) Buriak, J. M. Organometallic Chemistry on Silicon and Germanium Surfaces. *Chem. Rev*. **2002**, *102*, 1271–1308.

(33) Huang, F. K.; Horton, R. C.; Myles, D. C.; Garrell, R. L. Selenolates as Alternatives to Thiolates for Self-Assembled Monolayers: A SERS Study. *Langmuir* **1998**, *14*, 4802–4808.

(34) Monnell, J. D.; Stapleton, J. J.; Jackiw, J. J.; Dunbar, T.; Reinerth, W. A.; Dirk, S. M.; Tour, J. M.; Allara, D. L.; Welss, P. S. Ordered Local Domain Structures of Decaneselenolate and Dodecaneselenolate Monolayers on Au{111}. *J. Phys. Chem. B* **2004**, *108*, 9834–9841.

(35) Hohman, J. N.; Kim, M.; Schüpbach, B.; Kind, M.; Thomas, J. C.; Terfort, A.; Weiss, P. S. Dynamic Double Lattice of 1-Adamantaneselenolate Self-Assembled Monolayers on Au{111}. *J. Am. Chem. Soc.* **2011**, *133*, 19422–19431.

(36) Guttentag, A. I.; Barr, K. K.; Song, T. Bin; Bui, K. V.; Fauman, J. N.; Torres, L. F.; Kes, D. D.; Ciomaga, A.; Gilles, J.; Sullivan, N. F.; Yang, Y.; Allara, D. L.; Zharnikov, M.; Weiss, P. S. Hexagons to Ribbons: Flipping Cyanide on Au{111}. *J. Am. Chem. Soc.* **2016**, *138*, 15580–15586.

(37) Lim, M. S.; Feng, K.; Chen, X.; Wu, N.; Raman, A.; Nightingale, J.; Gawalt, E. S.; Korakakis, D.; Hornak, L. A.; Timperman, A. T. Adsorption and Desorption of Stearic Acid Self-Assembled Monolayers on Aluminum Oxide. *Langmuir* **2007**, *23*, 2444–2452.

(38) Serino, A. C.; Anderson, M. E.; Saleh, L. M. A.; Dziedzic, R. M.; Mills, H.; Heidenreich, L. K.; Spokoyny, A. M.; Weiss, P. S. Work Function Control of Germanium through Carborane-Carboxylic Acid Surface Passivation. *ACS Appl. Mater. Interfaces* **2017**, *9*, 34592–34596.

(39) Kamenetska, M.; Dell'angela, M.; Widawsky, J. R.; Kladnik, G.; Verdini, A.; Cossaro, A.; Cvetko, D.; Morgante, A.; Venkataraman, L. Structure and Energy Level Alignment of Tetramethyl Benzenediamine on Au(111). *J. Phys. Chem. C* **2011**, *115*, 12625–12630.

(40) Venkataraman, L.; Klare, J. E.; Tam, I. W.; Nuckolls, C.; Hybertsen, M. S.; Steigerwald, M. L. Single-Molecule Circuits with Well-Defined Molecular Conductance. *Nano Lett.* **2006**, *6*, 458–462.

(41) Yu, M.; Bovet, N.; Satterley, C. J.; Bengió, S.; Lovelock, K. R. J.; Milligan, P. K.; Jones, R. G.; Woodruff, D. P.; Dhanak, V. True Nature of an Archetypal Self-Assembly System: Mobile Au-Thiolate Species on Au(111). *Phys. Rev. Lett.* **2006**, *97*, 1–4.

Chapter 2: Influence of Terminal Carboxyl Group on Structure and Reactivity of Functionalized *m*-Carboranethiolate Self-Assembled Monolayers*

*Chapter 2 has been modified with permission from the following manuscript:
Dominic P. Goronzy, Jan Staněk, Erin Avery, Han Guo, Zdeněk Bastl, Michal Dušek, Nathan M. Gallup, Saliha Gün, Monika Kučeráková, Brian J. Levandowski, Jan Macháček, Václav Šícha, John C. Thomas, Adem Yavuz, K. N. Houk, Mehmet Fatih Danışman, Ersen Mete, Anastassia N. Alexandrova, Tomáš Baše, and Paul S. Weiss Influence of Terminal Carboxyl Groups on the Structure and Reactivity of Functionalized m-Carboranethiolate Self-Assembled Monolayers. Chemistry of Materials 2020, 32(1), 6800-6809.

2.1 INTRODUCTION

Two-dimensional self-assembled materials, in addition to their utility for numerous applications, are important tools in advancing our understanding of the principles of self-assembly.[1-4] As such, developing building blocks is of fundamental importance in enabling the investigation of specific steric and electronic effects or intermolecular interactions within self-assembled monolayers (SAMs).[5] Organic molecules have been extensively explored in this field, offering possible analogies to naturally occurring biological systems and allowing studies of the impact of defined chemical modifications.[2] Introduction of additional ω-functionality such as carboxyl groups resulted in different properties of the surfaces, determined by hydrogen-bonding intermolecular interactions and hydrophilicity.[6-8] Several systems, including carboxyl-terminated alkanethiols and mercaptobenzoic acids, have been investigated as convenient building blocks on both flat and colloidal surfaces.[9-11] In these particular systems, the anchoring thiol and the exposed carboxyl groups are separated by either conformationally flexible aliphatic -$(CH_2)_x$- alkyl chains or sheet-like aromatic -(C_6H_4)- benzene rings with different steric requirements and mutual interactions.

In our laboratories, we have introduced carborane building blocks that, due to symmetry, have lower total numbers and fewer defects within their molecular monolayers compared to organic systems.[5,12,13] These differences are at least partly due to their rigid molecular architectures with lower conformational freedom. Carborane–based systems enable us to obtain surface assemblies of different isomers in identical or highly similar surface patterns. The *para*-carboranethiol cage analogue of *para*-mercaptobenzoic acid has been shown to assemble into a hexagonal pattern identical to that of its non-carboxylated parent analogue, with no influence of the carboxyl group on the nearest neighbor spacing.[11] The closest hexagonal packing of

carboranethiol molecules on flat surfaces simply compares to the tightest filling of the surface by solid spheres, *i.e.*, the projection of the cage onto the surface, similar to previously observed behavior of other architecturally rigid bulk molecules such as adamantane derivatives.[14-16] The structurally rigid bodies of carboranes enable unprecedented variability of isomeric structures whilst the surface lattice remains either the same or is only gently modified.[5,17-20] In this regard, special attention has been paid to the dipole moment orientation, which is mainly given by the positioning of the carbon atoms in the cage, and to its effect on work function changes.[21-25]

Building on these advances, we prepared two isomeric bifunctional cage molecules based on the *meta*-carborane skeleton, juxtaposing them to their organic analogue, *meta*-mercaptobenzoic acid, as well as the previously studied *para*-isomer as building blocks for SAMs. Both new isomers show practically identical orientations of functional groups with respect to the centroid of the *meta*-carborane cage but differ in chemical and physical properties as determined by the electron-donating and withdrawing properties of the molecular cage scaffold. In addition, they differ in their symmetry; one of them belonging to a rather rarely investigated group of chiral cage borane derivatives.[26] Assemblies of chiral molecules on surfaces are currently of interest due to their spin-filtering effects in electron transport.[27-30]

The interactions of both functional groups, interspaced by the *meta*-carborane skeleton, were analyzed in SAMs *vis-à-vis* the differences of the two isomers. Furthermore, the effect of increased lateral interactions on the assembly of these monolayers was experimentally examined and the results were compared to computational models. Lastly, the change in behavior of the carboxyl functional group was probed, as it moves from an unrestricted three-dimensional environment to the exposed interface of a surface-bound two-dimensional array.

2.2 Results and Discussion

2.2.1 Intrinsic properties and characteristics of carboxylated *meta*-carboranes

Isomeric bifunctional carborane species were synthesized from the respective thiol derivatives of *meta*-carborane by their lithiation and subsequent reaction with CO_2 followed by acidic hydrolytic quenching: 1-SH-1,7-$C_2B_{10}H_{11}$ (**M1**) produced 1-COOH-7-SH-1,7-$C_2B_{10}H_{10}$ (**M1-COOH**) and 9-SH-1,7-$C_2B_{10}H_{11}$ (**M9**) was transformed into *racem*-1-COOH-9-SH-1,7-$C_2B_{10}H_{10}$ (**M9-COOH**). Detailed procedures and a schematic representation are available in the supporting information (Scheme S1). X-ray diffraction studies confirmed that the two isomers have nearly identical geometries with the angle α[C_{COOH}, centroid, S_{SH}] of 114.54° in **M1-COOH** and 115.31° in **M9-COOH**. Figure 1 shows the crystallographically determined structures of these two isomers. Computationally optimized geometries, also shown in Figure 1, were consistent with experimental data and include the projections of the orientations and the relative strengths of the dipole moments. Both isomeric molecules exhibit different molecular symmetries due to the specific positioning of functional groups on the *meta*-carborane cluster core, which are reflected in their ^{11}B NMR and ^{1}H NMR spectra (Figures 2.S1-2.S5, Tables 2.S1-2.S3). For both of these isomers the carboxyl group is attached to an electron-accepting carbon vertex; the thiol functional group in **M1-COOH** is also attached to an electron-accepting carbon vertex, in contrast to an electron-donating boron vertex in **M9-COOH**. The **M9-COOH** isomer is chiral with both enantiomers resolved in a racemic single-crystal structure analyzed by X-ray diffraction (Figures 2.S6-2.S8, Tables 2.S4 and 2.S5). The two isomers exhibit similar intermolecular hydrogen interactions in their supramolecular crystal structures, dominated by the carboxyl and thiol functional groups. Additionally, the two molecules showed similar isotopic distributions in their ESI mass spectra and were further characterized by infrared spectroscopy (Figures 2.S9-2.S20).

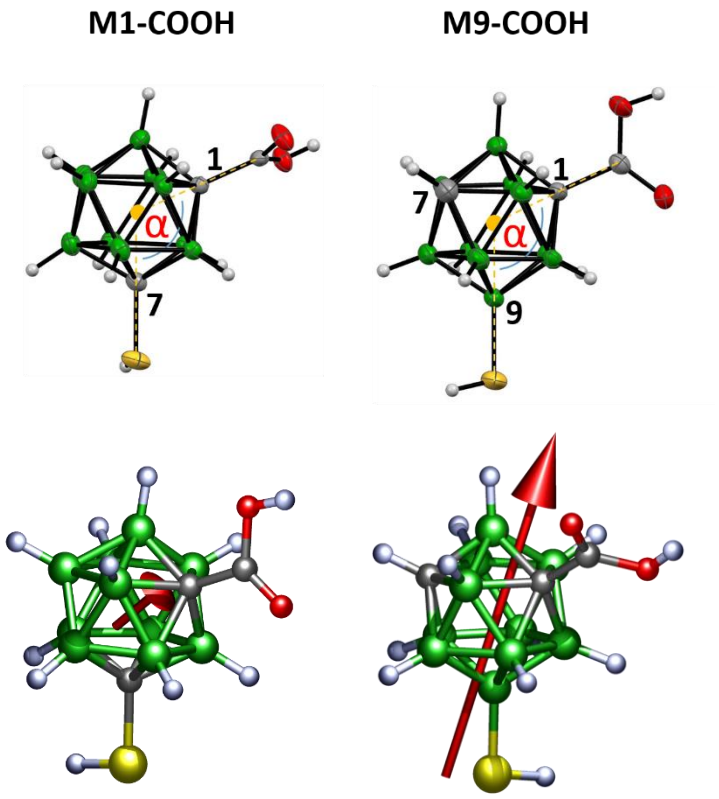

Figure 2.1. Structures of carboxylated *meta*-carboranethiol isomers. Crystallographically determined molecular structures of **M1-COOH** and **M9-COOH** with 50% probability ellipsoids for the non-hydrogen atoms (upper panel). The lower schematics of both isomers show computationally optimized structures with arrows indicating the orientations and the relative magnitudes of the dipole moments, 0.57 D for **M1-COOH** and 2.58 D for **M9-COOH**. The yellow dots in the crystallographically determined structures represent the centroids of the C_2B_{10} cage parts of the molecules. Boron atoms are shown in green, carbon atoms are shown in gray, oxygen atoms are shown in red, sulfur atoms are shown in yellow, and hydrogen atoms are shown in white.

The differences between the effects of the electron-accepting carbon and the electron-donating boron vertices on the thiol group are consistent with previous studies, which relate the

thiol group character to the type of the carborane skeleton (*ortho*-, *meta*-, or *para*-) and to the thiol group's position on the cage.[31-34] The new bifunctional molecular system with one carboxyl group and one thiol group enabled us to investigate their mutual influence on their positions on the *meta*-carborane cage. In the case of **M1-COOH**, both functional groups are attached to the carbon atoms, the electron-withdrawing vertices of the *meta*-carborane scaffold. In the isomer **M9-COOH**, the thiol group is attached to a boron atom, through which *meta*-carborane manifests a relatively strong electron-donating effect. Table 2.1 provides a summary of selected characteristic parameters related to the chemical nature of the functional groups; these properties are important for their intramolecular communication, as well as for their roles in self-assembly, as discussed below. The ^{1}H NMR shifts of the respective thiol groups and the carboxyl pK_a values of both isomers are displayed in Table 2.1 (See also Tables 2.S1 and 2.S2 and Figures 2.S4 and 2.S21). For comparison, the pK_a value of the *meta*-carborane-1-carboxylic acid (**M-COOH**) is also reported. Both **M1** and **M1-COOH** show practically the same values of ^{1}H NMR shift of their thiol groups, at *ca*. 3.4 - 3.5 ppm. In comparison, the ^{1}H NMR shifts of the thiol groups in both **M9** and **M9-COOH** are lower, at about 0.5 ppm, which is in accord with the electron-donating character of the boron vertex of *meta*-carborane. Note that the thiol chemical shifts in the ^{1}H NMR spectrum not only manifest the electron-accepting (as in **M1** or **M1-COOH**) and electron-donating (as in **M9** and **M9-COOH**) effects of the *m*-carboranyl cage moiety but also show, consistent with our previous findings, that the carboxyl group does not significantly influence the thiol group in this regard. By contrast, the thiol group interacts significantly with the molecular skeleton and thus increases the carboxyl group acidity as evident from the lower pK_a values in both isomers compared to **M-COOH** (1-COOH-*m*-$C_2B_{10}H_{11}$) (For characterization data on this molecule see Figures 2.S5, 2.S17, and 2.S20 and Table 2.S3).

Table 2.1. Experimental ^{1}H NMR chemical shifts of the thiol (SH) groups and the carboxyl (COOH) pK_a values of the new isomeric derivatives and their parent compounds.

Derivative	^{1}H NMR (SH)	pK_a (COOH)
M1	3.39	–
M1-COOH	3.46	3.01
M9	0.47	–
M9–COOH	0.52	3.23
M–COOH	–	3.76

2.2.2 Characterization of Self-Assembled Monolayers *via* Scanning Tunneling Microscopy

Scanning tunneling microscopy (STM) was used to image homogeneous SAMs of both **M1-COOH** and **M9-COOH** on Au{111}/mica with molecular resolution under ambient conditions. Both isomers form into hexagonal close-packed structures with nearest-neighbor distances of 8.4 ± 0.4 Å (Figures 2.2 and 2.S22). These results are remarkable given that in the previous study of the *para*-isomer, molecularly resolved images of the homogeneous carboxylic-acid terminated monolayer were unattainable.[11] We hypothesize the orientation of the carboxyl group directly into the environmental interface in the case of the *para*-isomer results in greater conformational freedom and greater interaction with ambient water, which thereby leads to a lack

of molecular resolution. Additionally, the attachment of a carboxyl group to the parent molecules, **M1** and **M9**, increases the steric demands of both isomeric molecules as compared with the lateral steric requirements of the parent non-carboxylated derivatives, which both have nearest-neighbor distances of 7.2 ± 0.4 Å.[12] The molecular symmetry differences between the isomers have no direct influence on the geometry of the surface lattice, as evidenced by isostructural monolayers with experimentally indistinguishable nearest neighbor spacings. Two phases were observed in the monolayers, which differed in apparent height by 1.0 ± 0.3 Å in both **M1-COOH** and **M9-COOH** SAMs. The higher apparent protrusion is the minority phase with coverage of 3 ± 1% in SAMs of both isomers (Figure 2.S23). This feature has been observed previously and attributed to a mixture of thiolate- and thiol-bound moieties, with the latter being the more protruding apparent height feature in STM images.[11] Alternatively, the carboxylic acid may have partially converted to an ester in the molecules in the minority phase, as the relative population size of the phase is consistent with spontaneous esterification. We also observed rotational domains in the monolayers and, as has been reported previously for other carboranethiol SAMs, these domains did not have prominent domain boundaries in STM images.[12]

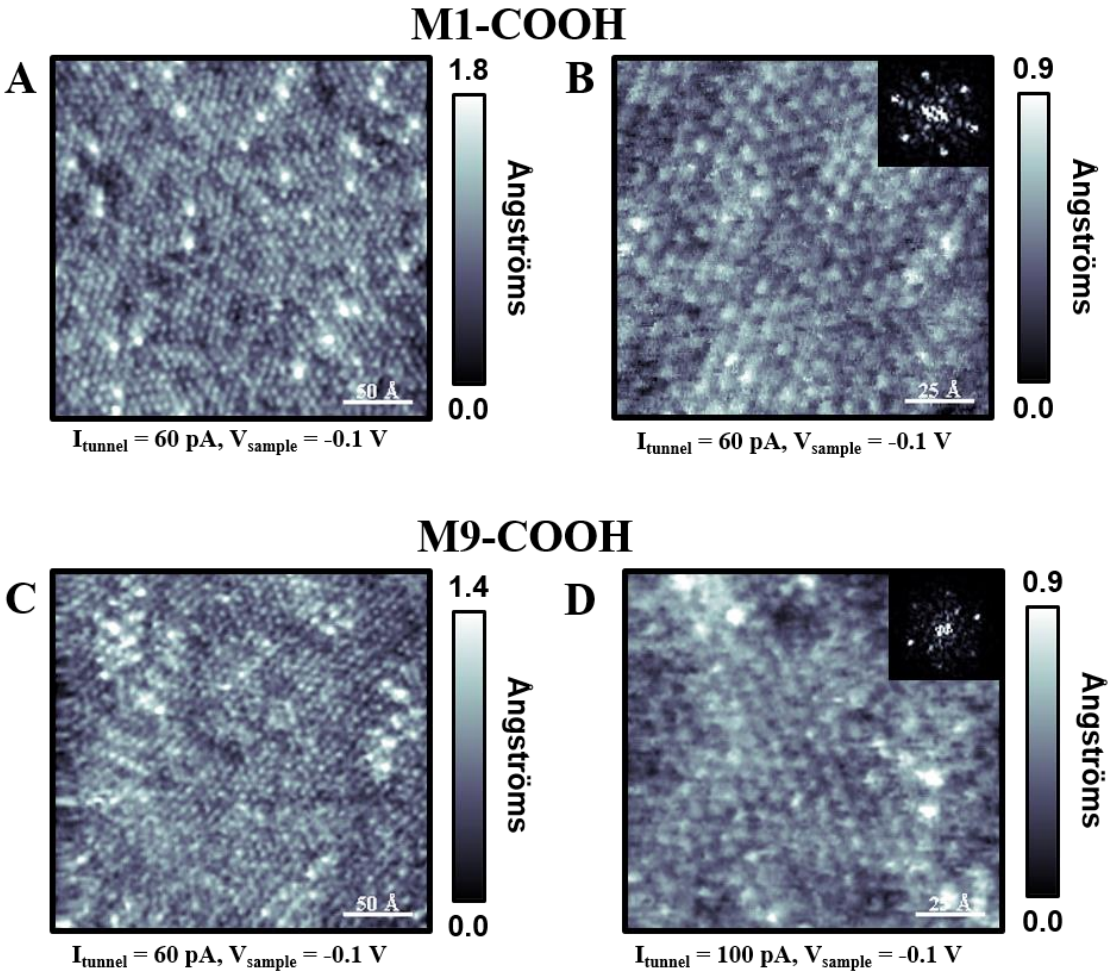

Figure 2.2. Scanning tunneling microscopy images of (A,B) **M1-COOH** and (C,D) **M9-COOH** self-assembled on Au{111}. All images were taken at ambient conditions. Insets depicting Fourier transforms of (B) and (D) show hexagonal close-packed arrays with identical nearest-neighbor distances of 8.4 ± 0.4 Å for both isomers.

The possible unit cells that are commensurate with the unreconstructed Au{111} substrate are (5 × 5) and (3 × 3), have nearest–neighbor distances of 8.3 Å and 8.64 Å, respectively, with reference to the 2.88 Å lattice constant of the substrate surface. Both are within experimental error of the determined values. The (3 × 3) unit cell consists of one SAM molecule binding with its

sulfur atom to a two-fold bridge site, while the (5 × 5) unit cell consists of three SAM molecules binding atop and three-fold hollow sites in a 1:2 ratio.

2.2.3 Computational Analysis of the Self-Assembled Monolayer Structure

As determined by the STM analysis, the presence of a carboxyl functional group increases the steric demands of the molecules within the SAM. To explore these lateral interactions further, we performed several computational analyses. In examining the space-filling model from projection onto the surface, we find that a molecular tilt of 13-16° minimizes the projection area and therefore maximizes the packing density. This minimum corresponds to a nearest-neighbor distance of 8.6 Å, which is in close agreement with what we observed experimentally with STM (Figure 2.3).

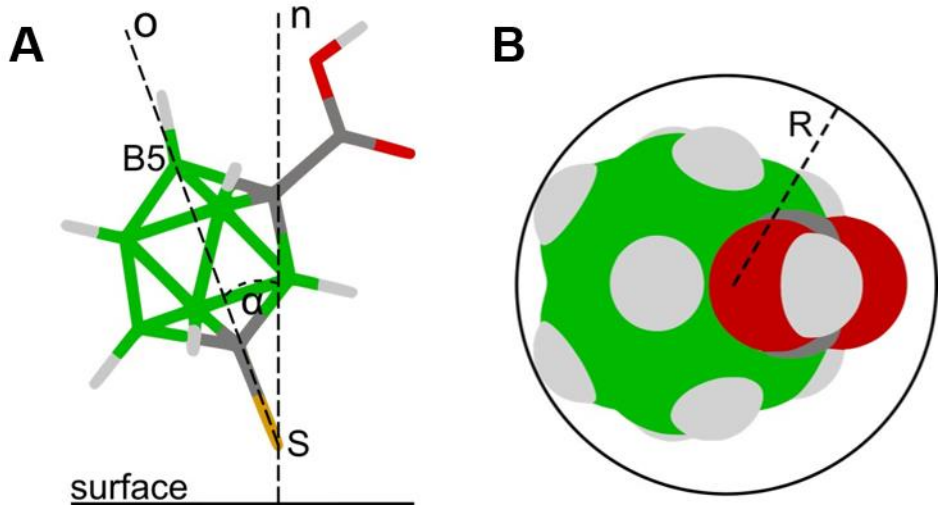

Figure 2.3. (A) Schematic representation of the isomeric molecule **M1-COOH** tilted 13-16° (α) from the surface normal and (B) the respective space-filling model projection onto the surface (R=8.6 Å).

Although this geometric, space-filling model is highly intuitive and the nearest-neighbor distance derived from it corresponds well to the experimental data, it also requires assumptions about the rigidity of the molecule, such as the static axis intersecting the sulfur atom and the antipodal boron vertex. We performed density functional theory (DFT) calculations using the SCAN-rVV10 functional for both isomeric species to provide rigorous details about the molecular tilt on the surface. Both the (3 × 3) and (5 × 5) unit cells were examined, but only the (3 × 3) unit cell corresponds to a densely packed monolayer and thus provides a comparison to the acquired experimental data. The computationally calculated nearest-neighbor distance of the (5 × 5) unit cell was 13.72 Å, which deviated significantly from what was experimentally measured. The results of the (3 × 3) unit cell model are summarized in Table 2.2 and depicted in Figure 2.4. Optimized geometries revealed two different conformations (A and B), one of which shows the molecule tilted backwards to expose the carboxyl group to the monolayer-environment interface (A); the other conformation shows the molecule leaning with the carboxyl group towards the neighboring molecule and hydrogen bonding in the lateral direction (B). While the first conformation can be understood as a result of favorable steric preferences, the second conformation could result from favorable lateral interactions between the positively charged carboxyl proton and negatively charged cluster vertices of the adjacent molecule. Similar interactions between acidic hydrogen atoms and BH cluster vertices of the appropriate charge have been reported previously to occur in 3D single crystals.[35] The energy difference between geometries A and B is relatively small, ~1 kJ·mol^{-1} (Figure 2.4), and as a result the configurations are practically indistinguishable.

Computationally, **M1-COOH** is found to be stable in both conformations while **M9-COOH** is only stable in configuration B. However, we do *not* see evidence for the existence

of two conformations in the STM data; we see neither a mixture of configurations A and B in SAMs of **M1-COOH** nor structural differences between the SAMs of the two isomers. It is possible that ambient STM cannot differentiate between the two configurations. Calculations show that the charge density that the STM probes is located mostly in the central cage of the molecule and, as such, the two configurations would look similar; this observation is further supported by simulated STM images (Figures 2.S24 and 2.S25). Thus, it is inconclusive whether both configurations occur in the SAMs simultaneously or only one configuration is present.

Moreover, as with many other cage-molecule SAMs, we do not observe the typical domain boundary defects that accompany molecular tilt, which the computational analysis predicts are required in order to achieve the experimentally observed packing density. One possible explanation for the absence of tilt defects is that long-range intermolecular interactions, which in the case of these molecules could be a combination of hydrogen-bonding and favorable dipole-dipole interactions, have azimuthally locked the molecules into one orientation. Note that only in configuration B, in which molecules lean on their neighbors and form rows, are hydrogen-bonding interactions possible and computationally predicted. Both hydrogen-bonding networks and dipole-dipole interactions have previously been shown to overcome structural domain boundaries in SAMs.[22,36] Additionally, given the propensity of carboxylic acids to form dimers, we modeled this interaction. The model predicted that this interaction is only stable with a significantly larger nearest neighbor spacing in a (6 × 3) unit cell (Figure 2.S26). Given this model and the fact that we do not see any evidence of dimers in the STM data, it is unlikely that they are present in the SAMs. Lastly, we note that the computational model does not incorporate adatoms in the computation; adatoms have previously been shown to significantly contribute to the structural characteristics of SAMs on gold surfaces.[37-39]

Table 2.2. Dissociative chemisorption energies, E_C (eV), and molecular tilt angles $\Theta_{S\text{-}Cage}$ (°) and Θ_{Cage} (°) schematically shown in Figure 2.S27.

Configuration		E_C (eV)	$\Theta_{S\text{-}Cage}$ (°)	Θ_{Cage} (°)
M1-COOH	(3 × 3) A	-1.56	36.2	28.7
M1-COOH	(3 × 3) B	-1.57	21.6	16.7
M9-COOH	(3 × 3) B	-1.60	15.5	10.5

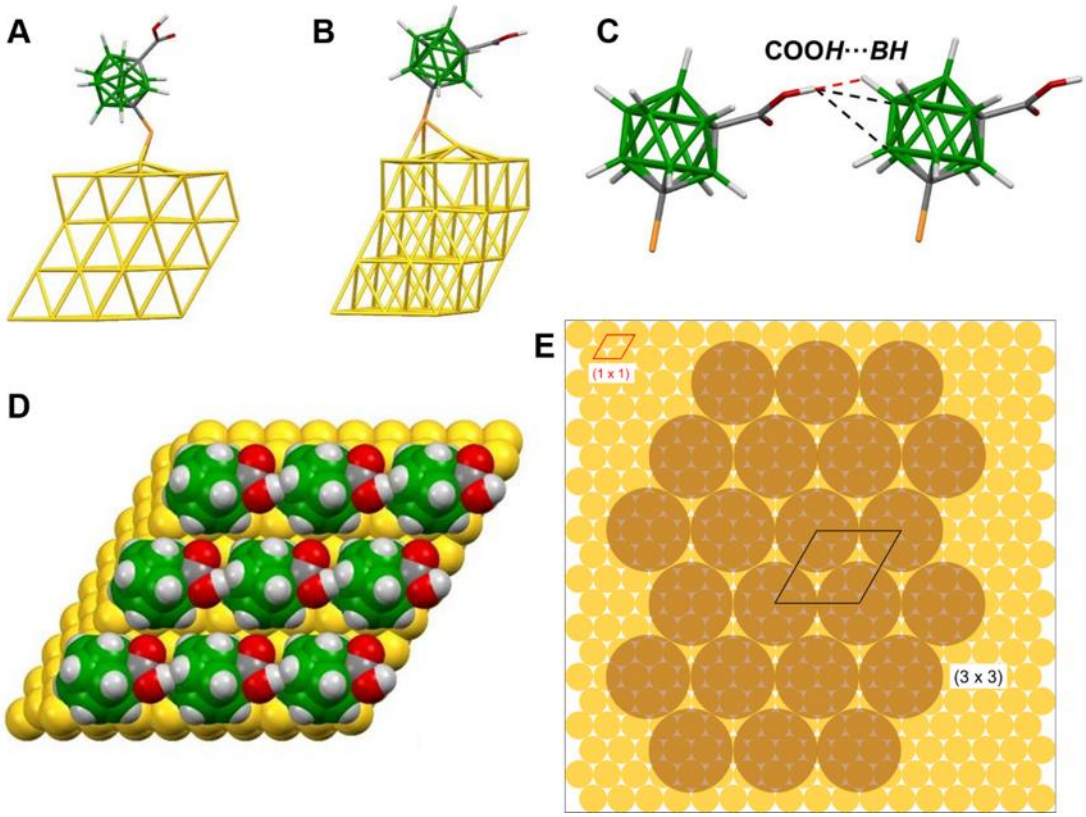

Figure 2.4. (A,B) Two stable calculated conformations of **M1-COOH**. (C) Schematic of calculated potential lateral hydrogen bonding of COOH—HB (red) and COOH—BH (black), with bond lengths of 1.826 Å and 2.833 Å, respectively. (D) Space-filling model and (E) schematic of a densely packed monolayer with a (3 × 3) unit cell with respect to the underlying gold.

2.2.4 Interactions with the Au{111} Substrate

The bonding of both isomeric molecules to gold surfaces was investigated by X-ray photoelectron spectroscopy (Table 2.3), which showed the molecules adsorb as thiolates. The measured atomic concentrations of boron and sulfur fitted the nominal stoichiometry of the molecules, $B_{10}S_1$. The measured binding energy values of S $2p_{3/2}$ electrons at 162.3 eV for **M1-COOH** and at 161.7 eV for **M9-COOH** indicated typical thiolate bonds. The difference of ~0.6 eV between the isomers is consistent with the previously discussed electron-accepting and donating properties of the particular *meta*-carborane vertices in the SAM molecules. In **M9-COOH**, the *meta*-carboranyl moiety increases the electron density on the thiolate sulfur atoms, which leads to the lower binding energy value of the S $2p_{3/2}$ electrons compared to **M1-COOH**.

Table 2.3. Measured core-level binding energies and full width half maxima (in parentheses) for Au films modified with **M1**, **M9**, **M1-COOH**, **M9-COOH**.

Sample	S $2p_{3/2}$
M1	162.2 (0.8)
M1-COOH	162.3 (0.8)
M9	161.7 (0.8)
M9-COOH	161.7 (0.8)

2.2.5 Carboxylic Acid at the Exposed Interface

Anchoring the isomeric molecules to gold surfaces gives us the opportunity to probe the chemical character of the exposed carboxyl groups, which enables the SAMs to engage in further

interactions and reactions. We have examined the carboxyl functional group by measuring dynamic contact angles (Table 2.4) and probed the accessibility for further chemical bonding with several ions. In both cases, the constituent makes the surface more hydrophilic compared to SAMs of their parent non-carboxylated derivatives **M1** and **M9**.

Table 2.4. Dynamic contact angles for parent **M1** and **M9** isomeric species, as reported in Ref.,[12] and the respective carboxylated analogues **M1-COOH** and **M9-COOH** assembled on gold surfaces. (N = 8)

Sample	Θ_a	Θ_r
M1[12]	82 ± 2	71 ± 1
M9[12]	72 ± 4	52 ± 1
M1-COOH	61 ± 1	42 ± 1
M9-COOH	66 ± 1	55 ± 1

Θ_a: advancing contact angle, Θ_r: receding contact angle

To study the sensitivity of the carboxyl group to the attachment of a thiol group at either the second carbon or the boron atom of the *meta*-carborane skeleton, we analyzed the carboxyl group acidity of both isomers assembled on gold surfaces, *i.e.*, after the thiol group scission and thiolate-gold bond formation. We probed the acidity on the surface *via* contact angle titration.[40] In this titration, the advancing contact angle is measured over a range of pH points. A decrease in the contact angle signifies deprotonation as the newly formed ion increases the surface hydrophilicity. The midpoint between the protonated and deprotonated states can be defined as the apparent surface pK_a. To control for confounding factors of acidic pH on surface assemblies, we used

starting pH between 2 and 4 in the titration experiments, with similar results. The results of the contact angle titration provided an apparent surface pK_a of 5.1 ± 0.6 and 4.8 ± 0.7 for **M1-COOH** and **M9-COOH**, respectively (Figure 2.5). By comparison, the control experiment **M9** SAM shows no change in contact angle as a function of pH (Figure 2.S28). Thus, the pK_a shifts from solution to surface by approximately two pH units for both isomers, consistent with previous observations with carboxyl-terminated monolayers.[40,41] The two isomers did not significantly differ in apparent surface pK_a although we may have missed smaller differences due to variability of measurements; controlling for several technical variables, including ambient humidity, batch-to-batch variation, and substrate fabrication did not reduce the measurement variability.

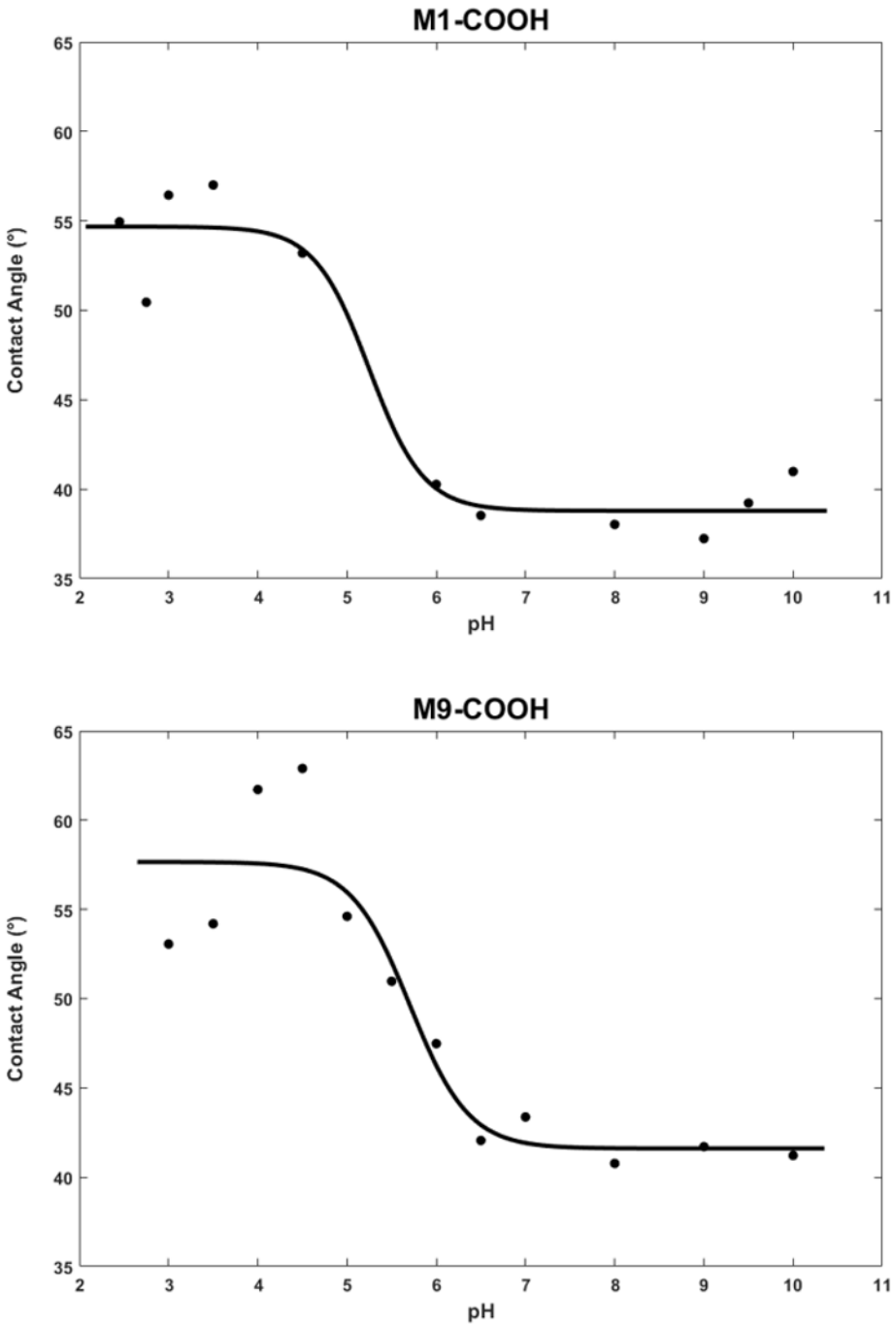

Figure 2.5. Representative contact angle titration curves for (top) **M1-COOH** and (bottom) **M9-COOH**. The surface pK_a for the two isomers are 5.1 ± 0.6 and 4.8 ± 0.7, respectively (N=5).

To understand the altered state of the carboxylic acid on the surface, we performed computational modeling and explored possible mechanisms that could drive the shift in pK_a from solution to surface. Previous studies have suggested that the decreased dielectric on the surface could be a driving force.[41,42] Alternatively or in addition, the thiol deprotonation upon surface binding may have a similar effect on the carboxylic acid. However, our computational analysis showed that the charge density of the adsorbate molecule when bound to the surface as a thiolate is similar to the molecule with a protonated thiol for both models with and without solvent (Figures 2.S29-2.S32 and Tables 2.S6 and 2.S7). Given these results, it appears unlikely that the shift in pK_a is a result of the thiol deprotonation upon surface binding and additionally that the thiol form might represent a reasonably simplified model for further computational analysis. We proceeded to calculate the predicted pK_a of a single molecule in water for both isomers. In both cases, the predicted pK_a was lower than what we observed experimentally in solution titrations with differences of 1.9 and 2.2 for **M1-COOH** and **M9-COOH**, respectively (Table 2.S8).

To assess the effect of the dielectric on the surface, we first looked at the pK_a shift due to interactions between neighboring molecules, in the form of a dimer model (Figure 2.S33). These calculations predicted increases in pK_a for both isomers with pK_a shifts from single-molecule to dimer configurations of 1.9 and 1.1 respectively for **M1-COOH** and **M9-COOH (**Table 2.S9**).** These shifts are comparable to, but somewhat smaller than what we see experimentally between solution and surface pK_a, suggesting that molecular interactions within the monolayers play major roles in the differences between the unrestricted three-dimensional and surface-constrained two-dimensional environments, but that there may be other influencing factors. Additionally, for the shifts given above, the molecular dimers were in configuration B as shown in Figure 4, with the carboxyl group positioned more laterally. We also modeled a dimer in configuration A for

M1-COOH, which had a pK_a shift of only 0.1 from the free molecule. This model suggests that the characteristics of configuration A are similar to a free molecule in solution, further indicating that it is configuration B that is present on the surface for both isomers. We further calculated a range of pK_a *vs.* dielectric by modeling the molecule in different solvation fields for both **M1-COOH** and **M9-COOH** (Figure 2.6)**.** For both isomers, the modeling shows exponential trends that as dielectric decreases, pK_a increases. The corresponding dielectric based on the pK_a in the dimer configuration is 17 for **M1-COOH** and 25 for **M9-COOH**. Overall, our computational analyses suggest that the shift in pK_a is driven by the dielectric of the environment that the carboxyl group experiences on the surface. The interactions with neighboring molecules factor into this dielectric, but proximity to the Au surface and partial desolvation also make contributions. The computational model does take into account the effect of desolvation, but does not take into account the presence of the surface. However, given that the Au surface is separated from the carboxyl group by the molecular backbone, we believe that this model is a reasonable simulation of the surface environment.

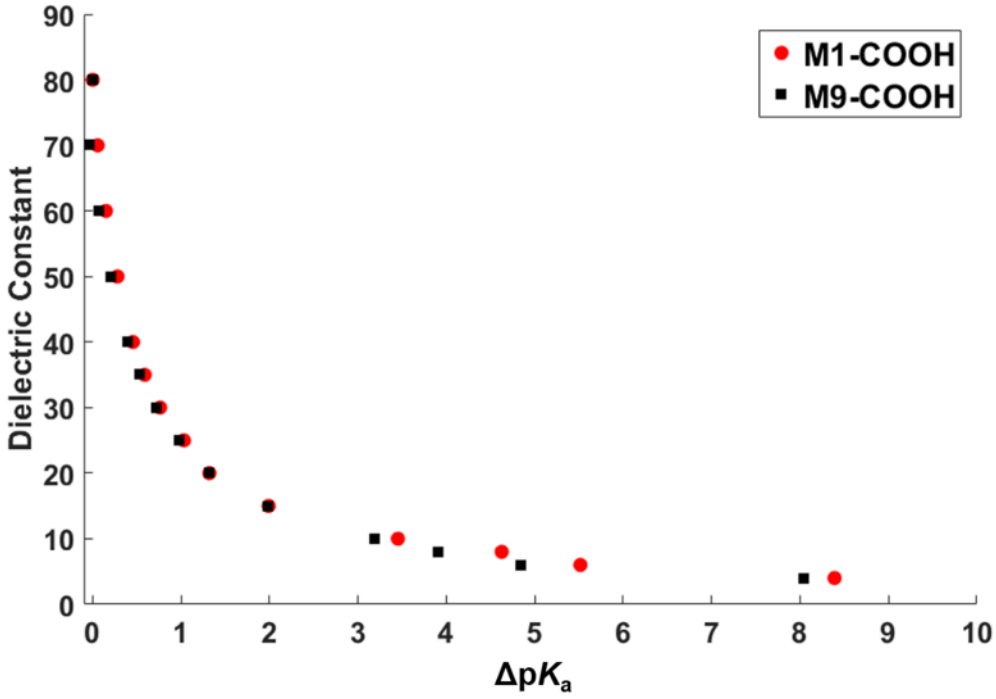

Figure 2.6. Computational results of the pK_a shift (ΔpK_a) in solvents with a range of dielectric constants for both isomers. The results show exponential relationships between the pK_a and the dielectric. Based on the pK_a calculated for the dimer configurations, the associated dielectrics are 17 and 25 for **M1-COOH** and **M9-COOH**, respectively.

Accessibility of carboxyl groups for surface-supported coordination chemistry was probed experimentally by examining the interactions between carboxyl-terminated SAMs and various ions.[43-45] The SAMs of the carboxylated isomers were exposed to dilute solutions of metal cations and the formation of metal coordination complexes was analyzed *via* XPS (summaries of the XPS investigations and the XPS spectra used for quantitative analysis are presented in the Supporting information, Tables 2.S10-2.S12 and Figures 2.S34 – 2.S45). A total of 16 representative ions from across the periodic table were used Na(I), Mg(II), Ca(II), Sr(II), Ba(II), Fe(II), Fe(III), Co(II), Ni(II), Cu(II), Zn(II), La(III), Sm(III), Tb(III), Tl(I), and Pb(II). All of the ions interacted with the

carboxyl-terminated SAMs and successfully replaced the intrinsically present Na(I) ions, which might originate from the solvents or glassware used for the preparation of the samples, as has been reported previously in literature[46] (detailed procedures for sample preparation for XPS are available in the Supporting information). Both starting SAMs of **M1-COOH** and **M9-COOH** were examined broadly; since the SAMs were found to have indistinguishable surface patterns and practically identical chemical behaviors, SAMs of **M9-COOH** were examined in greater detail. Also, SAMs of the **M9** isomer were used as control samples to test if the ions bind exclusively to the carboxylic moiety. The SAMs of **M9** were analyzed both before and after exposure to solutions of Na(I) and Mg(II) ions with no metal ions detected in those samples with XPS.

In addition, quantitative XPS analyses determining the metal ion/**M9-COOH** surface ratios for the pristine **M9-COOH** SAM and for the **M9-COOH** SAM modified with Mg(II) and Ba(II) ions, summarized in Table 2.5, indicate possible formation of bridging intermolecular surface complexes within the adsorbed monolayers, which is of interest due to its additional stabilizing effects.

Table 2.5. Measured ratios of the number of deposited metal ions to the number of **M9-COOH** molecules within the self-assembled monolayers (SAMs), together with the nominal kinetic energies of the photoelectrons used for the quantification of the metal ion (in parentheses).

SAM	Metal ion	Metal ion/**M9-COOH** ratio (binding energy used)
M9-COOH	Na	0.8 (415 eV)
M9-COOH + Mg(II)	Mg	0.3 (1180 eV), 0.5 (183 eV)
M9-COOH + Ba(II)	Ba	0.5 (706 eV)

Carboranethiol SAMs used in this study were labile under excess acidic conditions. Losses of surface coverage have been observed in XPS as the stoichiometries of the acidified monolayers exhibited higher content of the substrate gold when compared to the pristine SAMs, due to the removal of carboranethiol molecules (Table 2.S11). Our previous investigations of SAMs of *para*-carboranedithiol, 1,12-$(SH)_2$-1,12-$C_2B_{10}H_{11}$ (**P1,12**), *para*-carboranethiol, 1-SH-1,12-$C_2B_{10}H_{11}$ (**P1**), and of its carboxylated derivative, 1-COOH-12-SH-1,12-$C_2B_{10}H_{10}$ (**P1-COOH**) showed that a fraction of molecules physisorbed as thiols and are thus more prone to desorption.[11,47] The thiol and thiolate species are easily distinguishable in XPS. The S 2p binding energies (BEs) of both free and adsorbed thiols are shifted by about +2 eV with respect to the corresponding thiolate forms (Figure 2.7). Desorption has been observed for all the samples subjected to relatively strong acidic environments, *i.e.* SAMs of **M9** and **M9-COOH**, and **P1-COOH**, which have been used as a comparison and also as a reference to our previous studies. The labile character of SH-bound carborane moieties makes them easy to wash from the surface and consequently leaving only the

stronger thiolate-bound moieties and more of the bare gold surface exposed to XPS analysis. We assume that the anchoring thiolate group becomes protonated under acidic conditions, and the physisorbed thiol species are then easily washed away by rinsing in an excess of pure solvent,

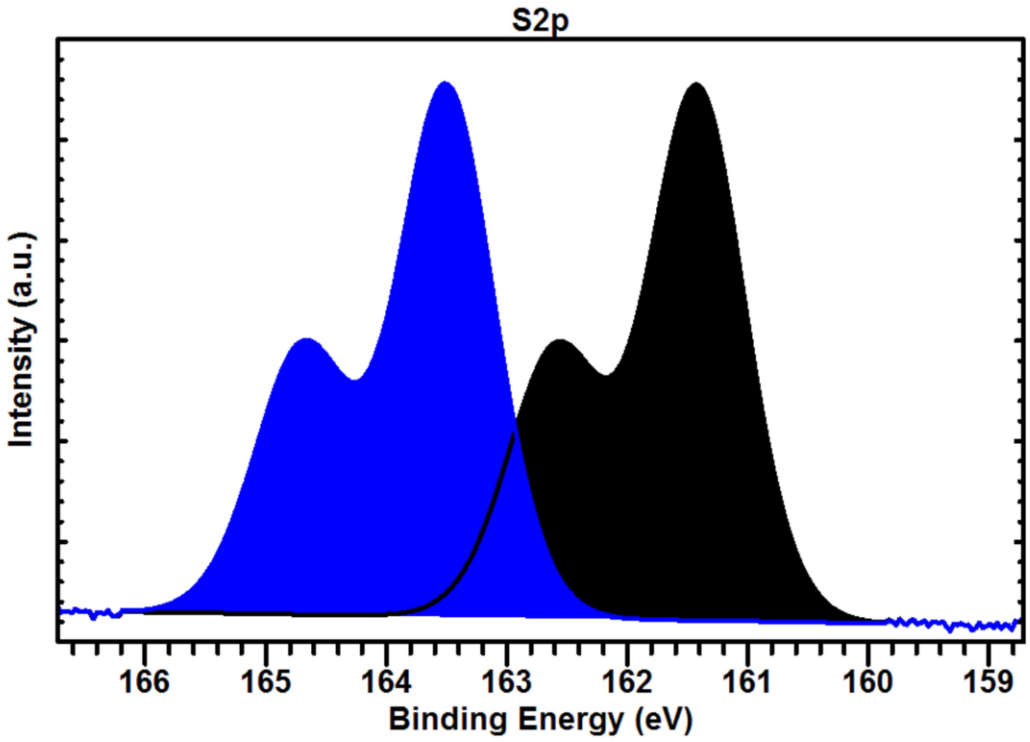

Figure 2.7. Experimental XPS spectra showing the difference in the binding energies of S 2p doublets of thiolate (black) and thiol (blue) forms of **M9-COOH**. The illustration shows an overlay of the respective mono- and di- sodium salts of 1-carboxyl-9-mercapto-*meta*-carborane S 2p regions.

2.3 CONCLUSIONS AND PROSPECTS

Two new isomeric bifunctional cage molecules, derived from 12-vertex *m*-carborane, were synthesized and characterized using structural and spectroscopic methods. Both new building blocks for self-assembled monolayers on Au surfaces have greater steric demands compared to their parent non-carboxylated derivatives. The impact on the structural and chemical properties of these building blocks on the properties of their respective SAMs was investigated. These molecules represent systems that enable analyses of intramolecular communication between functional groups interspaced by *meta*-carborane skeletons. The effects of the carboxyl group are neither detected on the free thiol group in the ^{1}H NMR spectrum nor on the BE value of S $2p_{3/2}$ electrons upon surface adsorption. Both isomers show greater carboxyl group acidities compared to 1-COOH-*meta*-carborane reference, which are attributed to the effects of the thiol groups. This result is of general interest due to the *pseudo*-aromatic character of carboranes and their skeletal interactions with a wide range of functional groups. Although the molecules of both isomers exhibit different symmetries with one isomer being chiral, they arrange into identical hexagonal close-packed arrays on Au{111}. The greater steric demands of both isomers compared to their parent non-carboxylated molecules lead only to increases of the nearest neighbor spacings from 7.2 ± 0.4 Å to 8.4 ± 0.4 Å, relative to unfunctionalized carboranethiols, which is in good agreement with tilting the molecules 13-16° to minimize their lateral steric requirements and to maximize packing density. The addition of a lateral carboxyl group thus exerts a significant influence on the nearest neighbor spacings in the SAM. Analyses of the surface structure also suggest the presence of long-range interactions, which could be due to a combination of hydrogen-bonding and favorable dipole-dipole interactions within the monolayer. The interactions of both isomeric molecules with gold surfaces were investigated by XPS, which shows that the molecules adsorb

as thiolates. More detailed measurements show that the binding energies of S $2p_{3/2}$ electrons are influenced by electron-accepting and electron-donating properties of the carboranyl moiety. The assemblies also showed changes in the behavior of the carboxyl terminus at the environmental interface of the monolayer, resulting in pK_a shifts of ~2 pH units. Based on computational modeling, this shift appears to be a result of the dielectric of the environment that the carboxyl group experiences; this dielectric is determined by the interactions between neighboring molecules, proximity to the Au surface, and partial desolvation. The exposed surfaces of the SAMs are also accessible for several different types of ions to interact with the carboxylic group. These results show that the carboxyl-terminated *meta*-carborane building blocks open the monolayers to further interactions with different types of ions or molecules.

Understanding the influence on assembly and the reactivity of the carboxylic group in these carboranethiolate monolayers lays the groundwork for performing additional chemistry and developing further applications using the reactive interfaces. The tunable characteristics of carboranethiolate SAMs along with their pristine and essentially defect-free morphology make them advantageous for use in nanoscale devices and organic electronics. These terminal carboxylic acids provide an avenue for fabricating three-dimensional heterostructures by facilitating such techniques as atomic layer deposition. Furthermore, given the acid-base reactivity of these SAMs there is also opportunity for their use in pH sensors. The addition of a reactive platform to these monolayers, combined with their already existing useful features, provides a foundation for both fundamental chemistry questions and further applications, which would not be feasible with other systems.

Shifts in pK_a, similar to those we report on in this study, have been observed in protein systems and are linked to the dielectric of the microenvironment.[48-50] Our interest and detailed

analysis of the surface-bound carboxyl functionalities and their respective chemical state and behavior is applicable to designing materials with adjustable and bio-responsive functions. To expand on this idea, amino acids in proteins experience multiple microenvironments and their pK_a values, along with the structure of the protein, adjust accordingly to facilitate function and catalysis.[48,51,52] These functionalized carboranethiolate monolayers serve as model platforms to study the driving forces relevant to pK_a changes in more complex biological and chemical systems.[52,53] Given the two-dimensional nature of these monolayers, they are particularly relevant for comparison to naturally occurring membrane-bound biological structures with constraints similar to those found in 2-dimensional self-organized arrays.

2.4 Materials and Methods

2.4.1 Chemicals

The starting *meta*-carborane, 1-SH-*m*-carborane (**M1**), and 9-SH-*m*-carborane (**M9**) were purchased from Katchem s.r.o. and used as received in further synthesis. *n*-Butyllithium (2.5 M in hexanes) was purchased from Sigma-Aldrich. Diethylether (p.a. grade, Penta s.r.o., Czech Republic) was additionally dried with sodium in the presence of benzophenone (99.8%, purchased from Sigma-Aldrich). Aqueous solution of hydrochloric acid (33%, p.a. grade) and magnesium sulphate anhydrous (p.a. grade) were both used as received from Penta s.r.o. NMR spectra were measured in $CDCl_3$ (99.8% D) as received from Eurisotop.

2.4.2 Synthesis

1-Mercapto-1,7-dicarba-*closo*-dodecaborane-7-carboxylic acid (**M1-COOH**) and 9-mercapto-1,7-dicarba-*closo*-dodecaborane-1-carboxylic acid (**M9-COOH**) were synthesized by lithiation of their parental thiol derivatives with two equivalents of *n*-BuLi and subsequent reaction with carbon dioxide, followed by quenching with an aqueous solution of hydrochloric acid (Scheme 2.S1).

1-COOH-1,7-$C_2B_{10}H_{11}$

(M-COOH)

meta–Carborane (4 g, 27.7 mmol) was dissolved in ~80 ml of dry and freshly distilled diethyl ether under argon atmosphere and cooled to ~-78 °C (dry ice/acetone). *n*–Butyllithium (10.2 ml, 25.5 mmol) was added dropwise over 5 min and the mixture was further stirred for 1 h. Excess dry ice was added and the mixture was then left at room temperature to warm up slowly, within approximately 1 h, under argon atmosphere. A white precipitate was observed in the mixture. Distilled water (50 ml) was added, the mixture was well shaken, and the ether fraction was separated. The aqueous solution was acidified with 30 ml of aqueous solution of hydrochloric acid (~15%) and white solid immediately precipitated. The mixture was extracted 3× with 30 ml of Et_2O and the collected ether fractions were dried over anhydrous $MgSO_4$ overnight. The mixture was filtered, solvent evaporated under reduced pressure on a rotary evaporator and the crude product was crystallized from a saturated pentane/chloroform (1/1) solution in a freezer (-20 °C) as a white crystalline product. Yield: 1.7 g (33%). This synthesis follows protocols in the literature and the characterization results were in full agreement with published reports.[34,54,55]

1-COOH-9-SH-1,7-$C_2B_{10}H_{10}$

(M9-COOH)

9-Mercapto-*meta*-carborane (3.0 g, 17.0 mmol) was dissolved in ~200 ml of dry and freshly distilled diethyl ether under argon atmosphere and cooled to ~-78 °C (dry ice/acetone). *n*-Butyllithium (15.0 ml, 37.5 mmol) was added dropwise over ~10 min. White solid precipitated shortly after the addition of *n*-butyllithium and the mixture was further stirred for 1 h. Excess dry ice was added and the mixture was then left at room temperature to warm up slowly (~1 h) under argon atmosphere. White precipitate was observed in the mixture. Distilled water (300 ml) was added, the mixture was well shaken and the ether fraction was separated. The aqueous solution was acidified with 30 ml of aqueous solution of hydrochloric acid (~15%) and white solid immediately precipitated. The mixture was extracted 3 × 30 ml of Et_2O and the collected ether fractions were dried over anhydrous $MgSO_4$ overnight. The mixture was filtered, solvent was evaporated under reduced pressure on a rotary evaporator, and the crude product was purified by sublimation (80 °C, 6.0×10^{-2} mbar) to yield 1.3 g (35%) of white crystalline product.

1-COOH-7-SH-1,7-$C_2B_{10}H_{10}$

(M1-COOH)

1-Mercapto-*meta*-carborane (1.0 g, 5.7 mmol) was dissolved in ~80 ml of dry and freshly distilled diethyl ether under argon atmosphere and cooled to ~-78 °C (dry ice/acetone). *n*–Butyllithium (5.0 ml, 12.5 mmol) was added dropwise over ~10 min. White solid precipitated within 30 min after the addition of *n*-butyllithium and the mixture was further stirred for 1 h. Excess dry ice was added and the mixture was then left at room temperature to warm up slowly (~1 h) under argon satmosphere. A white precipitate was observed in the mixture. Distilled water (50 ml) was added, the mixture was well shaken, and the ether fraction was separated. The aqueous solution was

acidified with 30 ml of aqueous solution of hydrochloric acid (~15%) and a white solid immediately precipitated. The mixture was extracted 3 × 30 ml of Et_2O and the collected ether fractions were dried over anhydrous $MgSO_4$ overnight. The mixture was filtered, the solvent was evaporated on a rotary evaporator under reduced pressure, and the crude product was purified by sublimation (80 °C, 1.0×10^{-1} mbar) to yield 0.83 g (66%) of white crystalline product.

2.4.3 NMR spectroscopic characterization

^{11}B, ^{1}H, and ^{13}C NMR spectra of both new compounds were measured using a Varian Mercury Plus NMR spectrometer under standard conditions. The NMR samples were prepared by dissolving ~5 mg of the sample in 0.5 ml of the solvent. ^{11}B chemical shifts are given relative to $[BF_3(Ot)_2]$, and ^{1}H and ^{13}C chemical shifts relative to TMS. The reference frequencies were estimated based on the frequency of the lock signal as a secondary standard. All resonances were assigned to the respective atoms (Tables 2.S1-2.S3) (Figures 2.S1-2.S5).

2.4.4 X-ray structural analysis

The molecular structures of both **M1-COOH** and **M9-COOH** isomeric species were obtained by single-crystal X-ray diffraction analysis (Tables 2.S4 and 2.S5 and Figure 2.S6-2.S8).

2.4.5 Crystallography

Crystals suitable for single-crystal X-ray crystallography were obtained by slow sublimation in a sealed ampoule over a few weeks. The data were measured at 120 K with up to 0.87 Å resolution on an Oxford Diffraction diffractometer Gemini using mirror-collimated Cu K_α radiation (Gemini ultra Cu) from a sealed X-ray tube, and CCD detector Atlas. Data were processed using program CrysAlis PRO, with empirical absorption correction. Structures were

solved by charge flipping with Superflip[56] and refined with Jana2006, http://jana.fzu.cz (Structure Determination Software Programs, Institute of Physics, Prague, Czech Republic).[57] The sample was a twin rotated by 180° around the reciprocal axis c*. This twinning operation generated overlaps of some diffraction spots; the overlaps were detected by the data processing program CrysAlis PRO and encoded to the reflection file in a form of so-called hklf5 format. Using this format, the partial overlaps due to twinning could be taken into the account by the refinement program Jana2006. This procedure considerably improved the sensitivity of refinement to hydrogen atoms.

All hydrogen atoms appeared in difference Fourier maps. Hydrogen atoms attached to boron were constrained to have the same B-H distance while hydrogen atoms attached to oxygen of carboxyl were refined with the O-H distance ~0.8Å. All crystallographic figures were made in mercury (https://www.ccdc.cam.ac.uk/solutions/csd-system/components/mercury/). Selected collection and refinement data are listed in Tables 2.S4 and 2.S5 together with the CCDC number. Supplementary crystallographic data can be obtained free of charge via http://www.ccdc.cam.ac.uk/conts/retrieving.html, or from the Cambridge Crystallographic Data Centre, 12 Union Road, Cambridge CB2 1EZ, UK; fax: (+44) 1223-336-033; or e-mail: deposit@ccdc.cam.ac.uk

2.4.6 Acid-base titration

All derivatives were titrated with an aqueous solution of sodium hydroxide, and the titration curves are displayed in Figure 2 . S21. Titrations were performed in an ethanol/water solution due to the solubility of the carborane derivatives and their respective salts. The results show that both isomers are diprotic acids. Dissociation of the COOH group prior to the SH group is in accord with the acidity constant order, and corresponds to our computational results at the CC2/def2-TZVP level of theory. A comparison of both isomers **M1-COOH** and **M9-COOH** with 1,7-carborane-1-carboxylic acid, 1-COOH-1,7-$C_2B_{10}H_{11}$, enables the analysis of the effect of SH attachment to both carbon and boron atom of the skeleton.

2.4.7 Mass spectrometry analysis

The two isomeric species (**M1-COOH** and **M9-COOH**) show similar patterns in their electrospray ionization (ESI) mass spectra (Figures 2.S9-2.S17). Mass spectrometry measurements were performed on a Thermo Scientific LCQ Fleet Ion Trap instrument using ESI with helium (5.0 Messer) as a collision gas in the ion trap. The sample was dissolved in acetonitrile (concentration ~100 ng/ml) and introduced through a fused-silica sample tube of 0.100 mm (inner

diameter) × 0.19 mm (outer diameter) to the ion source from a Hamilton syringe using infusion at 15 µL/min, source voltage 5.47 kV, tube lens voltage -44.71 V, capillary voltage -23.06 V, capillary temperature 165.01 °C, and N_2 (isolated from air in NitroGen N1118LA, Peak Scientific) as a nebulizing sheath gas (flow rate 14.97 p.d.u.). Only negative ions of the respective molecular peaks were detected.

2.4.8 Infrared Spectra of M1-COOH and M9-COOH

Infrared spectra (Figs. 2.S18-2.S20) of both isomeric compounds (~1-1.5 mg) were measured in KBr pellets using a Nicolet Nexus 670 FTIR spectrometer.

2.4.9 Geometric Structural Analysis

The computed structure of M1-COOH as a set of atomic coordinates was imported to EXCEL software. Translation and rotation transformation matrices were then used to move the molecule such that the S atom is in the beginning of the coordination system, the molecular axis intersecting the S atom and the antipodal B atom is in the z coordinate axis and the plane intersecting the S atom, the antipodal B atom, and the C atom, to which the −COOH group is bonded, are in the yz plane.

Rotation transformation matrix together with the van der Waals atomic radii were used to find the densest packing of molecules on the surface. For isotropic packing the molecule was rotated around the x axis to scan for the tilt in which the distance of the most distant component (atom coordinates + VdW atomic radii) from the z axis acquires the smallest value, this distance is the nearest neighbor distance. The method was easily reversed to find the tilt for isotropic packing with the nearest neighbor distance of 8.6 Å.

2.4.10 Conformational analysis

Molecular conformational analysis was done by quantum chemistry calculations, which were performed by the NWChem package.[58] The geometries were optimized[59] by means of density functional theory (DFT) with the hybrid exchange–correlation functional PBE0[60] using Jensen's triple-zeta basis pc-2.[61] A series of optimizations were performed on internal coordinates with the torsion angles defining the orientation of the carboxyl and thiol groups with respect to the carborane cages kept fixed. Subsequently, the NMR shielding parameters were calculated by DFT with the same XC functional using Jensen's triple–zeta basis pcS-2 optimized[S62] for this type of calculation. Individual conformations were sorted according to their calculated energies, and their relative Boltzmann factors at the laboratory temperature 300 K used as the weights for the mean values of their chemical shifts.

2.4.11 Scanning tunneling microscopy analysis

Samples for imaging were prepared on Au{111}/mica substrates (Agilent Technologies, Santa Clara, CA), which were hydrogen-flame annealed with 10 passes at a rate of 0.4 Hz prior to monolayer deposition. Substrates were placed into a capped vial with 1 mL of a 1 mM solution of the respective isomer in ethanol. Ethanol was used as received (Sigma-Aldrich, St. Louis, MO). The samples were left at room temperature (*ca.* 25 °C) or heated at 78 °C in a Barnstead Thermolyne 1400 furnace (ThermoFisher Scientific, Waltham, MA) for 24 h; no difference was observed between these conditions. Subsequently, samples were cleaned with neat ethanol and dried with a stream of nitrogen gas before loading into the custom-built Besocke-style scanning tunneling microscope with a platinum/iridium tip (80:20) under ambient conditions.[63] Samples

were held within a −1 to −0.1 V bias range, and 256 × 256 pixel images were collected in constant-current mode. The known lattice of the 1-dodecanethiolate SAMs on Au{111} was used for calibration. Image analyses was done using MATLAB (Mathworks, Natick, MA) and Gwyddion (http://gwyddion.net/).

2.4.12 Simulated scanning tunneling microscopy analysis

The constant-current STM images are simulated using the Tersoff-Hamann method[64] using VASP. The two optimized **M1-COOH** SAMs on the 3 × 3 four-layer Au(111) slab with periodic boundary conditions are used as the input structures. The isovalue for the charge density is 10^{-4}, and the images are generated for energy from the Fermi energy (E_F) to E_F – 0.1 eV, to simulate the experimental condition V_{sample} = -0.1 V. (Figures 2.S24 and 2.S25)

2.4.13 Contact angle measurements

Samples were prepared by the same procedures as for STM sample preparation, except substrates were silicon wafers coated in a 5 nm chromium adhesion layer and 100 nm of gold. Contact angle measurements were performed using an FTA1000 drop shape instrument contact angle goniometer (First Ten Angstroms, Inc., Portsmouth, VA) under ambient conditions (21- 23 °C, 50-60% relative humidity). A drop of DI water, with a volume of 4 µL was applied to the surface. The drop was then allowed to settle on the substrate for 4 s; thereafter a cycle of pumping in and out by the syringe was started with 1.25 s pumping and 8.75 s of rest on the surface, to assess the advancing and receding contact angles. For each drop, 800 images were recorded and analyzed using FTA32 software based on the Young-Laplace equation. Each data point represents three drops taken at different locations on the substrate. For contact angle titrations, a range of buffers from pH 2 to 12

at 50 mM were used. For each pH point the substrate was immersed in the buffer for ~1 h, dried with nitrogen, and then measured with a droplet of the buffer solution.

2.4.14 Computational modeling of pK_a

To study the local dielectric effects, we performed *ab initio* calculations to compute the pK_a values for **M1-COOH** and **M9-COOH** SAMs. To reduce the computational cost, the monolayer is represented by a two-molecule model, in which the Au(111) surface is replaced by a H atom. To validate our model, we performed Bader charge analysis[65] on the molecular model and the **M1-COOH** SAMs, optimized on a 3 × 3 four-layer Au(111) surface, both with periodic boundary conditions using VASP.[66-69] In the molecular model, the substitute H position is relaxed while the positions of other atoms are fixed at their SAM positions. The implicit solvation model implemented in VASPsol[70,71] is used for molecules in water. The results show that the charges on the carboxyl group are similar between the molecular model and the SAM on surface. The charge difference is less than 0.001 per atom in gas phase and less than 0.01 in water for the carboxyl group, which indicates that the molecular model is reasonable for pK_a calculations.

To maintain the local environment of the carboxyl group in SAMs, the SAM is represented by two molecules with the same distance as they are on surface, and only the carboxyl group between the two molecules is allowed to deprotonate in our calculations. The pK_a values can be calculated from free energies of protonated and deprotonated structures by

$$\mathrm{p}K_a = [\mathrm{G}_{aq}(\mathrm{AH}) - \mathrm{G}_{aq}(\mathrm{A^-}) - \mathrm{G}_{aq}(\mathrm{H^+})]/(2.303\mathrm{RT})$$

and the experimental value for free energy of H^+, $G_{aq}(H^+) = 269.0$ kcal/mol is used in the calculations.[72] We use GAUSSIAN 09 package[73] to perform electronic structure and frequency calculations at B3LYP/6-31+G(d) level.[74-77] The CPCM model is used to model the solvation

effects.[78,79] We also plot the dielectric curve for free molecules in solvent. In these calculations, both protonated and deprotonated structures are fully relaxed.

2.4.15 X-ray photoelectron spectroscopy (XPS)

Platypus Template-Stripped Gold Chips were used as the substrate for all of the experiments. The Platypus chips were cleaved short before use to minimize their exposure to air. For the deposition of **M9**, **M9-COOH** and 1-COOH-12-SH-1,12-$C_2B_{10}H_{10}$ (**P1-COOH**), the substrate was immersed in to a 96% ethanol solution of the corresponding compound (concentrations ranging from 1 to 4 mmol·dm^{-3}) for 50 to 70 min. Ethanoic solutions of the carboxylated species were prone to turn opaque several hours after their preparation; thus, fresh solutions were prepared every time. The chips were then rinsed with 96% ethanol, dried in a stream of argon or nitrogen, and stored under inert atmosphere, and subsequently used for further modification or measurements within the next 30 min.

For the subsequent modification of SAMs of **M9** and **M9-COOH** with metal ions, the freshly prepared samples were immersed in to an aqueous solution of the corresponding salt (concentration of 7 ± 3 mmol·dm^{-3}), *i.e.*, NaCl, $MgSO_4$, $CaCl_2$, $SrCl_2$, $BaCl_2$, $Pb(NO_3)_2$, $Fe_2(SO_4)_3$, $Ni(NO_3)_2$, $Co(NO_3)_2$, $CuSO_4$, $ZnSO_4$, $La_2(SO_4)_3$, $Sm_2(SO_4)_3$ and $Tb_2(SO_4)_3$. The Fe(II) ions were deposited from aqueous solutions with 7 mmol·dm^{-3} concentration of $FeSO_4$ acidified with HCl to give 2.8 μmol·dm^{-3} H_3O^+ ion concentration. All the solutions, but that of Na_2SO_4, $FeSO_4$, $Fe_2(SO_4)_3$ and $MgSO_4$, which were prepared fresh, were prepared two days in advance. Each sample was treated separately to avoid cross-contamination. The immersion time was 50 to 70 min, the samples were then briefly rinsed with 96% ethanol, dried under an argon or nitrogen stream, and stored under inert atmosphere until analyzed, that is, for 30 min at most.

For exposure of the SAMs of **M9**, **M9-COOH** and **P1-COOH** to acidic conditions, the freshly prepared samples were immersed in a 1.15 mM aqueous solution of HCl for 1 hour, then briefly rinsed with 96% ethanol, dried under an argon or nitrogen stream, and stored under inert atmosphere until analyzed, that is for 30 min at most.

Sulfate compounds used for determination of relative sensitivity factors (RSFs), as discussed below, were crushed under ambient conditions into a fine powder, which was then pressed onto double-sided scotch tape and immediately mounted into the XPS instrument for analysis.

X-ray photoelectron spectroscopy analysis was performed on a XPS Kratos Axis Supra instrument, using ESCApe software. Aluminum anode with 15 mA emission current was used, charge compensation electron gun was used with filament current of 0.43 A, filament bias of 1.05 V and charge balance of 4.6 V for all the samples but bare gold, for which the electron gun was turned off. The charge compensation was, however, not necessary for the SAM samples, as they behaved as conductors. The hybrid lenses and a slot or 110 μm apertures were used in the electron optics setup. The analysis was done under vacuum of 10^{-8} to 10^{-9} torr for the SAM samples, the analyses of the powdered sulfates were done under less favorable vacuum, but not rising above 10^{-7} torr. The obtained data were processed in CasaXPS software. Transmission function was used as obtained from the Kratos Axis Supra instrument technician. Shirley-type background was used for all the photoelectron (PE) lines of the reference sulfate samples, and for the Au 4f PE lines of all the SAM samples. The linear-type background was used for all the PE lines, but the Au 4f PE lines, in all of the SAM samples. The RSFs given in Kratos Axis library were used for Au 4f, B 1s, O 1s, C 1s and S 2p PE lines. The RSFs for Na 1s, Mg 1s, Mg KLL

and Ba 3d PE and Auger lines were obtained from XPS analysis of sulfates with known stoichiometries.

To acquire the empirical RSFs, the spectra obtained for powdered Na_2SO_4, $MgSO_4$, and $BaSO_4$, were analyzed in accordance to the approach of Marel *et al.* for multilayer systems,[80] the samples were assumed to consist of a homogeneous, infinitely thick substrate sulfate, contaminated with a thin film of hydrocarbons containing both carbon and oxygen. The intensities for the oxygen 1s PE line were split to match the sulfate stoichiometry, and the excess intensity was assigned to the adventitious overlayer. The intensity of the PE line corresponding to the acquired. RSF, was determined artificially based on the known stoichiometry of the sulfate and the experimentally acquired intensity of the sulfur 2p PE line. The attenuation length used in the Marel's model was substituted with the inelastic mean free path which was obtained from the NIST Electron Inelastic-Mean-Free-Path Database software[81] using a TPP-2M equation for a $C_{26}H_{54}$ molecules with a band gap of 5 eV and density of 0.9 $g \cdot cm^{-3}$. The RSF value was obtained by division of the measured intensity with the computed one, after the determination of the correct thickness of the adventitious overlayer. The intensities obtained for the SAM samples were divided by the corresponding RSFs and normalized to yield a stoichiometry with 10 boron atoms, no correction for the multilayer attenuation was used for the SAM samples.

2.5 Additional Figures and Tables

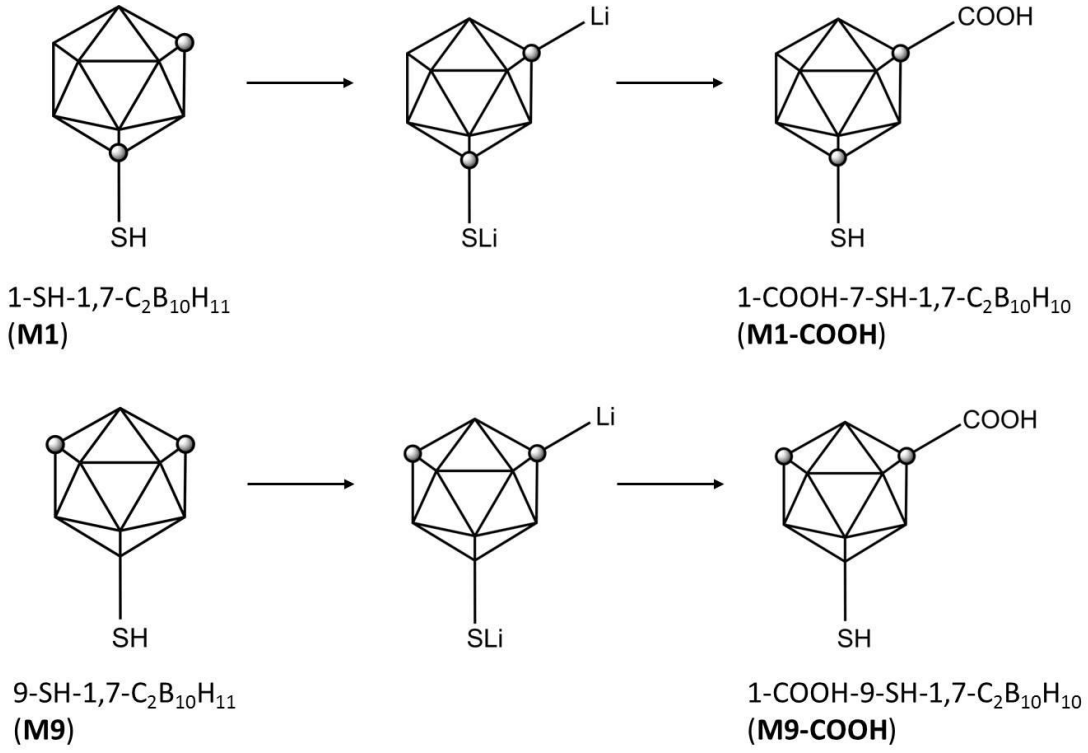

Scheme 2.S1. Synthesis of carboxylic acids of 1-SH-1,7-$C_2B_{10}H_{11}$ (**M1**) and 9-SH-1,7-$C_2B_{10}H_{11}$ (**M9**).

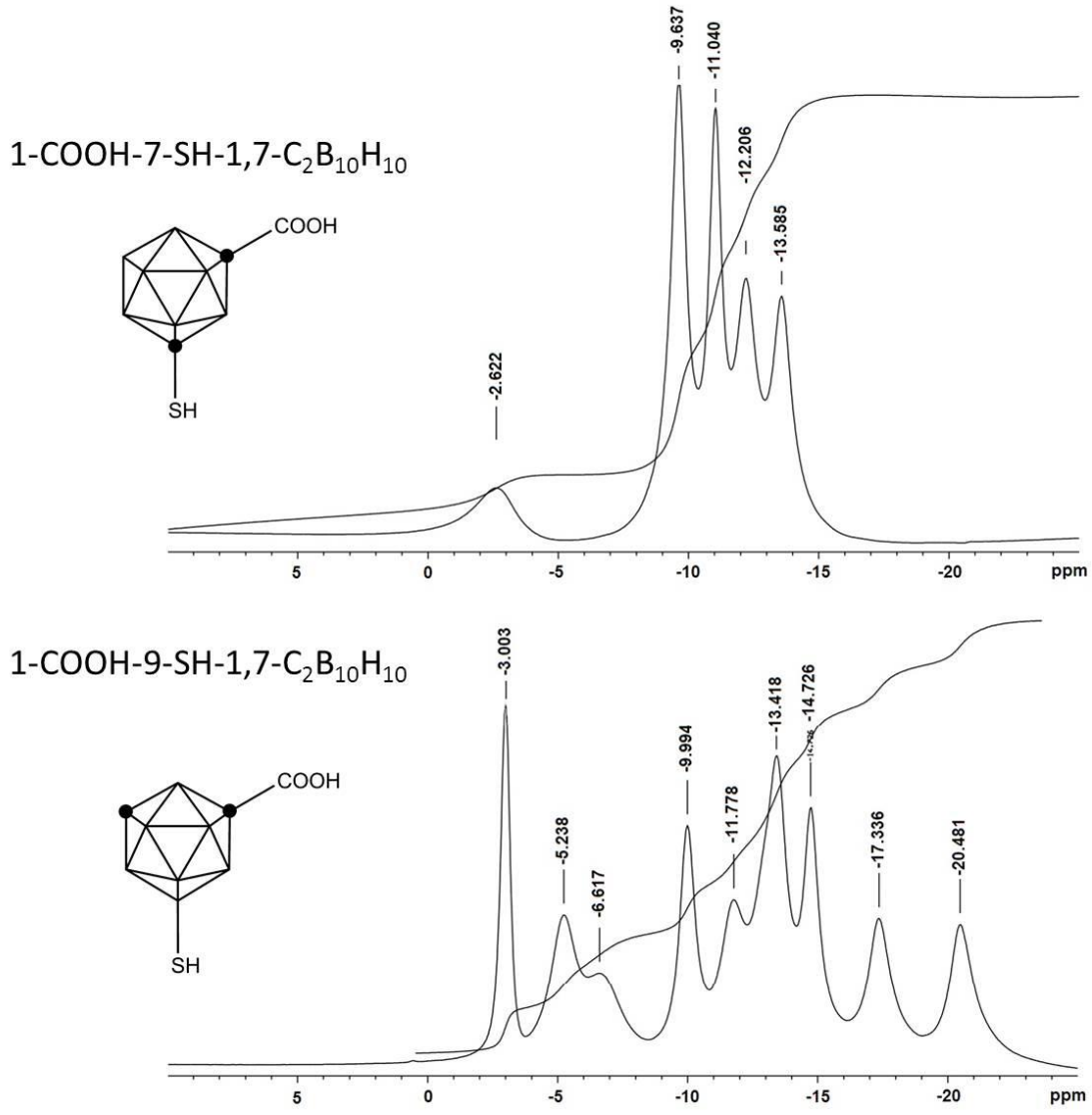

Figure 2.S1. Experimental ^{11}B NMR spectra of (top) 1-COOH-7-SH-1,7-$C_2B_{10}H_{10}$ (**M1-COOH**) and (bottom) 1-COOH-9-SH-1,7-$C_2B_{10}H_{10}$ (**M9-COOH**).

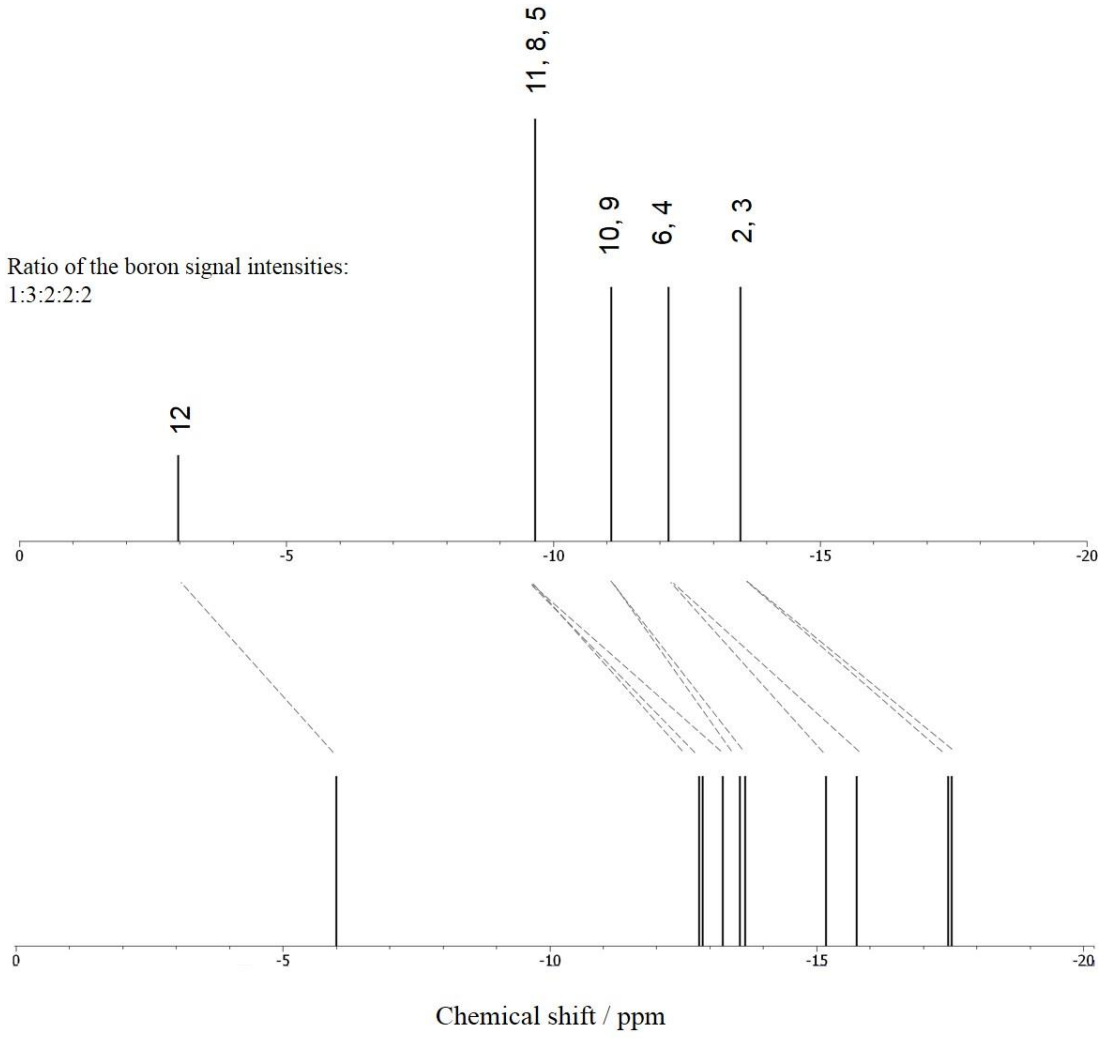

Figure 2.S2. Correlation between the (top) experimental and (bottom) computational ^{11}B NMR spectra of 1-COOH-7-SH-1,7-$C_2B_{10}H_{10}$ (**M1-COOH**).

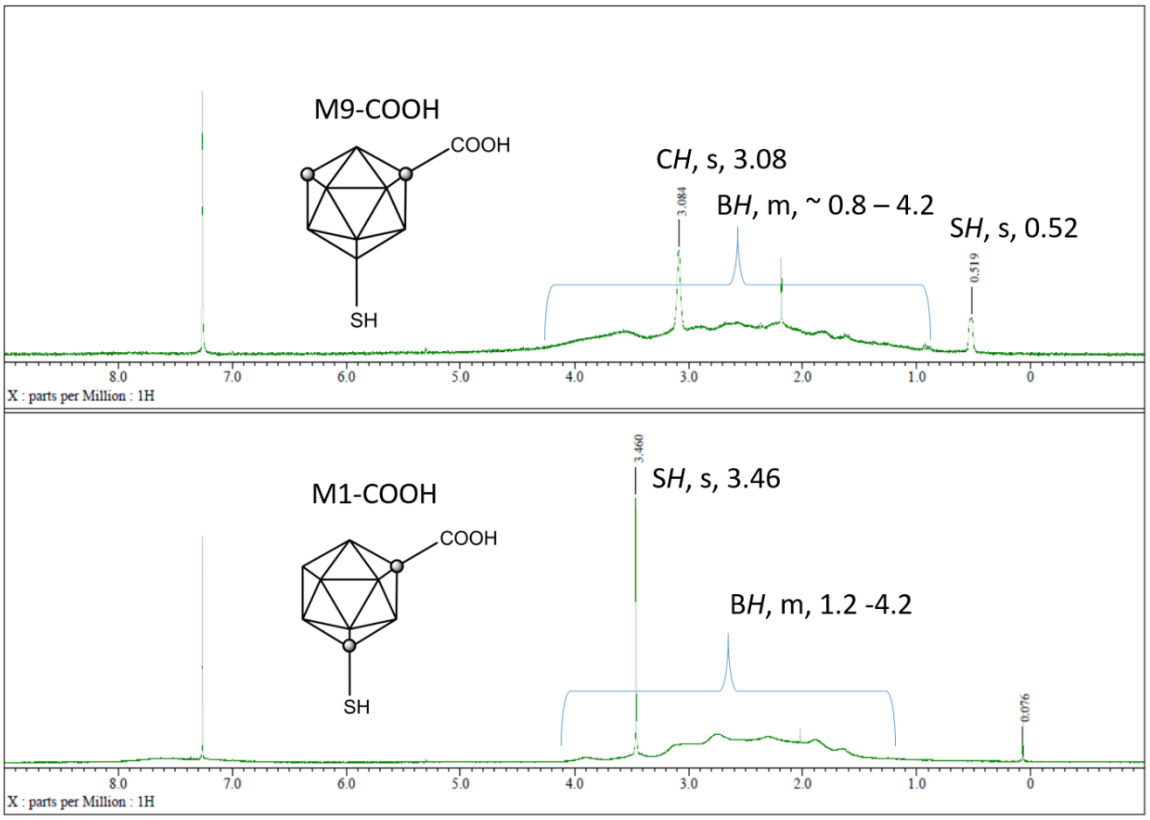

Figure 2.S3. Correlation between the (top) experimental and (bottom) computational ^{11}B NMR spectra of 1-COOH-9-SH-1,7-$C_2B_{10}H_{10}$ (**M9-COOH**).

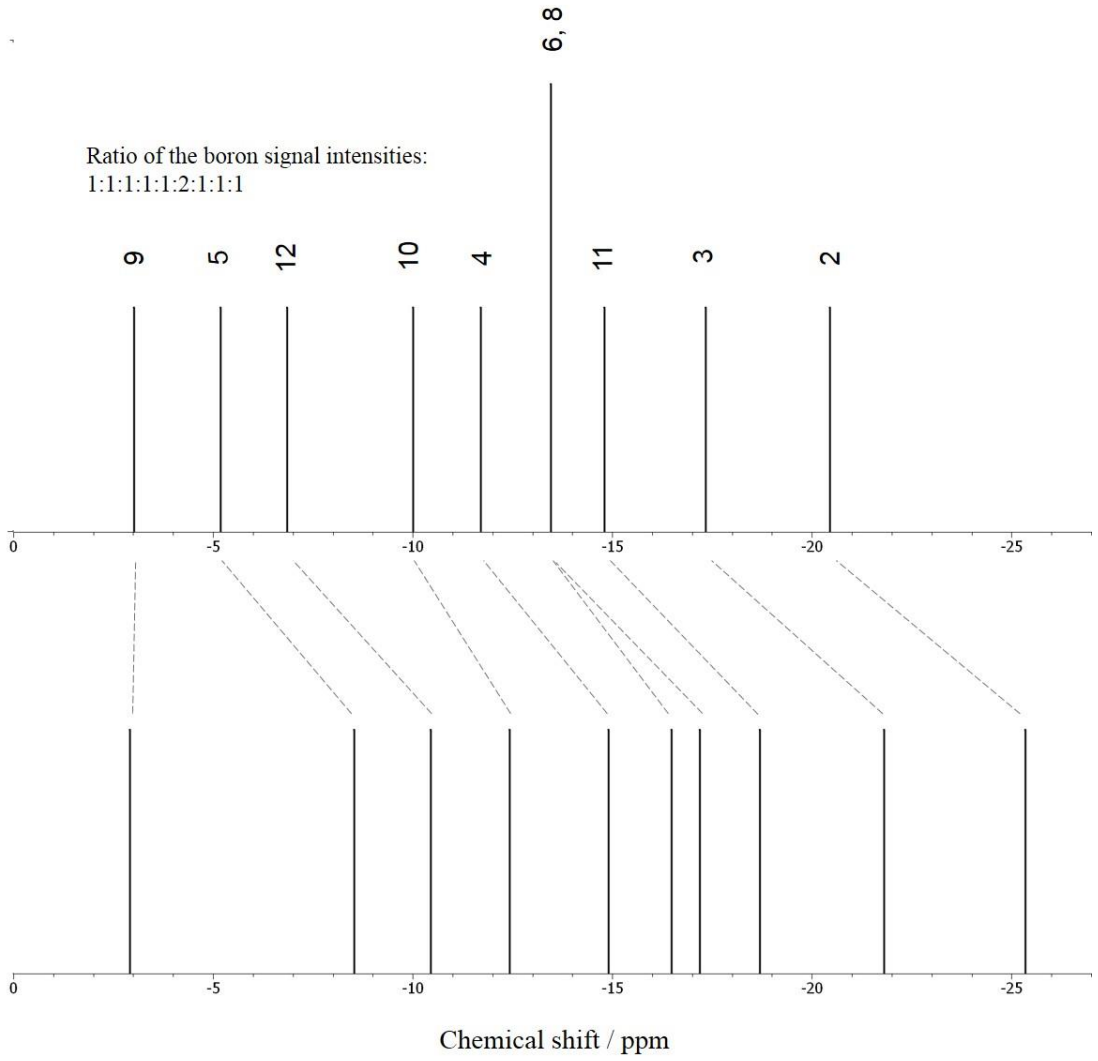

Figure 2.S4. Experimental ^{1}H NMR spectra of (top) 1-COOH-9-SH-1,7-$C_2B_{10}H_{10}$ (**M9-COOH**) and (bottom) 1-COOH-7-SH-1,7-$C_2B_{10}H_{10}$ (**M1-COOH**).

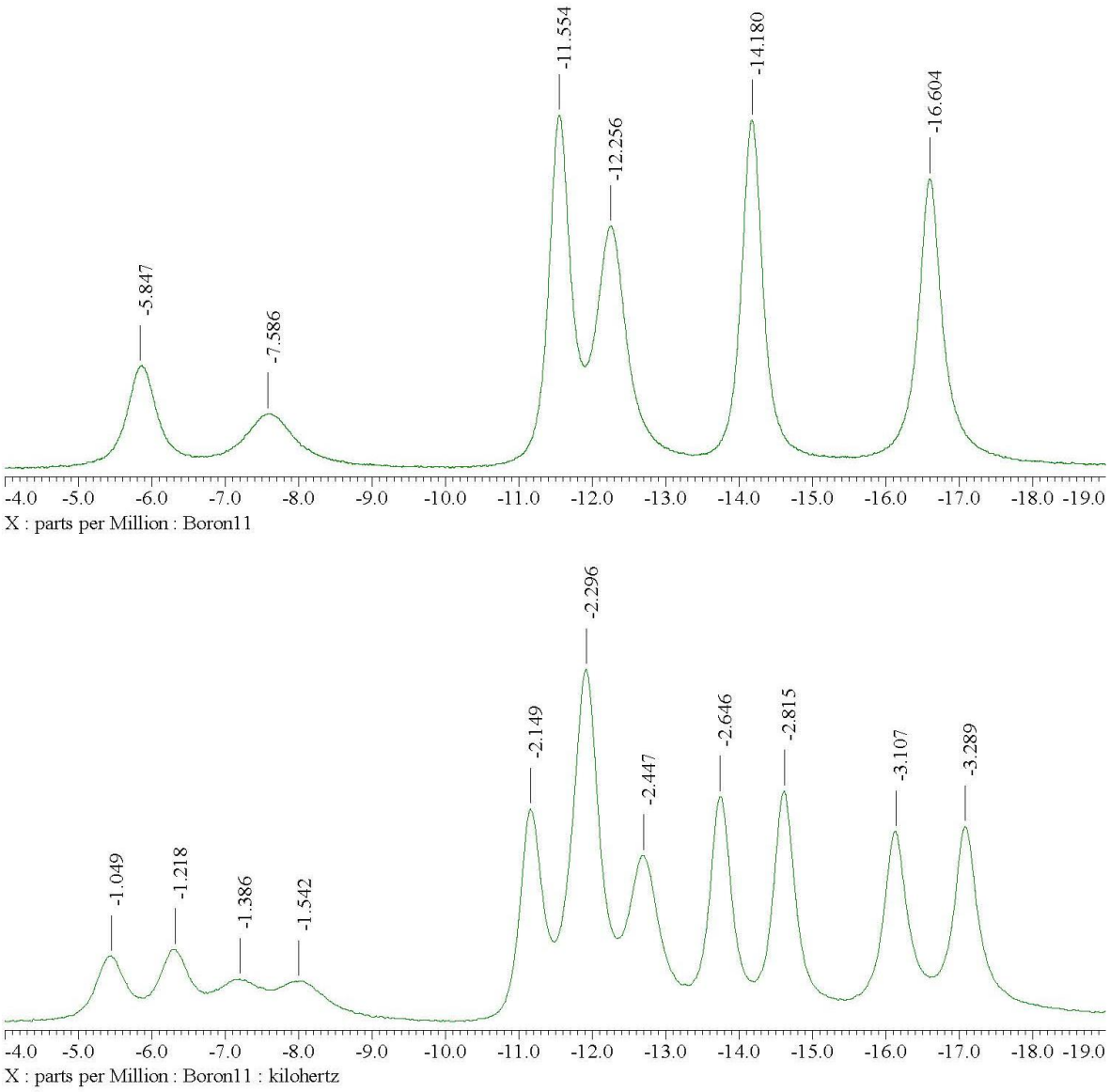

Figure 2.S5. (Top) Coupled and (bottom) decoupled experimental ^{11}B NMR spectra of 1-COOH-1,7-$C_2B_{10}H_{11}$ (**M-COOH**).

Table 2.S1. Measured ^{11}B, ^{13}C, and ^{1}H NMR chemical shift data for 1-COOH-7-SH-1,7-$C_2B_{10}H_{10}$ (**M1-COOH**) in $CDCl_3$ solution at 300 K.

	1-COOH-7-SH-1,7-$C_2B_{10}H_{10}$ (M1-COOH)			
Assign.	$\delta(^{11}B)^{exp}$	$\delta(^{11}B)^{calc}$	$\delta(^{1}H)^{exp}$	$\delta(^{13}C)^{calc}$
1	-	-	10.41^{COOH}	81.73^{CH}, 174.59^{COOH}
2	-13.51	-17.47		-
3	-13.51	-17.54		-
4	-12.16	-15.76		-
5	-9.66	-13.25		-
6	-12.16	-15.18		-
7	-	-	3.46^{SH}	77.78^{CH}
8	-9.66	-12.87		-
9	-11.09	-13.66		-
10	-11.09	-13.56		-
11	-9.66	-12.81		-
12	-2.98	-6.01		-

Table 2.S2. Measured ^{11}B, ^{13}C, and ^{1}H NMR chemical shift data for 1-COOH-9-SH-1,7-$C_2B_{10}H_{10}$ (**M9-COOH**) in $CDCl_3$ solution at 300 K.

	1-COOH-9-SH-1,7-$C_2B_{10}H_{10}$ (M9-COOH)			
Assign.	$\delta(^{11}B)^{exp}$	$\delta(^{11}B)^{calc}$	$\delta(^{1}H)^{exp}$	$\delta(^{13}C)^{calc}$
1	-	-	9.84^{COOH}	79.57^{CH}, 174.56^{COOH}
2	-20.46	-25.35	-	-
3	-17.34	-21.81		-
4	-11.71	-14.90		-
5	-5.19	-8.54		-
6	-13.47	-16.48		-
7	-	-	3.09^{CH}	62.38
8	-13.47	-17.19		-
9	-3.03	-2.92	0.47^{SH}	-
10	-10.02	-12.43		-
11	-14.80	-18.70		-
12	-6.86	-10.45		-

Table 2.S3. Measured ^{11}B, ^{13}C, and ^{1}H NMR chemical shift data for1-COOH-1,7-$C_2B_{10}H_{11}$ (**M-COOH**) in $CDCl_3$ solution at 300 K.

	1-COOH-1,7-$C_2B_{10}H_{10}$ **(M-COOH)**		
Assign.	$\delta(^{11}B)^{exp}$	$\delta(^{1}H)^{exp}$	$\delta(^{13}C)$exp
1	-	7.52	71.50^{CH}, 116.46^{COOH}
2	-16.00	2.92	-
3	-16.00	2.92	-
4	-12.26	2.41	-
5	-5.85	2.53	-
6	-12.26	2.41	-
7	-	3.01	54.90^{CH}
8	-14.18	2.23	-
9	-11.55	2.15	-
10	-11.55	2.15	-
11	-14.18	2.23	-
12	-7.59	2.31	-

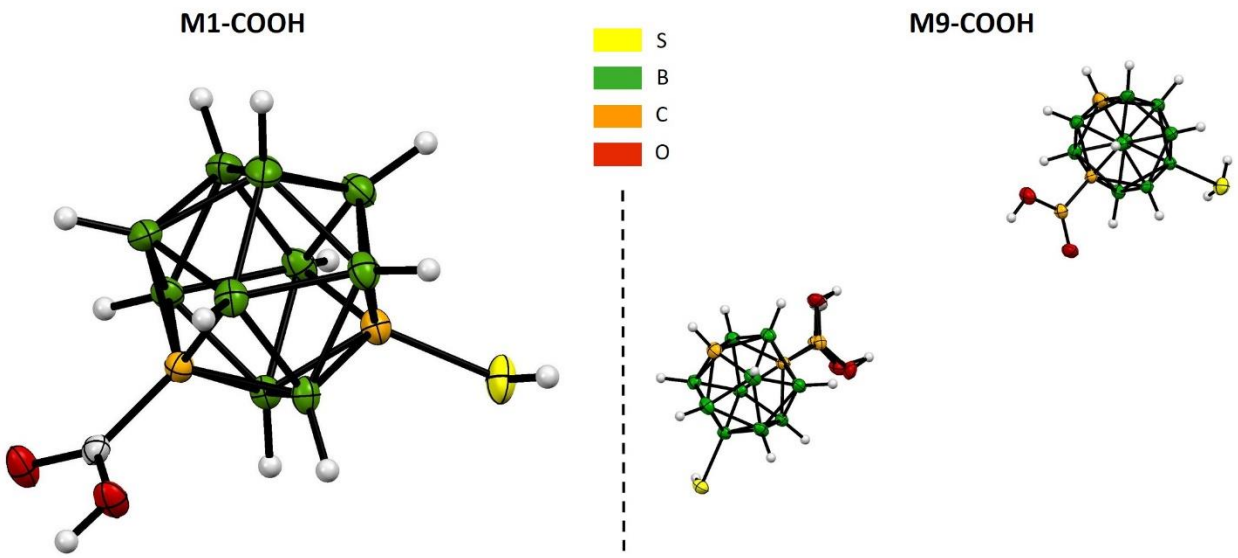

Figure 2.S6. Crystallographically determined molecular structures of 1-COOH-9-SH-1,7-$C_2B_{10}H_{10}$ (**M9-COOH**) and 1-COOH-7-SH-1,7-$C_2B_{10}H_{10}$ (**M1-COOH**).

The supramolecular structures of both **M1-COOH** and **M9-COOH**, as they appear in single crystals, are depicted in Figures 2.S5 and 2.S6. They both consist of molecular pairs bound in the typical association patterns of carboxylic functional groups with the O·(H)··O interatomic distances of 2.629 Å in **M1-COOH** and a range of 2.615-2.828 Å in **M9-COOH** due to the carboxyl group disorder. The thiol hydrogen atoms (-S*H*) in the structure of **M1-COOH** exhibit short contact interactions with an electronegative oxygen atom of the carboxylic functional group. The supramolecular structure of **M9-COOH** seems more complicated, as it exhibits an inherent SH group disorder and a greater number of short contact interactions than the number in which the SH group is involved, all schematically shown in Fig. 2.S6.

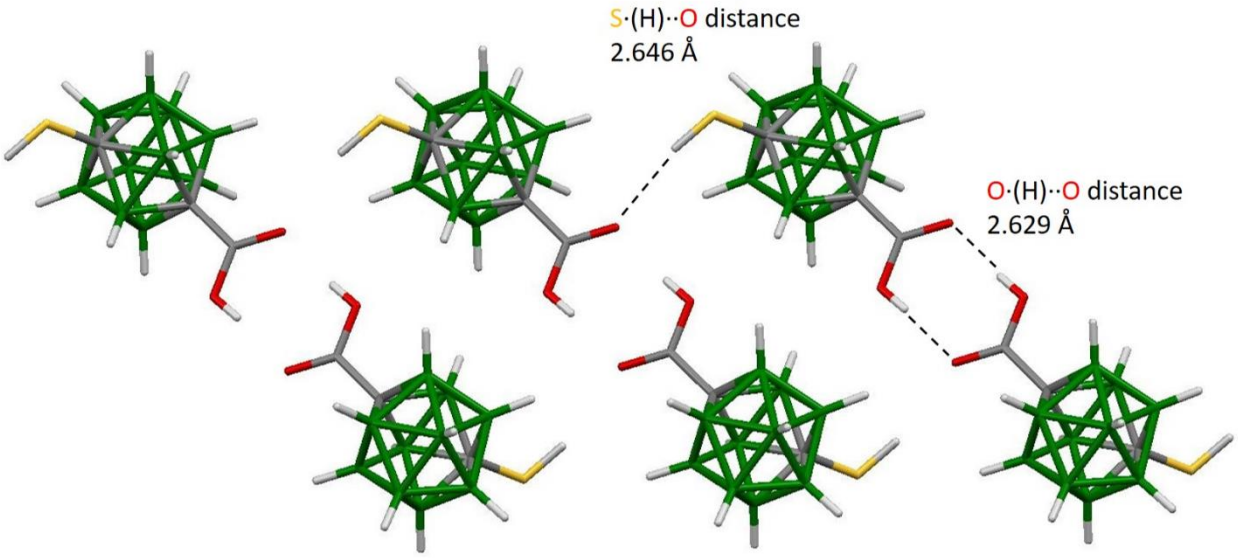

Figure 2.S7. Schematic of the supramolecular structure of the 1-COOH-7-SH-1,7-$C_2B_{10}H_{10}$

(**M1-COOH**) crystal showing short contact interactions.

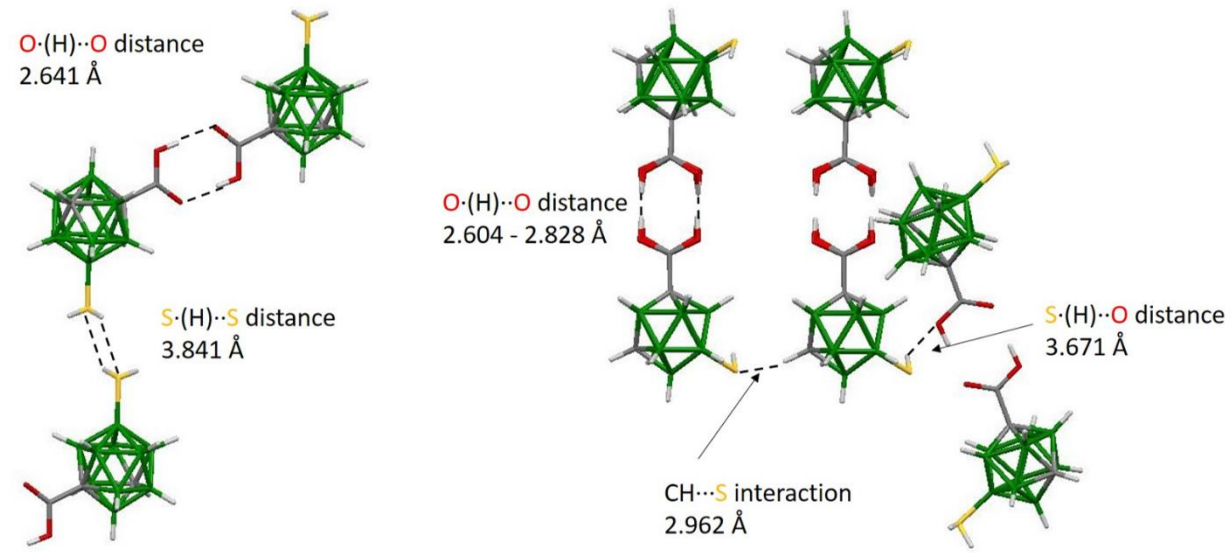

Figure 2.S8. Schematic of the supramolecular structure of the 1-COOH-9-SH-1,7-$C_2B_{10}H_{10}$

(**M9-COOH**) crystal showing short contact interactions.

Table 2.S4. Crystallographic collection and refinement data for 1-COOH-7-SH-1,7-$C_2B_{10}H_{10}$

(**M1-COOH**).

	M1-COOH
CCDC	1975664
Empirical formula	$C_3 H_{12} B_{10} O_2 S_1$
Diffractometer	four-cycle diffractometer Xcalibur, AtlasS2, Gemini ultra
M_r /g mol^{-1}	220.30
T/K	120
Wavelength / Å	1.54184
Crystal system	Monoclinic
Space group	$P2_1/n$
a/Å	7.8784(5)
b/Å	13.2904(10)
c/Å	11.1831(9)
α/deg	90
β/deg	93.449(6)
γ/deg	90
V/Å^3	1168.83(15)
Z	4
Calc. density/g cm^{-3}	1.2518

	M1-COOH
F(000)	448
Crystal size /mm^3	0.18 x 0.13 x 0.05
θ range /°	5.2 - 66.7
Index ranges /*hkl*	[-9,5]; [-13,15]; [-13,12]
Reflections collected (R_{int})	3661 (0.031)
Independent reflections	2009
Completeness /% to θ /°	98% to 65.59
Absorption correction	multi-scan
Max. and min. transmission	0.76 and 1
Data / restraints / parameters	2009/9/181
Goodness-of-fit on F^2	1.22
*R*1, *wR*2 [I>3!(I)]	0.0362, 0.0895
*R*1, *wR*2 (all data)	0.0473, 0.0966
Largest diff. peak and hole, $eÅ^{-3}$	0.21 and -0.22

Table 2.S5. Crystallographic collection and refinement data for 1-COOH-9-SH-1,7-C2B10H10 (**M9-COOH**).

	M9-COOH
CCDC	1975665
Empirical formula	C6 H24 B20 O4 S2
Diffractometer	four-cycle diffractometer Xcalibur, AtlasS2, Gemini ultra
*M*r /g mol−1	440.6
T/K	120
Wavelength / Å	1.54184
Crystal system	Monoclinic
Space group	C2/c
a/Å	32.2102 (4)
b/Å	6.9016 (1)
c/Å	23.2398 (5)
α/deg	90
β/deg	119.7080 (16)
γ/deg	90
V/Å3	4487.21 (15)
Z	8
Calc. density/g cm−3	1.304

	M9-COOH
μ mm^{-1}	2.24
F(000)	1792
Crystal size /mm^3	0.83 x 0.10 x 0.07
θ range /°	4.4 - 66.9
Index ranges /*hkl*	[-38,38]; [-7,8]; [-27,27]
Reflections collected (R_{int})	35917 (0.031)
Independent reflections	3932
Completeness /% to θ /°	0.99 to 66.9
Absorption correction	multi-scan
Max. and min. transmission	0.496 and 1
Data / restraints / parameters	3932/24/348
Goodness-of-fit on F^2	2.29
*R*1, *wR*2 [I>2!(I)]	0.0376, 0.1149
*R*1, *wR*2 (all data)	0.0404, 0.1173
Largest diff. peak and hole, e$Å^{-3}$	0.58 and -0.32

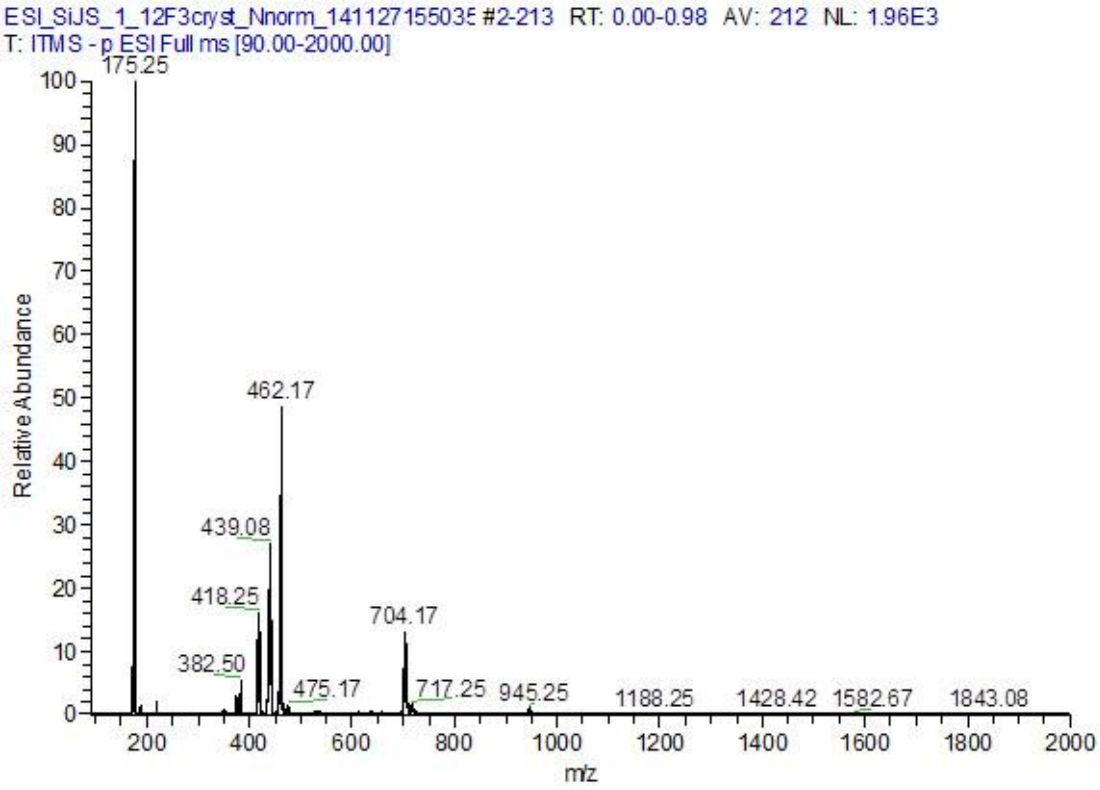

Figure 2.S9. Electrospray ionization mass spectrum of 1-COOH-9-SH-1,7-$C_2B_{10}H_{10}$ (**M9-COOH**).

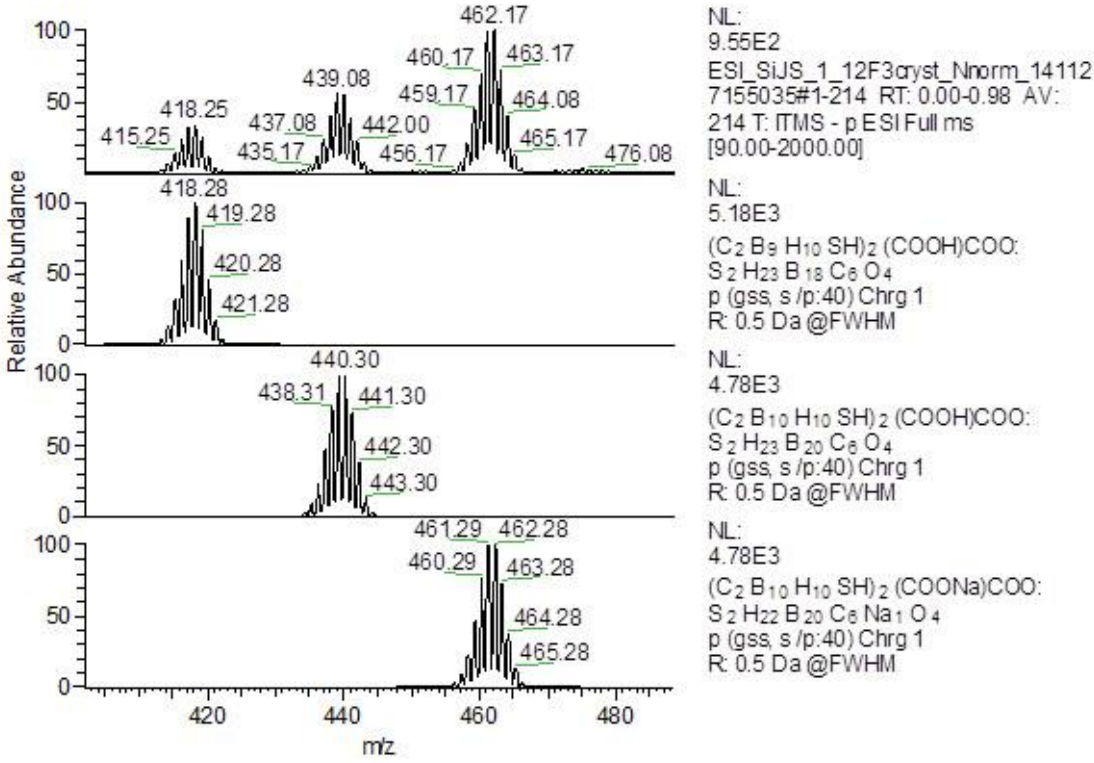

Figure 2.S10. (Top) Measured and (bottom) calculated isotopic distribution envelopes for the molecular masses corresponding to 2M-2H+1Na, 2M-H and for 2M-H-2B.

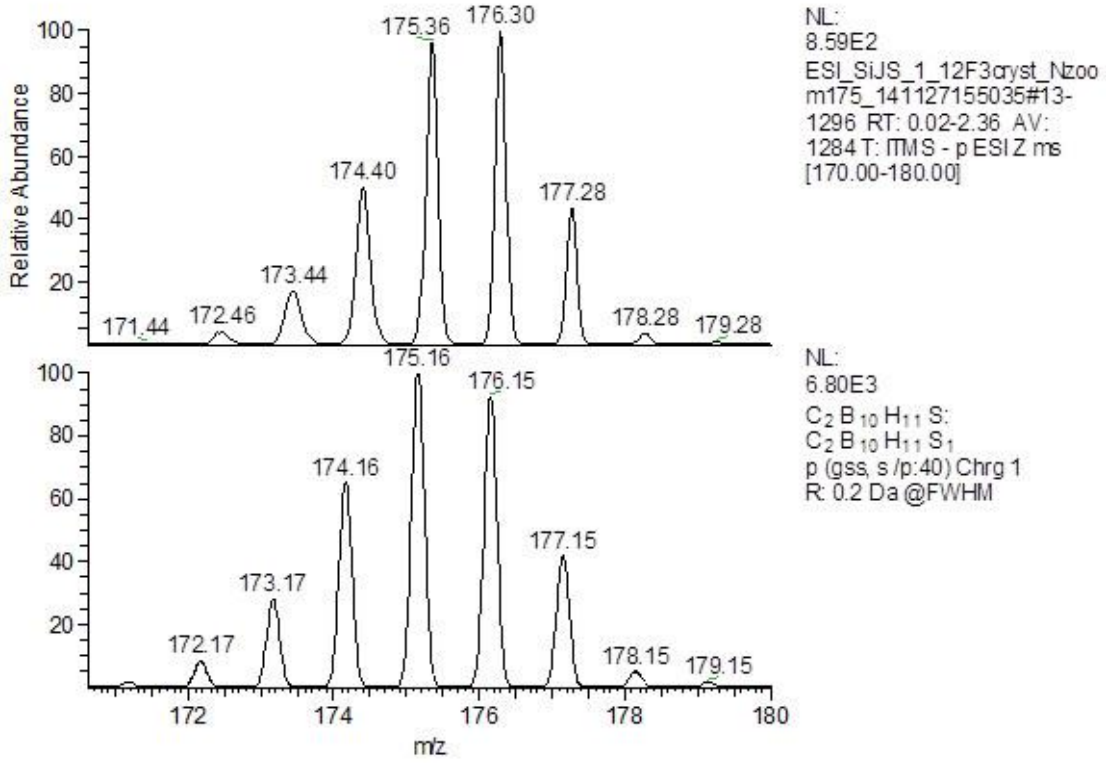

Figure 2.S11. (Top) Measured and (bottom) calculated isotopic distribution envelopes for the molecular mass corresponding to M-COOH.

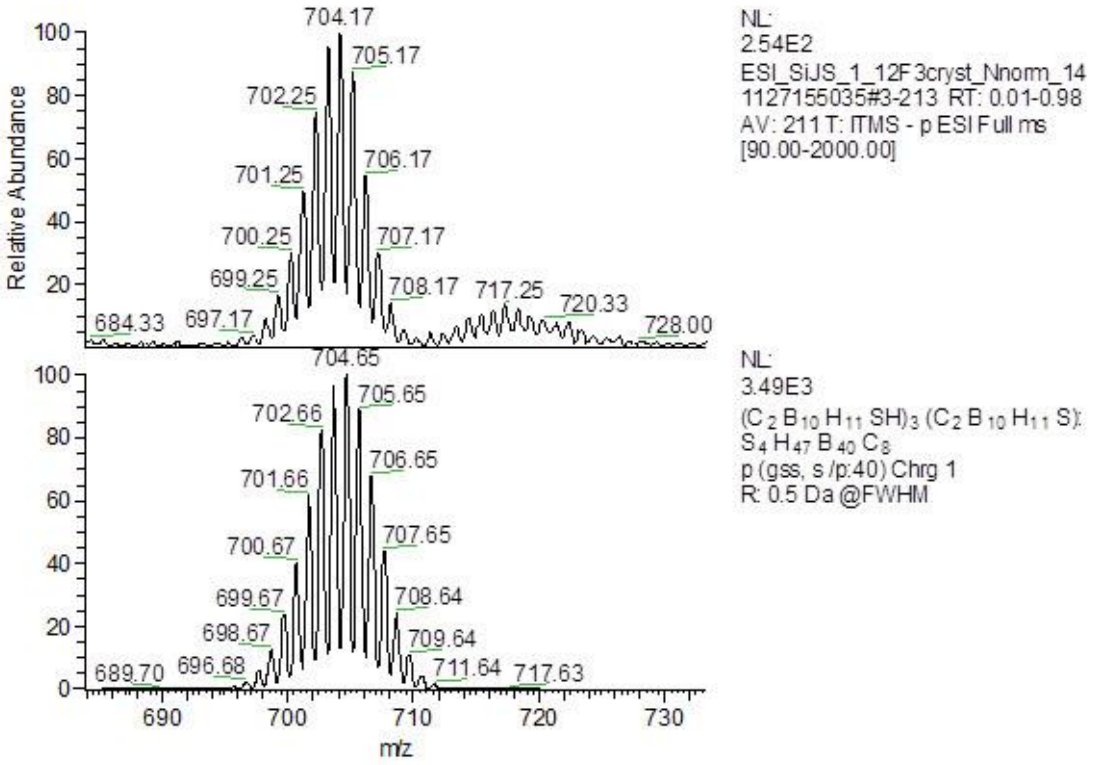

Figure 2.S12. (Top) Measured and (bottom) calculated isotopic distribution envelopes for the molecular mass corresponding to 4×(M-COOH).

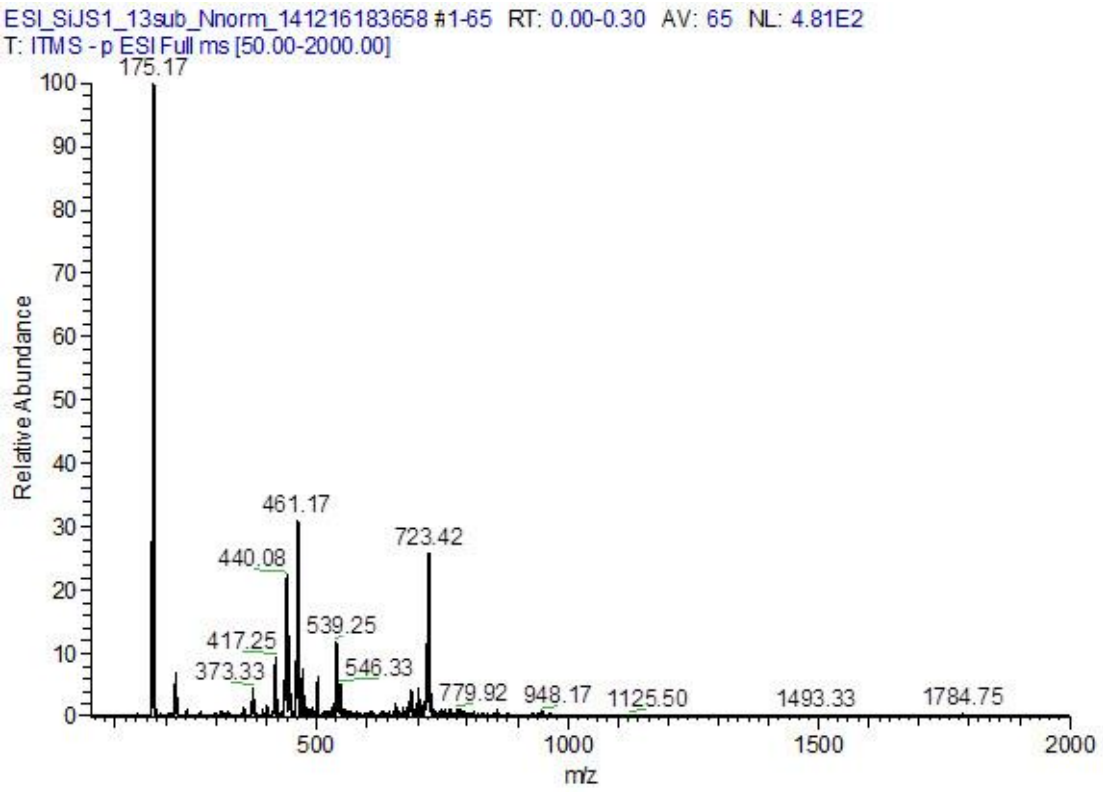

Figure 2.S13. Electrospray ionization mass spectrum of 1-COOH-7-SH-1,7-$C_2B_{10}H_{10}$ (**M1-COOH**).

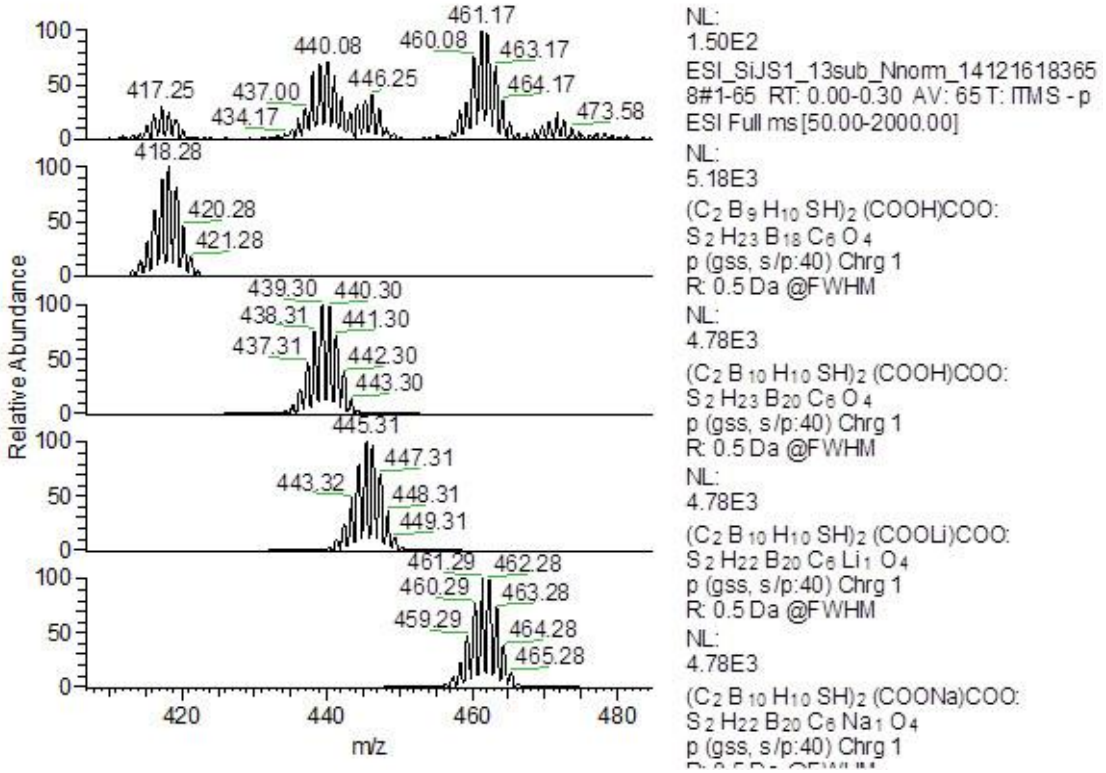

Figure 2.S14. (Top) Measured and (bottom) calculated isotopic distribution envelopes for the molecular masses corresponding to 2M-2H+1Na, 2M-H+1Li, 2M-H and to 2M-H-2B.

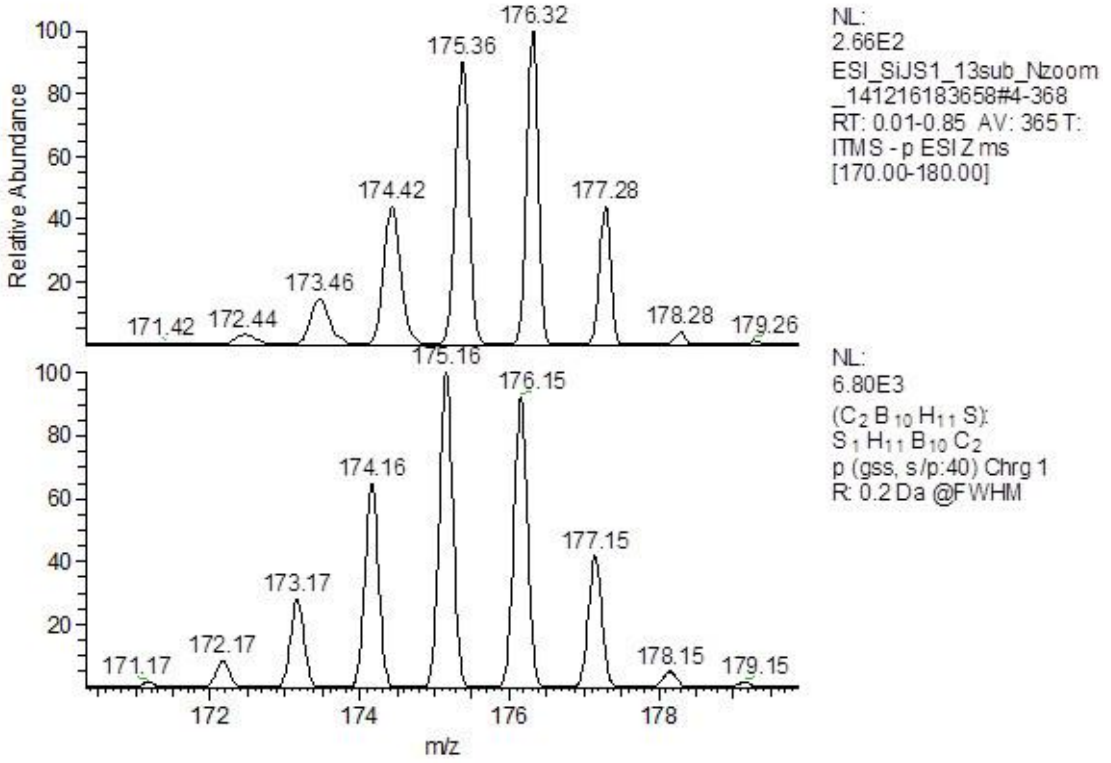

Figure 2.S15. (Top) Measured and (bottom) calculated isotopic distribution envelopes for the molecular mass corresponding to M-COOH.

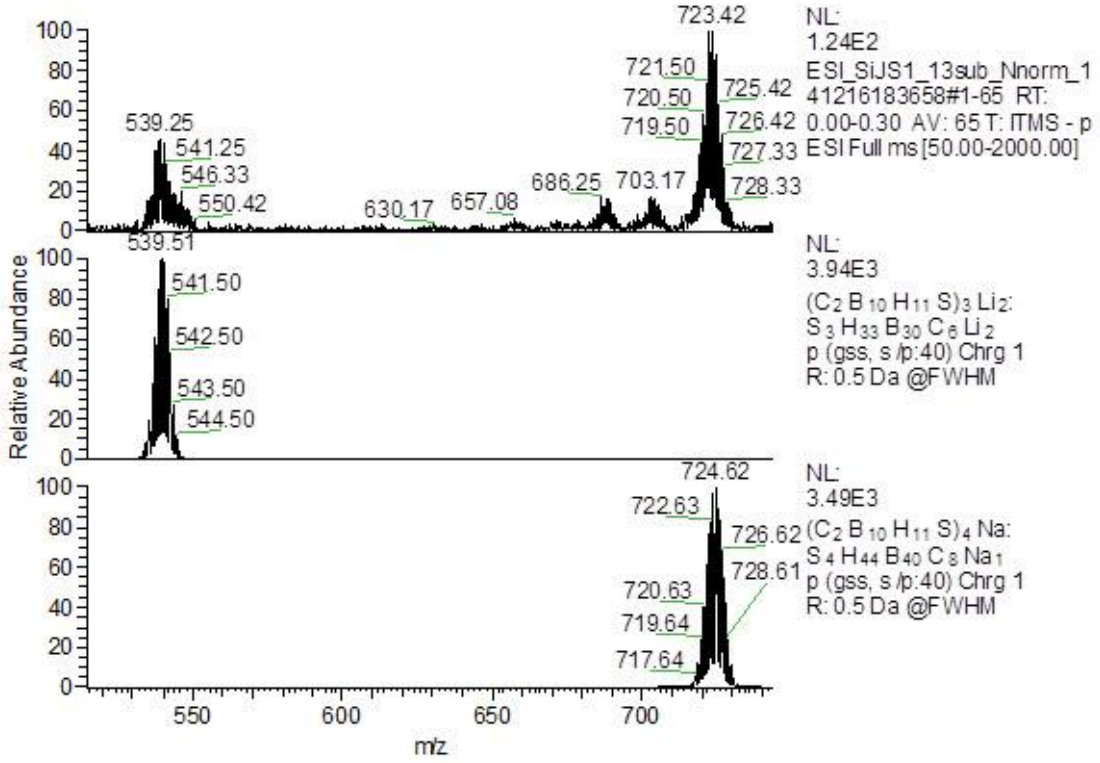

Figure 2.S16. (Top) Measured and (bottom) calculated isotopic distribution envelopes for the molecular mass corresponding to 3×(M-COOH)+2Li and 4×(M-COOH)+1Na.

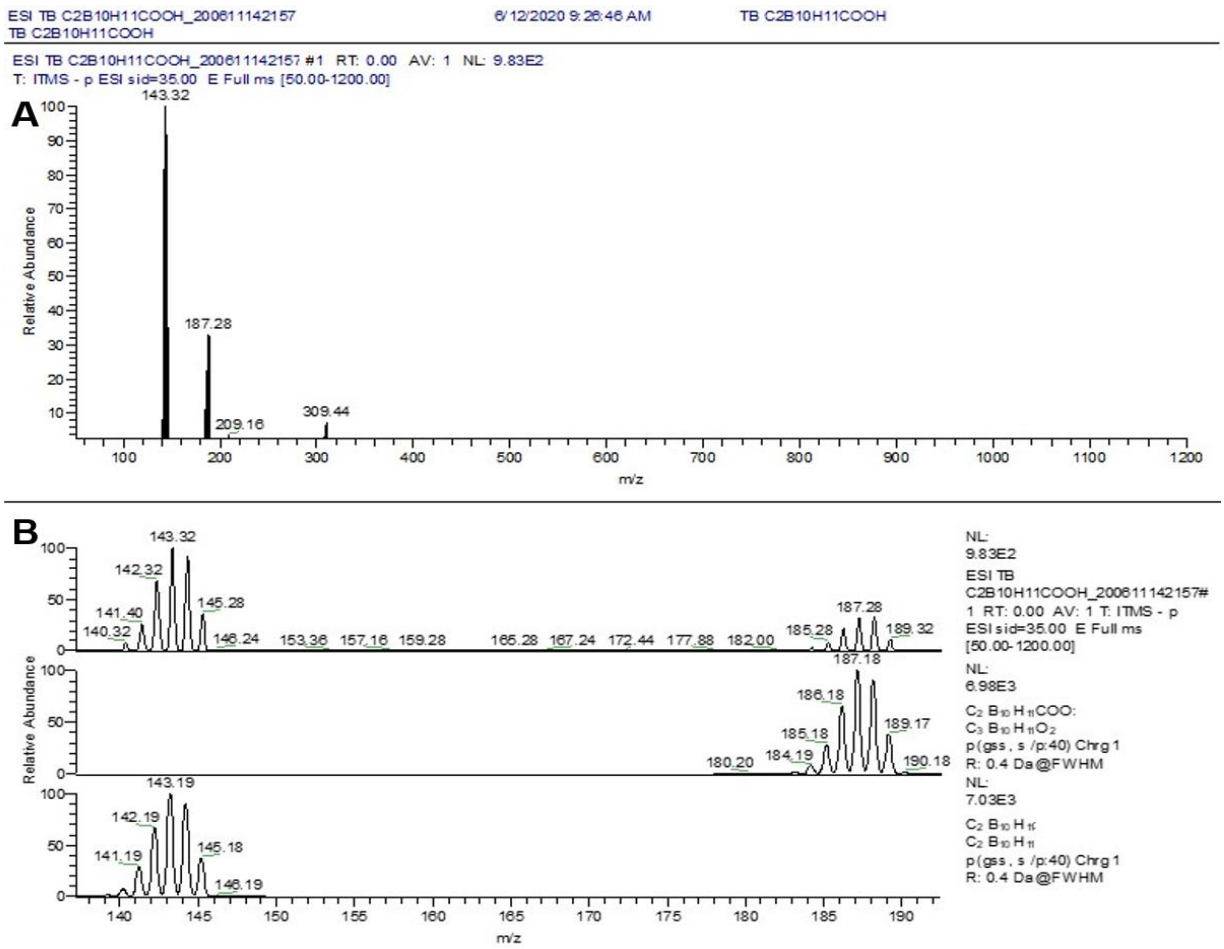

Figure 2.S17. (A) Electrospray ionization mass spectrum of 1-COOH-1,7-$C_2B_{10}H_{10}$ (**M-COOH**). (B) (Top) Measured and (bottom) calculated isotopic distribution envelopes for the molecular masses corresponding to M-H and M-COOH.

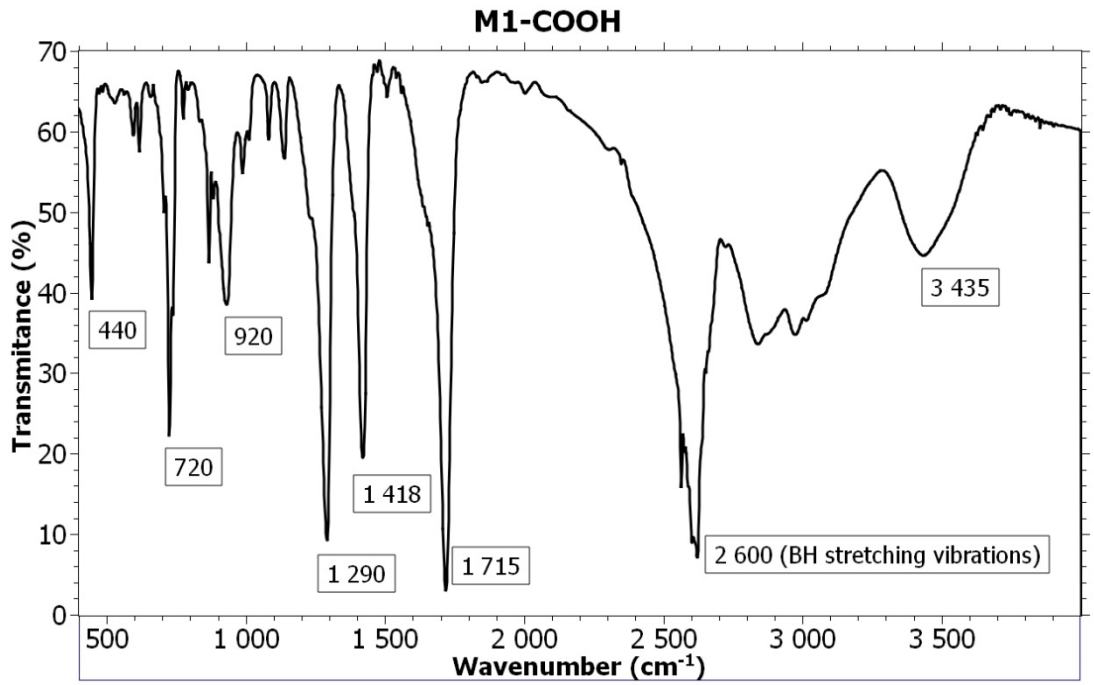

Figure 2.S18. Infrared spectrum of 1-COOH-7-SH-1,7-$C_2B_{10}H_{10}$ (**M1-COOH**).

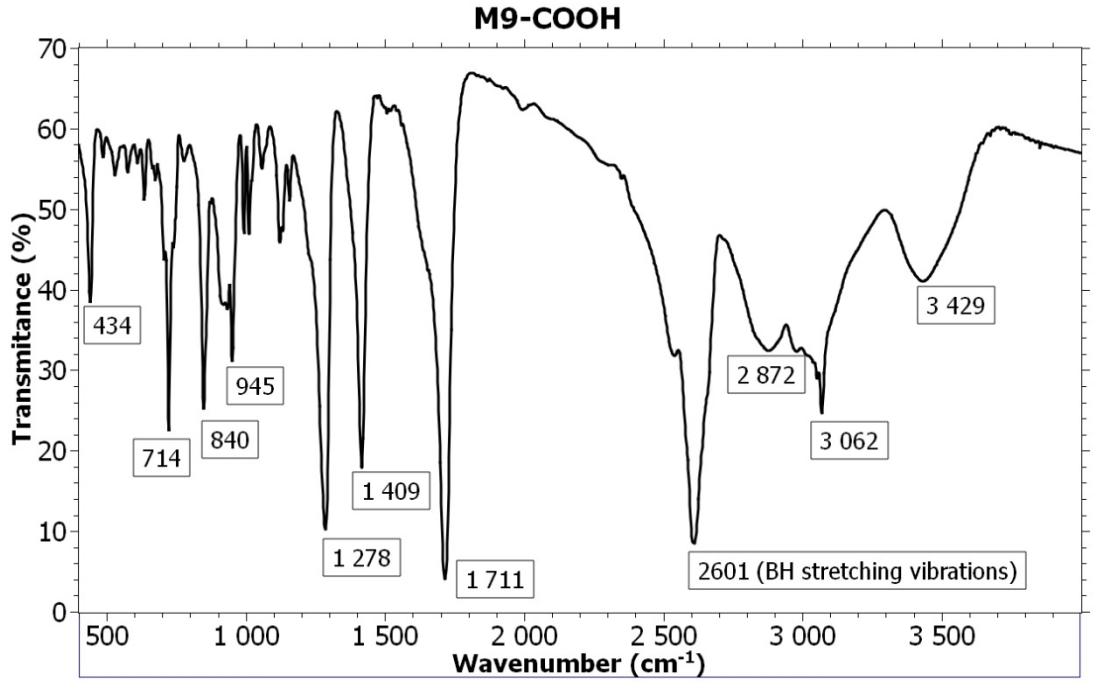

Figure 2.S19. Infrared spectrum of *racem*-1-COOH-9-SH-1,7-$C_2B_{10}H_{10}$ (**M9-COOH**).

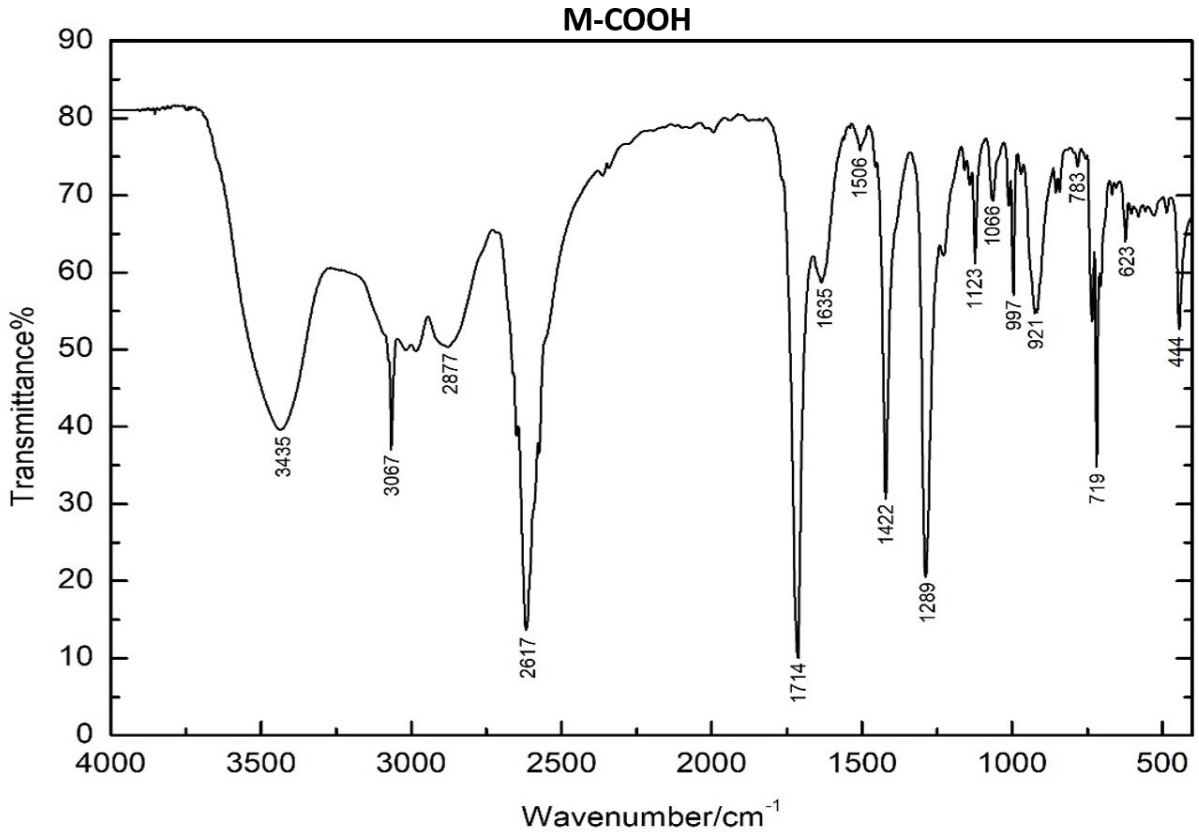

Figure 2.S20. Infrared spectrum of 1-COOH-1,7-$C_2B_{10}H_{10}$ (**M-COOH**).

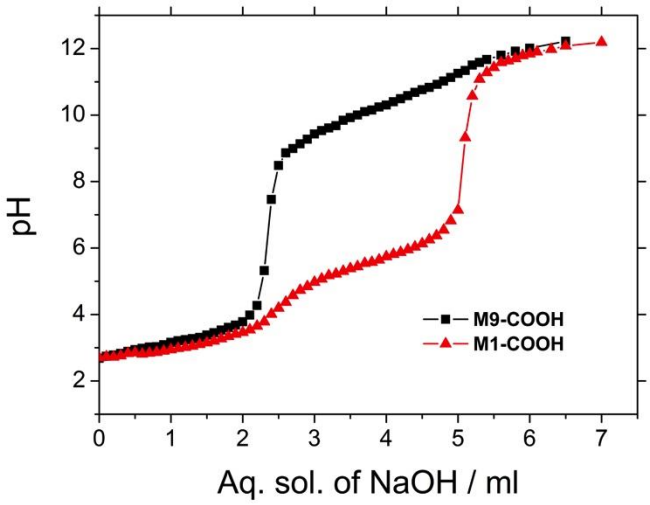

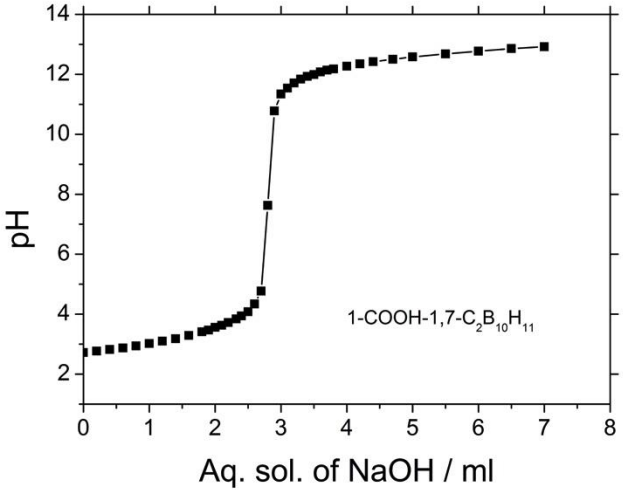

Figure 2.S21. Acid-base titration curves of 1-COOH-7-SH-1,7-$C_2B_{10}H_{10}$ (**M1-COOH**), 1-COOH-9-SH-1,7-$C_2B_{10}H_{10}$ (**M9-COOH**) and 1-COOH-1,7-$C_2B_{10}H_{11}$.

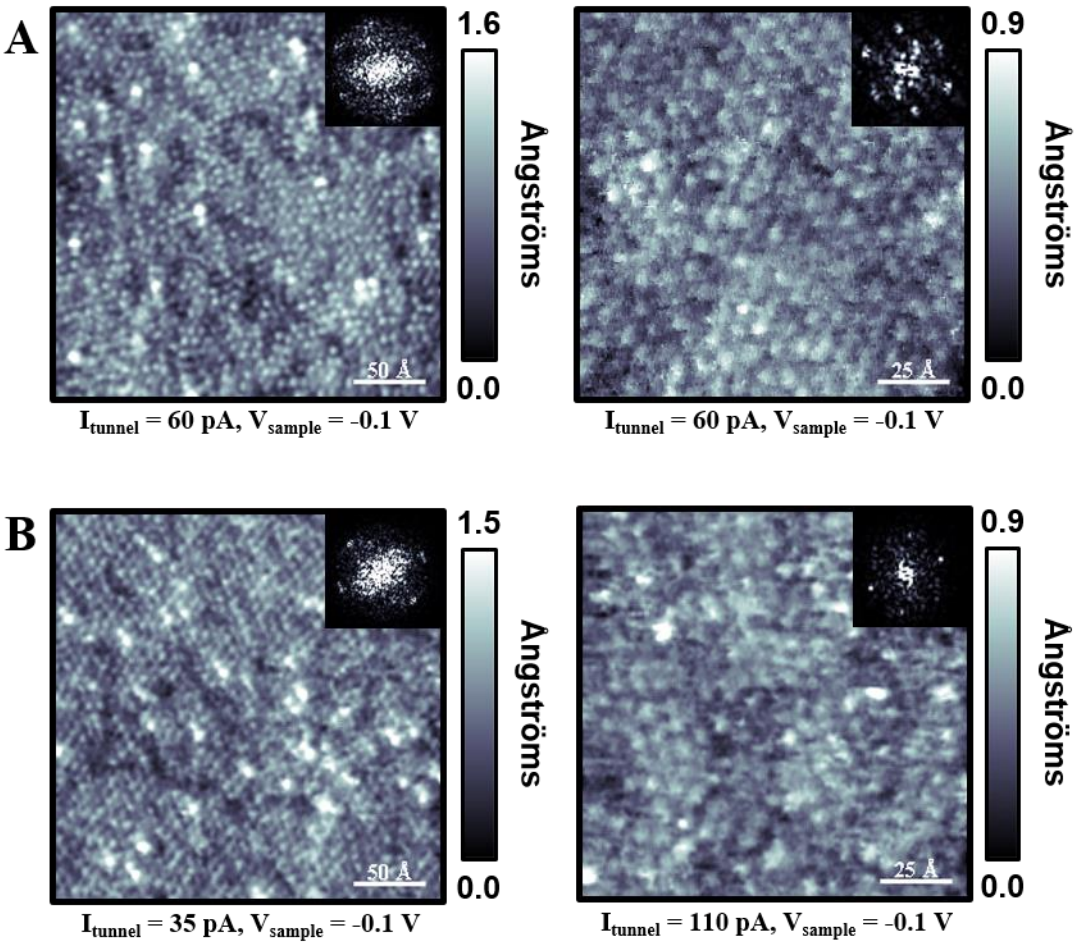

Figure 2.S22. Compilation of scanning tunneling microscopy images, with hexagonally close- packed arrays of (A) 1-COOH-7-SH-1,7-$C_2B_{10}H_{10}$ (**M1-COOH**) and (B) 1-COOH-9-SH-1,7-$C_2B_{10}H_{10}$ (**M9-COOH**) on Au{111}/mica. Both isomers show two-phase monolayers with nearest neighbor distances of 8.4 ± 0.4 Å. Each image inset depicts a Fourier transform used to measure the lattice spacings.

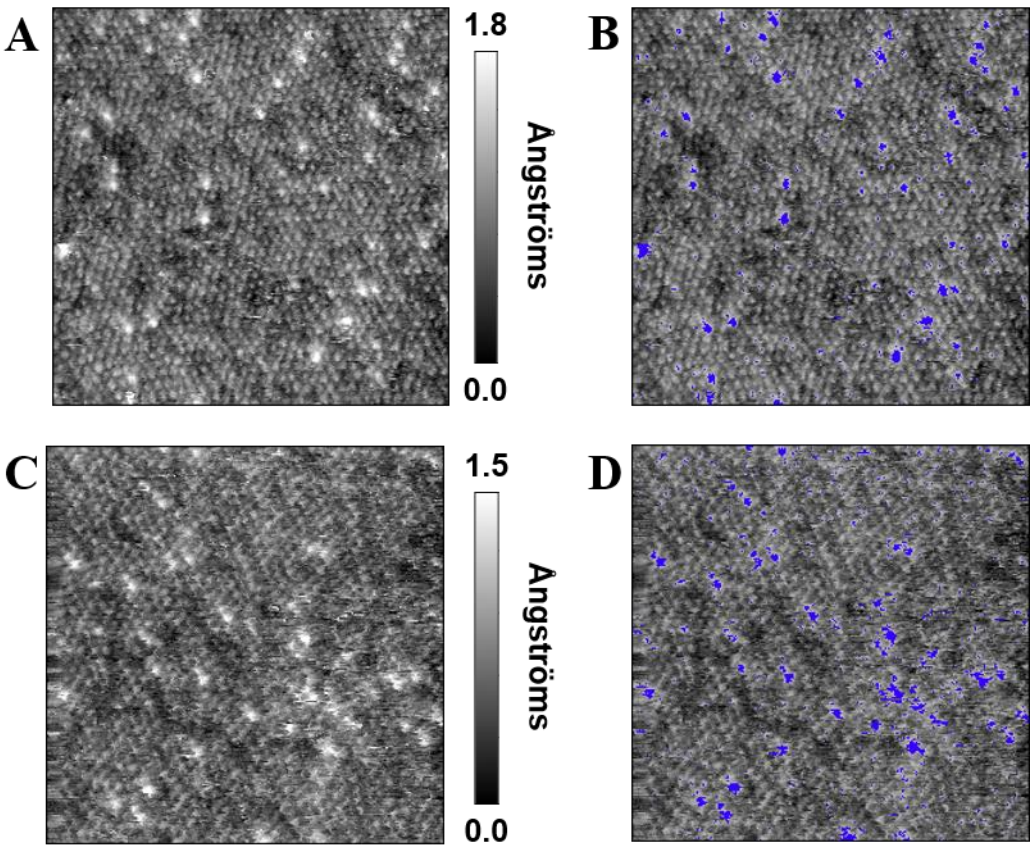

Figure 2.S23. (A) Scanning tunneling microscopy image of 1-COOH-7-SH-1,7-$C_2B_{10}H_{10}$ (**M1-COOH**) and (B) thresholded by apparent height. By using this masking technique, we analyze the two phases of the self-assembled monolayer, showing that the higher intensity protrusion composes 3±1%. (C,D) The same analysis was performed for 1-COOH-9-SH-1,7-$C_2B_{10}H_{10}$ (**M9-COOH**), showing identical characteristics.

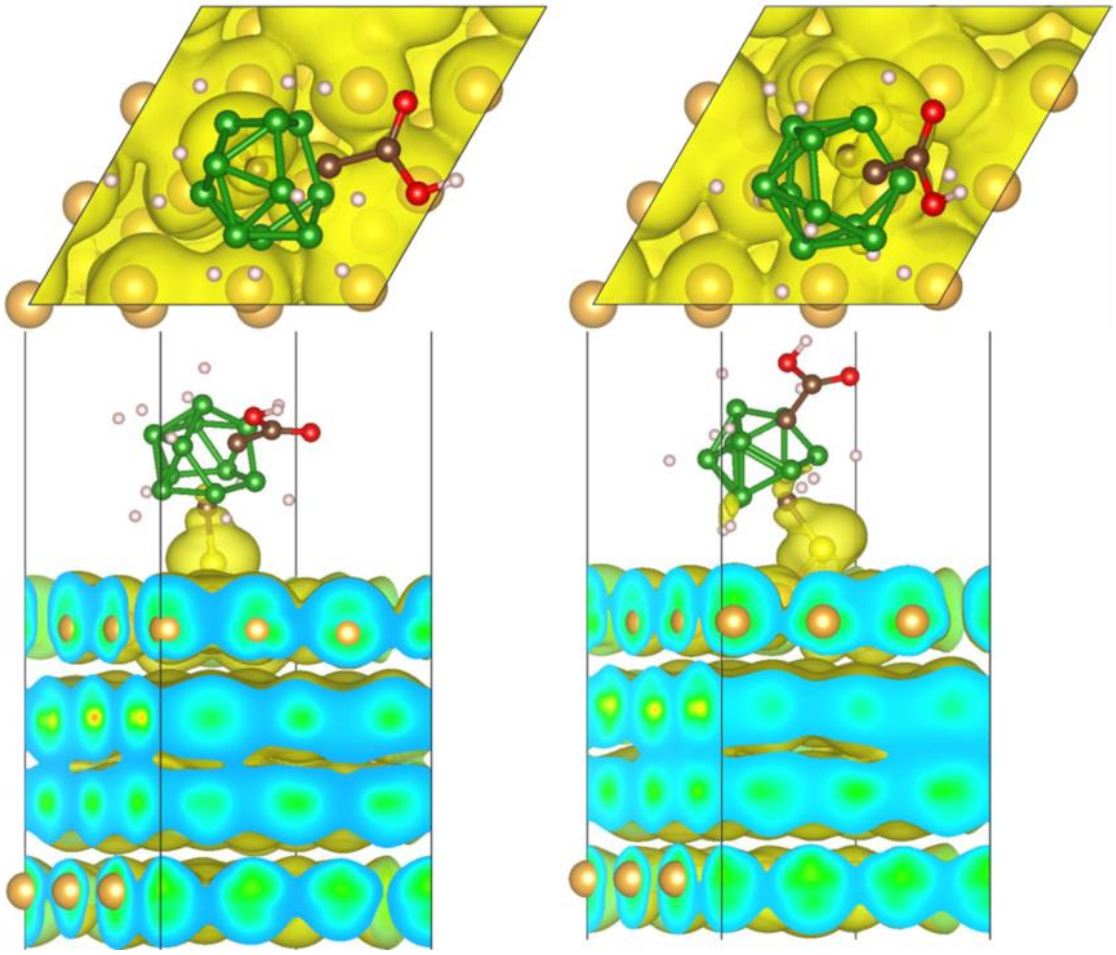

Figure 2.S24. Partial charge density plots from E_F – 0.1 to E_F of 1-COOH-7-SH-1,7-$C_2B_{10}H_{10}$ (**M1-COOH**) in (left) configuration B and (right) configuration A. The images are plotted with an isodensity value of 10^{-4}.

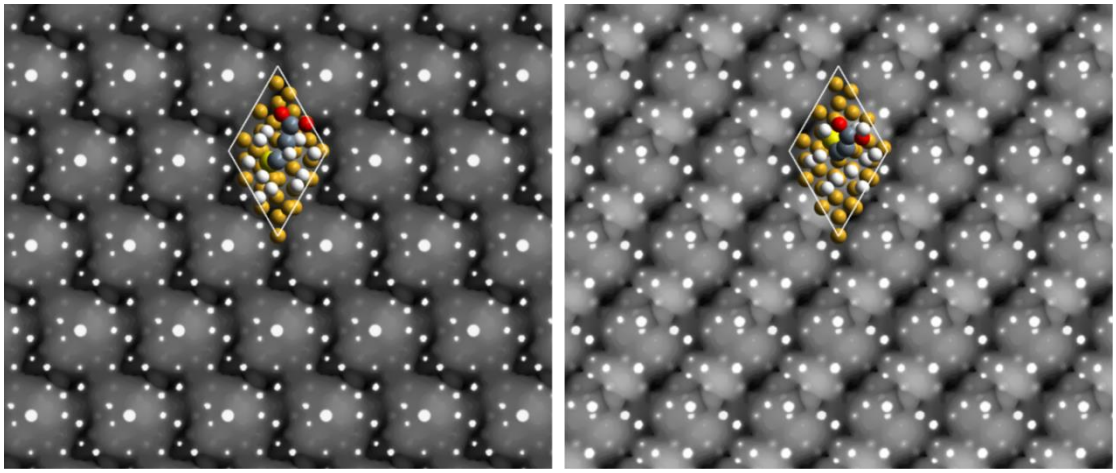

Figure 2.S25. Simulated constant current scanning tunneling microscopy images of 1-COOH-7-SH-1,7-$C_2B_{10}H_{10}$ (**M1-COOH**) in (left) configuration B and (right) configuration A. The isovalue for the charge density is 10^{-4}, and the range of bands is from EF – 0.1 to EF, to simulate the experimental conditions V_{sample} = -0.1 V.

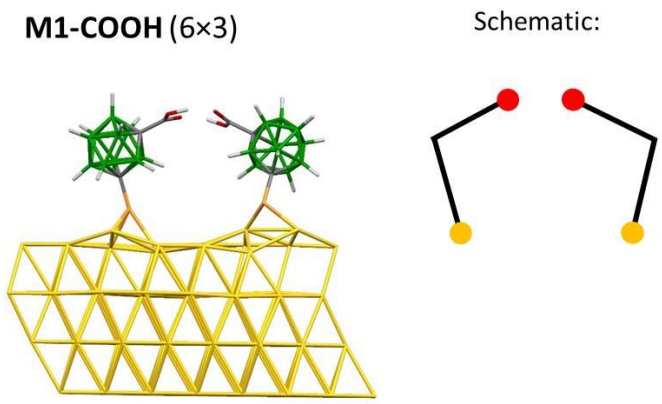

Figure 2.S26. Two molecules of 1-COOH-7-SH-1,7-$C_2B_{10}H_{10}$ (**M1-COOH**) interacting *via* their carboxyl functional groups.

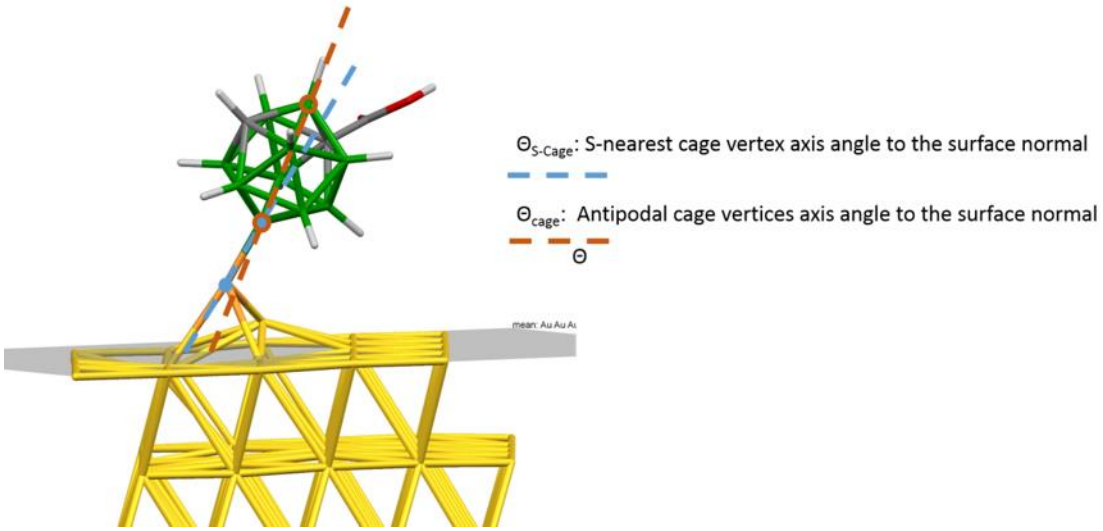

Figure 2.S27. Schematic representation of two axes: *S atom - nearest Cage vertex* ($\Theta_{S\text{-}Cage}$) axis (blue dashed line) and *antipodal cage vertices* (Θ_{Cage}) axis (orange dashed line). The values of $\Theta_{S\text{-}Cage}$ and Θ_{Cage} are the respective angles of these axes to the surface normal.

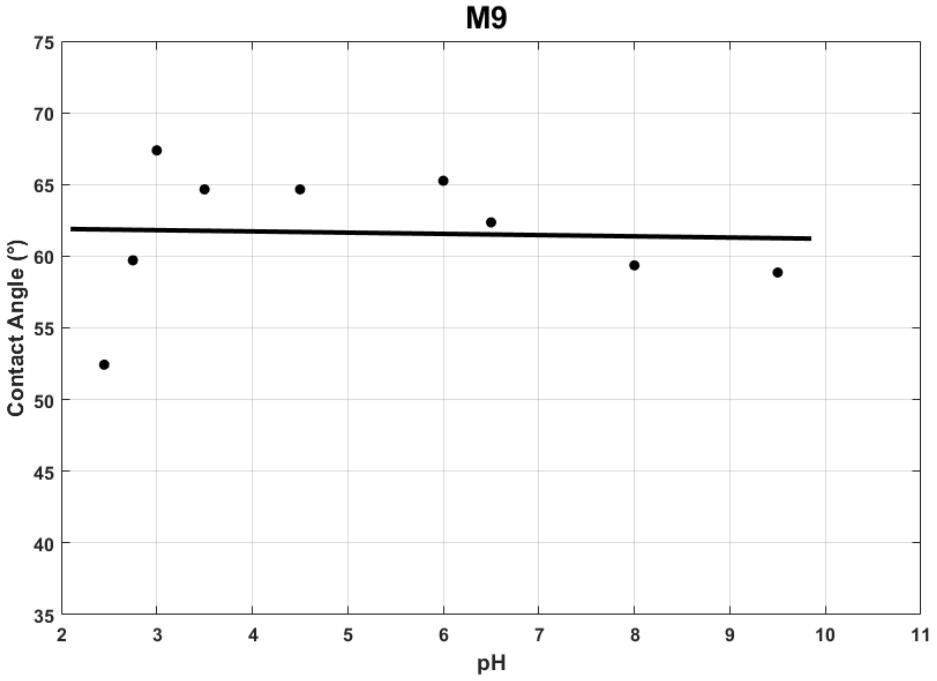

Figure 2.S28. Contact angle titration control performed on a 9-SH-1,7-$C_2B_{10}H_{11}$ (**M9**) self-assembled monolayer, which does *not* have a terminal acid group and therefore the contact angle is *not* a function of pH.

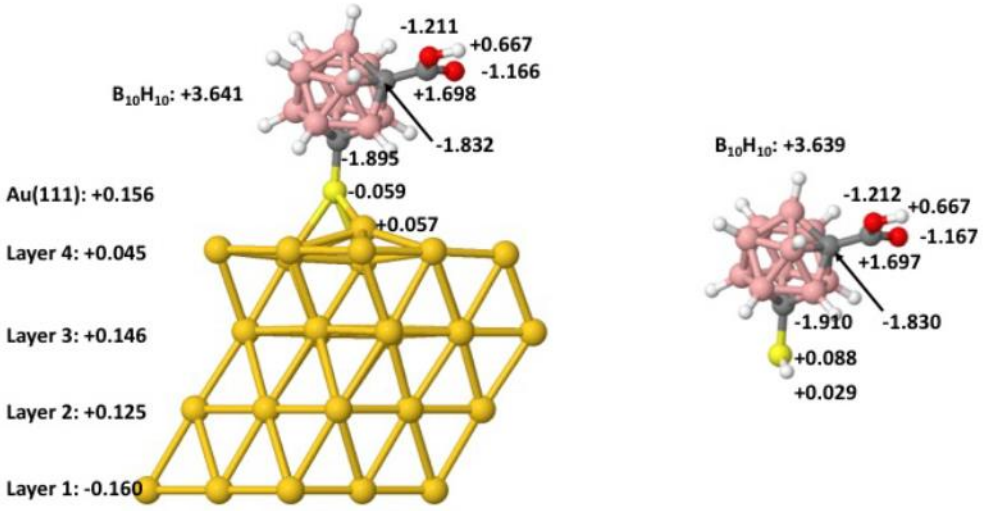

Figure 2.S29. Bader charges for 1-COOH-7-SH-1,7-$C_2B_{10}H_{10}$ (**M1-COOH**) oriented in configuration B (left) on a surface and (right) as a molecule in vacuum.

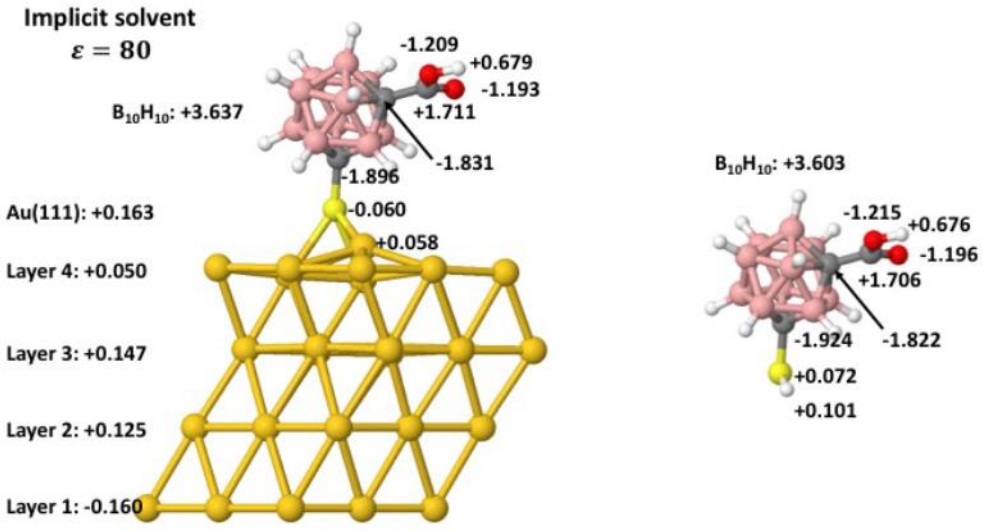

Figure 2.S30. Bader charges for 1-COOH-7-SH-1,7-$C_2B_{10}H_{10}$ (**M1-COOH**) oriented in configuration B (left) on a surface and (right) as a molecule in water.

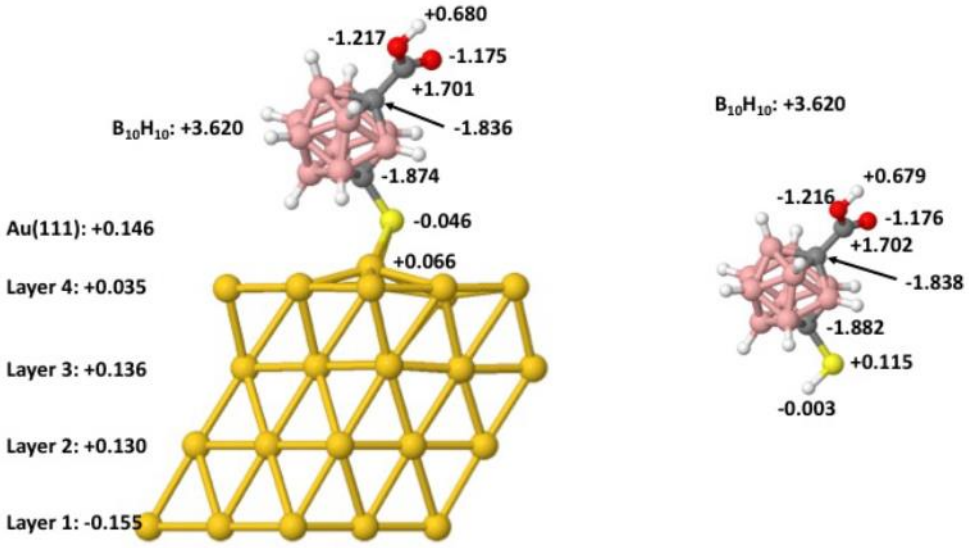

Figure 2.S31. Bader charges for 1-COOH-7-SH-1,7-$C_2B_{10}H_{10}$ (**M1-COOH**) oriented in configuration A (left) on a surface and (right) as a molecule in vacuum.

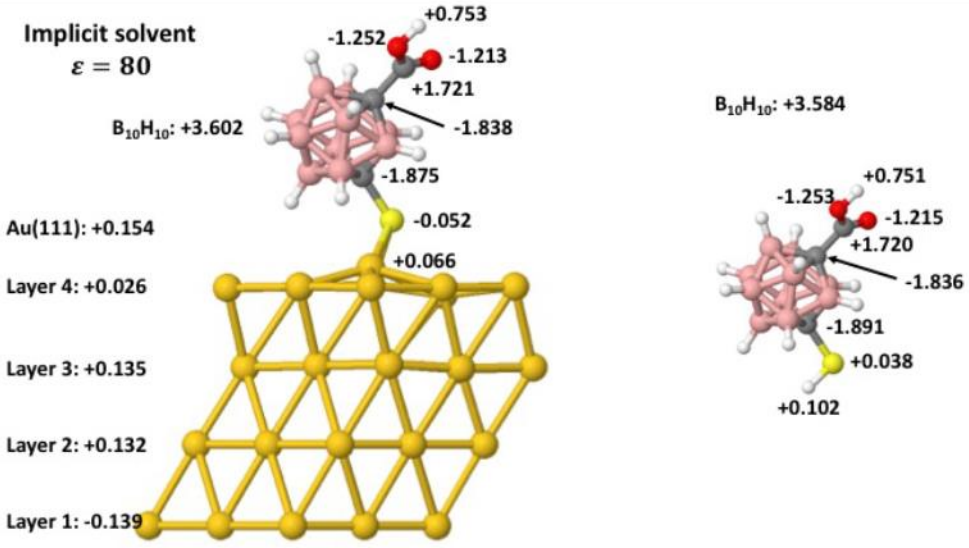

Figure 2.S32. Bader charges for 1-COOH-7-SH-1,7-$C_2B_{10}H_{10}$ (**M1-COOH**) oriented in configuration A (left) on a surface and (right) as a molecule in water.

Table 2.S6. Bader charges of 1-COOH-7-SH-1,7-$C_2B_{10}H_{10}$ (**M1-COOH**) in vacuum.

	M1-COOH Configuration A		M1-COOH Configuration B	
	On Au{111}	Free Molecule	On Au{111}	Free Molecule
H1	0.680	0.679	0.667	0.667
O2	-1.217	-1.216	-1.211	-1.212
O3	-1.175	-1.176	-1.166	-1.167
C4	1.701	1.702	1.698	1.697
-COOH	-0.01	-0.012	-0.012	-0.015
C5	-1.836	-1.838	-1.832	-1.83
C6	-1.874	-1.882	-1.895	-1.91
$B_{10}H_{10}$	3.62	3.62	3.641	3.639
$B_{10}H_{10}C_2$	-0.09	-0.1	-0.086	-0.101
S	-0.046	0.115	-0.059	0.088
Au{111}/H	0.146	-0.003	0.156	0.029

Table 2.S7. Bader charges of 1-COOH-7-SH-1,7-$C_2B_{10}H_{10}$ (**M1-COOH**) in water.

	M1-COOH Configuration A		M1-COOH Configuration B	
	On Au{111}	Free Molecule	On Au{111}	Free Molecule
H1	0.753	0.751	0.679	0.676
O2	-1.252	-1.253	-1.209	-1.215
O3	-1.213	-1.215	-1.193	-1.196
C4	1.721	1.72	1.711	1.706
-COOH	0.009	0.003	-0.013	-0.029
C5	-1.838	-1.836	-1.831	-1.822
C6	-1.875	-1.891	-1.896	-1.924
$B_{10}H_{10}$	3.602	3.584	3.637	3.603
$B_{10}H_{10}C_2$	-0.111	-0.143	-0.09	-0.144
S	-0.052	0.038	-0.06	0.072
Au{111}/H	0.154	0.102	0.163	0.101

Table 2.S8. Energies of neutral (AH) and deprotonated (A^-) single molecules and the difference (Diff) between the two states for 1-COOH-7-SH-1,7-$C_2B_{10}H_{10}$ (**M1-COOH**) and 1-COOH-9-SH-1,7-$C_2B_{10}H_{10}$ (**M9-COOH**) in water. E_{ele} is the electronic energy. G is the thermal Gibbs free energy, which includes a thermal correction and a zero-point correction to the electronic energy. $E_s(H^+)$ = -269 kcal/mol (-0.42869 a.u.) is from experiments.

Isomer		E_{ele} (a.u.)	Correction (a.u.)	G(a.u.)	pK_a	Expt. pK_a
M1-COOH	A^-	-918.441	0.13859	-918.303	1.11	3.01
	AH	-918.884	0.15045	-918.734		
	Diff	0.44294	-0.01186	0.43109		
M9-COOH	A^-	-918.48	0.13996	-918.34	1.02	3.23
	AH	-918.923	0.15209	-918.77		
	Diff	0.44303	-0.01213	0.4309		

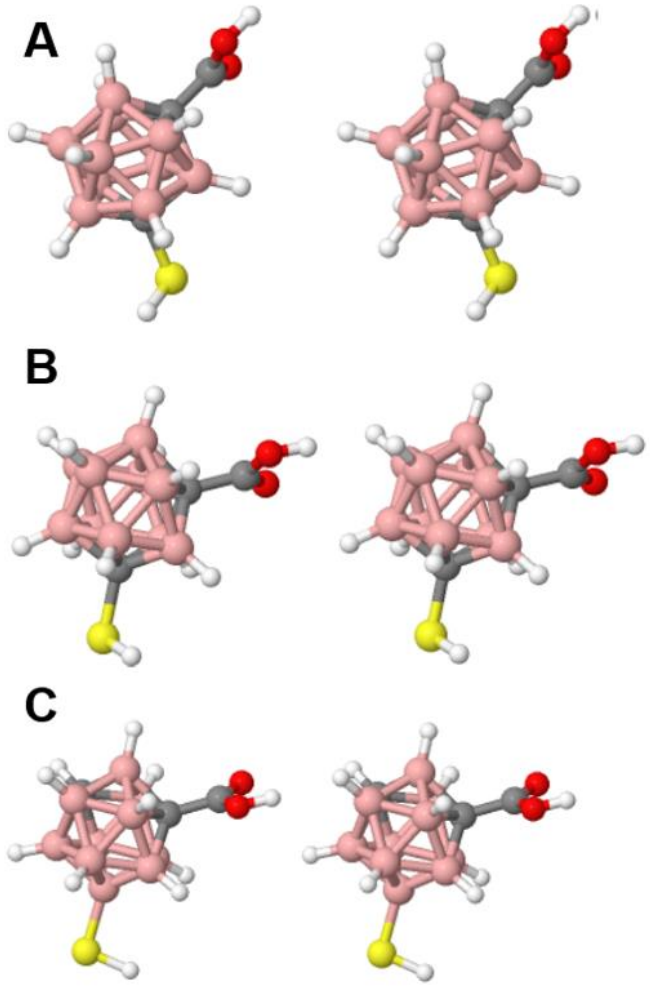

Figure 2 . S33. Dimer geometries of (A) 1-COOH-7-SH-1,7-$C_2B_{10}H_{10}$ (**M1-COOH**) in configuration A, (B) **M1-COOH** in configuration B, and (C) 1-COOH-9-SH-1,7-$C_2B_{10}H_{10}$ (**M9-COOH**).

Table 2.S9. Energies of neutral (AH) and deprotonated (A^-) and the difference (Diff) between the two states for dimer molecules of 1-COOH-7-SH-1,7-$C_2B_{10}H_{10}$ (**M1-COOH**) in configuration A, **M1-COOH** in configuration B, and 1-COOH-9-SH-1,7-$C_2B_{10}H_{10}$ (**M9-COOH**), all in water. E_{ele} is the electronic energy. G is the thermal Gibbs free energy, which includes a thermal correction and a zero-point correction to the electronic energy. $E_s(H^+)$ = -269 kcal/mol (-0.42869 a.u.) is from experiments.

Isomer		E_{ele} (a.u.)	Correction (a.u.)	G(a.u.)	pK_a	Expt. pK_a
M1-COOH Config. A	A^-	-1837.32	-0.02642	-1837.35	1.21	5.10
	AH	-1837.76	-0.01423	-1837.78		
	Diff	0.44352	-0.0122	0.43133		
M1-COOH Config. B	A^-	-1837.32	-0.02558	-1837.34	2.99	
	AH	-1837.76	-0.0137	-1837.78		
	Diff	0.44706	-0.01189	0.43518		
M9-COOH	A^-	-1837.39	-0.02566	-1837.42	2.14	4.80
	AH	-1837.84	-0.01319	-1837.85		
	Diff	0.44581	-0.01246	0.43334		

Table 2.S10. Photoelectron (PE) lines used for qualitative XPS analysis of carborane-carboxylated SAMs exposed to solutions of the denoted ions, together with the observed core level binding energy (BE) and full-width-half-maximum (FWHM) values. The BE values were determined as the BE with the highest intensity for the region of the observed PE line, and as such are not to be used for chemical state analysis. The BE values were referenced to the Au 4f PE lines with the BE value of 84.0 eV. SAMs of 1-COOH-9-SH-1,7-$C_2B_{10}H_{10}$ (**M9-COOH**) were examined.

SAM	PE line	BE (eV)	FWHM (eV)
	Au $4f_{7/2}$	84.0	0.67
	Sr $3d_{5/2}$	134.0	1.34
M9-COOH + Sr(II)[g]	S $2p_{3/2}$	161.7	0.84
	B 1s	189.3	1.20
	C 1s	285.3	1.69
	S $2p_{3/2}$	162.1	2.18
	B 1s	189.7	1.88
M9-COOH + Fe(II)	C 1s	285.0	2.53
	O 1s	531.8	2.71
	Fe $2p_{3/2}$	711.7	6.85
	Au $4f_{7/2}$	84.0	0.71
	S $2p_{3/2}$	161.8	0.83
M9-COOH + Co(II)[g]	B 1s	189.2	1.22
	C 1s	284.9	1.93
	O 1s	532.0	1.89

	Co $2p_{3/2}$	781.4	1.76
M9-COOH + Ni(II)[g]	Au $4f_{7/2}$	84.0	0.66
	S $2p_{3/2}$	161.9	0.87
	B 1s	189.3	1.40
	C 1s	284.9	1.91
	O 1s	531.9	2.56
	Ni $2p_{3/2}$	856.0	1.59
M9-COOH + Cu(II)	S $2p_{3/2}$	162.5	2.32
	B 1s	189.8	2.07
	C 1s	285.0	2.53
	Cu $2p_{3/2}$	932.6	3.11
M9-COOH + Zn(II)	S $2p_{3/2}$	162.0	1.98
	B 1s	189.6	2.15
	C 1s	285.0	2.74
	O 1s	532.3	2.72
	Zn $2p_{3/2}$	1022.7	2.58
M9-COOH + La(III)	S $2p_{3/2}$	162.1	2.15
	B 1s	189.6	1.53
	C 1s	285.0	2.45
	O 1s	532.5	2.55
	La $3d_{5/2}$	839.2	5.70

	La $3d_{3/2}$	855.9	5.42
M9-COOH + Sm(III)	S $2p_{3/2}$	162.0	1.88
	B 1s	189.7	1.62
	C 1s	285.0	2.33
	O 1s	532.8	2.64
	Sm $3d_{5/2}$	1085.5	4.67
M9-COOH + Tb(III)	Tb $4d_{3/2}$	152.6	6.71
	S $2p_{3/2}$	162.0	1.87
	B 1s	189.3	2.31
	C 1s	285.0	2.86
	O 1s	532.2	2.62
	Tb $3d_{5/2}$	1243.6	9.79
	Tb $3d_{3/2}$	1277.0	4.15
M9-COOH + Tl(I)	Tl 4f	118.3	1.01
	S $2p_{3/2}$	162.2	1.33
	B 1s	189.7	1.38
	C 1s	285.0	1.68
	O 1s	531.4	2.37
M9-COOH + Pb(II)	Pb $4f_{7/2}$	139.6	1.36
	S $2p_{3/2}$	162.2	1.07
	B 1s	189.8	1.27
	C 1s	285.0	2.01

	Pb $4d_{5/2}$	414.6	3.28
	Pb $4d_{3/2}$	436.5	2.52
	O 1s	531.9	2.33

[g]The BEs of the sample are referenced to the Au 4f PE line with the corresponding value of 84.0 eV.

Table 2.S11. Stochiometries obtained by quantitative XPS analysis of pristine, as well as ion-modified SAMs, together with the binding energy (BE), kinetic energy (KE), and full-width-half-maximum (FWHM) values of the corresponding photoelectron (PE) lines. The BE values weredetermined as the BE with the highest intensity for the region of the observed PE line, and as such are not to be used for chemical state analysis. The BE values were referenced to the Au 4f PE lines with the BE value of 84.0 eV. No additional elements were detected. SAMs of 1-COOH-9-SH-1,7-$C_2B_{10}H_{10}$ (**M9-COOH**), 9-SH-1,7-$C_2B_{10}H_{11}$(**M9**), and 1-COOH-12-SH-1,12-$C_2B_{10}H_{10}$ (**P1-COOH**) were examined.

SAM	PE line	Stoichiometry	BE (eV)	FWHM (eV)
M9-COOH + Mg(II)	Au $4f_{7/2}$	40.4	84.0	0.80
	S $2p_{3/2}$	0.8	161.7	0.86
	B 1s	10.0	189.3	1.38
	C 1s	10.5	284.9	1.93
	Mg KLL	0.3	306.3	1.84
	O 1s	3.7	531.9	2.25
	Mg 1s	0.5	1304.6	1.52
M9-COOH + Ba(II)	Au $4f_{7/2}$	41.9	84.0	0.84
	S $2p_{3/2}$	0.9	161.6	2.17
	B 1s	10.0	189.4	1.54
	C 1s	26.3	285.0	1.75
	O 1s	3.1	531.6	2.23
	Ba $3d_{5/2}$	0.5	780.6	1.65

M9-COOH	Au $4f_{7/2}$	50.7	84.0	0.81
	S $2p_{3/2}$	0.7	161.8	0.85
	B 1s	10.0	189.4	1.39
	C 1s	21.9	284.8	2.00
	O 1s	4.0	532.3	2.87
	Na 1s	0.8	1071.7	1.51
M9-COOH + H_3O^+	Au $4f_{7/2}$	74.4	84.0	0.80
	S $2p_{3/2}$	0.8	161.7	0.68
	B 1s	10.0	189.1	1.29
	C 1s	38.3	284.5	1.57
	O 1s	6.1	532.3	3.21
	Na1s	0.9	1071.6	1.53
M9	Au $4f_{7/2}$	55.5	84.0	0.80
	S $2p_{3/2}$	0.9	161.8	1.07
	B 1s	10.0	189.5	1.45
	C 1s	32.5	284.7	1.35
	O 1s	6.3	532.3	1.36
	Na 1s	0.0	~1071.9	-
M9 + H_3O^+	Au $4f_{7/2}$	64.0	84.0	0.80
	S $2p_{3/2}$	0.9	161.7	0.94
	B 1s	10.0	189.4	1.44

	C 1s	24.4	284.5	1.51

	O 1s	6.1	532.1	1.50
	Na 1s	0.1	1071.5	0.69
P1-COOH	Au $4f_{7/2}$	42.7	84.0	0.80
	S $2p_{3/2}$	0.8	162.4	0.89
	B 1s	10.0	189.0	1.00
	C 1s	11.1	284.6	2.33
	O 1s	2.9	531.8	2.28
	Na 1s	0.3	1071.7	1.53
P1-COOH + H_3O^+	Au $4f_{7/2}$	86.6	84.0	0.79
	S $2p_{3/2}$	1.0	163.4	0.65
	B 1s	10.0	189.0	1.20
	C 1s	31.8	284.3	1.42
	O 1s	3.5	532.0	2.45
	Na 1s	0.4	1071.4	1.47

Table 2.S12. Photoelectron (PE) lines used for quantitative XPS analysis of sulfates used as reference samples for determination of relative sensitivity factors. No additional elements were detected on the sample surfaces. Binding energy (BE); full-width-half-maximum (FWHM). The BE values were determined as the BE with the highest intensity for the region of the observed PE line. The BEs are referenced to the C 1s PE lines with the corresponding value of 285.0 eV.

Sample	PE line	BE (eV)	FWHM (eV)
Na_2SO_4	C 1s	285.0	1.38
	S $2p_{3/2}$	168.9	1.92
	Na KLL	497.3	1.98
	O 1s	531.9	1.46
	Na 1s	1071.6	1.51
$MgSO_4$	S $2p_{3/2}$	169.6	2.16
	C 1s	285.0	1.69
	Mg KLL	307.7	2.46
	O 1s	532.6	1.87
	Mg 1s	1305.3	1.88
$BaSO_4$	S $2p_{3/2}$	168.9	2.10
	C 1s	285.0	1.69
	O 1s	532.0	1.76
	Ba $3d_{5/2}$	780.4	1.89
	Ba $3d_{3/2}$	795.7	1.92

Figure 2.S34. The survey and detailed XPS spectra together with the background used for subtraction, as measured for SAMs of 1-COOH-9-SH-1,7-$C_2B_{10}H_{10}$ (**M9-COOH**) modified with Mg(II).

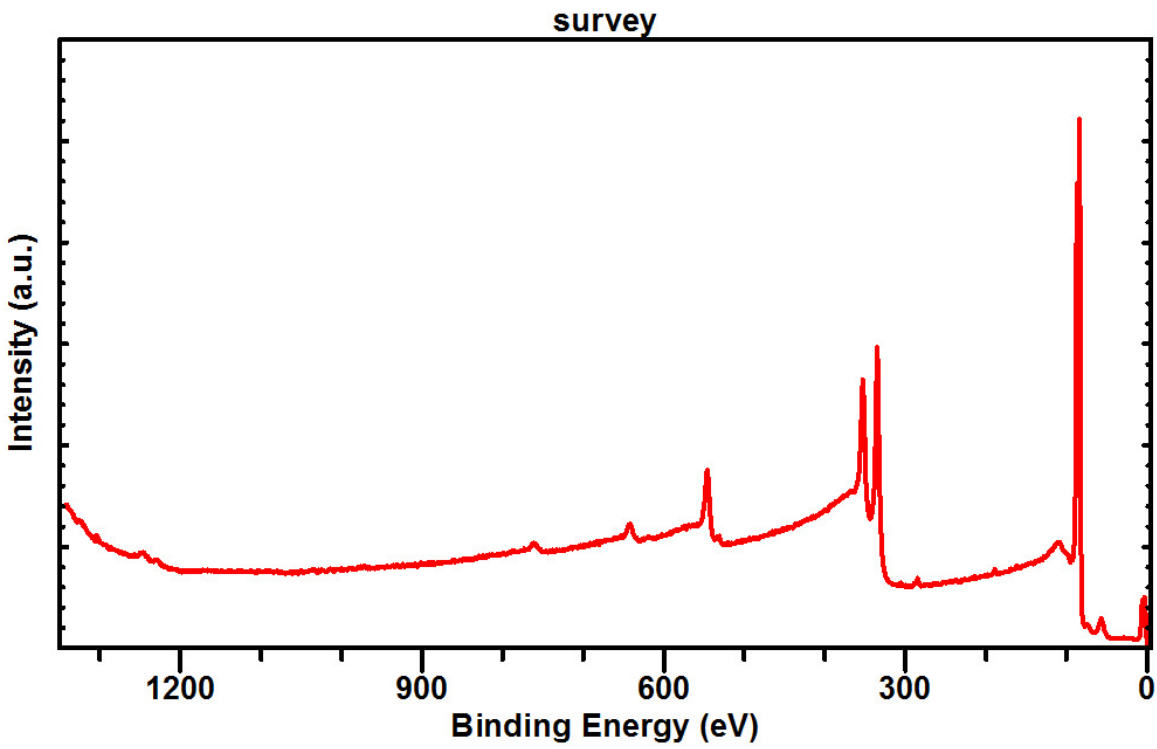

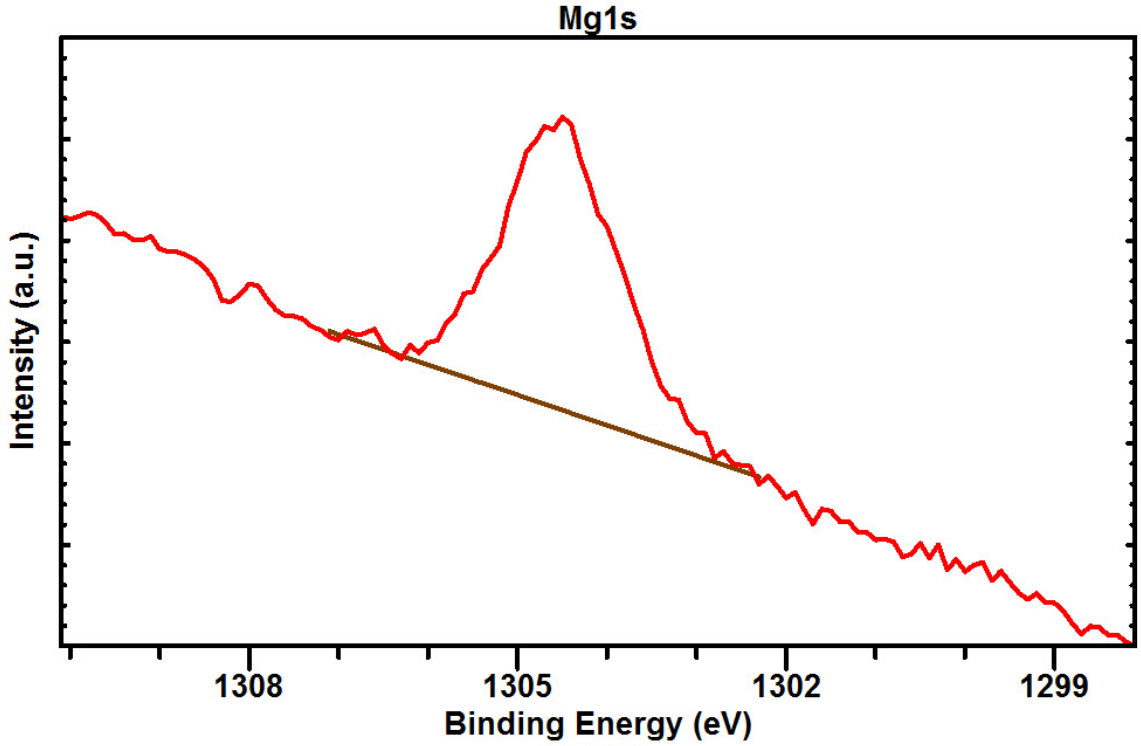
Mg1s
Intensity (a.u.)
1308
1305
1302
1299
Binding Energy (eV)

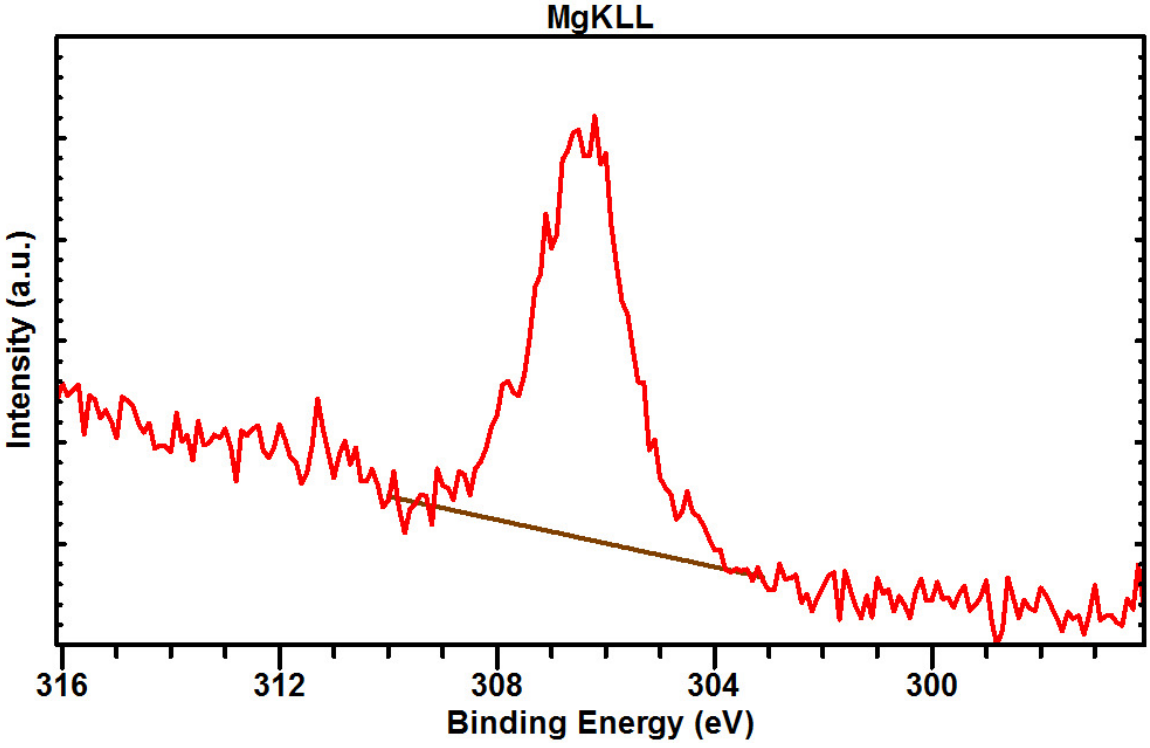
MgKLL
Intensity (a.u.)
316
312
308
304
300
Binding Energy (eV)

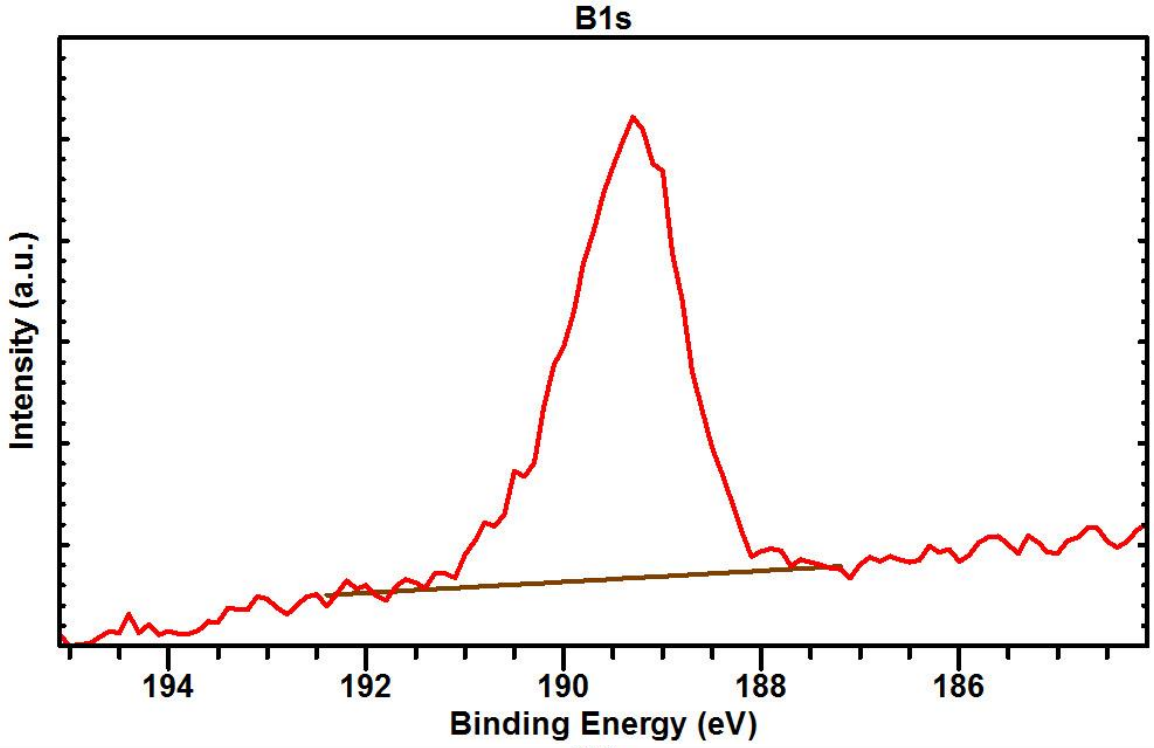
B1s
Intensity (a.u.)
194
192
190
188
186
Binding Energy (eV)

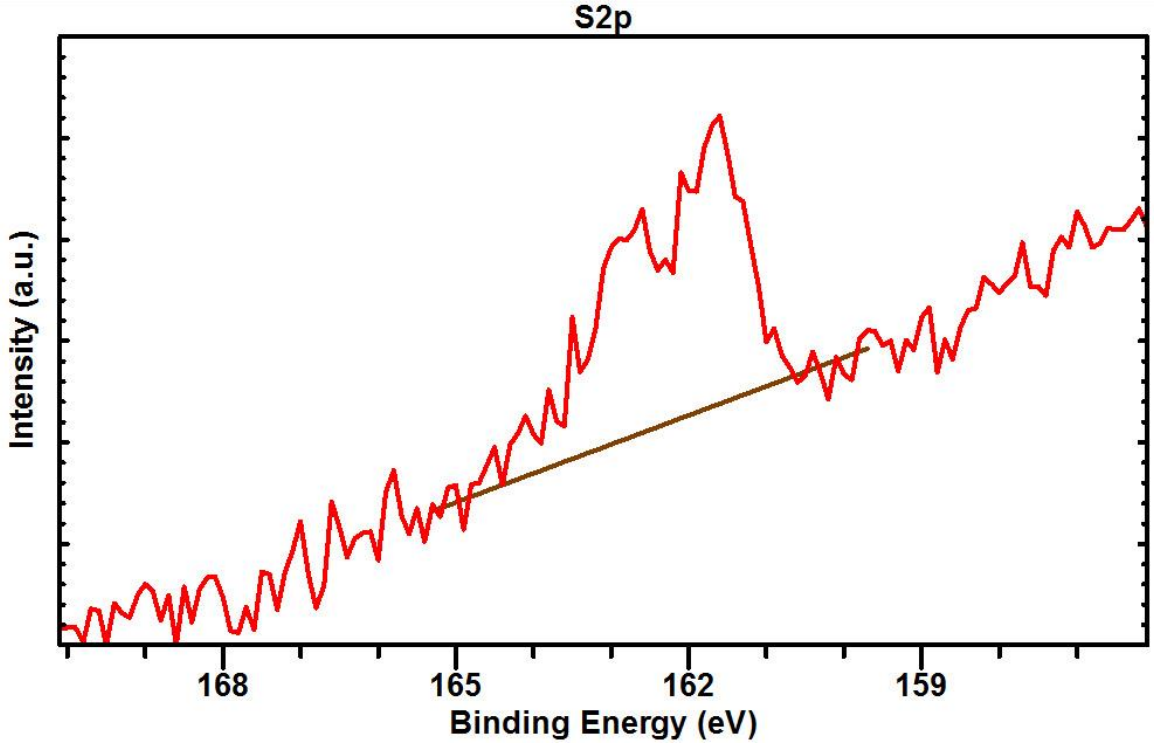
S2p
Intensity (a.u.)
168
165
162
159
Binding Energy (eV)

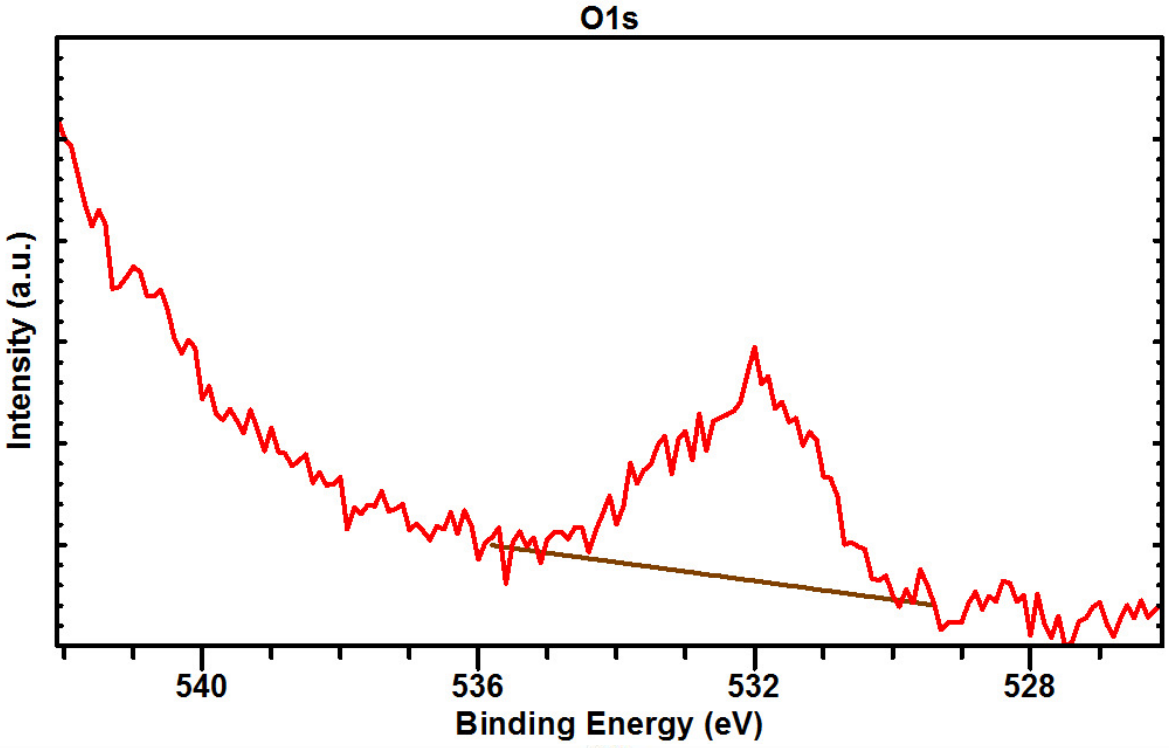
O1s
Intensity (a.u.)
540
536
532
528
Binding Energy (eV)

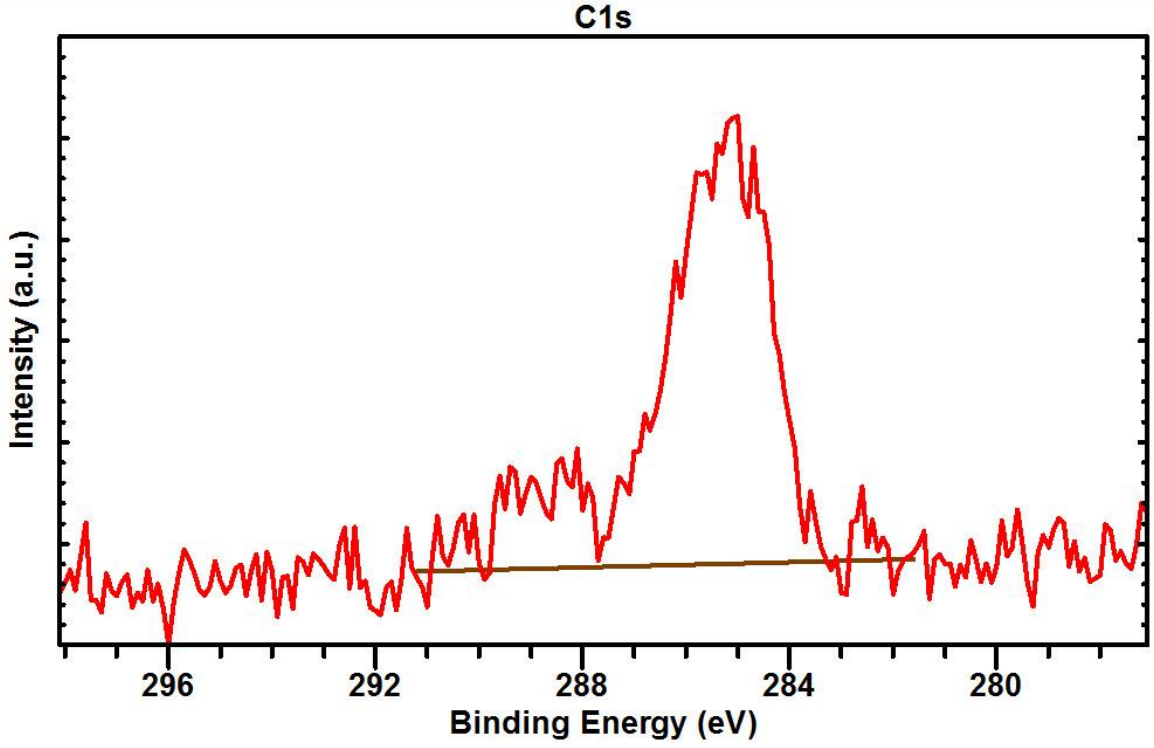
C1s
Intensity (a.u.)
296
292
288
284
280
Binding Energy (eV)

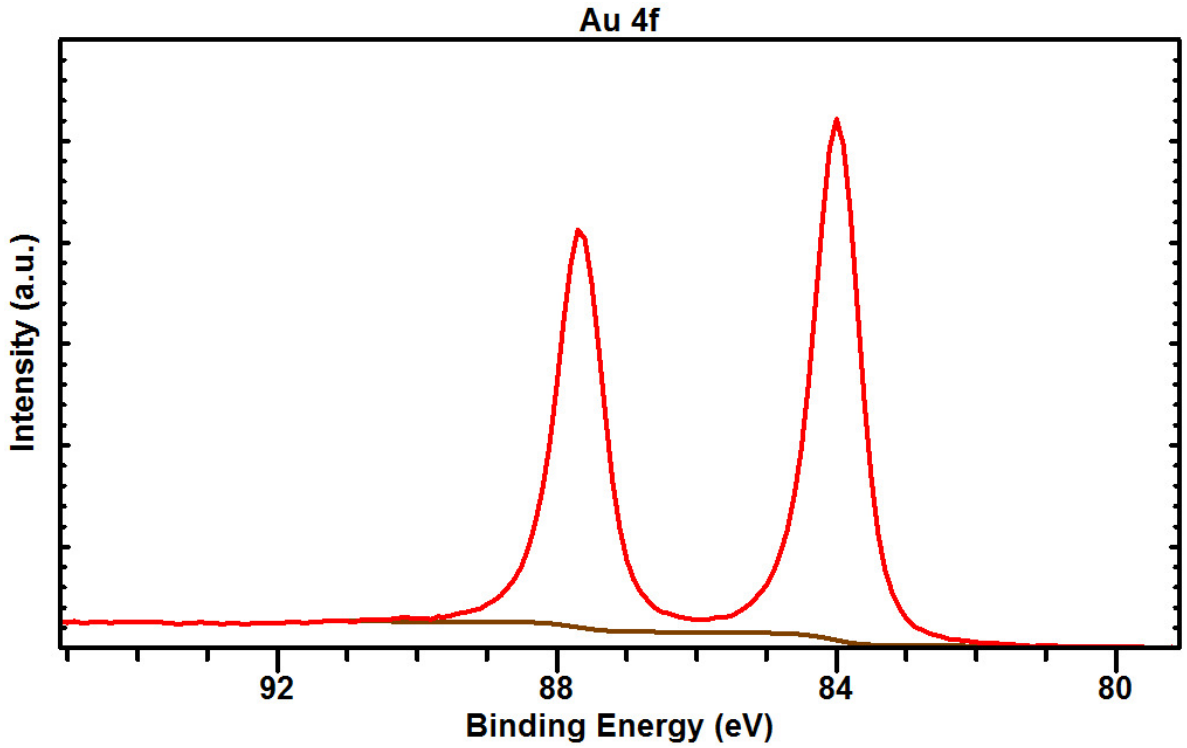
Au 4f
Intensity (a.u.)
92
88
84
80
Binding Energy (eV)

Figure 2.S35. The survey and detailed XPS spectra together with the subtracted background, as measured for SAMs of 1-COOH-9-SH-1,7-$C_2B_{10}H_{10}$ (**M9-COOH**) modified with Ba(II).

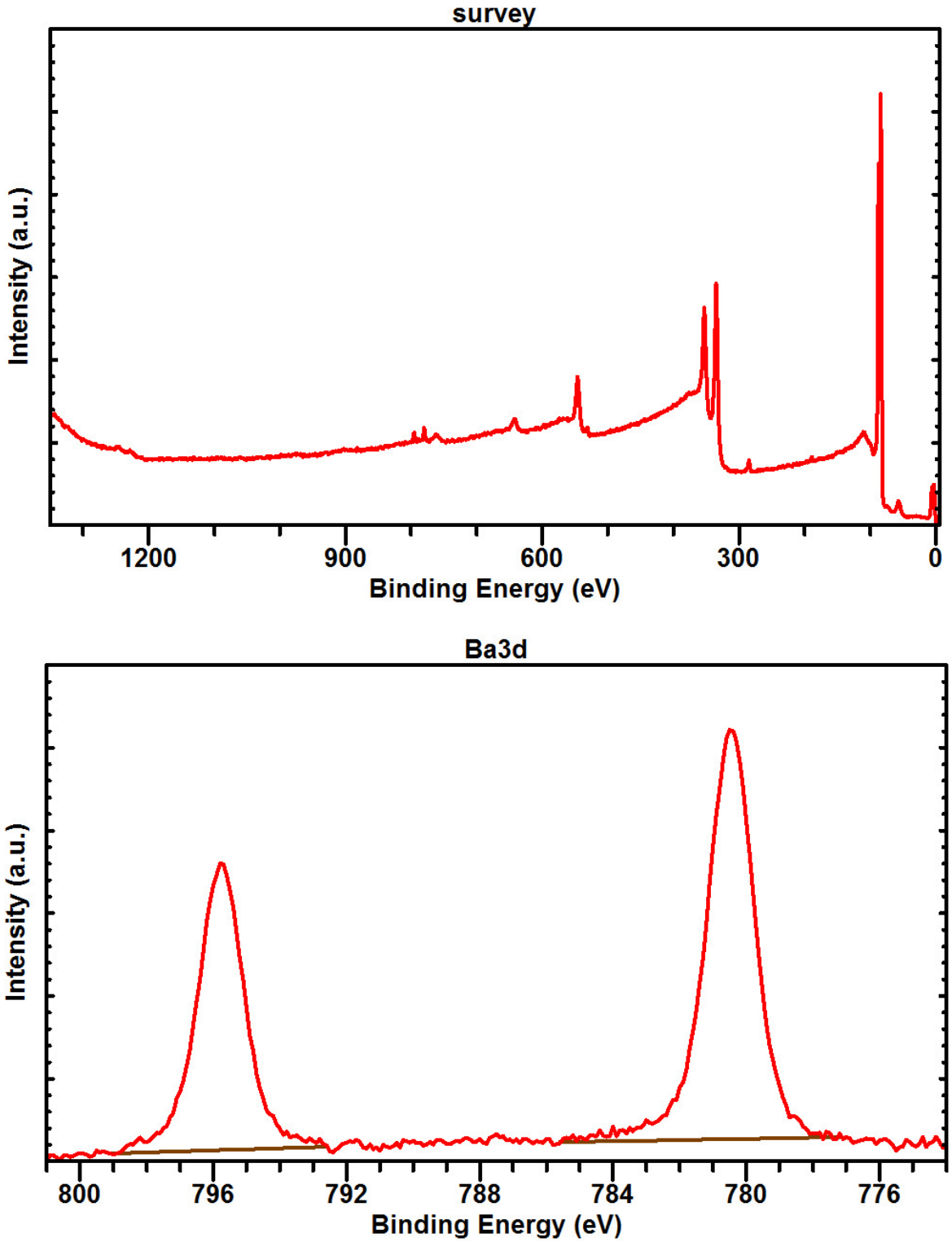

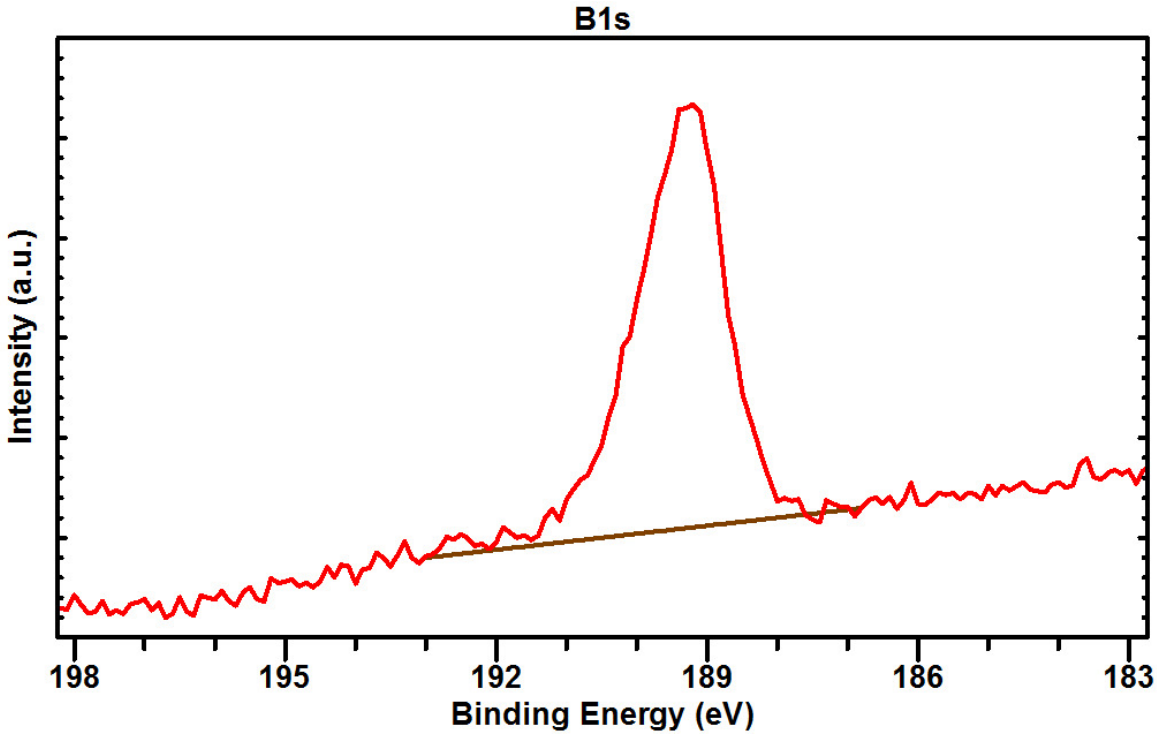
B1s
Intensity (a.u.)
198
195
192
189
186
183
Binding Energy (eV)

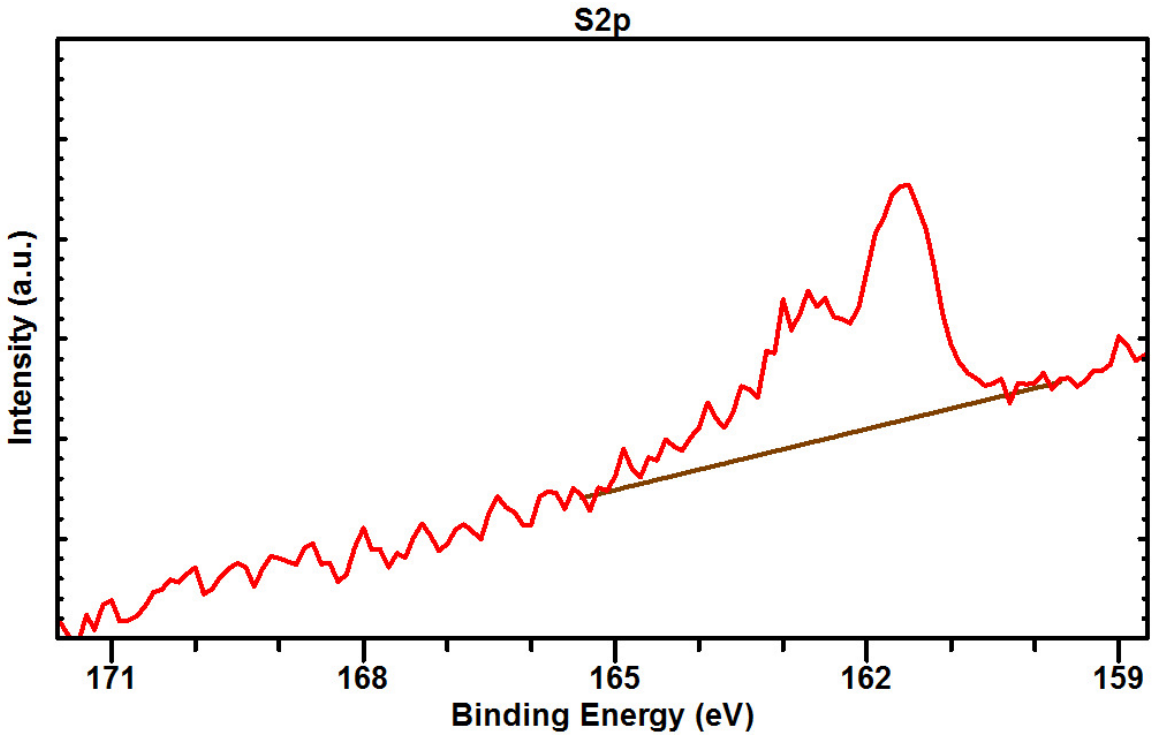
S2p
Intensity (a.u.)
171
168
165
162
159
Binding Energy (eV)

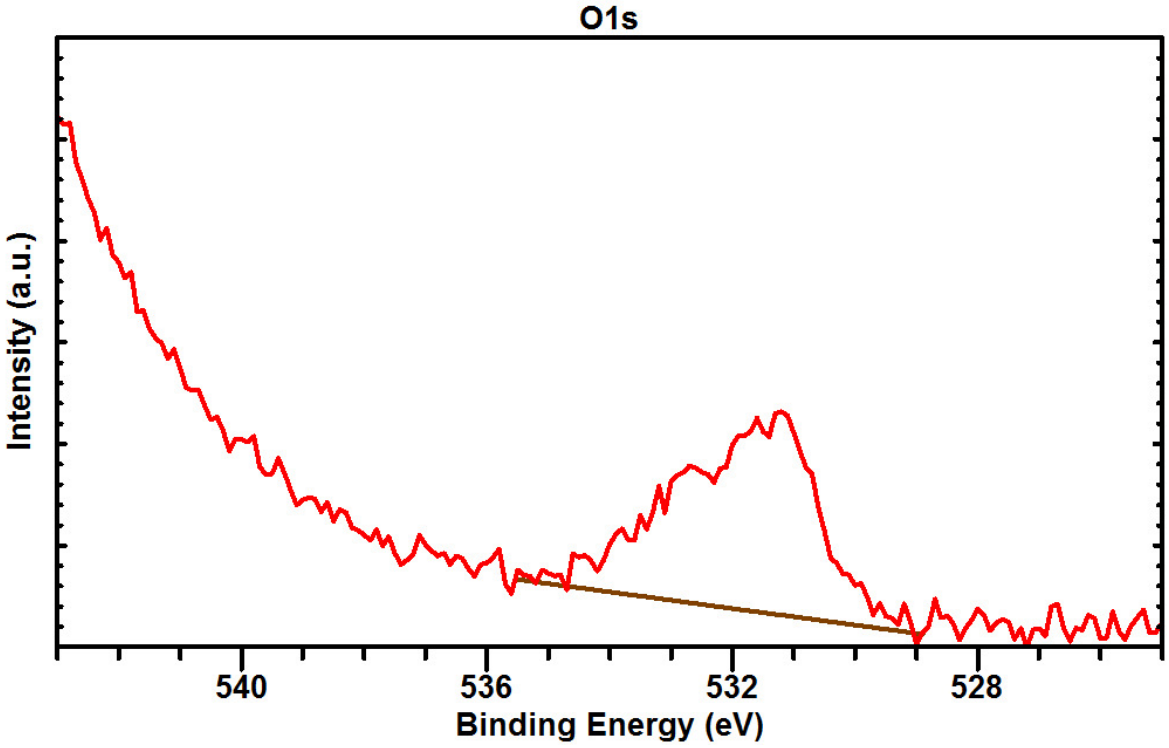
O1s
Intensity (a.u.)
540
536
532
528
Binding Energy (eV)

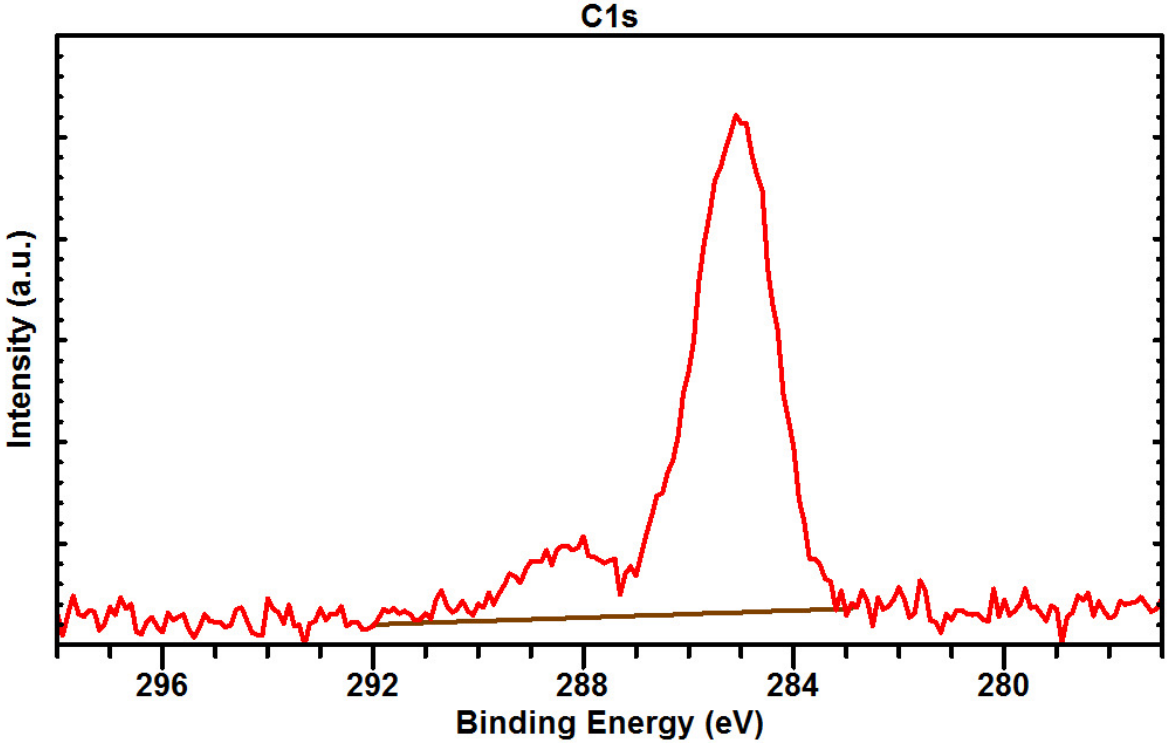
C1s
Intensity (a.u.)
296
292
288
284
280
Binding Energy (eV)

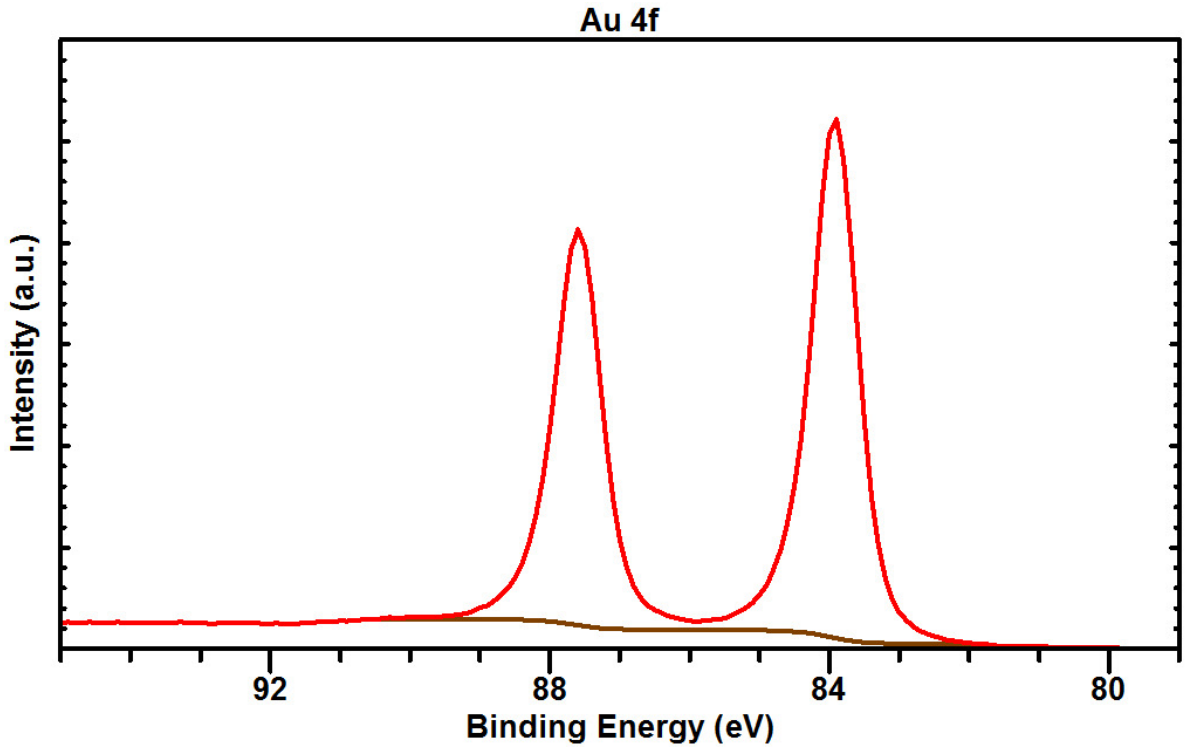
Au 4f
Intensity (a.u.)
92
88
84
80
Binding Energy (eV)

Figure 2.S36. The survey and detailed XPS spectra together with the background used for subtraction, as measured for pristine SAMs of 1-COOH-9-SH-1,7-$C_2B_{10}H_{10}$ (**M9-COOH**)

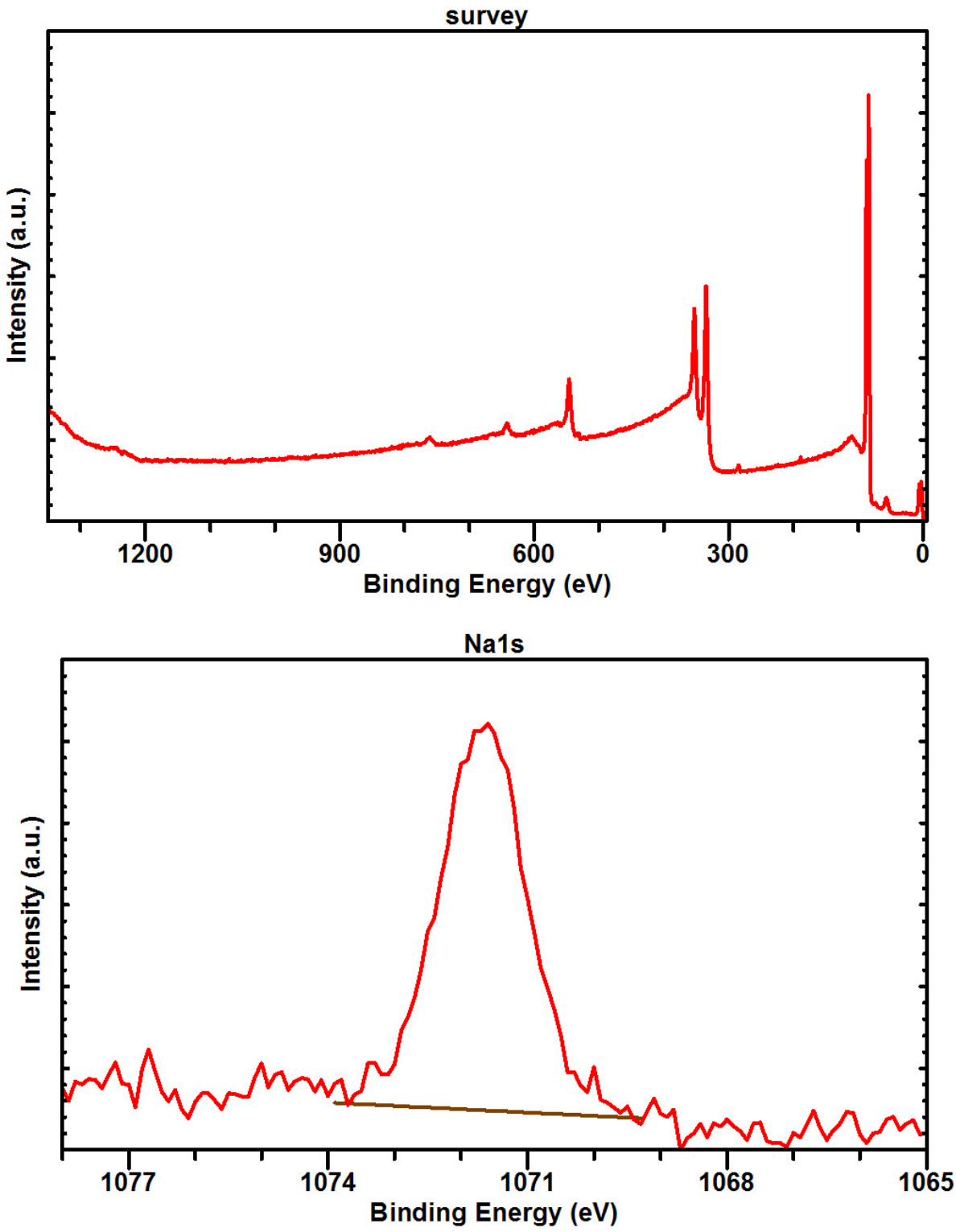

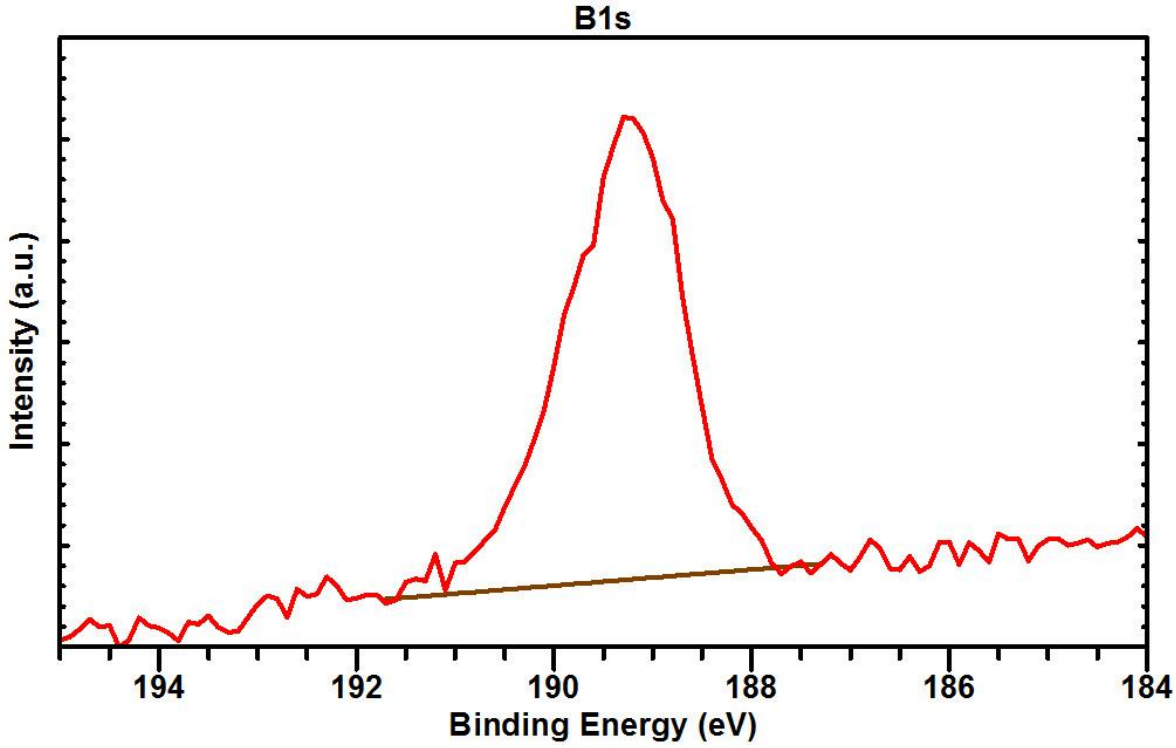
B1s
Intensity (a.u.)
194
192
190
188
186
184
Binding Energy (eV)

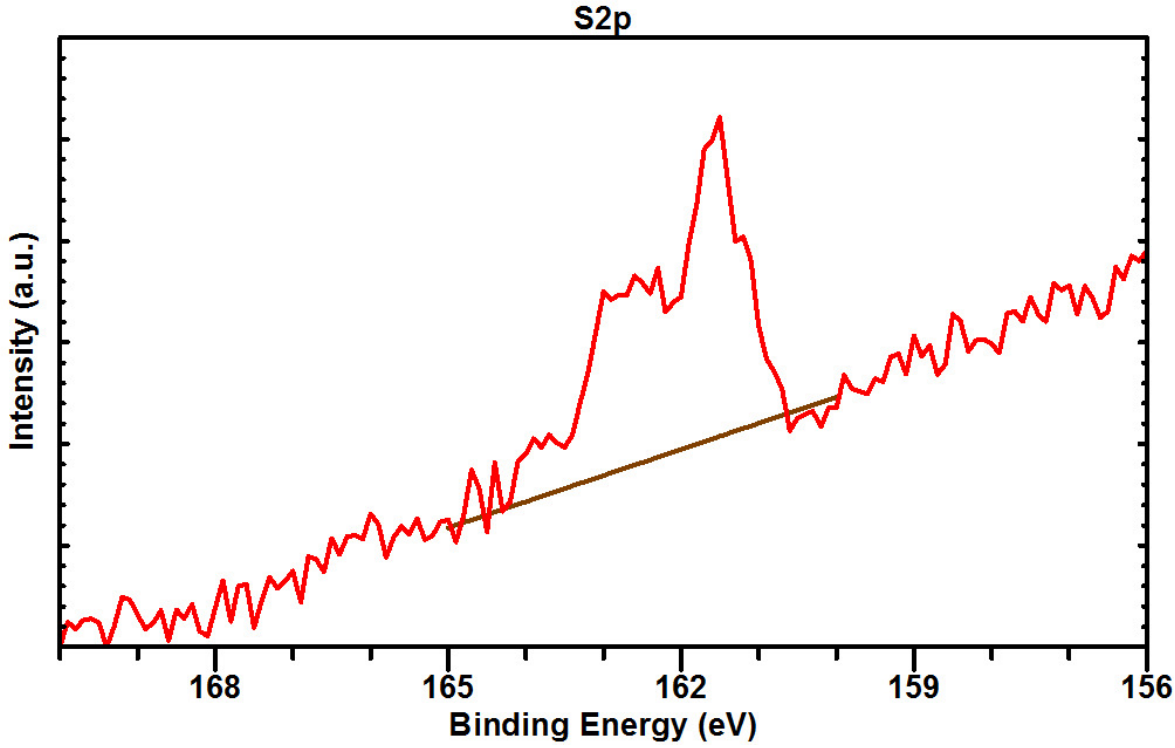
S2p
Intensity (a.u.)
168
165
162
159
156
Binding Energy (eV)

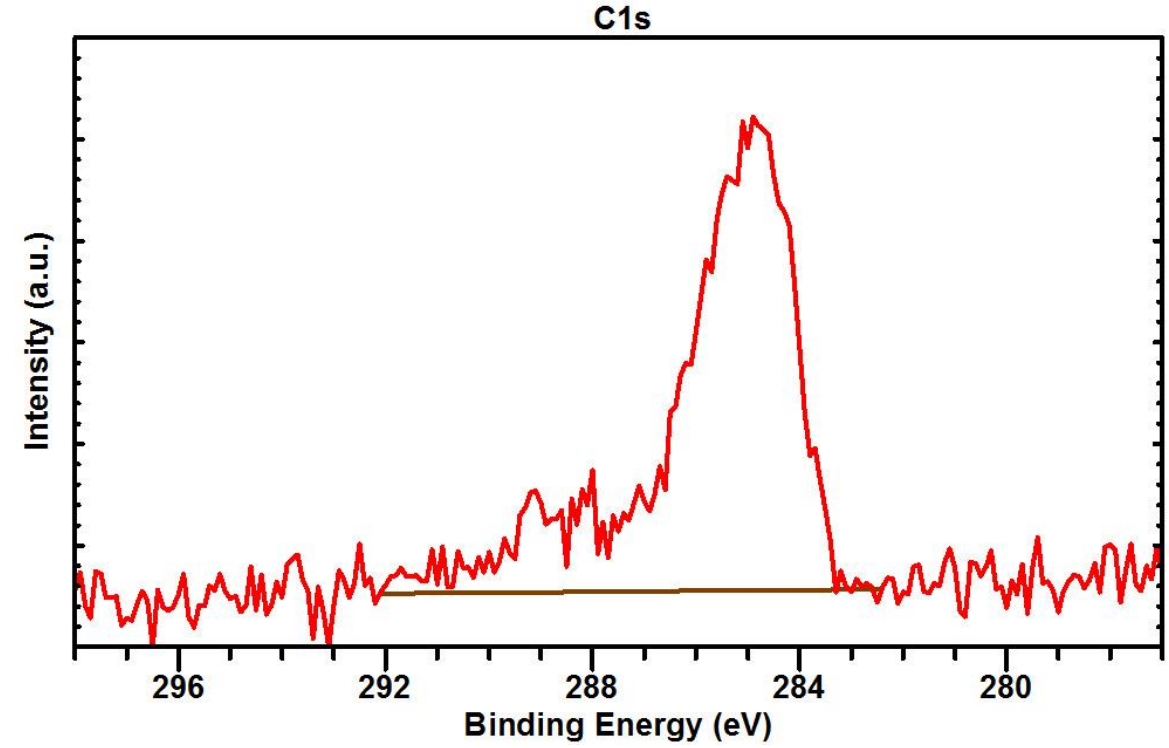
C1s
Intensity (a.u.)
296
292
288
284
280
Binding Energy (eV)

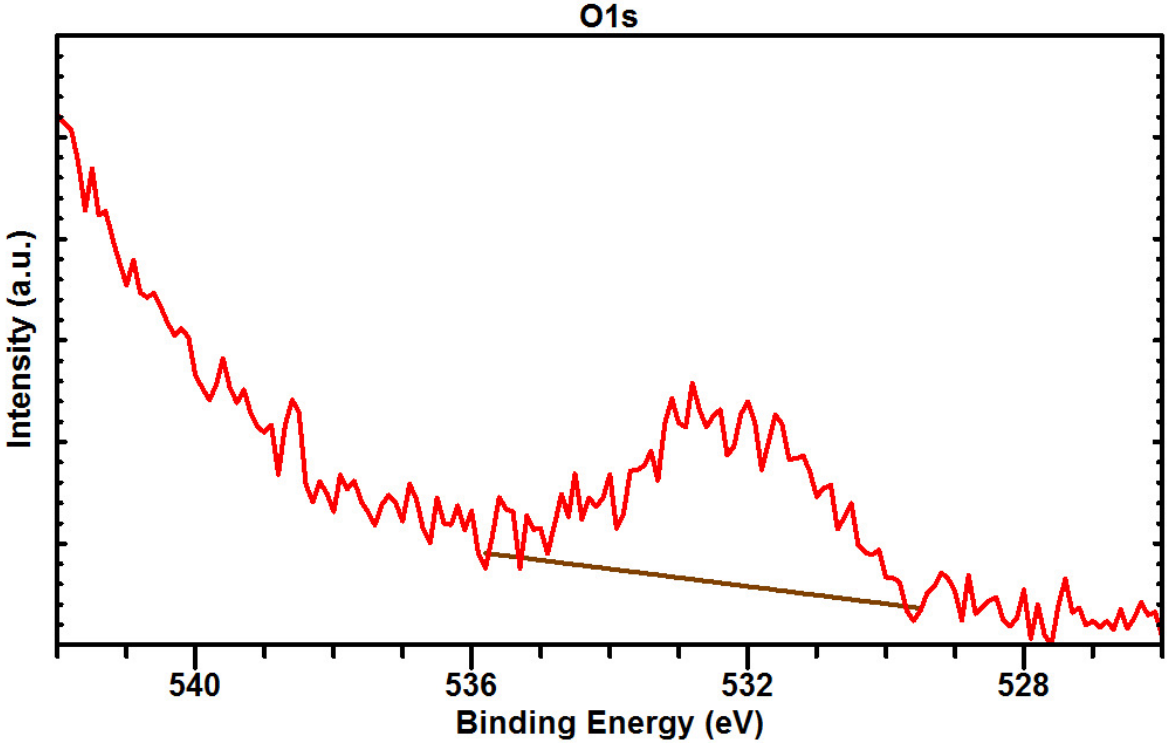
O1s
Intensity (a.u.)
540
536
532
528
Binding Energy (eV)

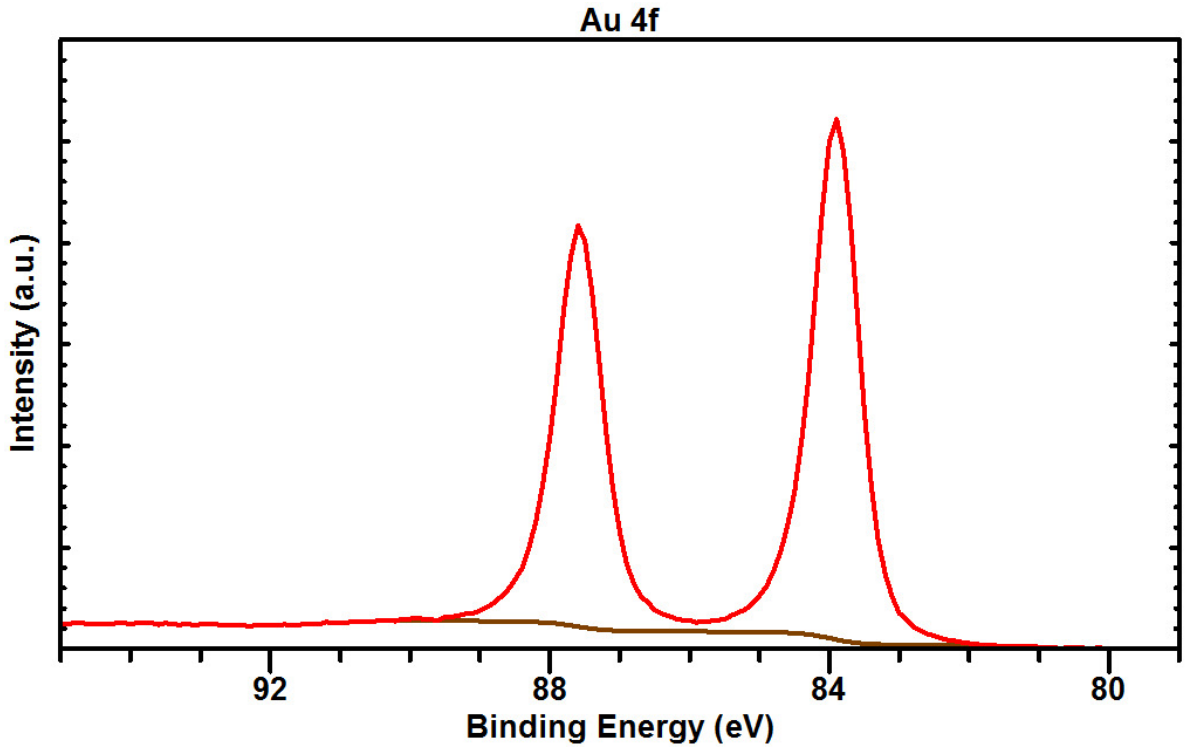
Au 4f
Intensity (a.u.)
92
88
84
80
Binding Energy (eV)

Figure 2.S37. The survey and detailed XPS spectra together with the background used for subtraction, as measured for SAMs of 1-COOH-9-SH-1,7-$C_2B_{10}H_{10}$ (**M9-COOH**) modified with H_3O^+.

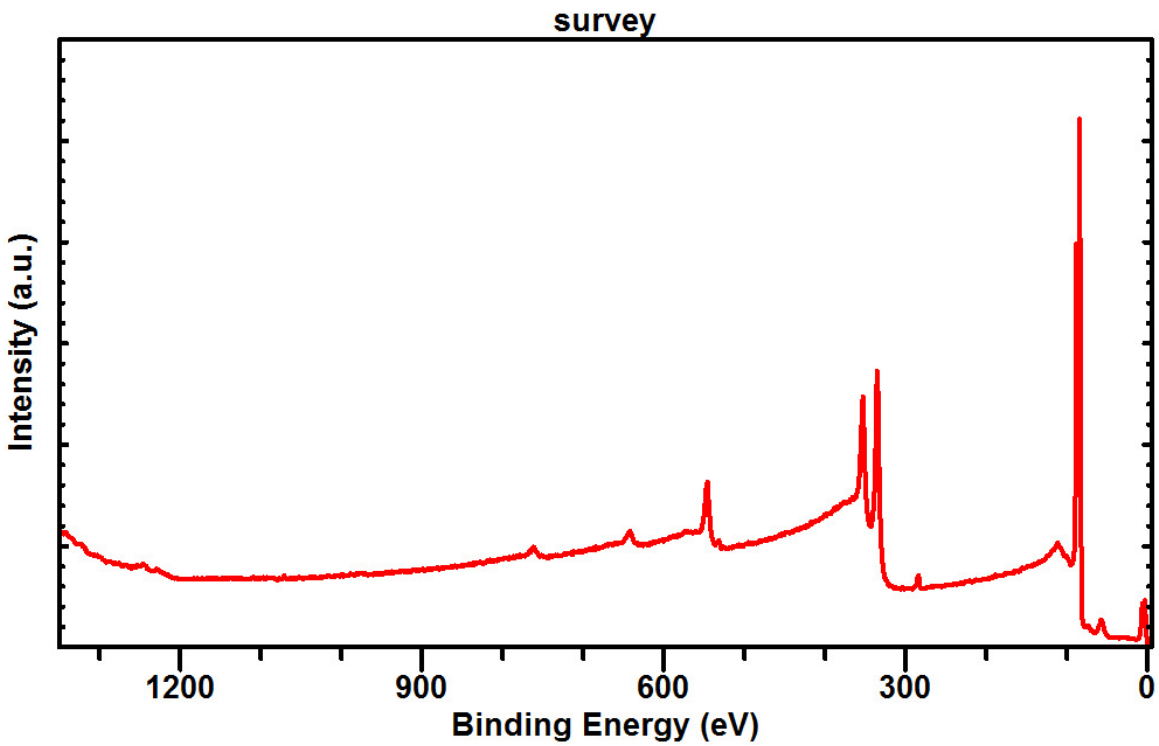

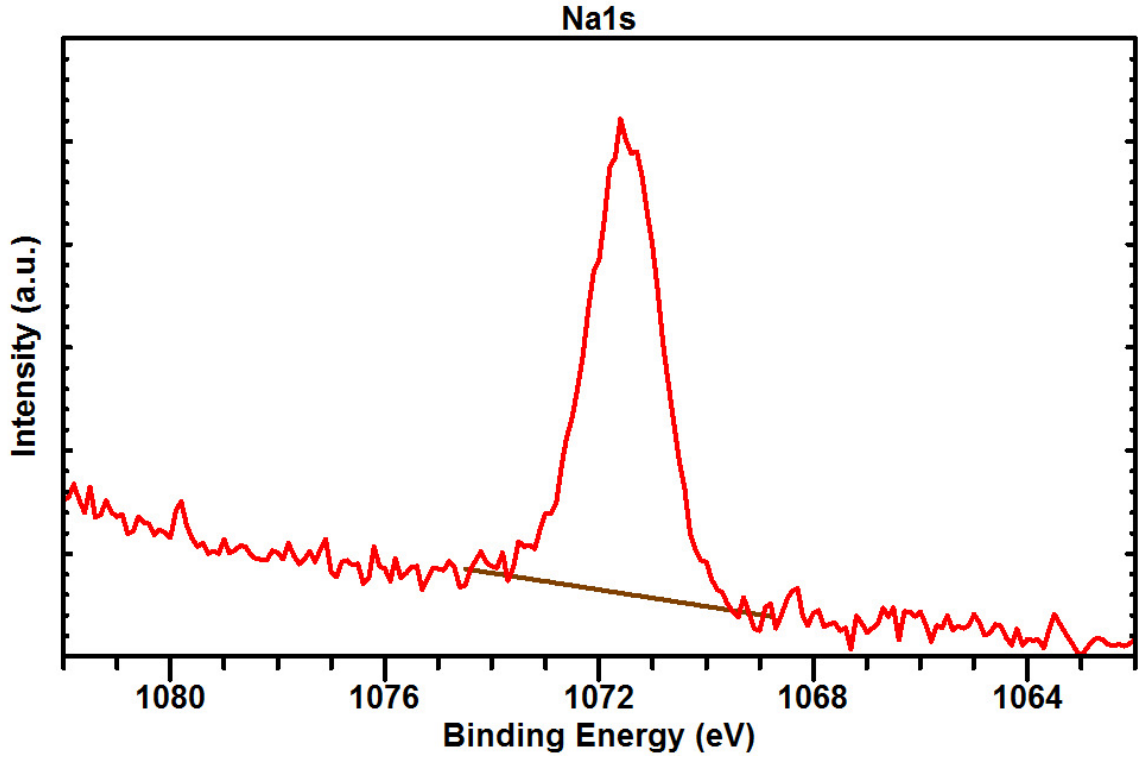
Na1s
Intensity (a.u.)
1080
1076
1072
1068
1064
Binding Energy (eV)

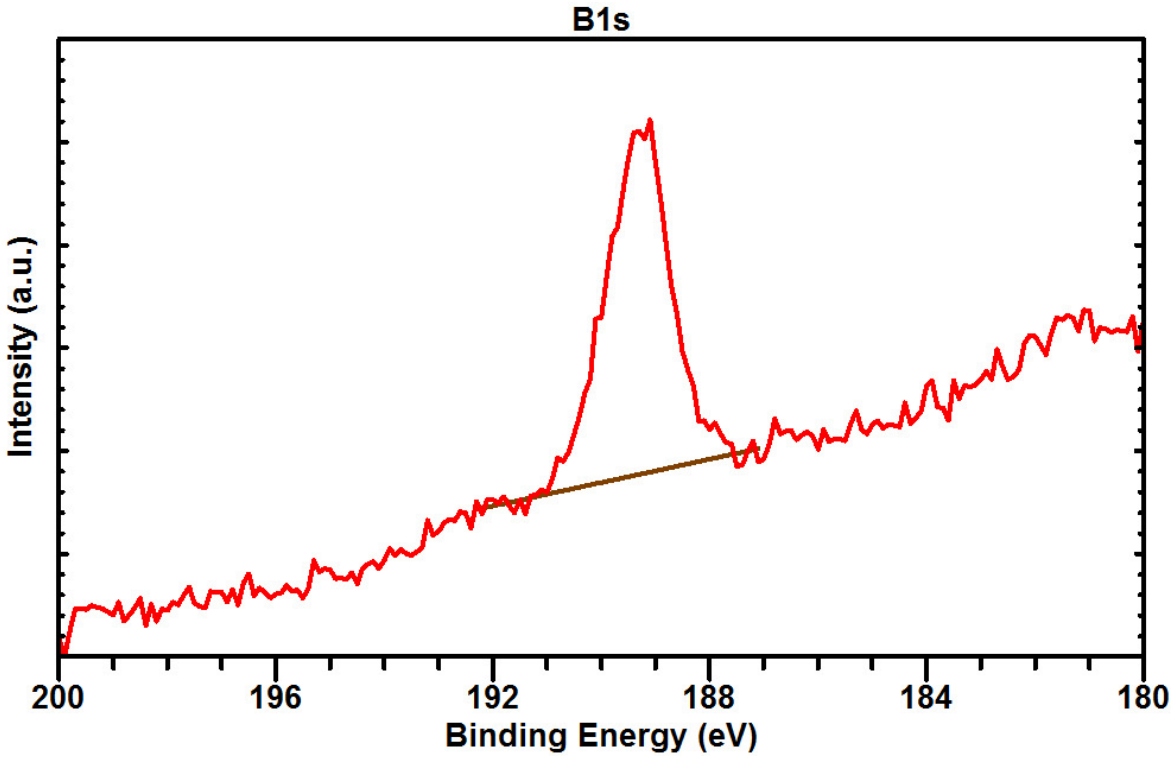
B1s
Intensity (a.u.)
200
196
192
188
184
180
Binding Energy (eV)

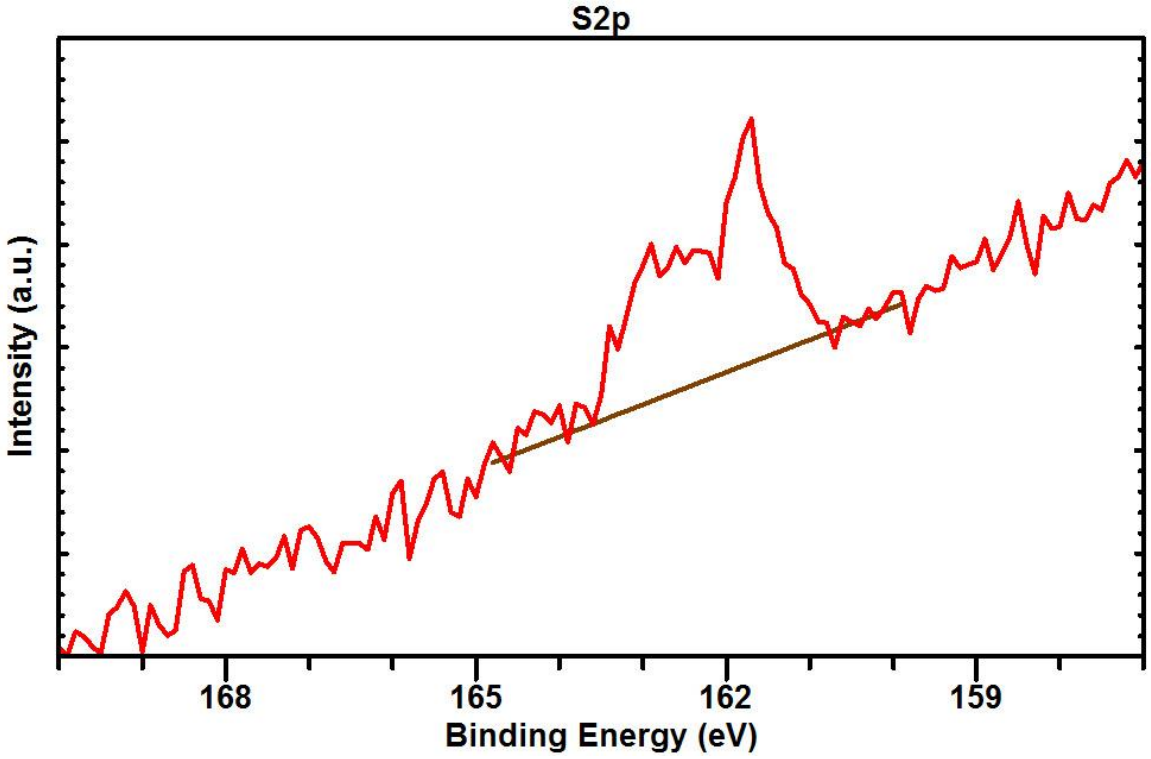
S2p
Intensity (a.u.)
168
165
162
159
Binding Energy (eV)

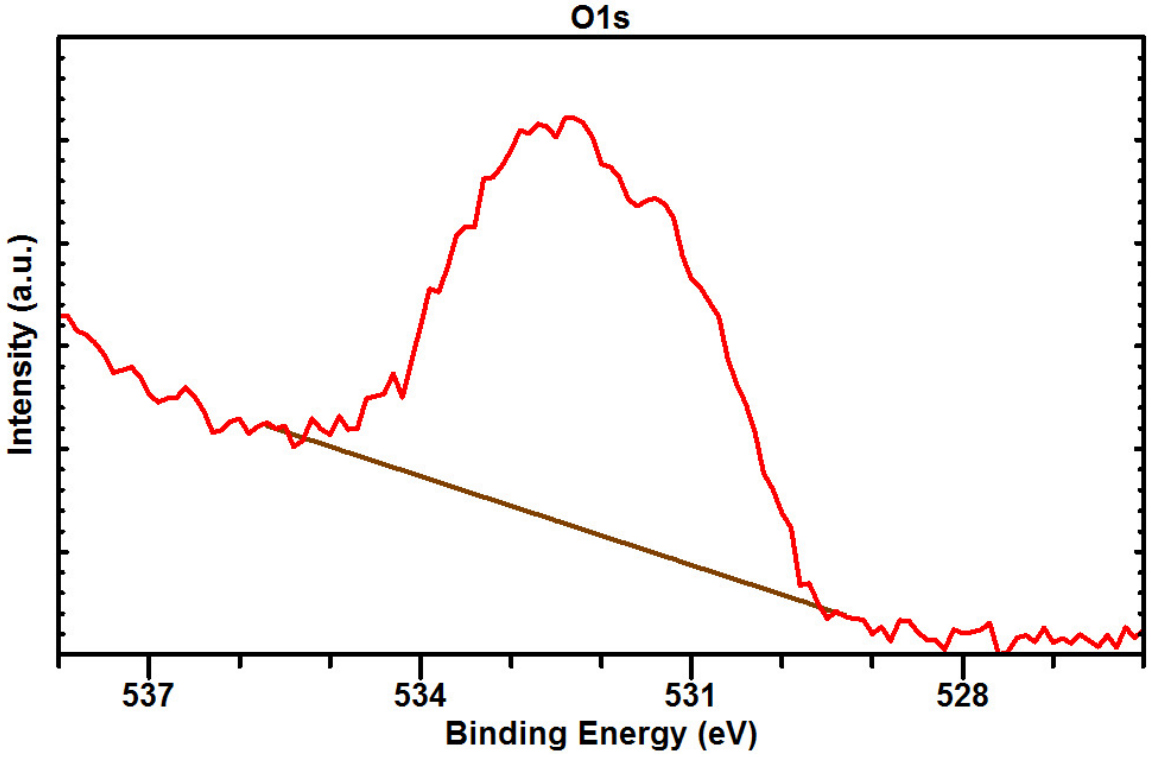
O1s
Intensity (a.u.)
537
534
531
528
Binding Energy (eV)

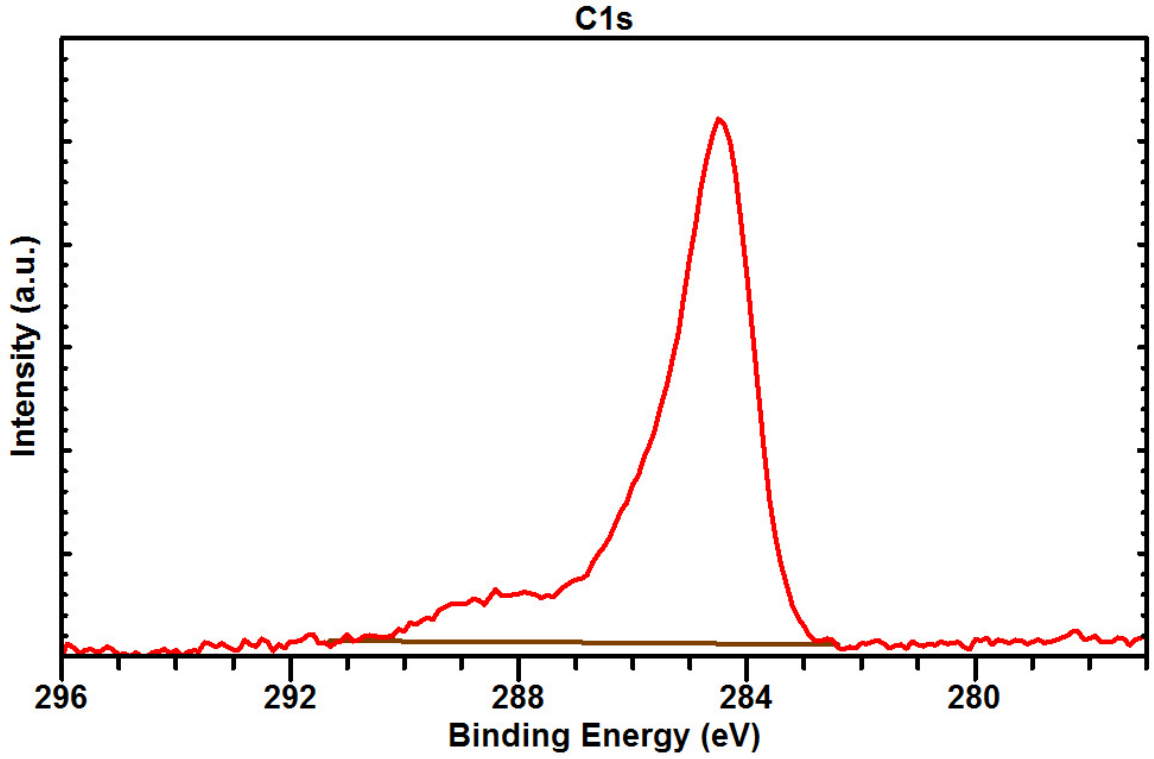
C1s
Intensity (a.u.)
296
292
288
284
280
Binding Energy (eV)

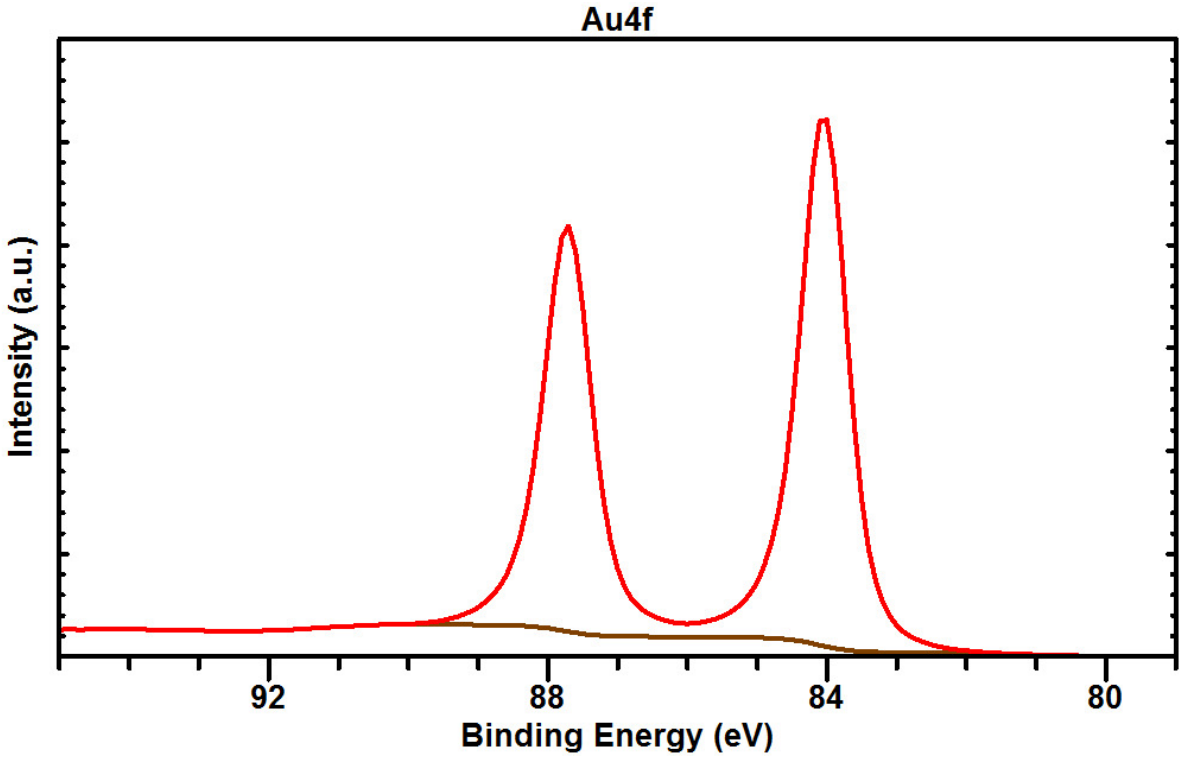
Au4f
Intensity (a.u.)
92
88
84
80
Binding Energy (eV)

Figure 2.S38. The survey and detailed XPS spectra together with the background used for subtraction, as measured for pristine SAMs of 9-SH-1,7-$C_2B_{10}H_{11}$ (**M9**).

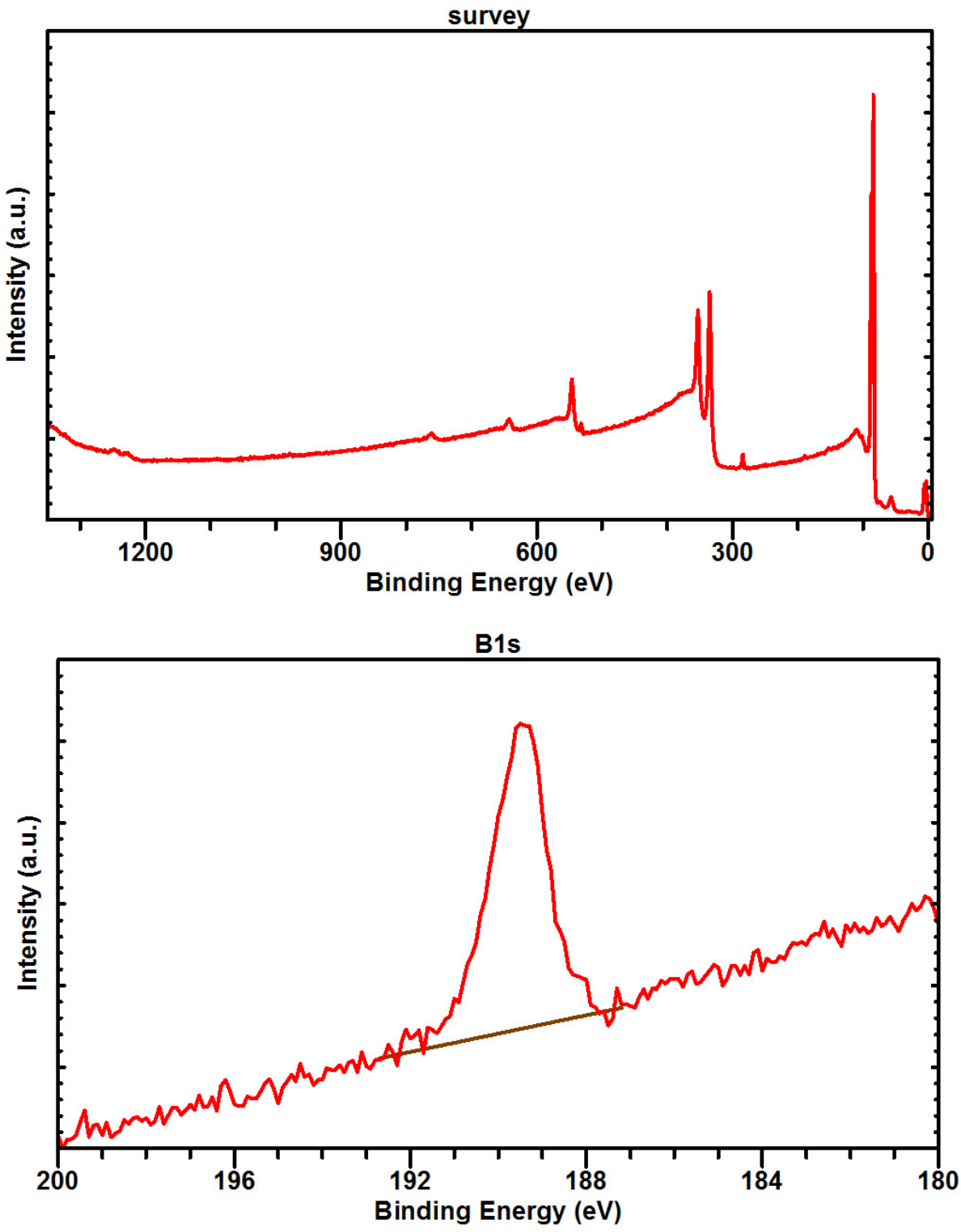

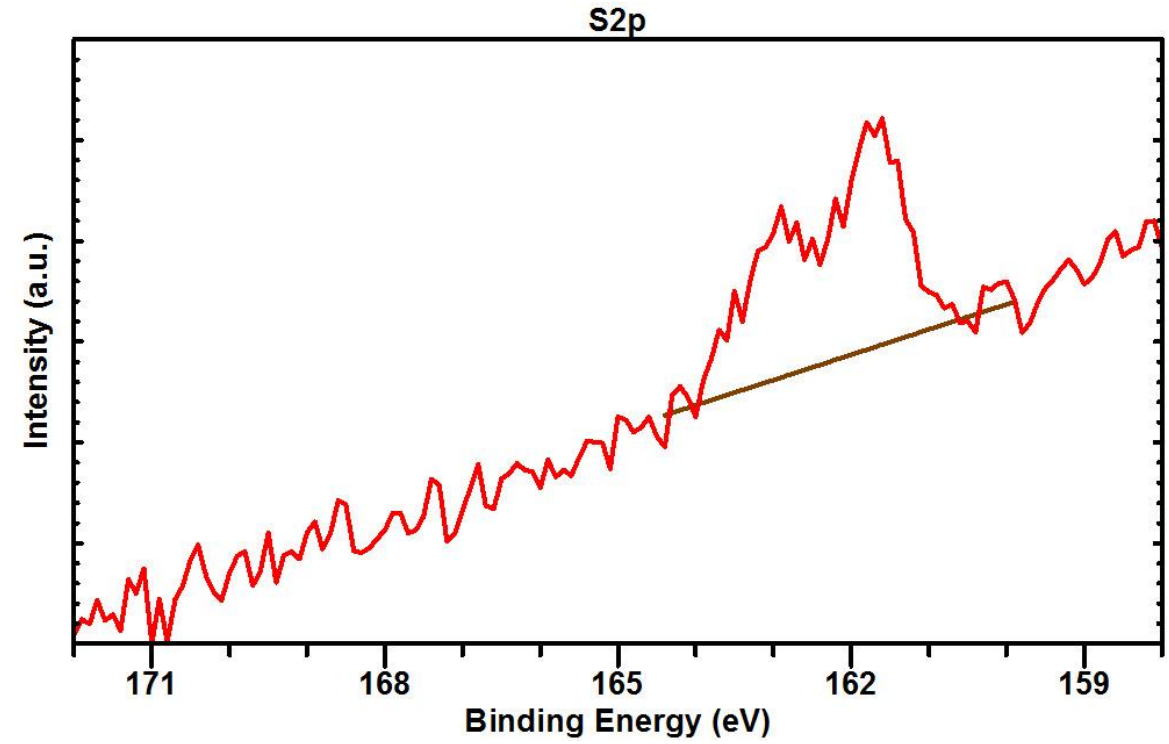
S2p
Intensity (a.u.)
171
168
165
162
159
Binding Energy (eV)

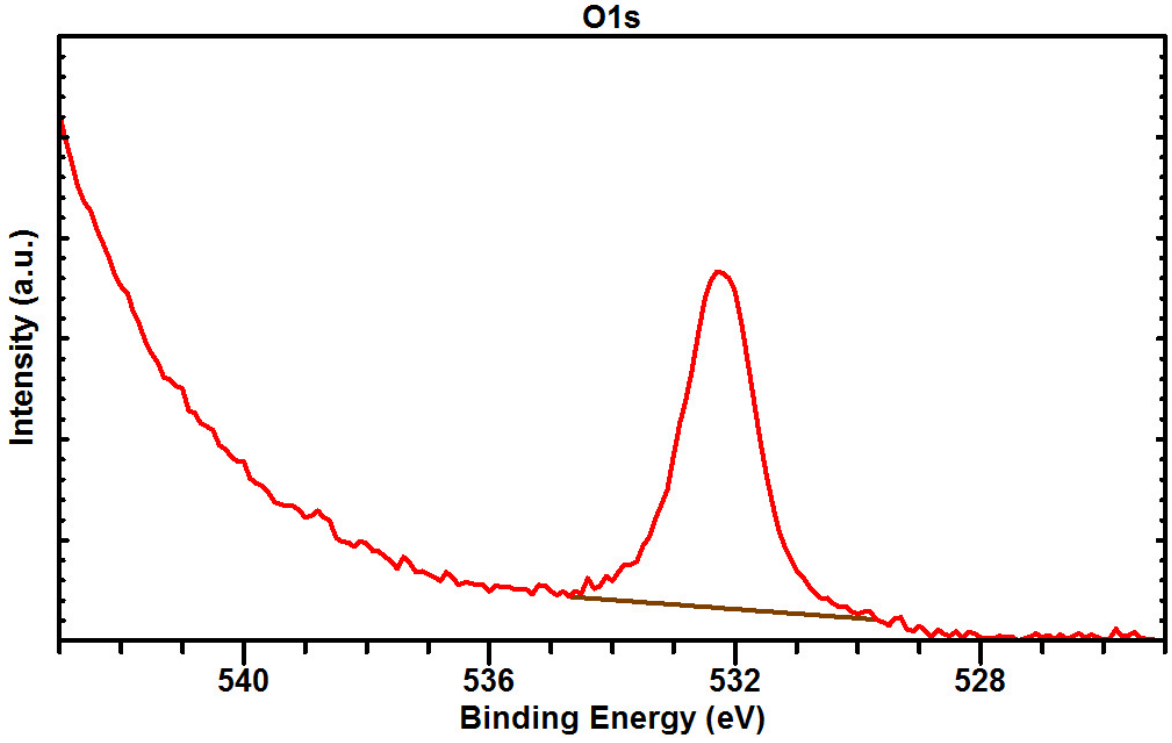
O1s
Intensity (a.u.)
540
536
532
528
Binding Energy (eV)

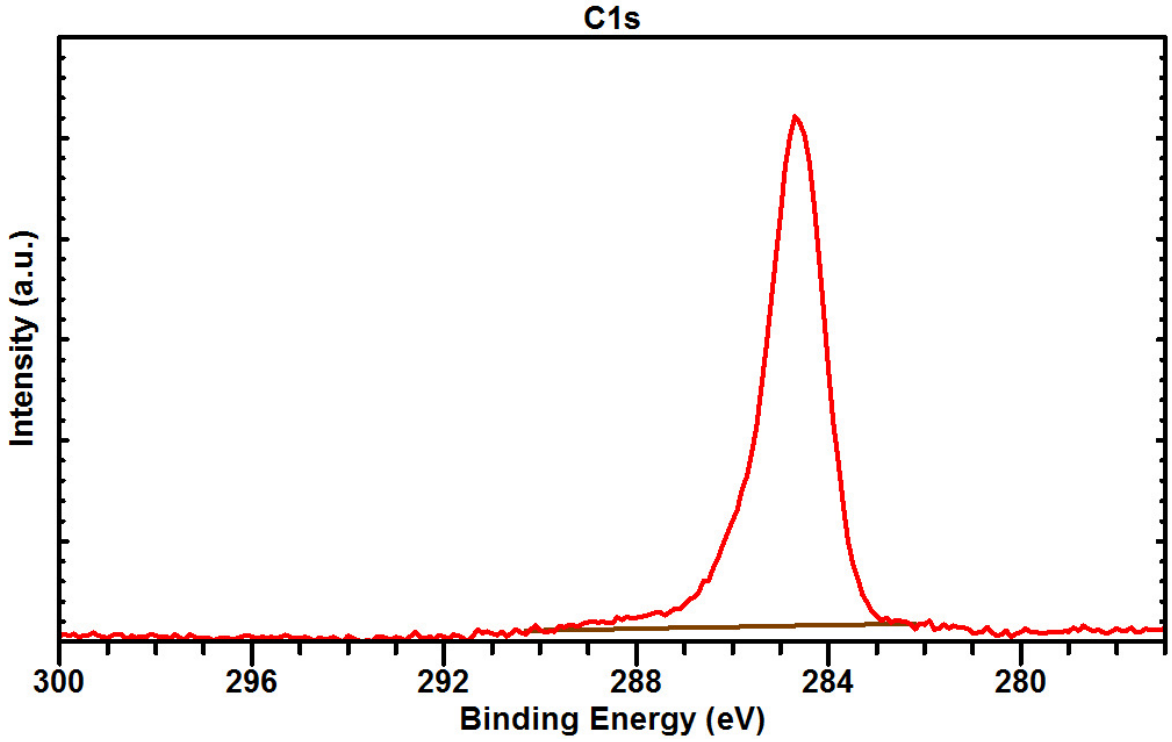
C1s
Intensity (a.u.)
300
296
292
288
284
280
Binding Energy (eV)

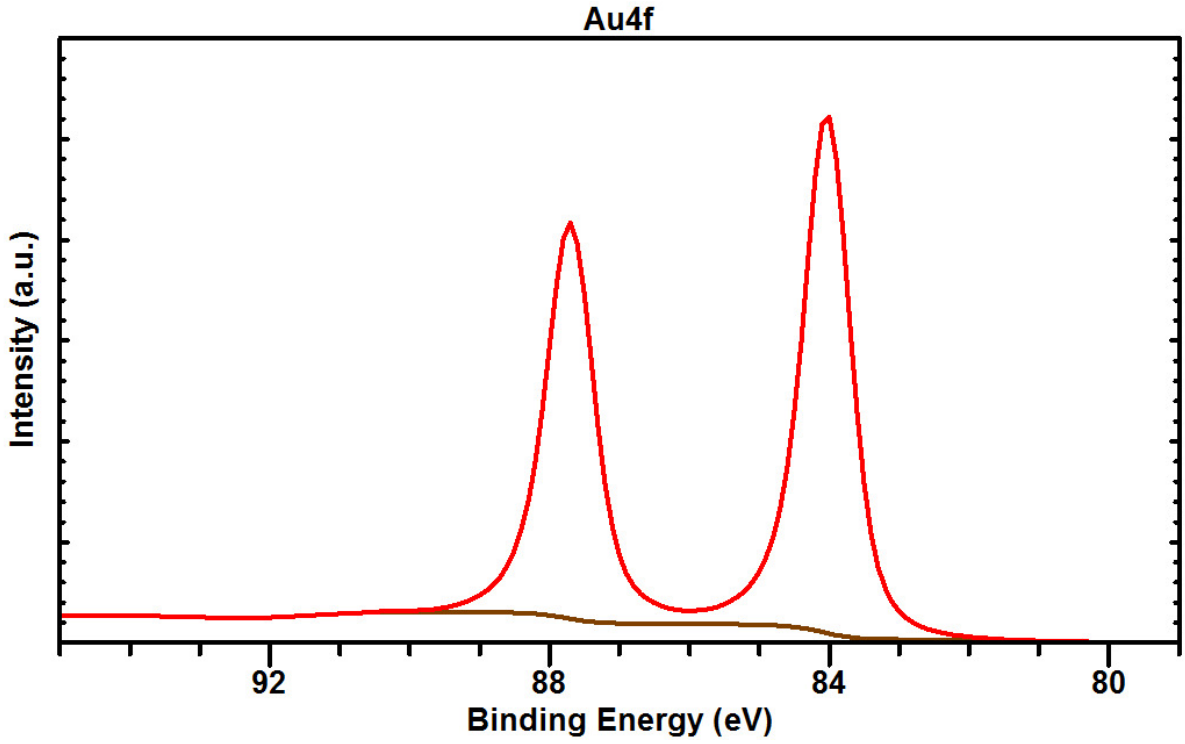
Au4f
Intensity (a.u.)
92
88
84
80
Binding Energy (eV)

Figure 2.S39. The survey and detail XPS spectra together with the background used for subtraction, as measured for SAMs of 9-SH-1,7-$C_2B_{10}H_{11}$ (**M9**) modified with H_3O^+.

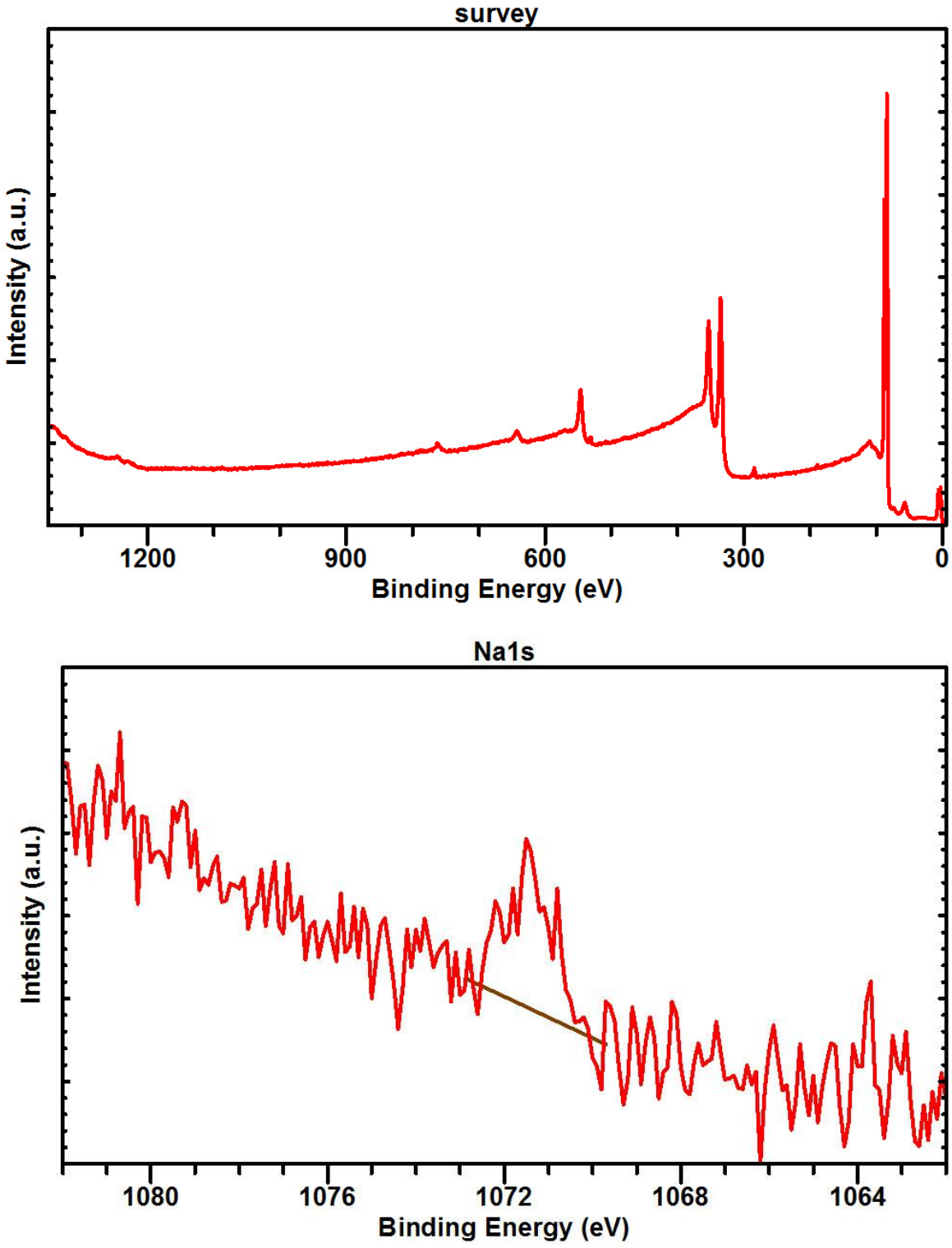

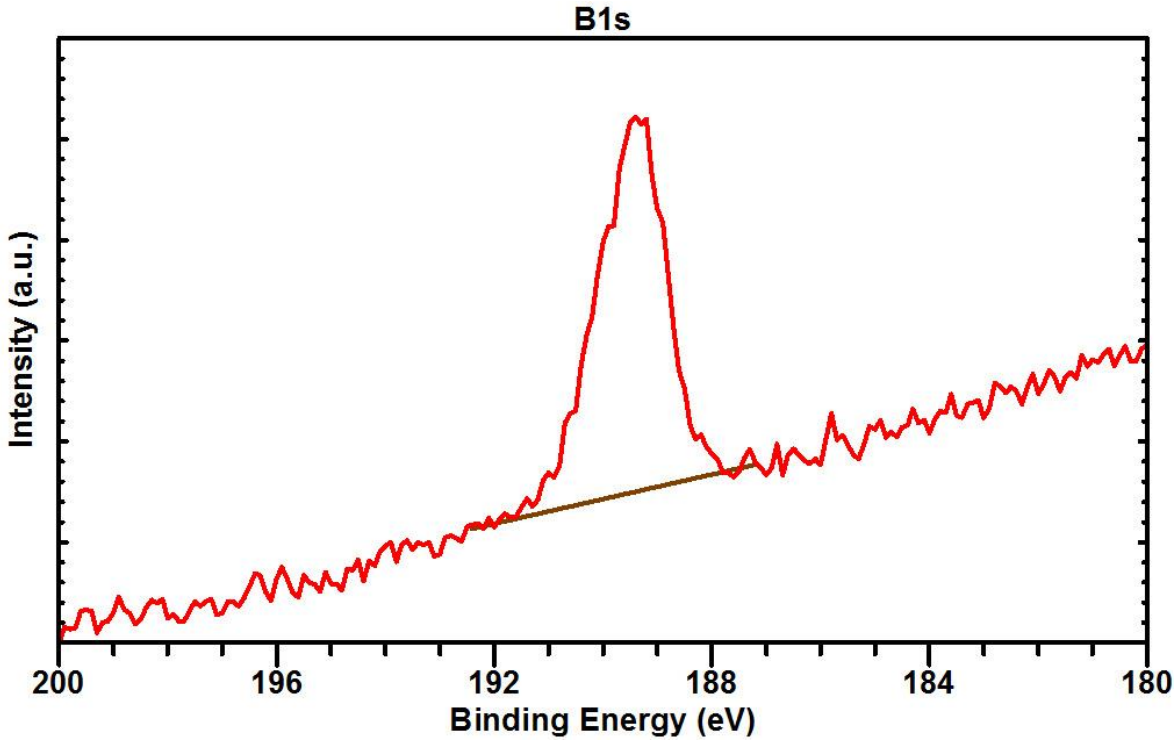
B1s
Intensity (a.u.)
200
196
192
188
184
180
Binding Energy (eV)

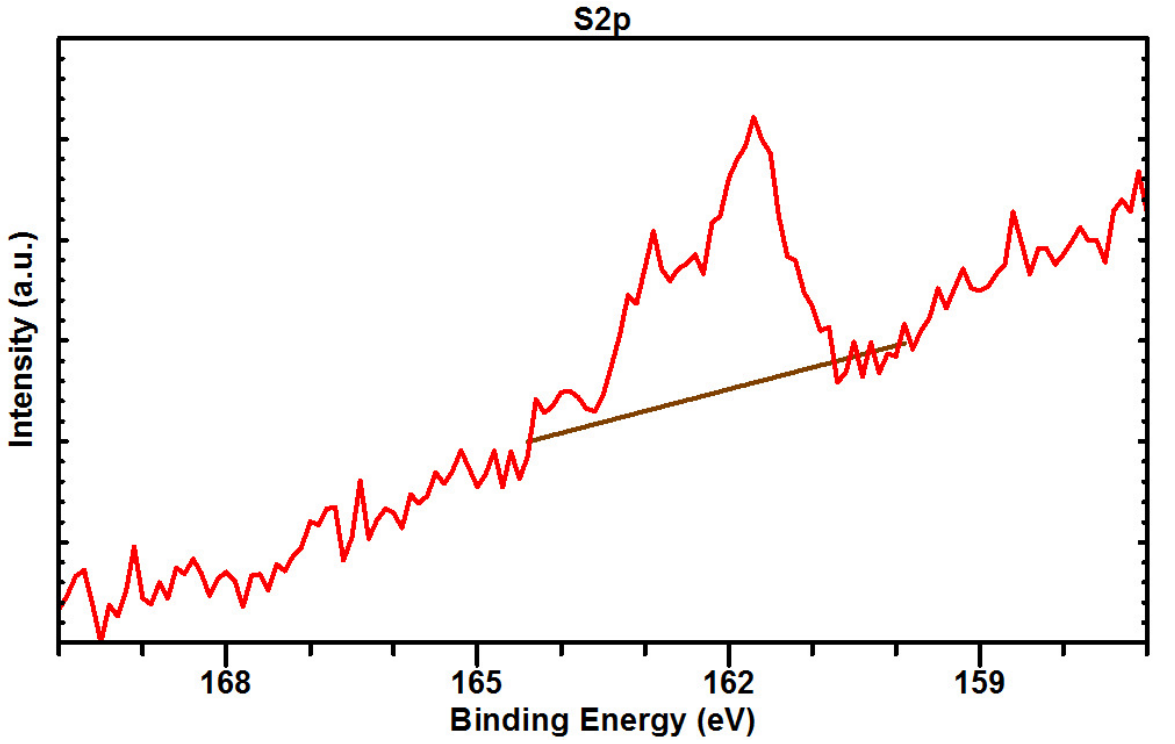
S2p
Intensity (a.u.)
168
165
162
159
Binding Energy (eV)

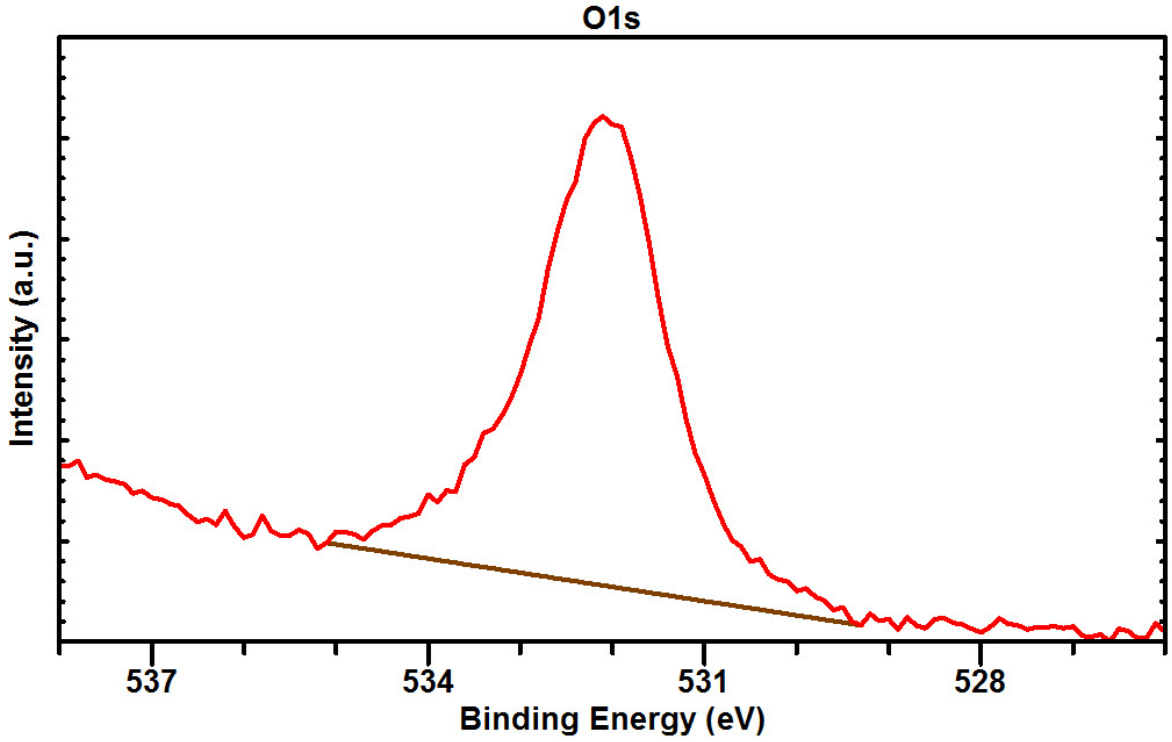
O1s
Intensity (a.u.)
537
534
531
528
Binding Energy (eV)

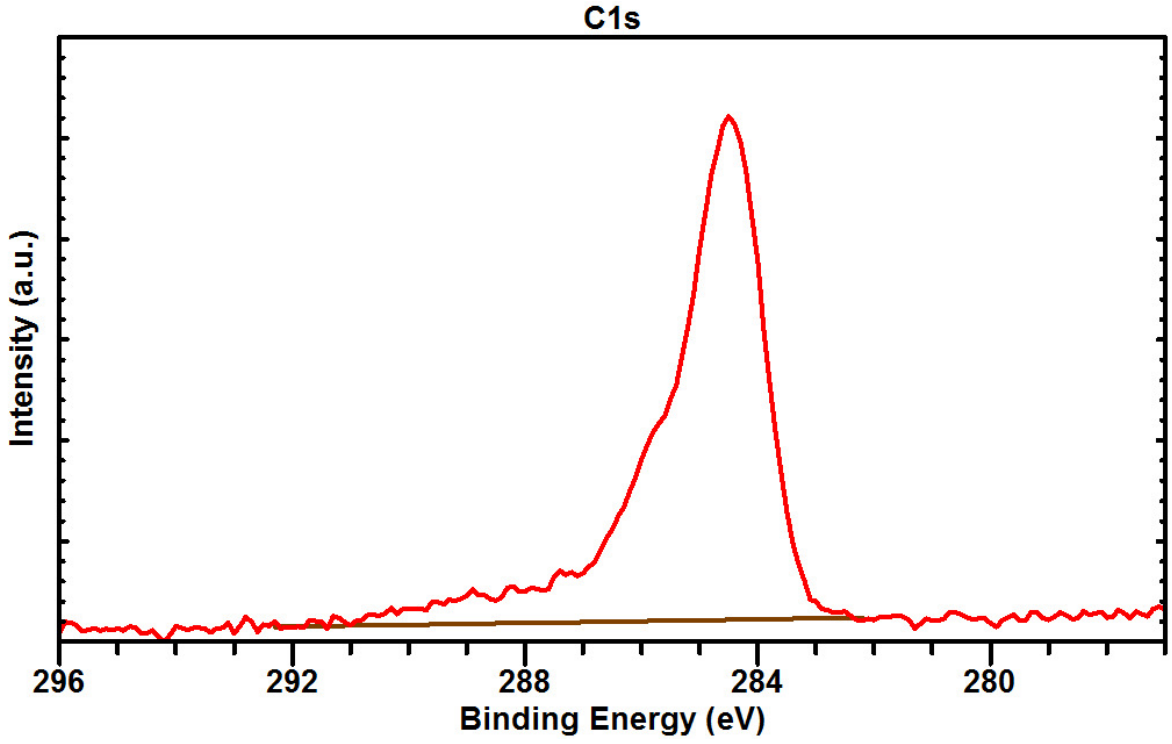
C1s
Intensity (a.u.)
296
292
288
284
280
Binding Energy (eV)

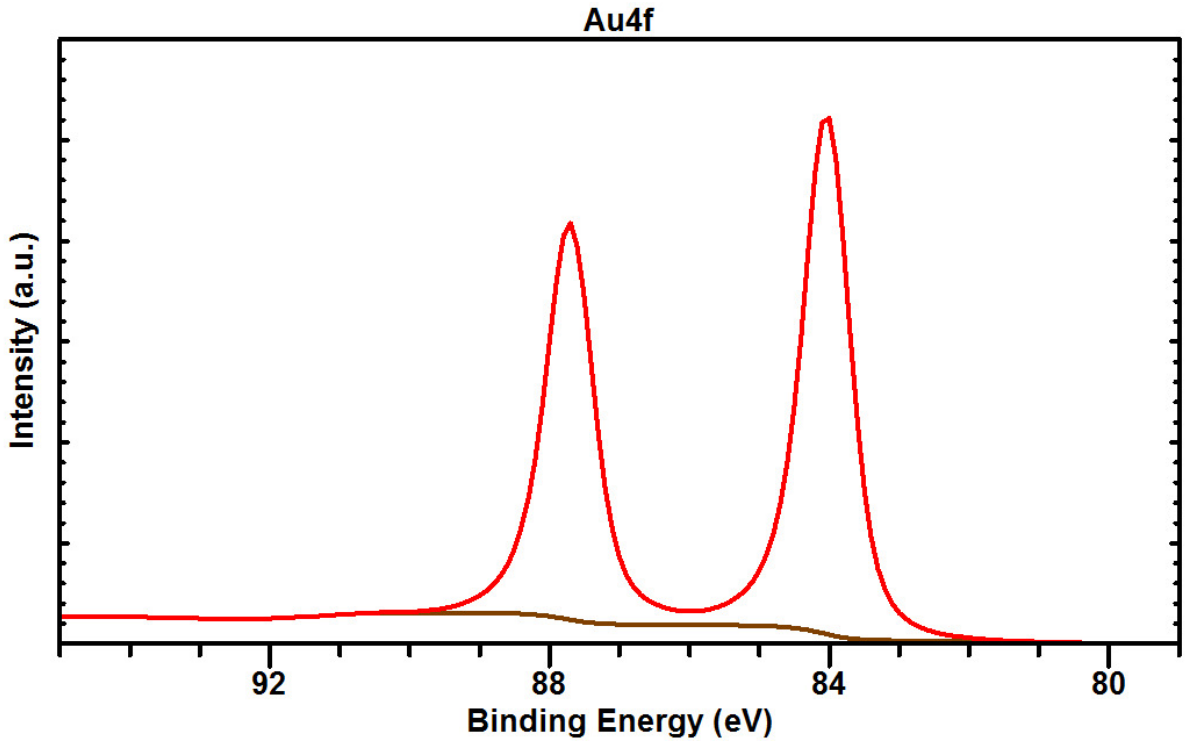
Au4f
Intensity (a.u.)
92
88
84
80
Binding Energy (eV)

Figure 2.S40. The survey and detailed XPS spectra together with the subtracted background, as measured for pristine SAMs of 1-COOH-12-SH-1,12-$C_2B_{10}H_{10}$ (**P1-COOH**).

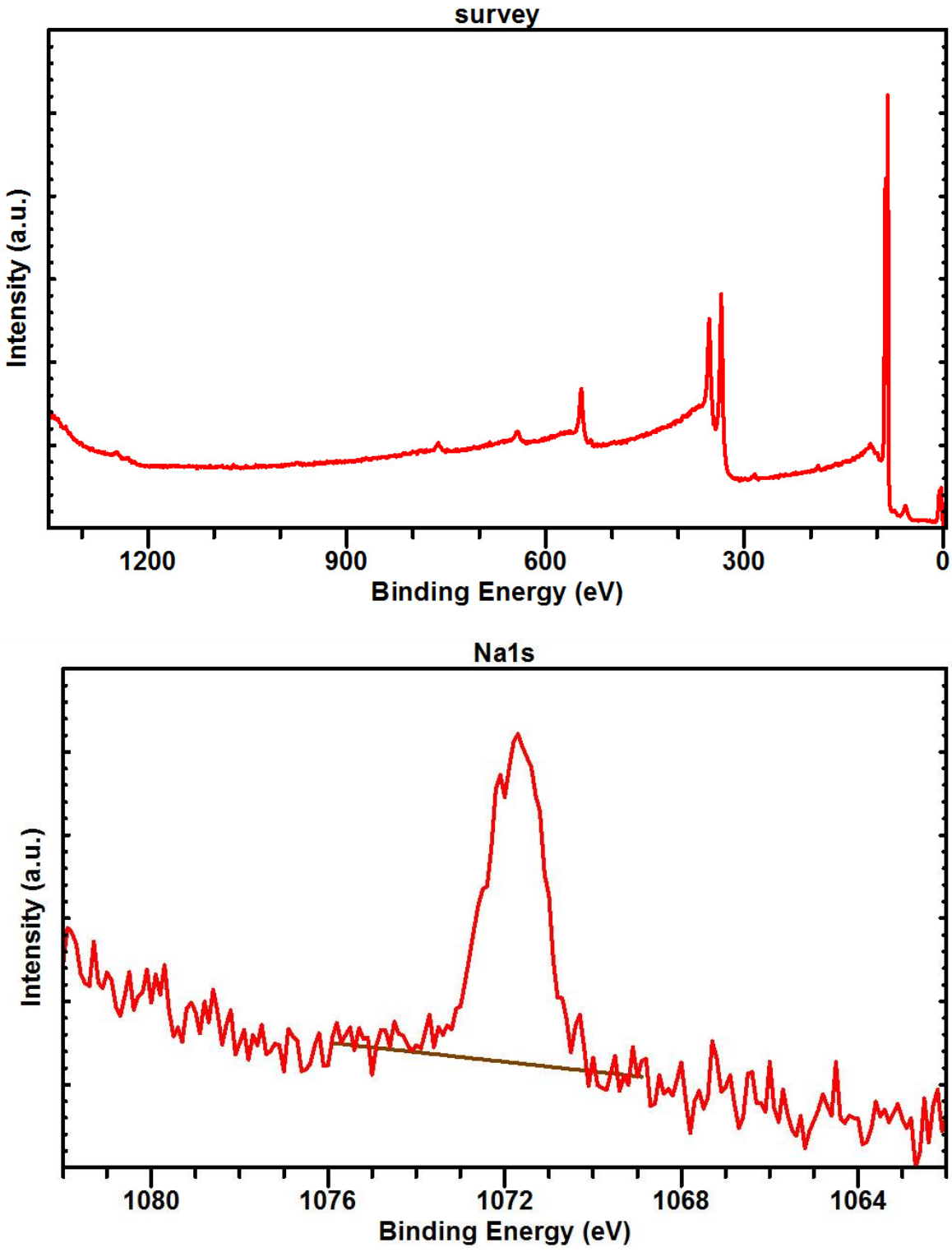

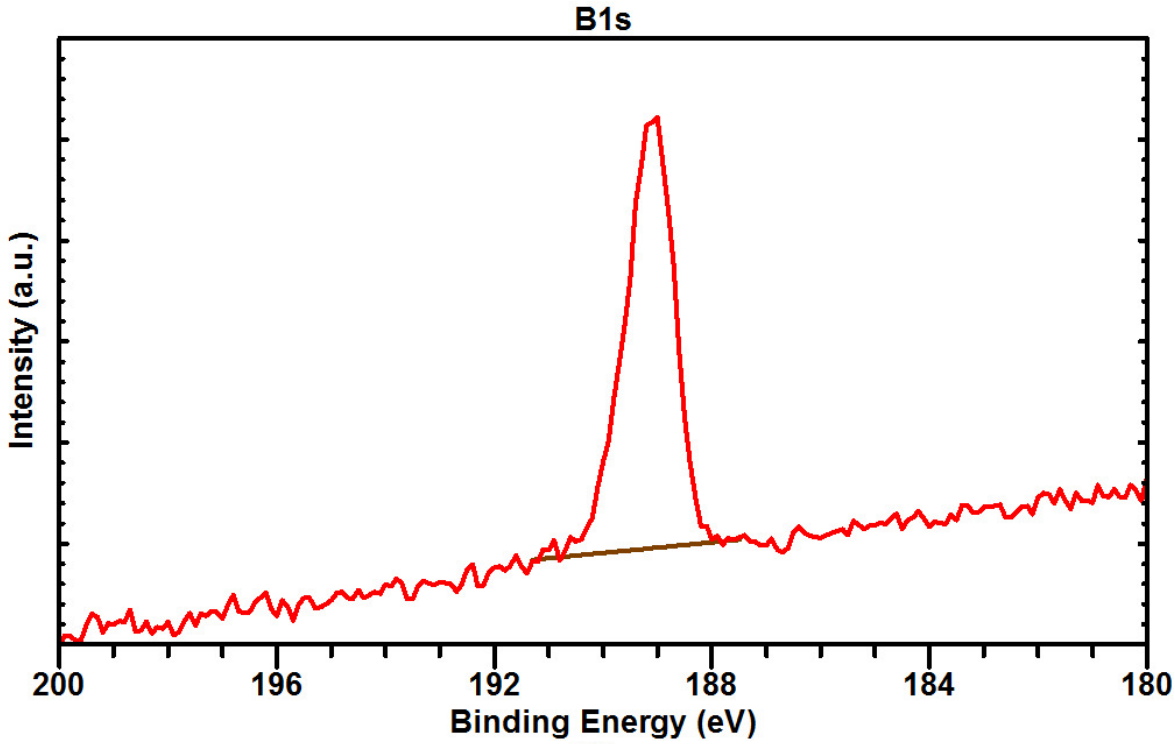
B1s
Intensity (a.u.)
200
196
192
188
184
180
Binding Energy (eV)

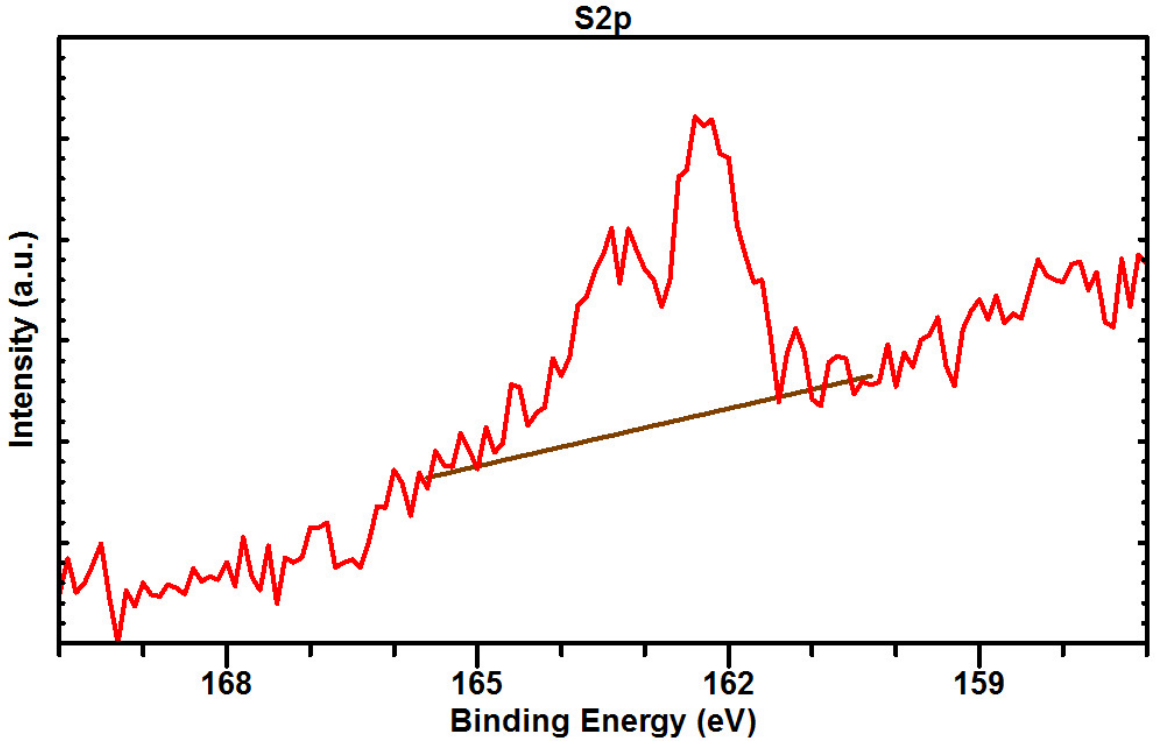
S2p
Intensity (a.u.)
168
165
162
159
Binding Energy (eV)

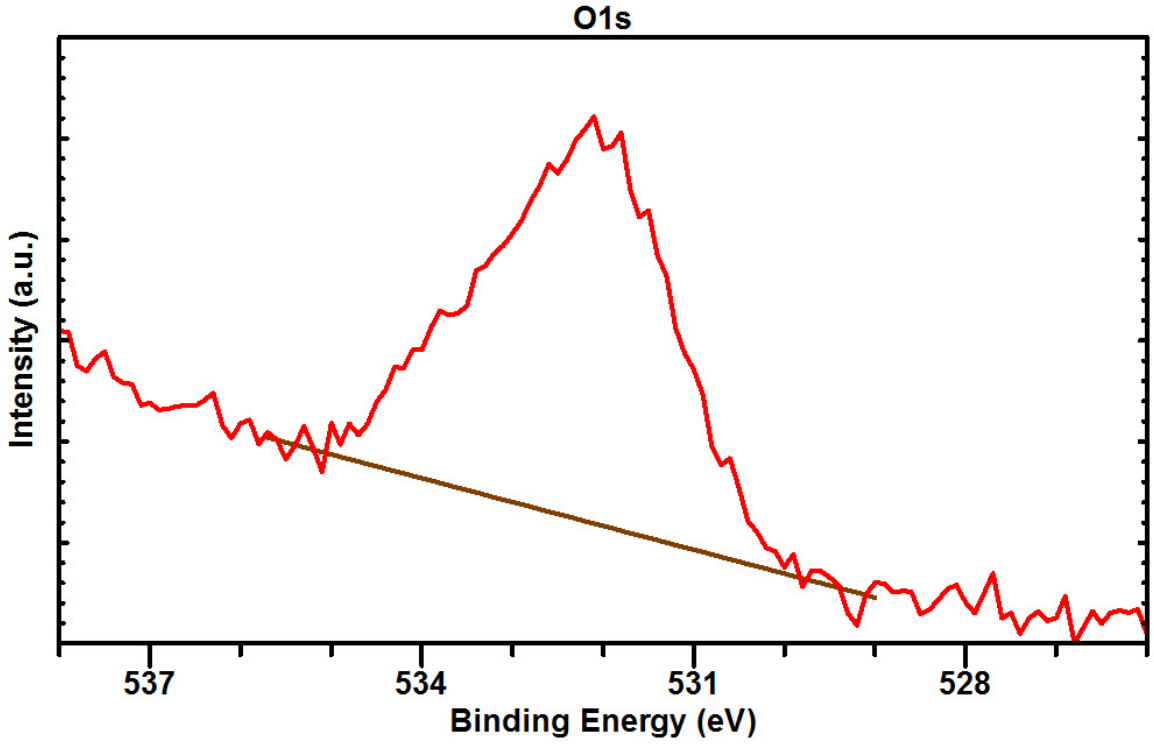
O1s
Intensity (a.u.)
537
534
531
528
Binding Energy (eV)

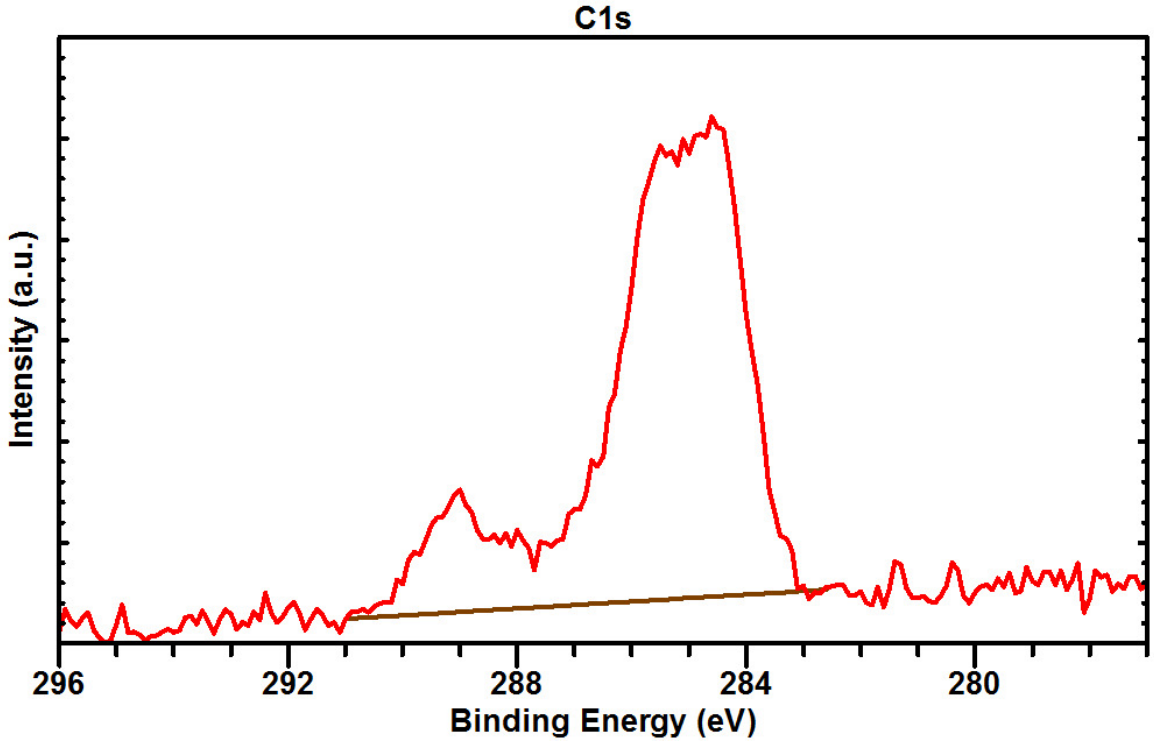
C1s
Intensity (a.u.)
296
292
288
284
280
Binding Energy (eV)

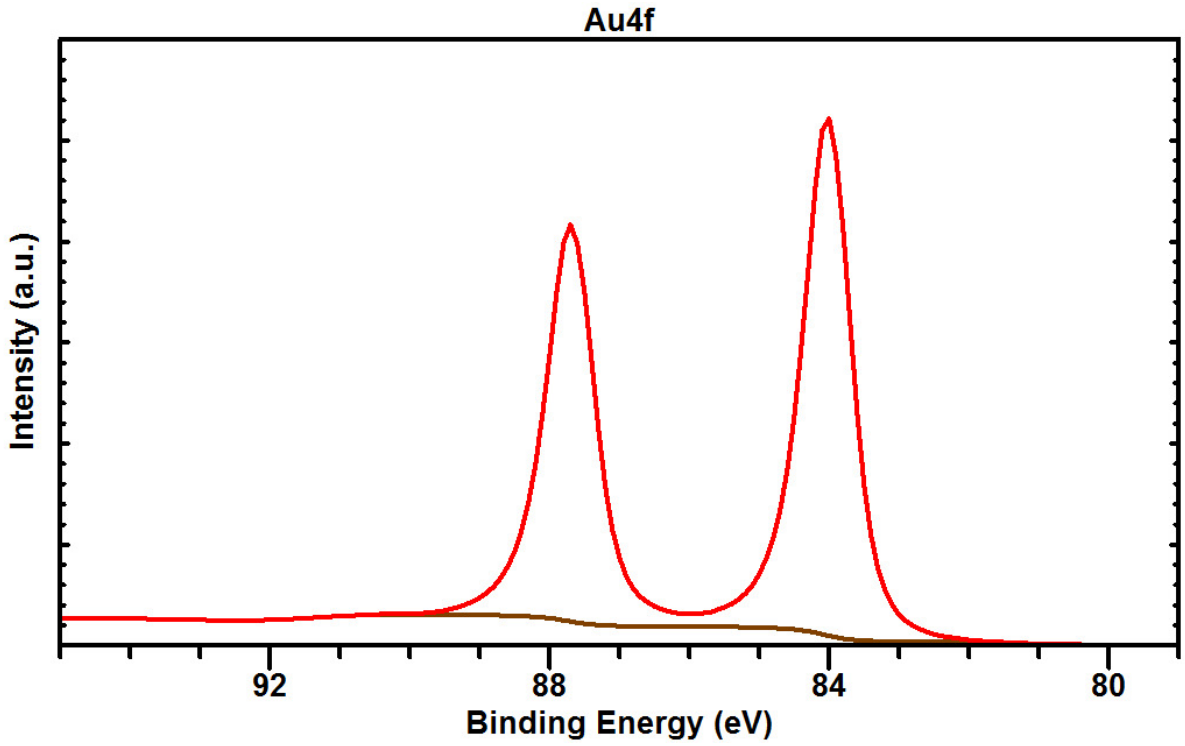
Au4f
Intensity (a.u.)
92
88
84
80
Binding Energy (eV)

Figure 2.S41. The survey and detailed XPS spectra together with the background used for subtraction, as measured for SAMs of 1-COOH-12-SH-1,12-$C_2B_{10}H_{10}$ (**P1-COOH**) modified with H_3O^+.

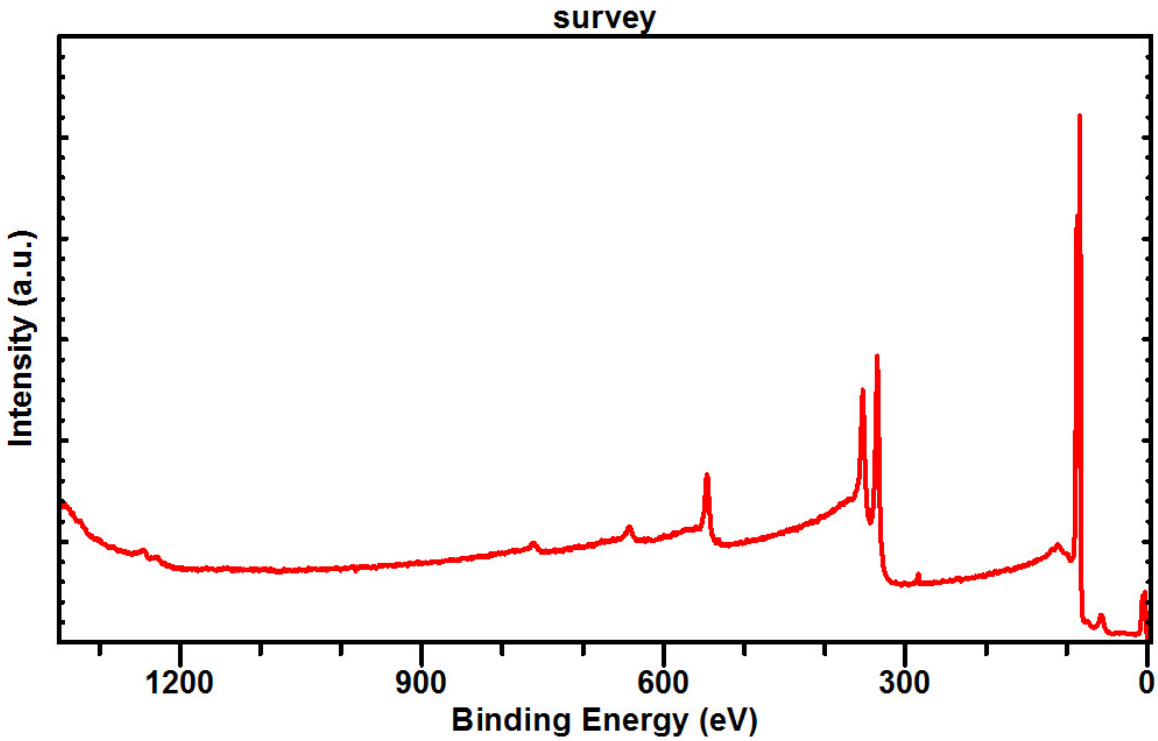

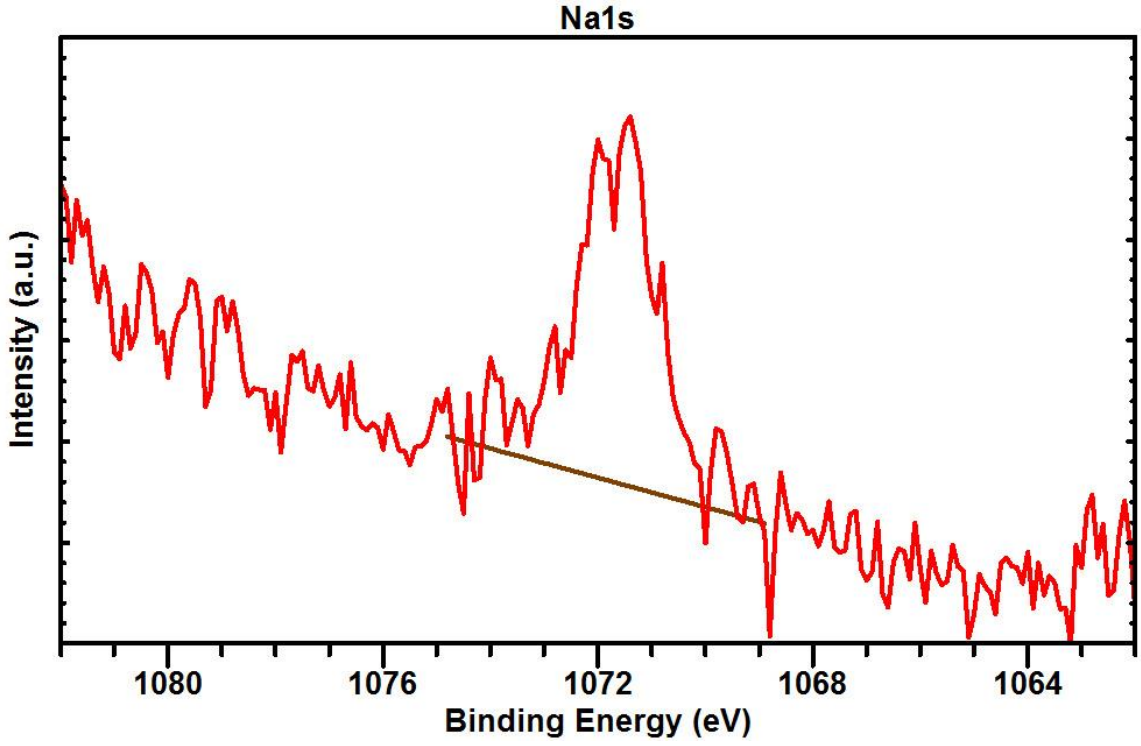
Na1s
Intensity (a.u.)
1080
1076
1072
1068
1064
Binding Energy (eV)

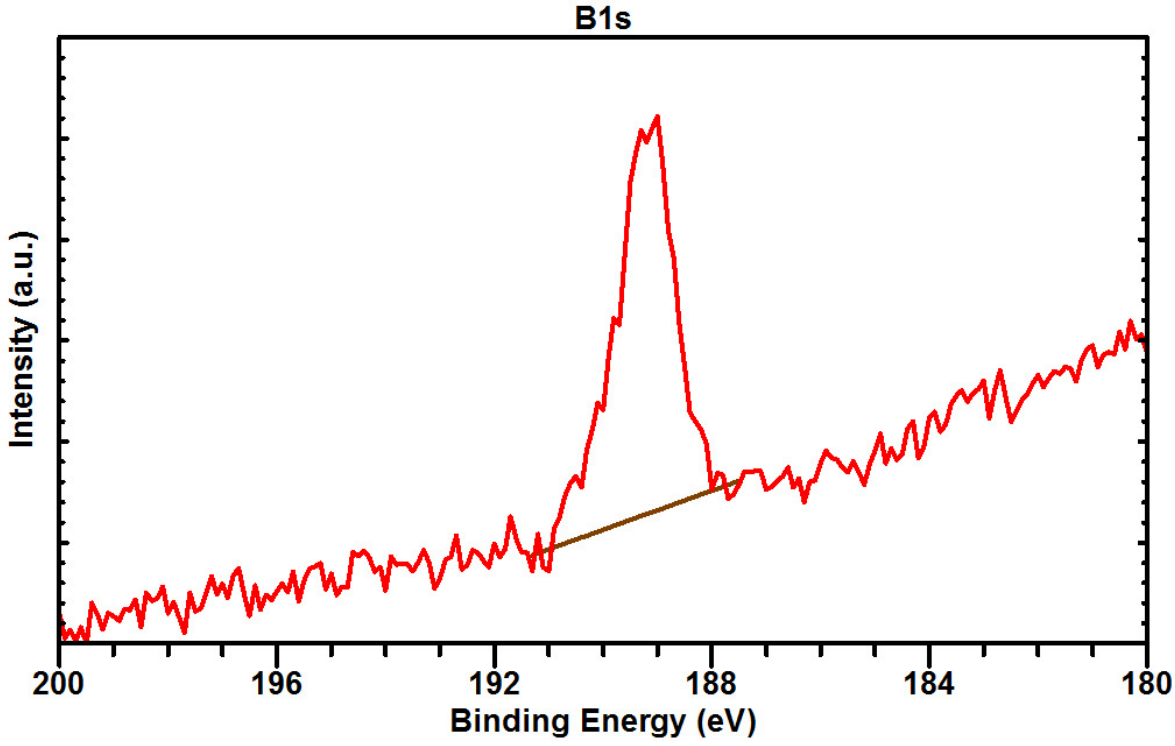
B1s
Intensity (a.u.)
200
196
192
188
184
180
Binding Energy (eV)

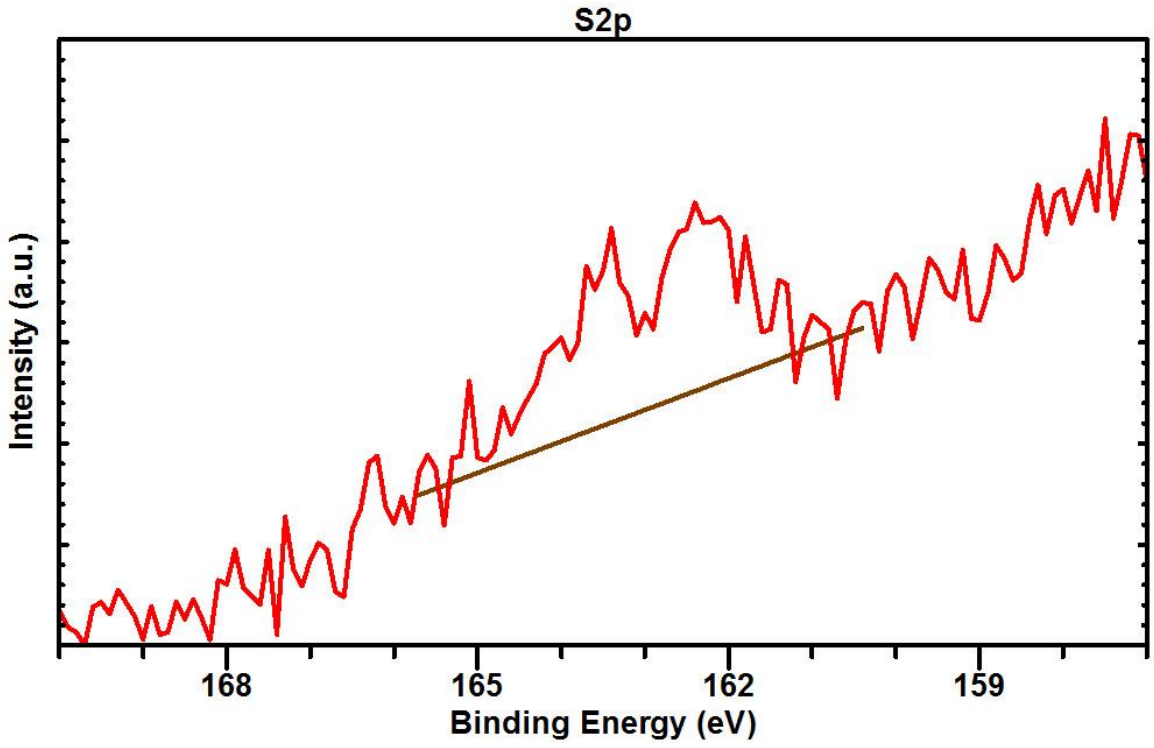
S2p
Intensity (a.u.)
168
165
162
159
Binding Energy (eV)

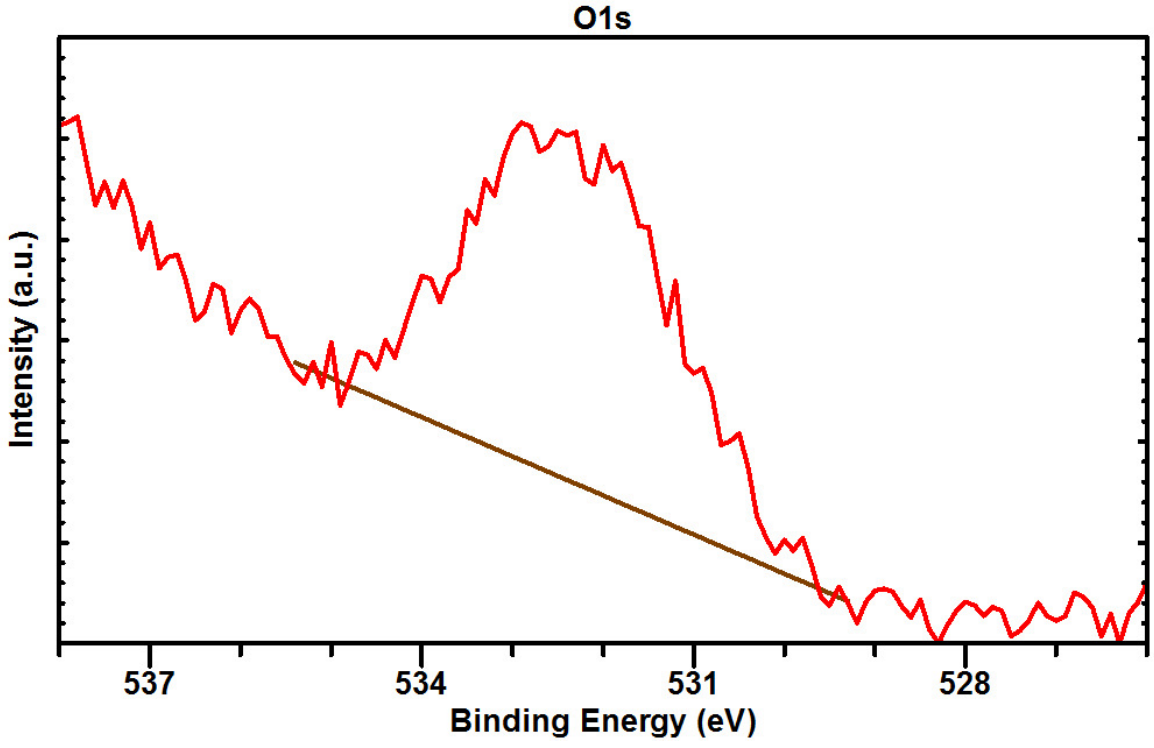
O1s
Intensity (a.u.)
537
534
531
528
Binding Energy (eV)

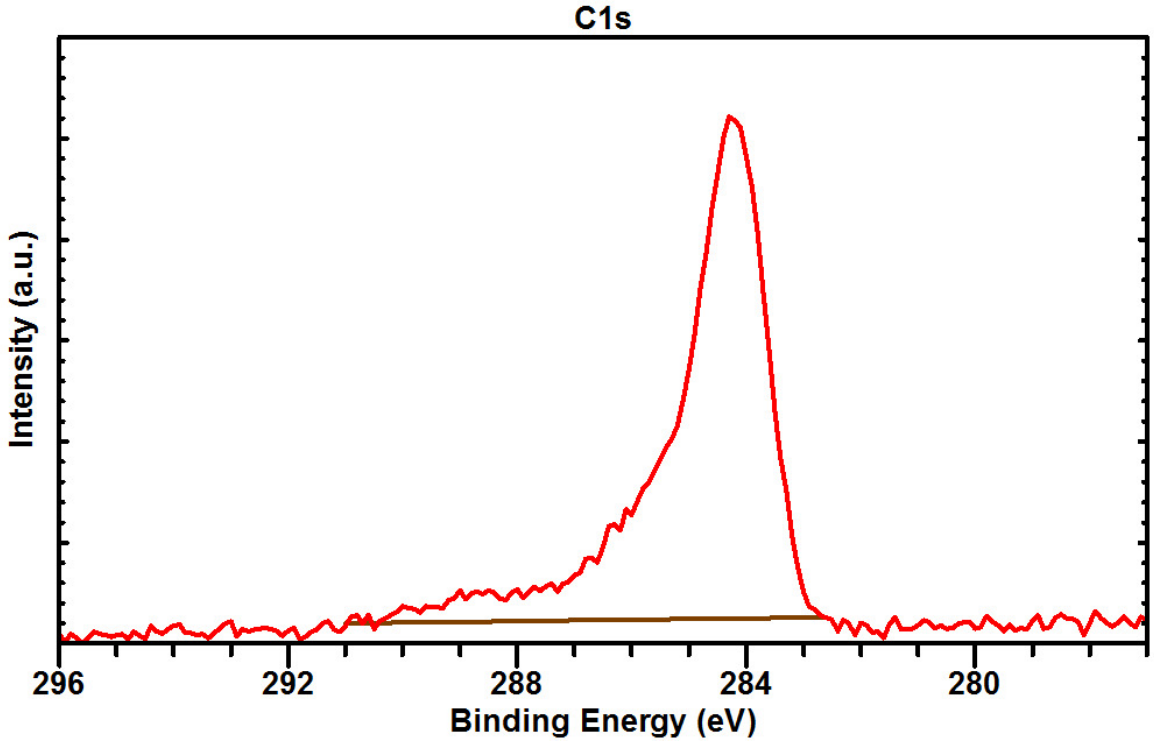
C1s
Intensity (a.u.)
296
292
288
284
280
Binding Energy (eV)

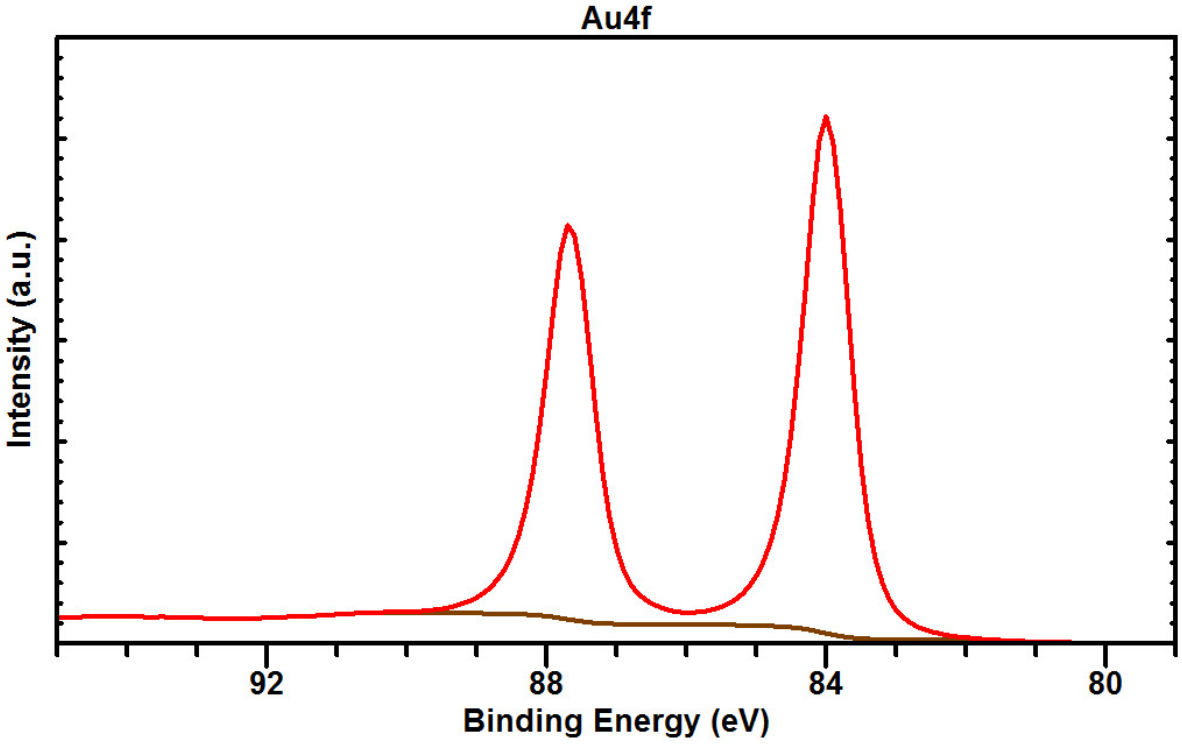
Au4f
Intensity (a.u.)
92
88
84
80
Binding Energy (eV)

Figure 2.S42. The survey and detailed XPS spectra together with the background used for subtraction, as measured for Na_2SO_4.

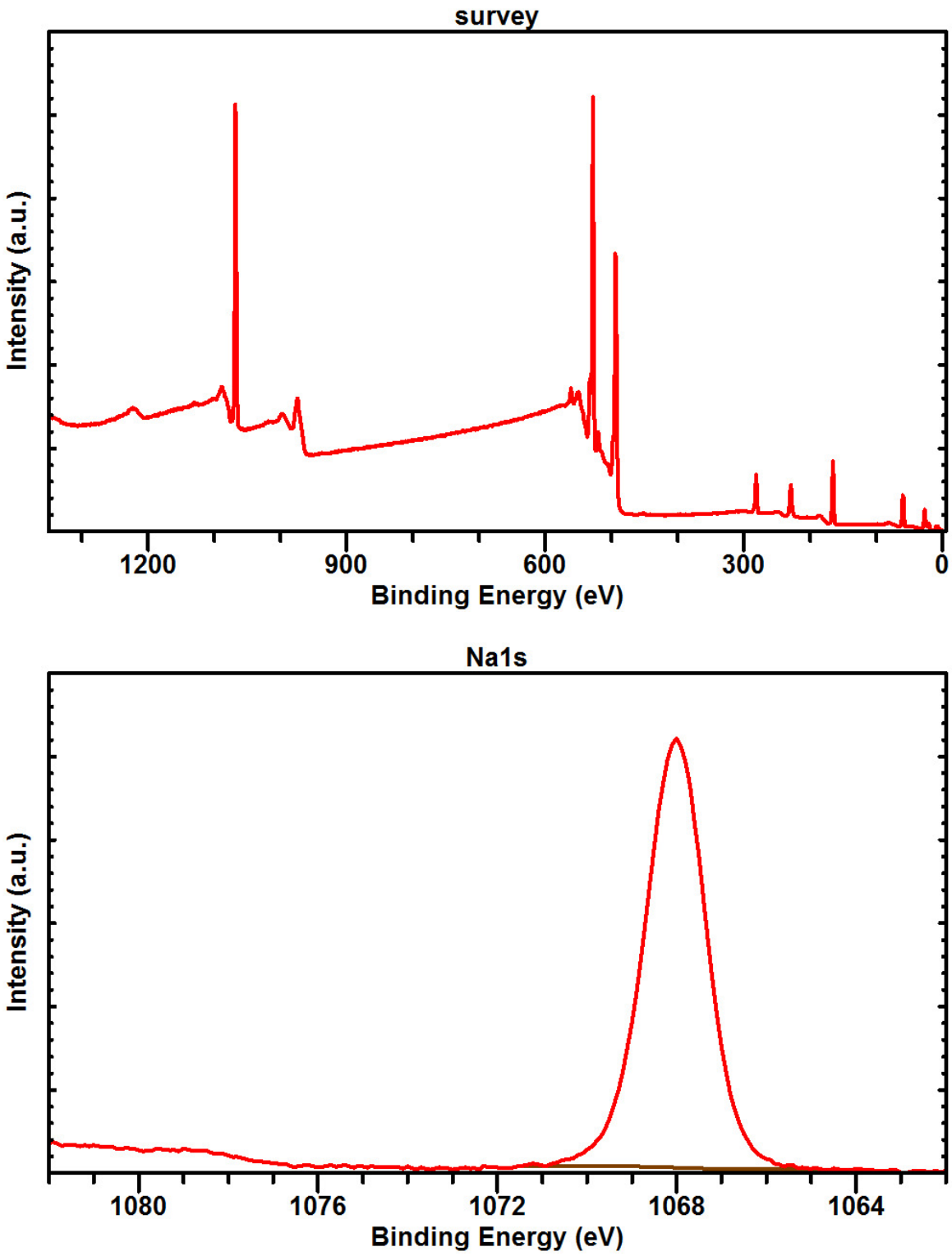

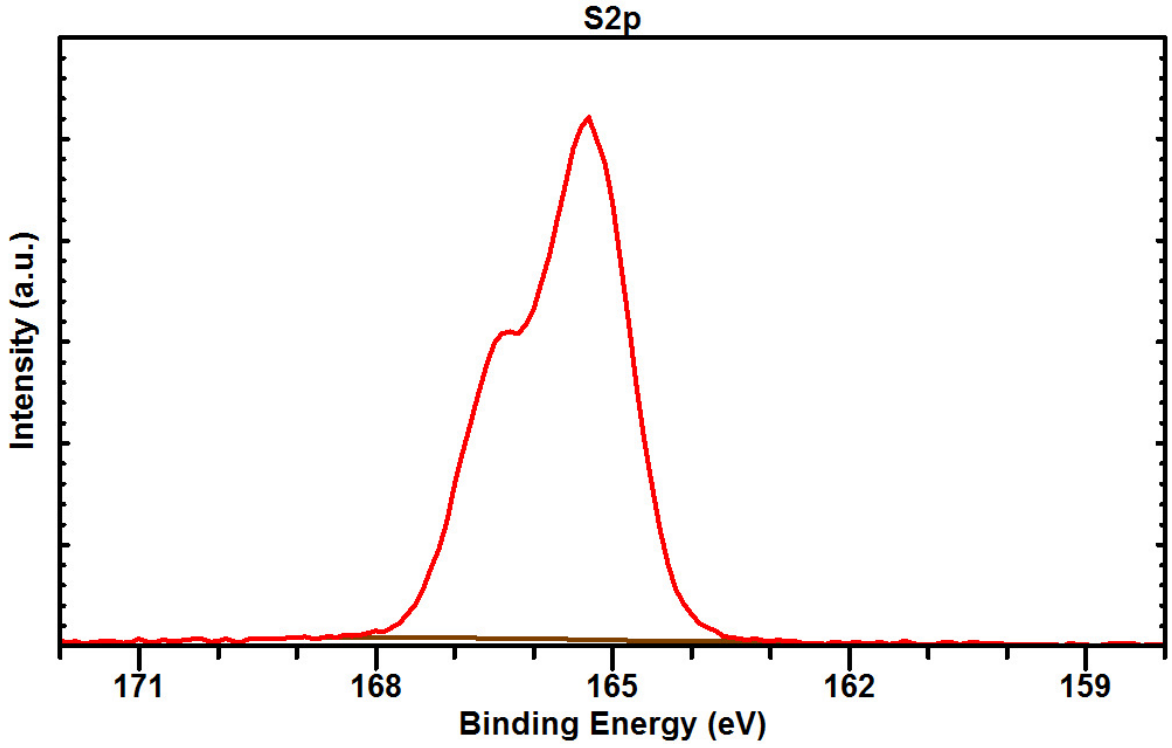
S2p
Intensity (a.u.)
171
168
165
162
159
Binding Energy (eV)

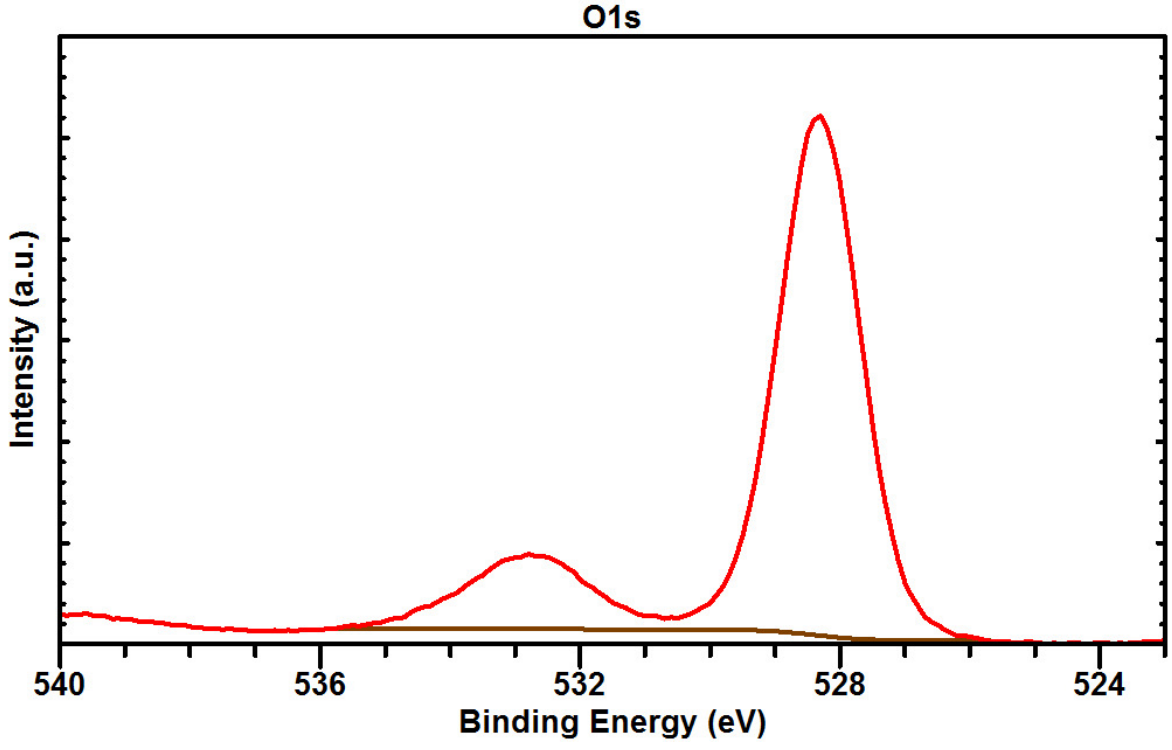
O1s
Intensity (a.u.)
540
536
532
528
524
Binding Energy (eV)

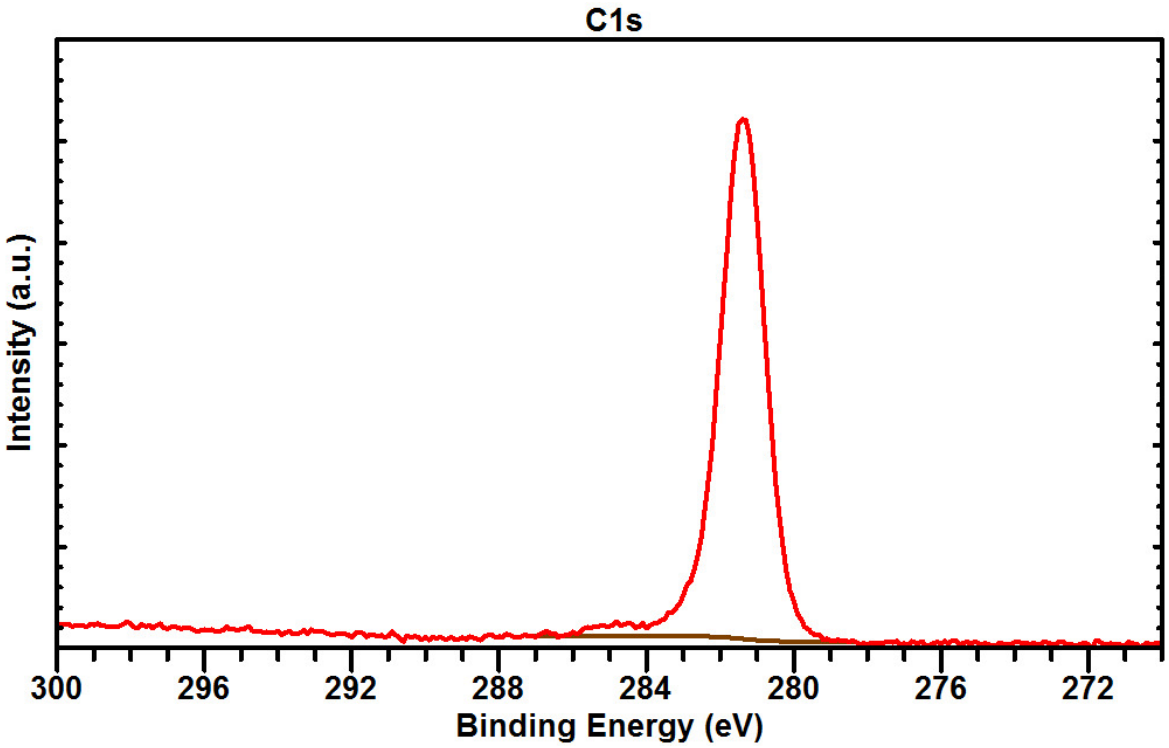
C1s
Intensity (a.u.)
300
296
292
288
284
280
276
272
Binding Energy (eV)

Figure 2.S43. The survey and detailed XPS spectra together with the background used for subtraction, as measured for $MgSO_4$.

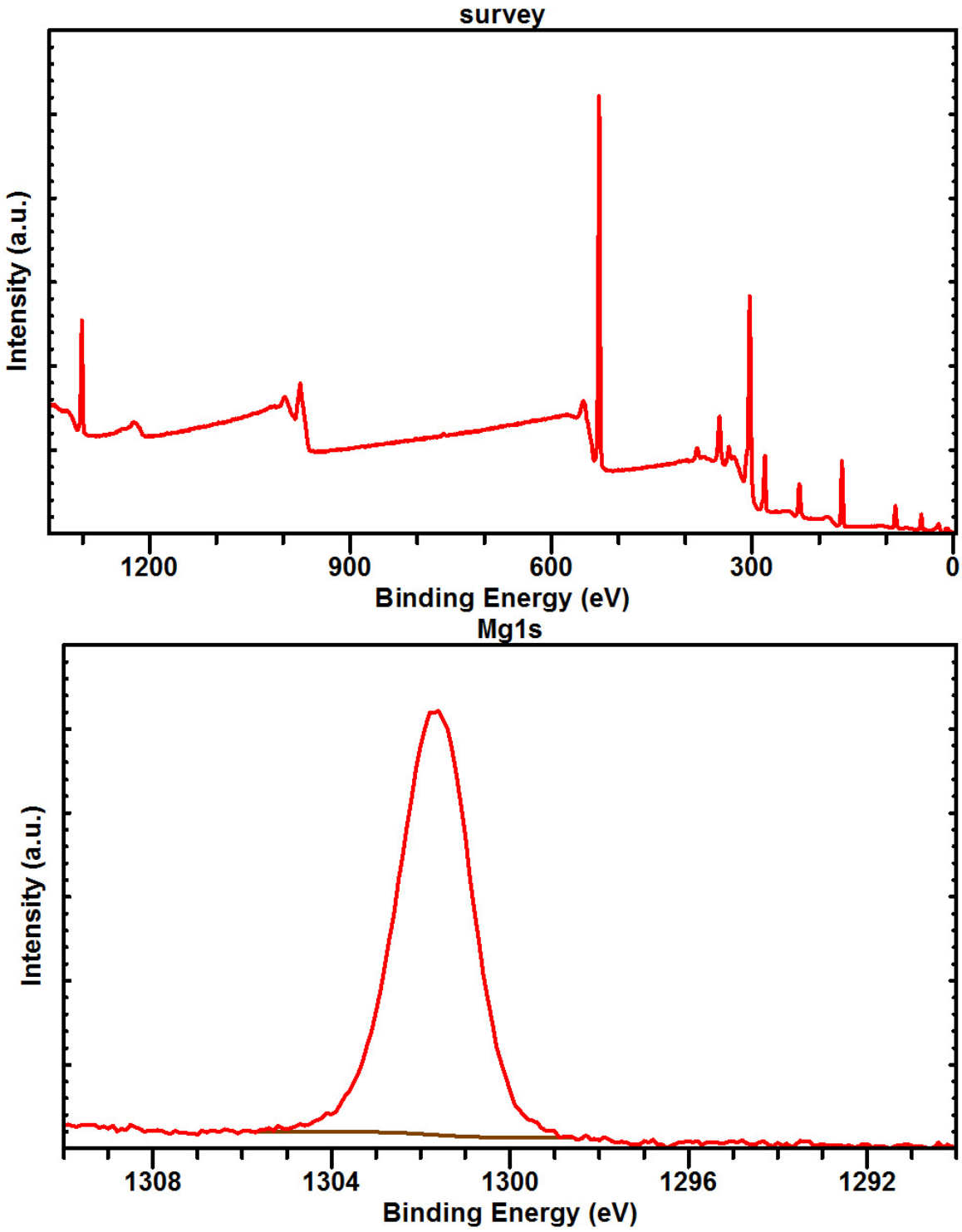

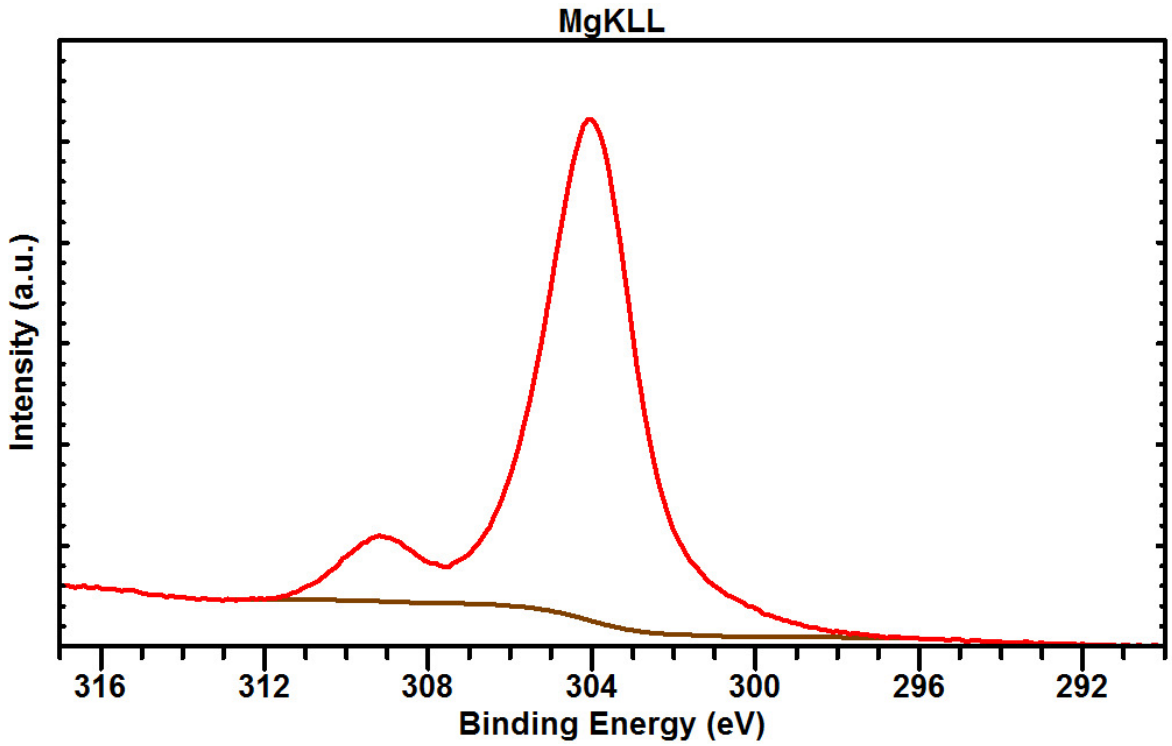
MgKLL
Intensity (a.u.)
316
312
308
304
300
296
292
Binding Energy (eV)

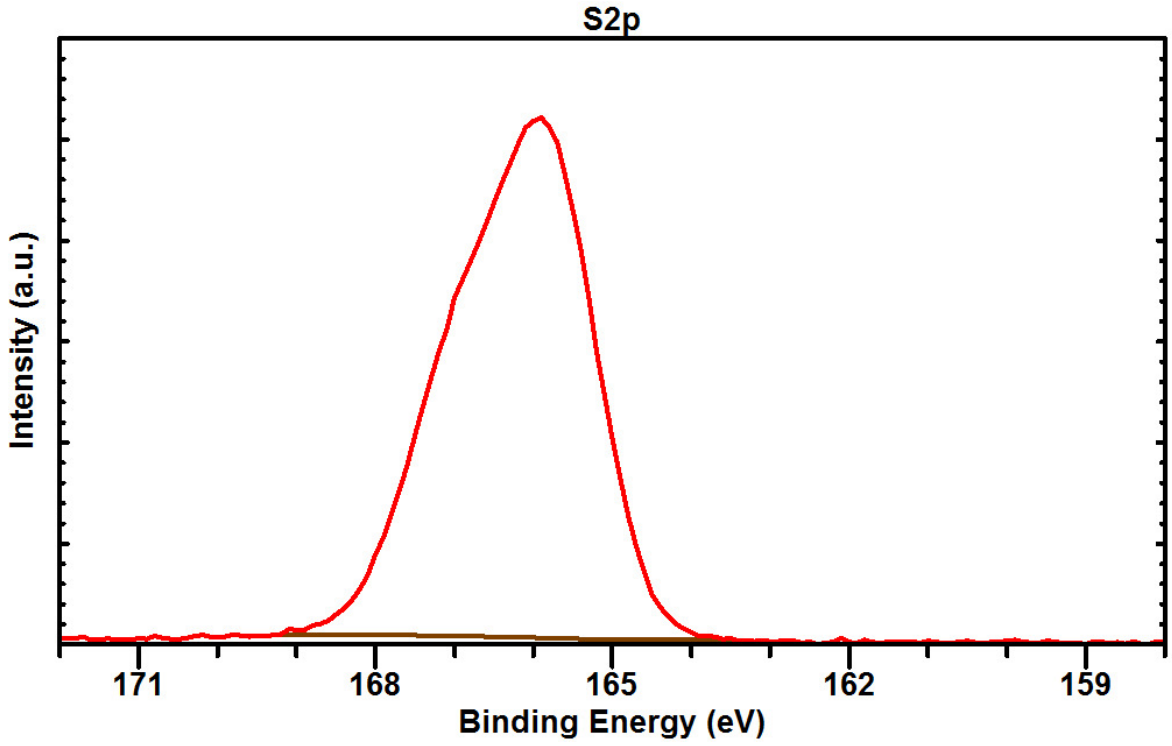
S2p
Intensity (a.u.)
171
168
165
162
159
Binding Energy (eV)

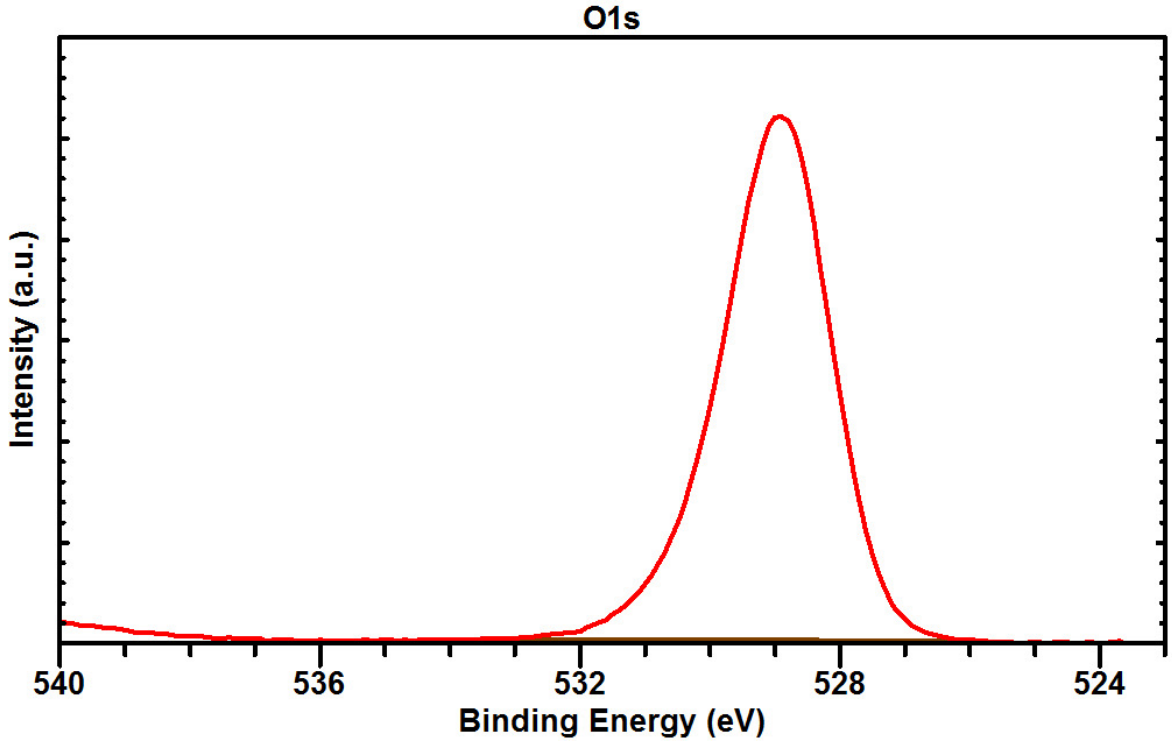
O1s
Intensity (a.u.)
540
536
532
528
524
Binding Energy (eV)

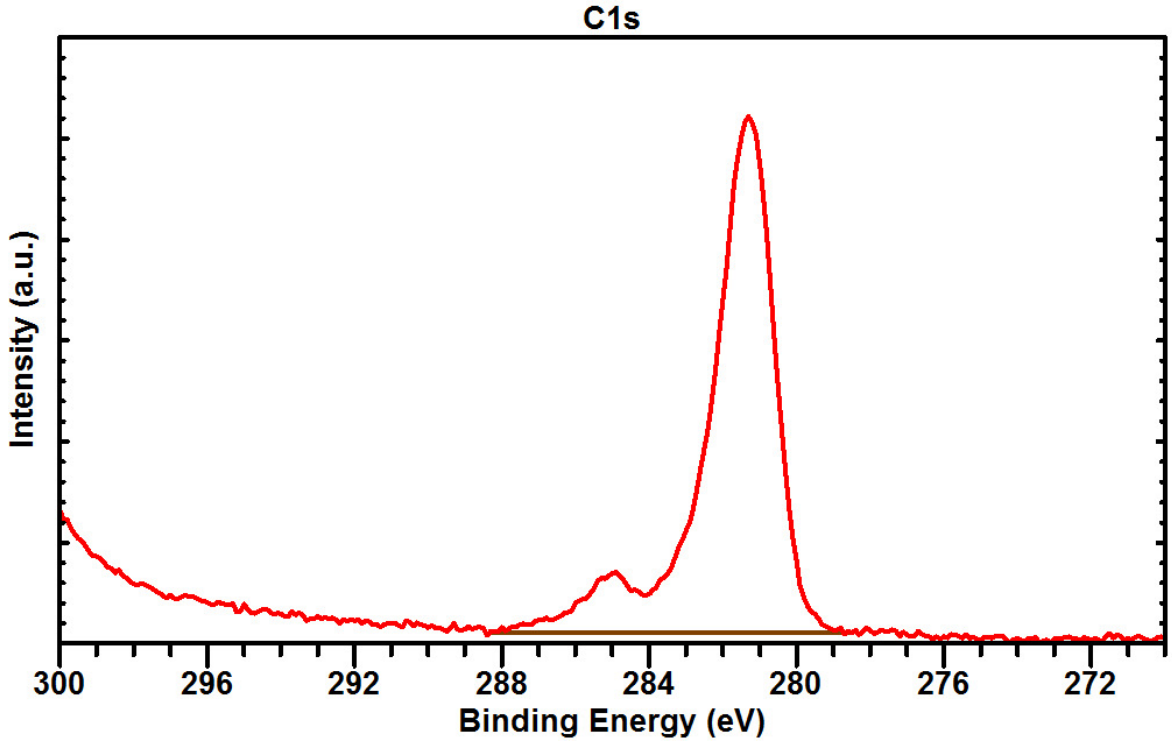
C1s
Intensity (a.u.)
300
296
292
288
284
280
276
272
Binding Energy (eV)

Figure 2.S44. The survey and detailed XPS spectra together with the background used for subtraction, as measured for $BaSO_4$.

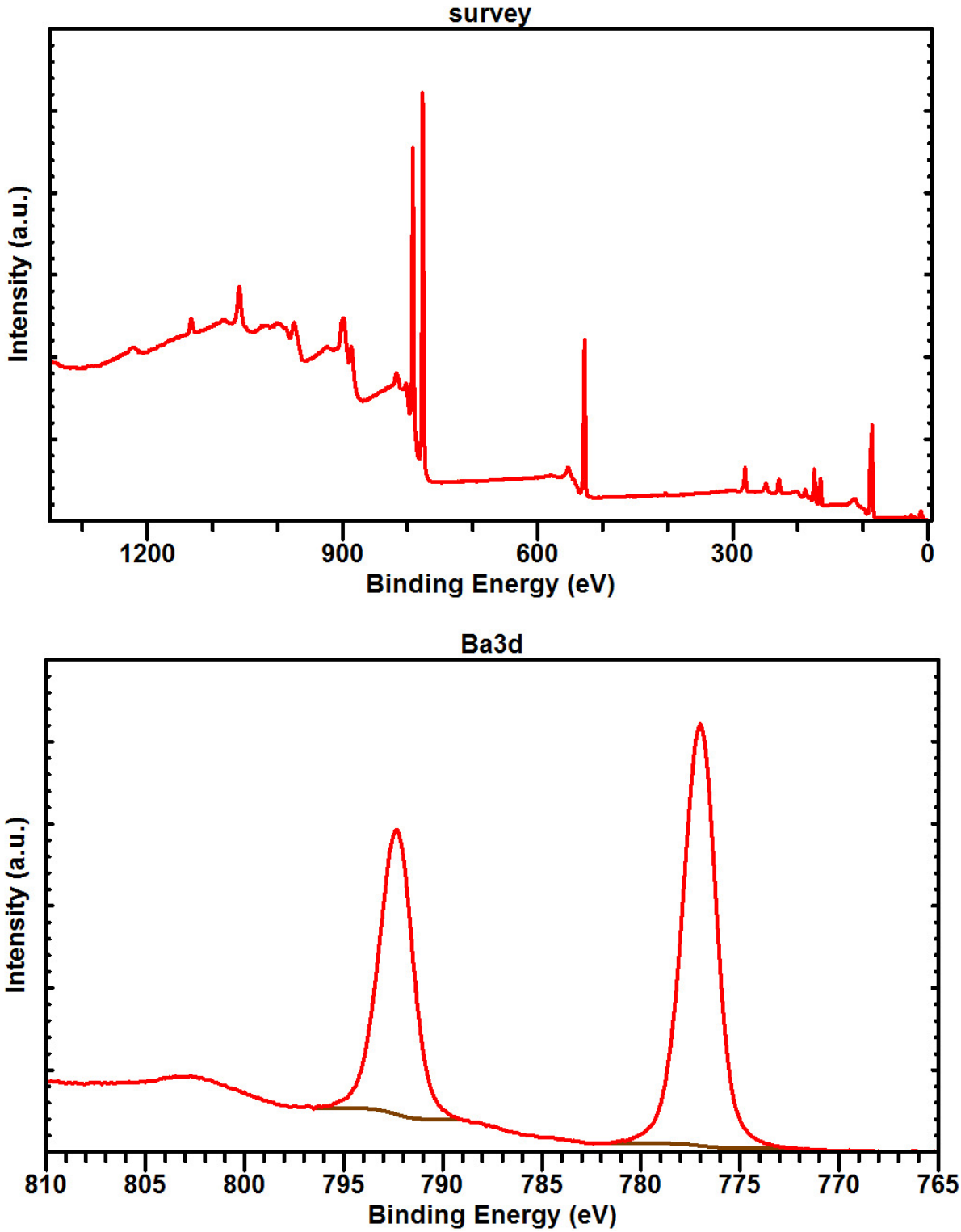

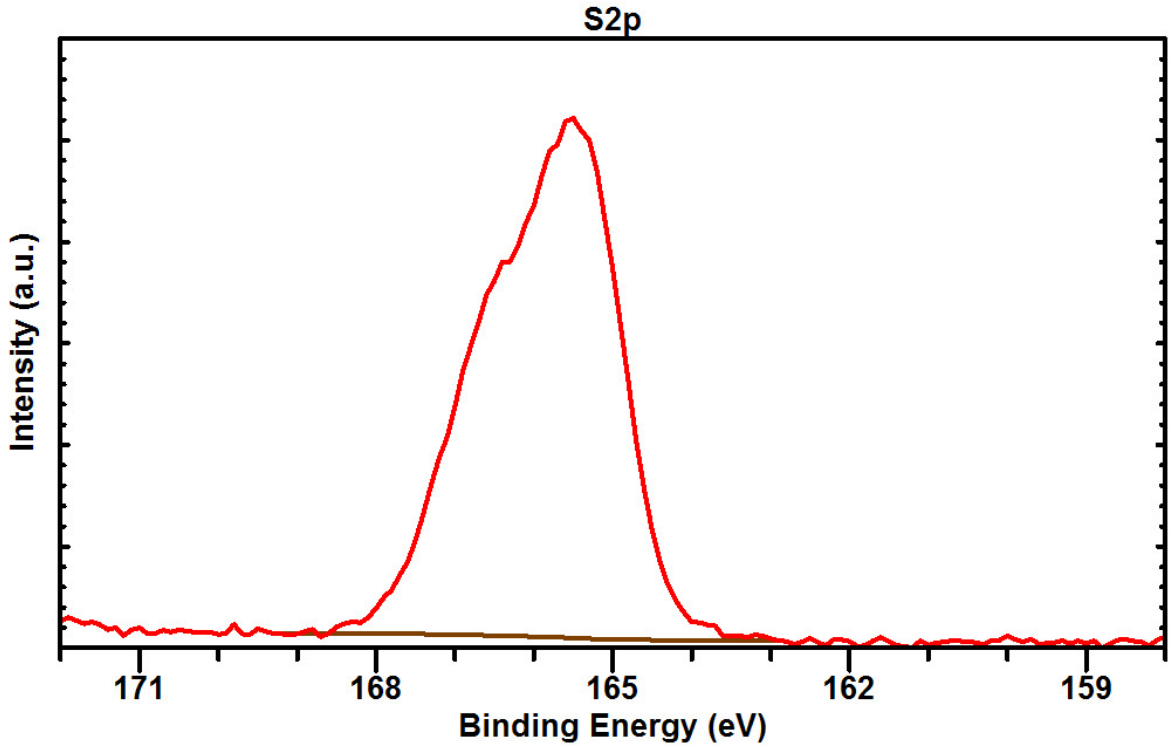
S2p
Intensity (a.u.)
171
168
165
162
159
Binding Energy (eV)

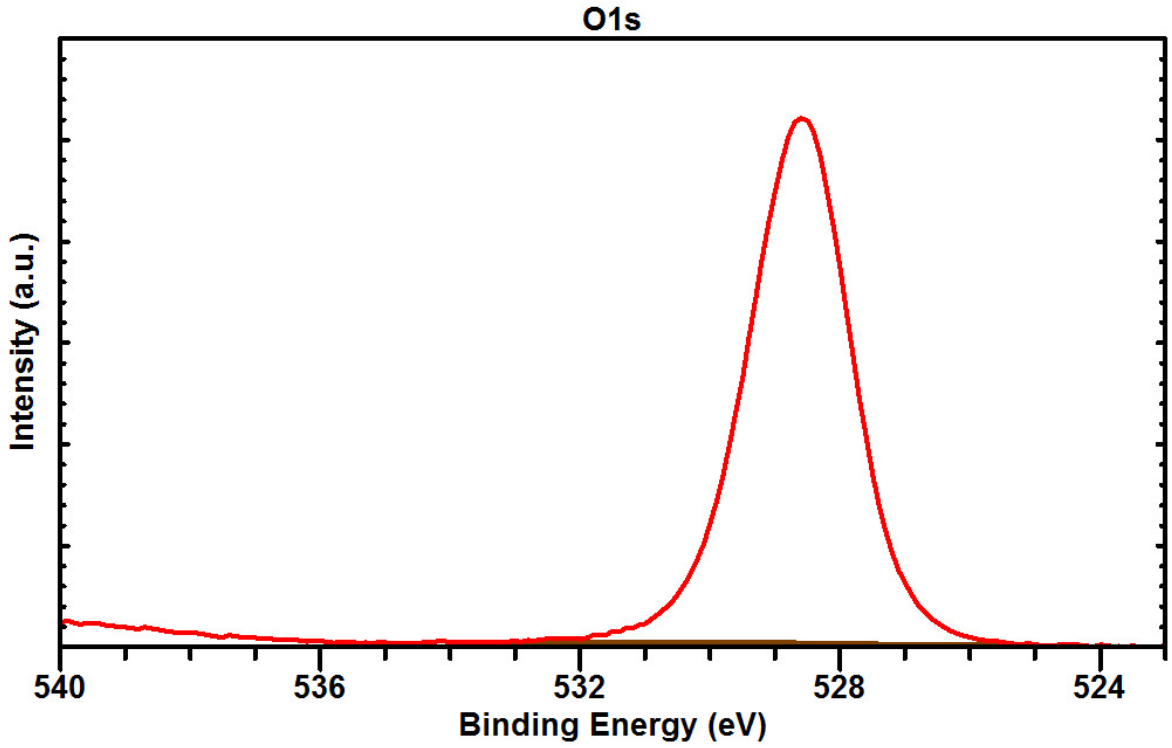
O1s
Intensity (a.u.)
540
536
532
528
524
Binding Energy (eV)

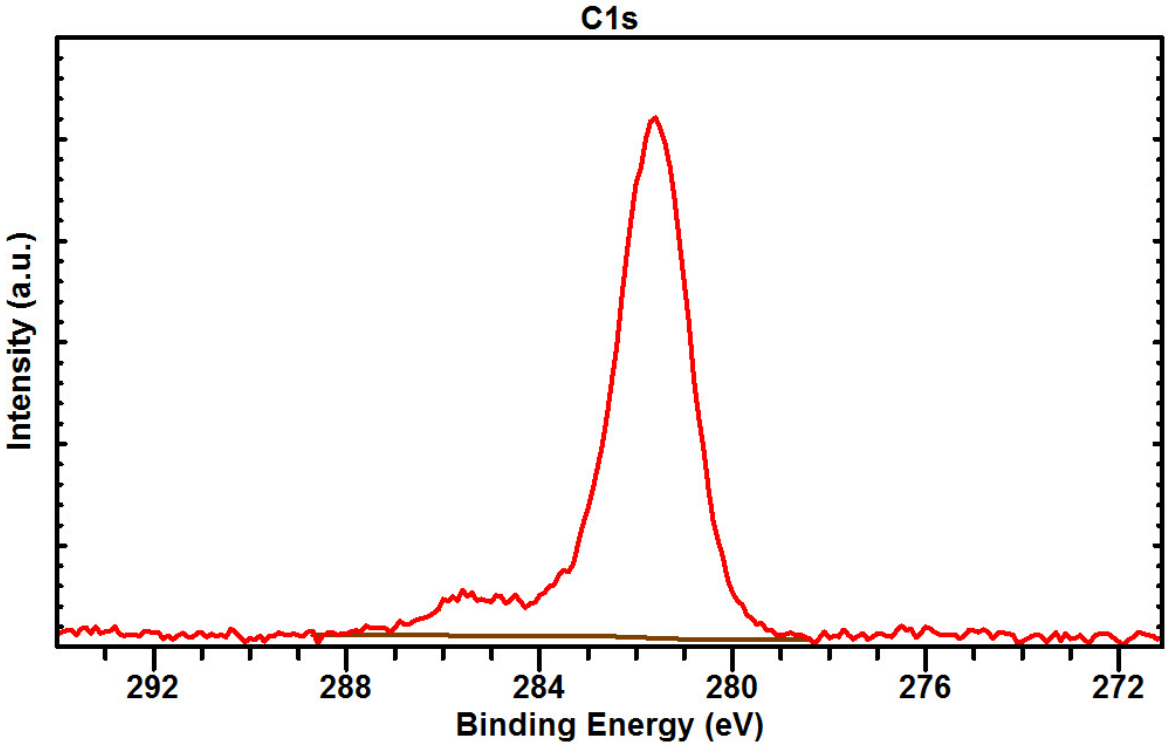
C1s
Intensity (a.u.)
292
288
284
280
276
272
Binding Energy (eV)

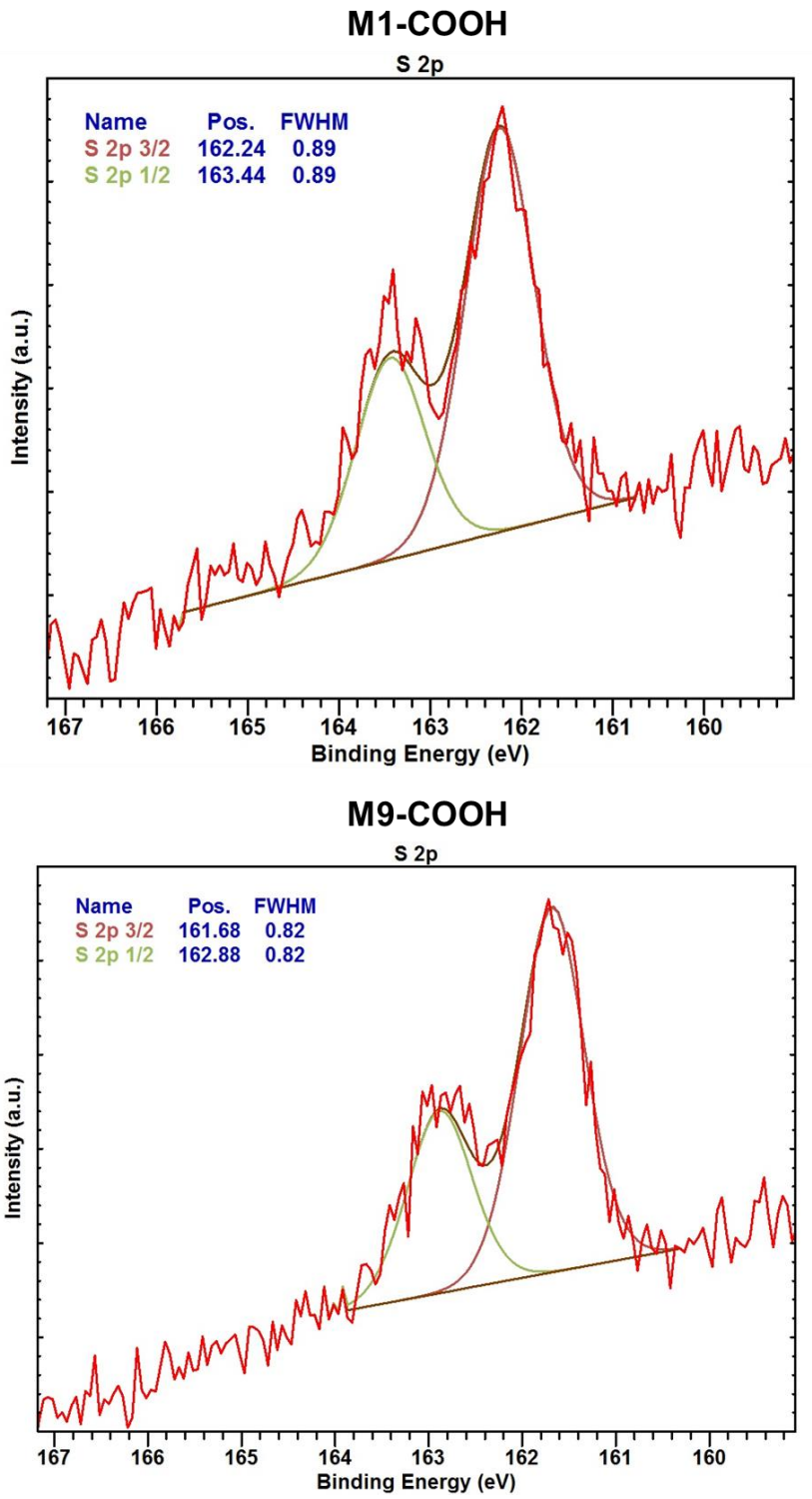

Figure 2.S45. Fitted S 2p spectra of (top) 1-COOH-7-SH-1,7-$C_2B_{10}H_{10}$ (**M1-COOH**) and (bottom) 1-COOH-9-SH-1,7-$C_2B_{10}H_{10}$ (**M9-COOH**) showing no other minor components.

2.6 REFERENCES

1. Love, J. C.; Estroff, L. A.; Kriebel, J. K.; Nuzzo, R. G.; Whitesides, G. M. Self-Assembled Monolayers of Thiolates on Metals as a Form of Nanotechnology. *Chem. Rev.* **2005,** *105,* 1103-1170.

2. Vericat, C.; Vela, M. E.; Benitez, G.; Carro, P.; Salvarezza, R. C. Self-Assembled Monolayers of Thiols and Dithiols on Gold: New Challenges for a Well-Known System. *Chem. Soc. Rev.* **2010,** *39,* 1805.

3. Claridge, S. A.; Liao, W.-S.; Thomas, J. C.; Zhao, Y.; Cao, H. H.; Cheunkar, S.; Serino, A. C.; Andrews, A. M.; Weiss, P. S. From the Bottom Up: Dimensional Control and Characterization in Molecular Monolayers. *Chem. Soc. Rev.* **2013,** *42,* 2725-2745.

4. Goronzy, D. P.; Ebrahimi, M.; Rosei, F.; Arramel; Fang, Y.; De Feyter, S.; Tait, S. L.; Wang, C.; Beton, P. H.; Wee, A. T. S.; Weiss, P. S.; Perepichka, D. F. Supramolecular Assemblies on Surfaces: Nanopatterning, Functionality, and Reactivity. *ACS Nano* **2018,** *12,* 7445-7481.

5. Hohman, J. N.; Claridge, S. A.; Kim, M.; Weiss, P. S. Cage Molecules for Self-Assembly. *Mater. Sci. Eng., R* **2010,** *70,* 188-208.

6. Laibinis, P. E.; Whitesides, G. M. Ω-Terminated Alkanethiolate Monolayers on Surfaces of Copper, Silver, and Gold Have Similar Wettabilities. *J. Am. Chem. Soc.* **1992,** *114,* 1990-1995.

7. Gershevitz, O.; Osnis, A.; Sukenik, C. N. Interfacial Chemistry on Carboxylate-Functionalized Monolayer Assemblies. *Isr. J. Chem.* **2005,** *45,* 321-336.

8. Burris, S. C.; Zhou, Y.; Maupin, W. A.; Ebelhar, A. J.; Daugherty, M. W. The Effect of Surface Preparation on Apparent Surface pK_a's of Ω-Mercaptocarboxylic Acid Self-Assembled Monolayers on Polycrystalline Gold. *J. Phys. Chem. C* **2008,** *112,* 6811-6815.

9. Hirata, N.; Suga, S.; Noguchi, Y.; Shibuta, M.; Tsunoyama, H.; Eguchi, T.; Nakajima, A. Highly Ordered Self-Assembled Monolayers of Carboxy- and Ester-Terminated Alkanethiols on Au(111): Infrared Absorption and Hyperthermal-Deposition Experiments with Cr(benzene)$_2$ Ions. *J. Phys. Chem. C* **2017,** *121,* 6736-6747.

10. Ackerson, C. J.; Jadzinsky, P. D.; Kornberg, R. D. Thiolate Ligands for Synthesis of Water-Soluble Gold Clusters. *J. Am. Chem. Soc.* **2005,** *127,* 6550-6551.

11. Thomas, J. C.; Boldog, I.; Auluck, H. S.; Bereciartua, P. J.; Dušek, M.; Macháček, J.; Bastl, Z.; Weiss, P. S.; Baše, T. Self-Assembled *p*-Carborane Analogue of *p*-Mercaptobenzoic Acid on Au{111}. *Chem. Mater.* **2015,** *27,* 5425-5435.

12. Hohman, J. N.; Zhang, P.; Morin, E. I.; Han, P.; Kim, M.; Kurland, A. R.; McClanahan, P. D.; Balema, V. P.; Weiss, P. S. Self-Assembly of Carboranethiol Isomers on Au{111}:

Intermolecular Interactions Determined by Molecular Dipole Orientations. *ACS Nano* **2009,** *3*, 527-536.

13. Kim, M.; Hohman, J. N.; Morin, E. I.; Daniel, T. A.; Weiss, P. S. Self-Assembled Monolayers of 2-Adamantanethiol on Au{111}: Control of Structure and Displacement. *J. Phys. Chem. A* **2009,** *113*, 3895-3903.

14. Fujii, S.; Akiba, U.; Fujihira, M. Geometry for Self-Assembling of Spherical Hydrocarbon Cages with Methane Thiolates on Au(111). *J. Am. Chem. Soc.* **2002,** *124*, 13629-13635.

15. Dameron, A. A.; Charles, L. F.; Weiss, P. S. Structures and Displacement of 1-Adamantanethiol Self-Assembled Monolayers on Au{111}. *J. Am. Chem. Soc.* **2005,** *127*, 8697-8704.

16. Willey, T. M.; Fabbri, J. D.; Lee, J. R. I.; Schreiner, P. R.; Fokin, A. A.; Tkachenko, B. A.; Fokina, N. A.; Dahl, J. E. P.; Carlson, R. M. K.; Vance, A. L.; Yang, W.; Terminello, L. J.; Buuren, T. v.; Melosh, N. A. Near-Edge X-Ray Absorption Fine Structure Spectroscopy of Diamondoid Thiol Monolayers on Gold. *J. Am. Chem. Soc.* **2008,** *130*, 10536-10544.

17. Baše, T.; Bastl, Z.; Plzák, Z.; Grygar, T.; Plešek, J.; Carr, M. J.; Malina, V.; Šubrt, J.; Boháček, J.; Večerníková, E.; Kříž, O. Carboranethiol-Modified Gold Surfaces. A Study and Comparison of Modified Cluster and Flat Surfaces. *Langmuir* **2005,** *21*, 7776-7785.

18. Grimes, R. N. Carboranes in the Chemist's Toolbox. *Dalton Trans.* **2015,** *44*, 5939-5956.

19. Spokoyny, A. M.; Machan, C. W.; Clingerman, D. J.; Rosen, M. S.; Wiester, M. J.; Kennedy, R. D.; Stern, C. L.; Sarjeant, A. A.; Mirkin, C. A. A Coordination Chemistry Dichotomy for Icosahedral Carborane-Based Ligands. *Nature Chemistry* **2011,** *3*, 590-596.

20. Yavuz, A.; Sohrabnia, N.; Yilmaz, A.; Danışman, M. F. Mixed Carboranethiol Self-Assembled Monolayers on Gold Surfaces. *Appl. Surf. Sci.* **2017,** *413*, 233-241.

21. Lübben, J. F.; Baše, T.; Rupper, P.; Künniger, T.; Macháček, J.; Guimond, S. Tuning the Surface Potential of Ag Surfaces by Chemisorption of Oppositely-Oriented Thiolated Carborane Dipoles. *J. Colloid Interface Sci.* **2011,** *354*, 168-174.

22. Thomas, J. C.; Schwartz, J. J.; Hohman, J. N.; Claridge, S. A.; Auluck, H. S.; Serino, A. C.; Spokoyny, A. M.; Tran, G.; Kelly, K. F.; Mirkin, C. A.; Gilles, J.; Osher, S. J.; Weiss, P. S. Defect-Tolerant Aligned Dipoles within Two-Dimensional Plastic Lattices. *ACS Nano* **2015,** *9*, 4734-4742.

23. Kim, J.; Rim, Y. S.; Liu, Y.; Serino, A. C.; Thomas, J. C.; Chen, H.; Yang, Y.; Weiss, P. S. Interface Control in Organic Electronics Using Mixed Monolayers of Carboranethiol Isomers. *Nano Lett.* **2014,** *14*, 2946-2951.

24. Vetushka, A.; Bernard, L.; Guseva, O.; Bastl, Z.; Plocek, J.; Tomandl, I.; Fejfar, A.; Baše, T.; Schmutz, P. Adsorption of Oriented Carborane Dipoles on a Silver Surface. *Phys. Status Solidi B* **2015,** *253*, 591-600.

25. Mete, E.; Yılmaz, A.; Danışman, M. F. A van der Waals Density Functional Investigation of Carboranethiol Self-Assembled Monolayers on Au(111). *Phys. Chem. Chem. Phys.* **2016,** *18*, 12920-12927.

26. Plešek, J. The Age of Chiral Deltahedral Borane Derivatives. *Inorg. Chim. Acta* **1999,** *289*, 45-50.

27. Abendroth, J. M.; Stemer, D. M.; Bloom, B. P.; Roy, P.; Naaman, R.; Waldeck, D. H.; Weiss, P. S.; Mondal, P. C. Spin Selectivity in Photoinduced Charge-Transfer Mediated by Chiral Molecules. *ACS Nano* **2019,** *13*, 4928-4946.

28. Gohler, B.; Hamelbeck, V.; Markus, T. Z.; Kettner, M.; Hanne, G. F.; Vager, Z.; Naaman, R.; Zacharias, H. Spin Selectivity in Electron Transmission through Self-Assembled Monolayers of Double-Stranded DNA. *Science* **2011,** *331*, 894-897.

29. Abendroth, J. M.; Nakatsuka, N.; Ye, M.; Kim, D.; Fullerton, E. E.; Andrews, A. M.; Weiss, P. S. Analyzing Spin Selectivity in DNA-Mediated Charge Transfer *via* Fluorescence Microscopy. *ACS Nano* **2017,** *11*, 7516-7526.

30. Abendroth, J. M.; Cheung, K. M.; Stemer, D. M.; El Hadri, M. S.; Zhao, C.; Fullerton, E. E.; Weiss, P. S. Spin-Dependent Ionization of Chiral Molecular Films. *J. Am. Chem. Soc.* **2019,** *141*, 3863-3874.

31. Bregadze, V. I. Dicarba-*Closo*-Dodecaboranes $C_2B_{10}H_{12}$ and Their Derivatives. *Chem. Rev.* **1992,** *92*, 209-223.

32. Plešek, J.; Heřmánek, S. Experimental Evaluation of Charge Distribution on Particular Skeletal Atoms in Icosahedral Carboranes by Means of HS-Derivatives. *Collect. Czech. Chem. Commun.* **1979,** *44*, 24-33.

33. Plešek, J.; Heřmánek, S. Syntheses and Properties of Substituted Icosahedral Carborane Thiols. *Collect. Czech. Chem. Commun.* **1981,** *46*, 687-692.

34. Grimes, R. N. Carboranes, 3rd Edition. Elsevier: 2016.

35. Baše, T.; Macháček, J.; Hájková, Z.; Langecker, J.; Kennedy, J. D.; Carr, M. J. Thermal Isomerizations of Monothiolated Carboranes $(HS)C_2B_{10}H_{11}$ and the Solid-State Investigation of 9-(HS)-1,2-$C_2B_{10}H_{11}$ and 9-(HS)-1,7-$C_2B_{10}H_{11}$. *J. Organomet. Chem.* **2015,** *798*, 132-140.

36. Thomas, J. C.; Goronzy, D. P.; Dragomiretskiy, K.; Zosso, D.; Gilles, J.; Osher, S. J.; Bertozzi, A. L.; Weiss, P. S. Mapping Buried Hydrogen-Bonding Networks. *ACS Nano* **2016,** *10*, 5446-5451.

37. Maksymovych, P.; Sorescu, D. C.; Yates, J. T. Gold-Adatom-Mediated Bonding in Self-Assembled Short-Chain Alkanethiolate Species on the Au(111) Surface. *Phys. Rev. Lett.* **2006,** *97*, 146103.

38. Moore, A. M.; Mantooth, B. A.; Donhauser, Z. J.; Yao, Y.; Tour, J. M.; Weiss, P. S. Real-Time Measurements of Conductance Switching and Motion of Single Oligo(Phenylene Ethynylene) Molecules. *J. Am. Chem. Soc.* **2007,** *129*, 10352-10353.

39. Hohman, J. N.; Kim, M.; Schüpbach, B.; Kind, M.; Thomas, J. C.; Terfort, A.; Weiss, P. S. Dynamic Double Lattice of 1-Adamantaneselenolate Self-Assembled Monolayers on Au{111}. *J. Am. Chem. Soc.* **2011,** *133*, 19422-19431.

40. Bain, C. D.; Whitesides, G. M. A Study by Contact Angle of the Acid-Base Behavior of Monolayers Containing Ω-Mercaptocarboxylic Acids Adsorbed on Gold: An Example of Reactive Spreading. *Langmuir* **1989,** *5*, 1370-1378.

41. Creager, S. E.; Clarke, J. Contact-Angle Titrations of Mixed Ω-Mercaptoalkanoic Acid/Alkanethiol Monolayers on Gold. Reactive vs Nonreactive Spreading, and Chain Length Effects on Surface pK_a Values. *Langmuir* **1994,** *10*, 3675-3683.

42. Paulo, T. F.; Abruña, H. D.; Diógenes, I. C. N. Thermodynamic, Kinetic, Surface pK_a, and Structural Aspects of Self-Assembled Monolayers of Thio Compounds on Gold. *Langmuir* **2012,** *28*, 17825-17831.

43. Hatzor, A.; Weiss, P. S. Molecular Rulers for Scaling Down Nanostructures. *Science* **2001,** *291*, 1019.

44. Mandal, S.; Reber, A. C.; Qian, M.; Weiss, P. S.; Khanna, S. N.; Sen, A. Controlling the Band Gap Energy of Cluster-Assembled Materials. *Acc. Chem. Res.* **2013,** *46*, 2385-2395.

45. Andrews, A. M.; Liao, W.-S.; Weiss, P. S. Double-Sided Opportunities Using Chemical Lift-Off Lithography. *Acc. Chem. Res.* **2016,** *49*, 1449-1457.

46. Arnold, R.; Azzam, W.; Terfort, A.; Wöll, C. Preparation, Modification, and Crystallinity of Aliphatic and Aromatic Carboxylic Acid Terminated Self-Assembled Monolayers. *Langmuir* **2002,** *18*, 3980-3992.

47. Baše, T.; Bastl, Z.; Šlouf, M.; Klementová, M.; Šubrt, J.; Vetushka, A.; Ledinský, M.; Fejfar, A.; Macháček, J.; Carr, M. J.; Londesborough, M. G. S. Gold Micrometer Crystals Modified with Carboranethiol Derivatives. *J. Phys. Chem. C* **2008,** *112*, 14446-14455.

48. Isom, D. G.; Castañeda, C. A.; Cannon, B. R.; García-Moreno E, B. Large Shifts in pK_a Values of Lysine Residues Buried inside a Protein. *Proc. Natl. Acad. Sci. U. S. A.* **2011,** *108*, 5260.

49. Harms, M. J.; Castañeda, C. A.; Schlessman, J. L.; Sue, G. R.; Isom, D. G.; Cannon, B. R.; García-Moreno E, B. The pK_a Values of Acidic and Basic Residues Buried at the Same Internal Location in a Protein Are Governed by Different Factors. *J. Mol. Biol.* **2009,** *389*, 34-47.

50. Karp, D. A.; Gittis, A. G.; Stahley, M. R.; Fitch, C. A.; Stites, W. E.; García-Moreno E, B. High Apparent Dielectric Constant inside a Protein Reflects Structural Reorganization Coupled to the Ionization of an Internal Asp. *Biophys. J.* **2007,** *92*, 2041-2053.

51. Rastogi, V. K.; Girvin, M. E. Structural Changes Linked to Proton Translocation by Subunit *C* of the ATP Synthase. *Nature* **1999,** *402*, 263-268.

52. Guo, B.; Middha, E.; Liu, B. Solvent Magic for Organic Particles. *ACS Nano* **2019,** *13*, 2675-2680.

53. Chen, H.; Huang, C.; Deng, Y.; Sun, Q.; Zhang, Q.-L.; Zhu, B.-X.; Ni, X.-L. Solvent-Switched Schiff-Base Macrocycles: Self-Sorting and Self-Assembly-Dependent Unconventional Organic Particles. *ACS Nano* **2019,** *13*, 2840-2848.

54. Dávalos, J. Z.; González, J.; Ramos, R.; Hnyk, D.; Holub, J.; Santaballa, J. A.; Canle-L, M.; Oliva, J. M. Acidities of *closo*-1-COOH-1,7-$C_2B_{10}H_{11}$ and Amino Acids Based on Icosahedral Carbaboranes. *J. Phys. Chem. A* **2014,** *118*, 2788-2793.

55. Ohta, K.; Konno, S.; Endo, Y. Complexation of α-Cyclodextrin with Carborane Derivatives in Aqueous Solution. *Chem. Pharm. Bull.* **2009,** *57*, 307-310.

56. Palatinus, L.; Chapuis, G. SUPERFLIP - A Computer Program for the Solution of Crystal Structures by Charge Flipping in Arbitrary Dimensions. *J. Appl. Crystallogr.* **2007,** *40*, 786-790.

57. Petříček, V.; Dušek, M.; Palatinus, L. Crystallographic Computing System JANA2006: General Features. *Z. Kristallogr.* **2014,** *229*, 345-352.

58. Valiev, M.; Bylaska, E. J.; Govind, N.; Kowalski, K.; Straatsma, T. P.; Van Dam, H. J. J.; Wang, D.; Nieplocha, J.; Apra, E.; Windus, T. L.; de Jong, W. A. NWChem: A Comprehensive and Scalable Open-Source Solution for Large Scale Molecular Simulations. *Comput. Phys. Commun.* **2010,** *181*, 1477-1489.

59. Johnson, B. G.; Fisch, M. J. An Implementation of Analytic Second Derivatives of the Gradient-Corrected Density Functional Energy. *J. Chem. Phys.* **1994,** *100*, 7429-7442.

60. Adamo, C.; Barone, V. Physically Motivated Density Functionals with Improved Performances: The Modified Perdew–Burke–Ernzerhof Model. *J. Chem. Phys.* **2002,** *116*, 5933-5940.

61. Jensen, F. Unifying General and Segmented Contracted Basis Sets. Segmented Polarization Consistent Basis Sets. *J. Chem. Theory Comput.* **2014,** *10,* 1074-1085.

62. Jensen, F. Basis Set Convergence of Nuclear Magnetic Shielding Constants Calculated by Density Functional Methods. *J. Chem. Theory Comput.* **2008,** *4*, 719-727.

63. Ferris, J. H.; Kushmerick, J. G.; Johnson, J. A.; Yoshikawa Youngquist, M. G.; Kessinger, R. B.; Kingsbury, H. F.; Weiss, P. S. Design, Operation, and Housing of an Ultrastable, Low Temperature, Ultrahigh Vacuum Scanning Tunneling Microscope. *Rev. Sci. Instrum.* **1998,** *69*, 2691.

64. Tersoff, J.; Hamann, D. R. Theory and Application for the Scanning Tunneling Microscope. *Phys. Rev. Lett.* **1983,** *50,* 1998-2001.

65. Tang, W.; Sanville, E.; Henkelman, G. A Grid-Based Bader Analysis Algorithm without Lattice Bias. *J. Phys.: Condens. Matter* **2009,** *21*, 084204.

66. Kresse, G.; Furthmüller, J. Efficient Iterative Schemes for *Ab Initio* Total-Energy Calculations Using a Plane-Wave Basis Set. *Phys. Rev. B* **1996,** *54*, 11169-11186.

67. Kresse, G.; Furthmüller, J. Efficiency of *Ab-Initio* Total Energy Calculations for Metals and Semiconductors Using a Plane-Wave Basis Set. *Comput. Mater. Sci.* **1996,** *6*, 15-50.

68. Kresse, G.; Hafner, J. *Ab Initio* Molecular-Dynamics Simulation of the Liquid-Metal– Amorphous-Semiconductor Transition in Germanium. *Phys. Rev. B* **1994,** *49*, 14251-14269.

69. Kresse, G.; Hafner, J. *Ab Initio* Molecular Dynamics for Liquid Metals. *Phys. Rev. B* **1993,** *47,* 558-561.

70. Mathew, K.; Hennig, R. G. Implicit Self-Consistent Description of Electrolyte in Plane-Wave Density-Functional Theory. *arXiv* **2016,** *1601.03346*.

71. Mathew, K.; Sundararaman, R.; Letchworth-Weaver, K.; Arias, T. A.; Hennig, R. G. Implicit Solvation Model for Density-Functional Study of Nanocrystal Surfaces and Reaction Pathways. *J. Chem. Phys.* **2014,** *140*, 084106.

72. Liptak, M. D.; Shields, G. C. Accurate pK_a Calculations for Carboxylic Acids Using Complete Basis Set and Gaussian-N Models Combined with CPCM Continuum Solvation Methods. *Journal of the American Chemical Society* **2001,** *123*, 7314-7319.

73. Frisch, M. J.; Trucks, G. W.; Schlegel, H. B.; Scuseria, G. E.; Robb, M. A.; Cheeseman, J. R.; Scalmani, G.; Barone, V.; Petersson, G. A.; Nakatsuji, H.; Li, X.; Caricato, M.; Marenich, A. V.; Bloino, J.; Janesko, B. G.; Gomperts, R.; Mennucci, B.; Hratchian, H. P.; Ortiz, J. V.; Izmaylov, A. F., *et al. Gaussian 16 Rev. C.01*, Wallingford, CT, 2016.

74. Stephens, P. J.; Devlin, F. J.; Chabalowski, C. F.; Frisch, M. J. *Ab Initio* Calculation of Vibrational Absorption and Circular Dichroism Spectra Using Density Functional Force Fields. *J. Phys. Chem.* **1994,** *98*, 11623-11627.

75. Becke, A. D. Density-Functional Thermochemistry. III. The Role of Exact Exchange. *J. Chem. Phys.* **1993,** *98*, 5648-5652.

76. Lee, C.; Yang, W.; Parr, R. G. Development of the Colle-Salvetti Correlation-Energy Formula into a Functional of the Electron Density. *Phys. Rev. B* **1988,** *37*, 785-789.

77. Vosko, S. H.; Wilk, L.; Nusair, M. Accurate Spin-Dependent Electron Liquid Correlation Energies for Local Spin Density Calculations: A Critical Analysis. *Can. J. Phys.* **1980,** *58*, 1200-1211.

78 Barone, V.; Cossi, M. Quantum Calculation of Molecular Energies and Energy Gradients in Solution by a Conductor Solvent Model. *J. Phys. Chem. A* **1998,** *102*, 1995-2001.

79. Cossi, M.; Rega, N.; Scalmani, G.; Barone, V. Energies, Structures, and Electronic Properties of Molecules in Solution with the C-PCM Solvation Model. *J. Comput. Chem.* **2003,** *24*, 669-681.

80. van der Marel, C.; Yildirim, M.; Stapert, H. R. Multilayer Approach to the Quantitative Analysis of X-Ray Photoelectron Spectroscopy Results: Applications to Ultrathin SiO_2 on Si and to Self-Assembled Monolayers on Gold. *J. Vac. Sci. Technol., A* **2005,** *23*, 1456-1470.

81. Powell, C. J.; Jablonski, A. NIST Electron Inelastic-Mean-Free-Path Database, Version 1.2. Gaithersburg: National Institute of Standards and Technology, 2010.

Chapter 3: Isomeric Molecule Mapping within Mixed Carboranedithiol Self-Assembled Monolayers

3.1 Introduction

The structure and properties of self-assembled materials are influenced by various types of packing interactions, similar to those observed in single crystals, commonly referred to as packing forces. These interactions often give rise to differences between the properties of a single molecule and an array of molecules in their bulk form.[1–4] It is natural to analyze strong interactions first and understand their role in the self-assembly, be it either the supramolecular framework of molecules in a single crystal or the geometrical surface pattern of a 2-D array of molecules immobilized on a surface. Elucidation of the forces at hand and the role they play in supramolecular assembly must be fully understood to design new and innovative materials and devices.

Boron cage molecules have recently attracted a lot of interest for in depth study of self-assembly. Due to bulky steric demands and rigid structure, self-assembled monolayers composed of these molecules portray more tolerance toward defects within the lattice and have shown a high degree of stability against thermal degradation and chemical substitution.[4–8] Of this category of molecules, a particularly novel class is the dicarba-*closo*-dodecaborane, also known as the carborane. Carboranes exhibit nearly perfect icosahedral symmetry and are composed of 12 atom vertices, 10 boron and 2 carbon, which participate in hexacoordinate, heavily delocalized bonds. The high electronegativity difference between carbon and boron atoms gives rise to a large and tailorable intrinsic dipole that is dependent on the position of the two carbon vertices within the cage.[9,10] Furthermore, carboranes can be functionalized at any position around the cage with an array of different functional groups such as alkyl chains, carboxylic acids, alcohols, halogens, and more.[10] This study focuses on using 1,2-dicarba-*closo*-dodecaborane, which has the largest intrinsic dipole of the three carborane isomers, as a scaffold functionalized with two thiol anchoring groups that further alter the dipole magnitude and direction.

Anchoring thiol groups can strongly interact with coinage metal surfaces limiting the orientation of tethered molecules thus exposing them to specific lateral interactions.[11–14] For example, Van der Waals interactions can affect molecular geometry and packing, leading to particular surface patterns.[15,16] A material's structure and function is thus pre-determined by competing forces which play an active role during the adsorption or, more generally, the self-assembly process.[17] Understanding these interactions is essential in order to design new materials of desired inner structure and properties.

Herein, we developed a system which enabled us to look further into these self-organized structures by changing only specific building blocks' properties while keeping their geometry and anchoring scheme identical. We substituted molecules in SAMs with molecules of different electron density distributions without changing the geometrical pattern of the monolayer. It has been previously shown that the 9,12-$(HS)_2$-1,2-$C_2B_{10}H_8$ and 1,2-$(HS)_2$-9,12-$C_2B_{10}H_8$ isomers have identical nearest neighbor lattice spacing.[18] In addition the valency of attachment of these isomers can be controlled, which in turn can control the percentage of surface sulfur coverage or apparent height distribution in the longitudinal direction of the SAM.[18] Such a system has the potential to reveal the effect of different dipole orientations and magnitudes of the molecules on their close neighbors and beyond, and unveil the existence of dipole-driven patterns within the geometrical surface patterns.

To identify individual isomeric molecules within their mixed SAMs we labelled some isomers with methyl substituents to change their longitudinal space requirements while leaving their lateral space requirements unchanged. Scanning tunneling microscopy (STM), has previously been used in many studies to elucidate the position and orientation of single molecules in SAM matrices.[17–23] The images acquired by STM represent a convolution of electronic and topographic

information about the surface. By using STM as a tool to probe this system, we elucidate the identity of each species in the heterogeneous monolayer and provide a means to map surface dynamics.

3.2 Results and Discussion

In this study, we examined two carboranedithiol isomers, 9,12-$(HS)_2$-1,2-$C_2B_{10}H_8$, 1,2-$(HS)_2$-9,12-$C_2B_{10}H_8$, and a dimethylated version 1,2-$(Me)_2$-9,12-$(HS)_2$-1,2-$C_2B_{10}H_8$ henceforth referred to as O9,12 carboranedithiol (O9,12), O1,2 carboranedithiol (O1,2), and Me1,2O9,12 carboranedithiol (Me1,2O9,12) respectively. The structures of these isomers are shown in Figure 3.1. Monolayers of these molecules were assembled on Au{111} substrates.

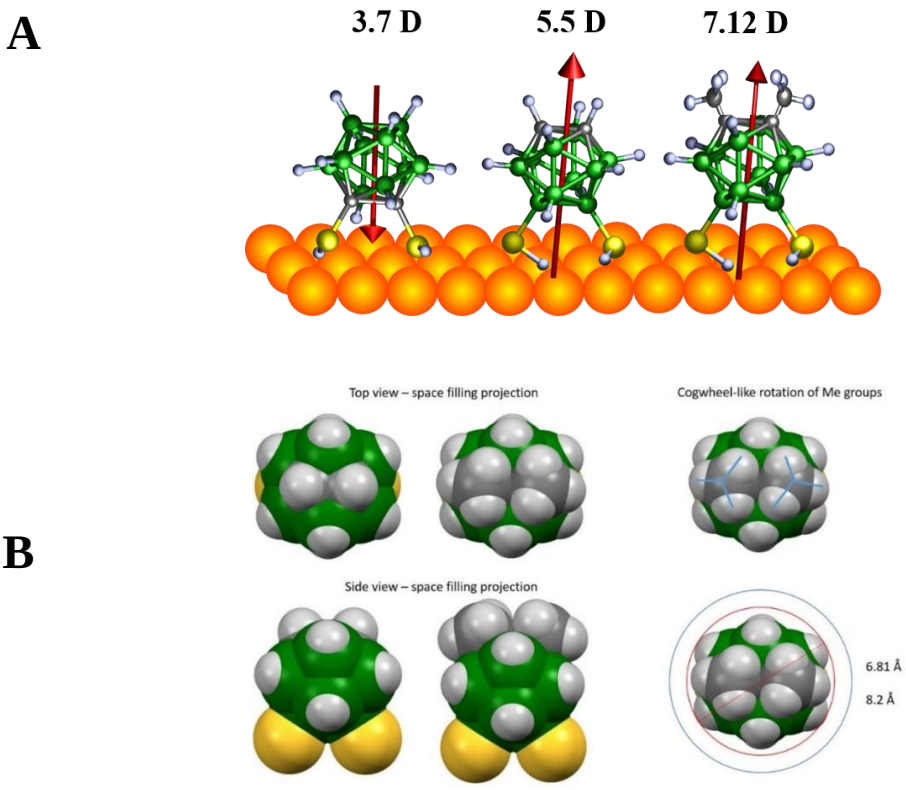

Figure 3.1 (A) Ball and stick models of O1,2 carboranedithiol (O1,2), O9,12 carboranedithiol (O9,12), and Me1,2O9,12 carboranedithiol (Me1,2O9,12) left to right and respective dipole moment and orientation when anchored to Au{111} substrate. (B) Space filling projection models of O9,12 and Me_2O9,12. The addition of the two methyl groups does not alter lateral space requirements but solely the height when anchored to the surface.

As reported in Table 3.1, the intramolecular distances of the three molecules are similar, supporting that the lateral steric demands are kept constant while altering the longitudinal spatial requirements. Our previous measurements on homogenous monolayers of the O1,2 and O9,12 monolayers reported both isomers form hexagonally close-packed (hcp) monolayers with nearest-neighbor spacings of 7.6 ± 0.5 Å.[18] This formation is best explained by a ($\sqrt{7} \times \sqrt{7}$)R19.12° superstructure that is found for several carboranethiol SAMs on Au{111}.[17,21]

Intramolecular distance (Å)	1,2-$(HS)_2$-1,2-$C_2B_{10}H_{10}$	9,12-$(HS)_2$-1,2-$C_2B_{10}H_{10}$	1,2-$(CH_3)_2$-9,12-$(HS)_2$-1,2-$C_2B_{10}H_8$
S-S	3.459	3.778, 3.823[a]	3.810
C(1)-C(2)	1.693	1.629, 1.640[a]	1.647
B(9)-B(12)	1.781	1.796, 1.797[a]	1.792
C(Me)-C(Me)	-	-	3.097
B(4)-B(7)	3.395	3.387, 3.380[a]	3.359

[a] Single-crystal data[24]

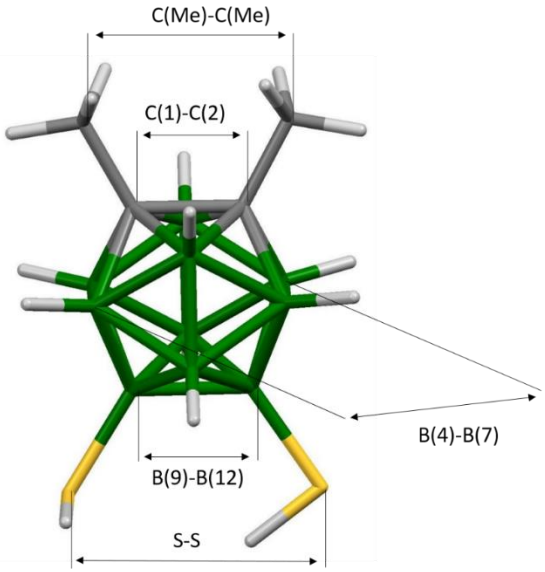

Table 3.1. Schematic of 1,2-$(CH_3)_2$-9,12-$(HS)_2$-1,2-$C_2B_{10}H_8$ and selected intramolecular distances determined by single crystal X-ray diffraction studies.

In addition to unrecognizable differences amongst nearest neighbor spacing distances, it was demonstrated that both isomers could be shifted almost entirely to their divalent state, anchoring both thiols to the gold surface.[18] This divalent anchoring eliminated any discrepancies observed in longitudinal height differences when measuring the z-height of heterogenous monolayers using STM as the monovalent state was present in negligible amounts.

We first studied Me1,2O9,12 to test if homogenous monolayers of this carboranedithiol behaved similarly to that of other unfunctionalized dithiol derivatives. Monolayer deposition of Me1,2O9,12 on Au{111} under both neutral and basic conditions was assessed using STM (figure 3.2). Under neutral conditions the Me1,2O9,12 monolayer showed a bimodal height distribution. This distribution was attributed to the existence of both thiol and thiolate adsorption on the substrate. Under basic solution deposition conditions,

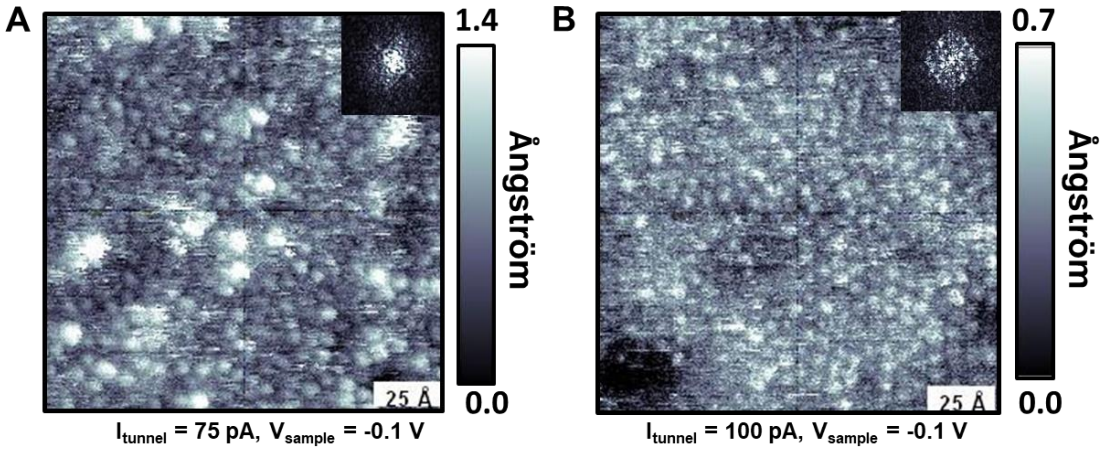

Figure 3.2. Scanning tunneling microscopy images of (A) Me1,2O9,12 deposited in neutral solution and (B) Me1,2O9,12 deposited in basic solution self-assembled on Au{111}. All images were recorded at ambient conditions. Insets depicting Fourier transforms of panels (A) and (B) show hexagonal close-packed arrays with identical nearest-neighbor distances of 7.4 ± 0.4 Å. Image A shows a bimodal height distribution attributed to a mixture of monovalent and divalent binding of the ligand to the substrate.

the bimodal height distribution disappeared, which was attributed to the monolayer being solely composed of the dithiolate species. The nearest neighbor spacing of 7.4 ± 0.4 Å was consistent with the lateral measurements and packing density of the unfunctionalized dithiols O1,2 and O9,12.[18]

Next, a mixed monolayer of the Me1,2O9,12 and O1,2 species was deposited in basic conditions on Au{111} substrate at a 9:1 ratio. This uneven ratio was chosen to account for the difference in surface affinity of the thiol bound to the boron in Me1,2O,9,12 compared with the thiol bound to the carbon in the O1,2 molecule, which is more acidic in nature due to the decreased electron density at the carbon vertex. In solution, the pK_{a1} of O1,2 and O9,12 were found to be 4.47 and 5.5, respectively.[24]

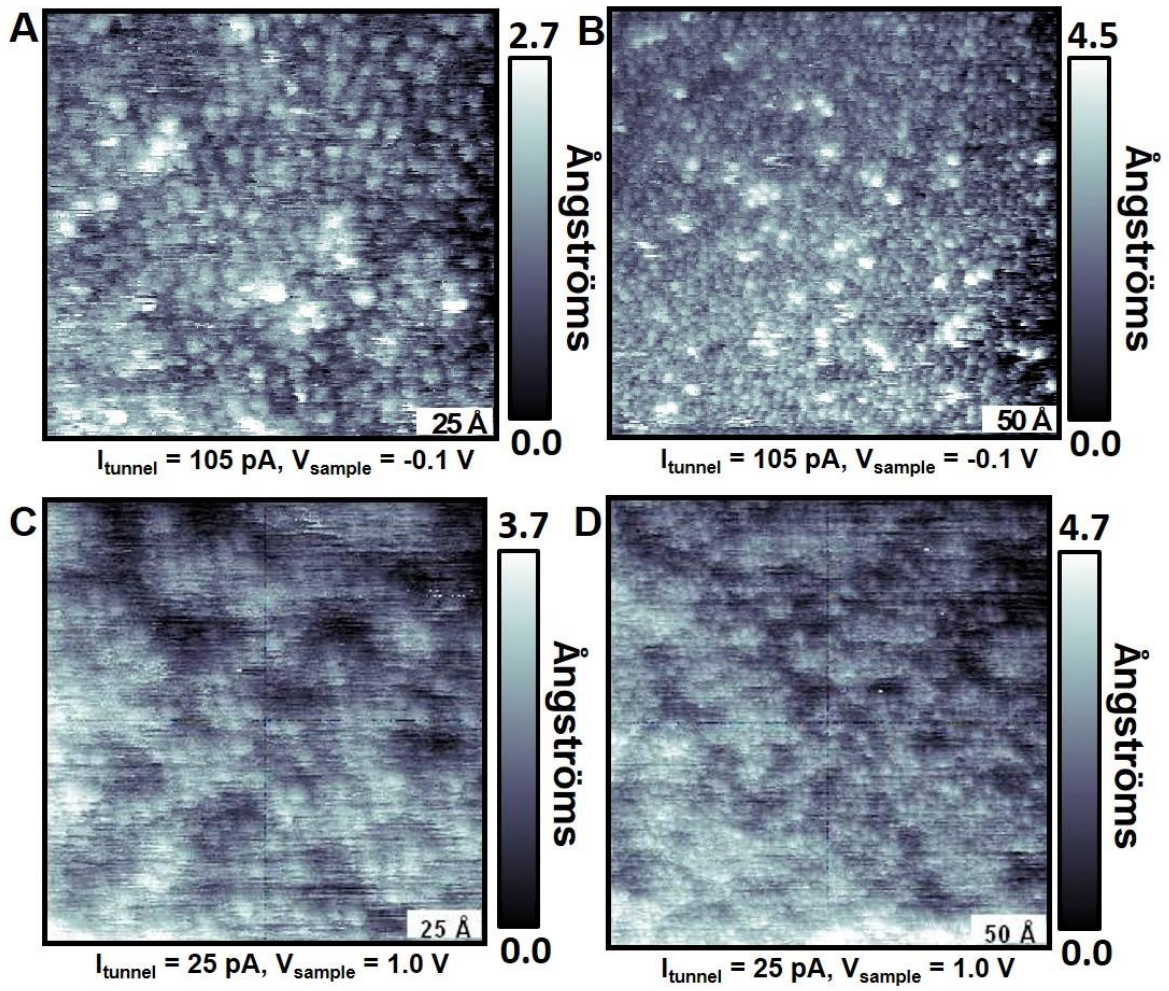

Figure 3.3 Scanning tunneling microscopy images of (A,B) Me1,2O9,12 and O1,2 deposited in basic solution and (C,D) Me1,2O9,12 and O1,2 deposited in neutral solution self-assembled on Au{111}. All images were recorded at ambient conditions.

This heterogenous monolayer was initially deposited under basic conditions to avoid the convolution of both monovalent and divalent species binding to the surface, as seen by the large distribution of observed longitudinal heights in Figure 3.3c,d where neutral deposition conditions were used. In the basic deposition system, small clusters (less than ~5 molecules) of larger apparent height were observed. This more protruding species was attributed to the Me1,2O9,12, due to its larger electronic and topographic height, and was found to compose about 10 ± 3% of all species

on the surface. The apparent height difference was calculated to be 2.2 ± 0.5 Å, calibrated from a Au step edge.

We also studied heterogenous monolayers of the O1,2 and O9,12 isomers deposited in a 9:1 ratio. These isomers share the same physical height but differ electronically due to their oppositely oriented and different dipole magnitudes. In this system, under basic deposition conditions, again two species of different apparent heights were observed along with small cluster formation of the larger height species (Figure 3.4). The protruding species is attributed to the O9,12 due to its dipole orientation and magnitude.

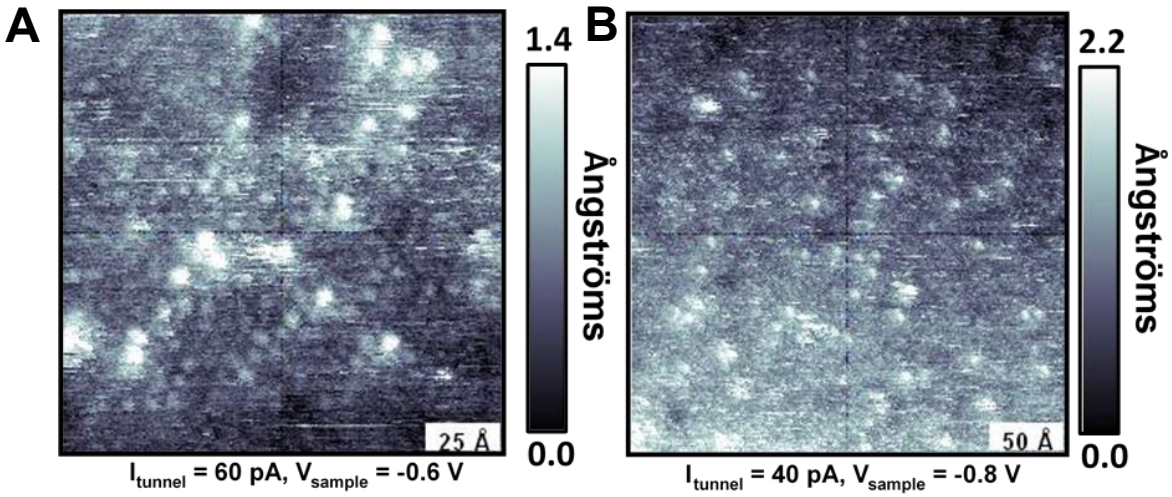

Figure 3.4 Scanning tunneling microscopy images of (A,B) O9,12 and O1,2 deposited in neutral solution self-assembled on Au{111}. All images were recorded at ambient conditions.

After experimentally observing both heterogeneous monlayers, we sought to elucidate the roles that neighboring oppositely oriented dipoles played along with other potential factors such as anchoring group orientation and geometry that would influence surface assembly arrangement. We performed Monte Carlo simulations where we simulated annealing to explore the optimal

distribution of dipoles with different orientations. Simulations were performed on 2D hexagonal lattice with lattice parameter a=7.6 Å. 2D periodic boundary conditions were used and dipole moments were 3.6 D and 5.7 D.

The ratio of dipoles with opposite orientation was fixed during the simulation and dipoles were randomly distributed in the lattice at the start of simulation. In each simulation step, we randomly choose two dipoles with opposite orientation and switched their positions in the lattice. We determined the energy difference ΔE connected with this switch. When the energy difference ΔE was negative, a new state was automatically accepted. In the case of positive ΔE, the probability of acceptance of this new state was calculated. The simulation ran as temperature was decreased to 0 K. Figure 3.5 shows the result of the calculation.

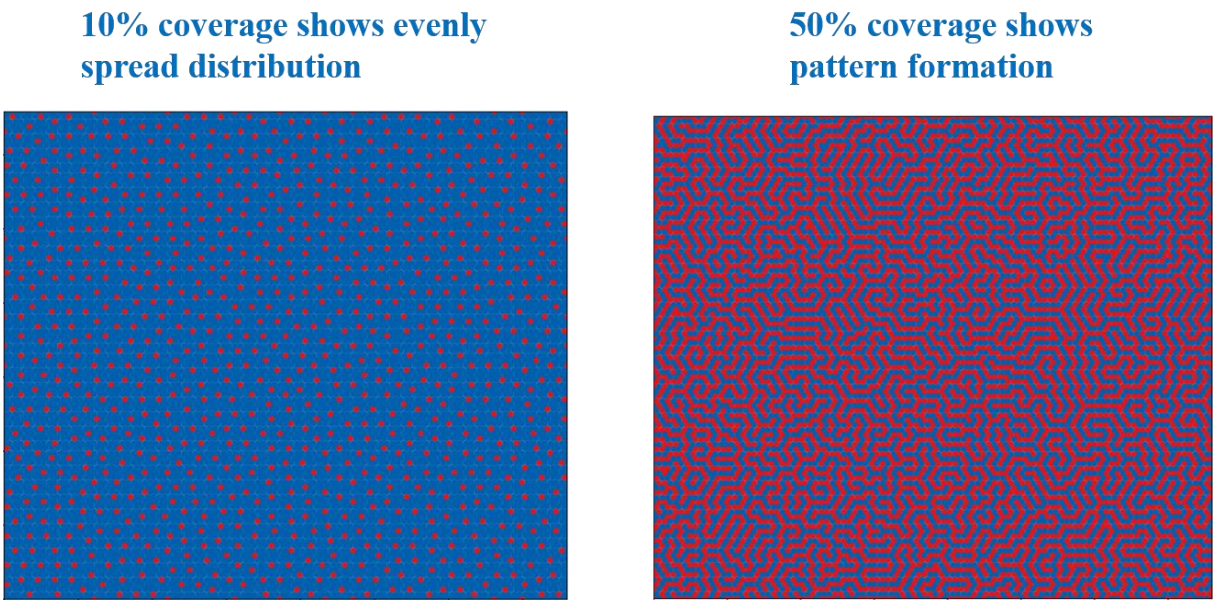

Figure 3.5. Result of Monte Carlo simulations at 10% and 50% coverage respectively. At the completion of the simulation, 10% coverage showed even distribution of oppositely oriented dipoles whereas the 50% coverage showed slight pattern formation across the SAM matrix.

At 10% coverage, which was what we observed experimentally, oppositely oriented dipoles were calculated to be evenly distributed throughout the SAM matrix. However, in the case

of the experimentally observed system, we did not observe an even distribution, but rather small cluster formation, demonstrating that while dipole-dipole interactions may have some effect on monolayer distribution, they are not the main driving force.

To take a further look into additional forces, we studied the effects of anchoring group symmetry and interaction. Mixed monolayers of O1,2 and O9,12 (or Me1,2O9,12, respectively) require analysis of the SH anchoring groups' properties as they significantly differ. The B-SH group sulfur atoms in O9,12 and Me1,2O9,12 have significantly higher electron densities than the C-SH sulfur atoms in O1,2. We not only point at the different character of these SH groups but analyzed their mutual SH···SH interactions, which can have an effect on surface assembly through the respective lateral interactions outlined in Figure 3.6.

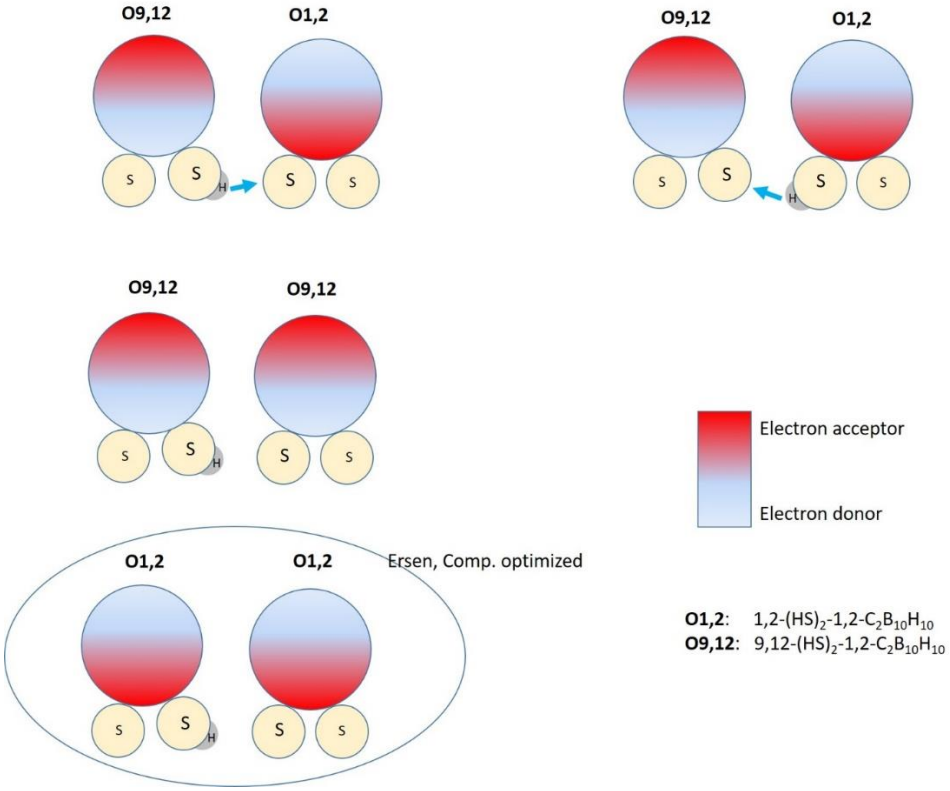

Figure 3.6 Schematic of different possible interactions of thiol and thiolate anchoring groups throughout heterogeneous monolayers of O1,2 and O9,12 isomers.

3.3 Conclusions and Prospects

Mixed monolayers of O1,2 and O9,12 or Me1,2O9,12 formed densely packed monolayers on Au{111} substrates with indistinguishable nearest neighbor spacings in comparison to homogenous monolayers in both basic and neutral conditions. Under basic deposition conditions, both heterogenous monolayers revealed two distinct surface species attributed to each of the molecules in their divalent binding state. In both systems, small clusters of the more protruding molecules were observed. Using computational analysis, Monte Carlo simulations revealed that alternating dipole dipole interactions were not the driving force behind the monolayer dynamics and that more in-depth analyses of other characteristics must be studied.

This system provides a novel platform for molecular isomeric mapping of surface deposition dynamics and lattice arrangement under different conditions. Further analysis of this system would be beneficial to elucidate the role that neighboring anchoring groups play on the lattice arrangement. Future experiemnts can explore the role that close proximitey thiol/thiolate interactions on different electron density vertices play in the self assembly process.

3.4 Materials and Methods

Scanning tunneling microscopy sample preparation and image analysis: O1,2, O9,12 and Me1,2O9,12 were synthesized as previously reported and stored in a glovebox environment with solutions prepared immediately before use.[24] Samples for imaging were prepared on Au{111}/mica substrates (Agilent Technology, Tempe, AZ), which were hydrogen-flame annealed with 10 passes at a rate of 0.4 Hz prior to SAM formation. Substrates were placed in 1 mM ethanolic solutions for 24 h at room temperature for neutral deposition conditions and 2:1 NaOH:carboranedithiol for basic deposition conditions. Ethanol was used as received (Sigma-

Aldrich, St. Louis, MO). After deposition, samples where rinsed with neat ethanol and dried under a stream of ultra high-purity nitrogen for at least three cycles. All STM measurements were performed with a custom-built Besocke-style STM with a platinum/iridium tip (80:20).[25] The known lattice of the 1 dodecanethiolate SAMs on Au{111} was used for calibration. The STM image analyses were performed using MATLAB (Mathworks, Natick, MA) and Gwyddion (http://gwyddion.net/).

Monte Carlo simulation analysis: We perform annealing simulations to explore the optimal distribution of dipoles with different orientation. Simulations were performed on 2D hexagonal lattice with lattice parameter a=7.6 Å. 2D periodic boundary conditions was used. Dipole moments were 3.6 D and 5.7 D.

The ratio of dipoles with opposite orientation was fixed during the simulation and dipoles were randomly distributed in the lattice at the start of simulation. In each simulation step, we randomly choose two dipoles with opposite orientation and switched their positions in the lattice. We determined the energy difference ΔE connected with this switch. When the energy difference ΔE was negative, the new state was automatically accepted. In the case of positive ΔE the probability of acceptance of this new state was:

$$\exp(\frac{-\Delta E}{k_B T}),$$

where k_B is the Boltzman constant and T is simulation temperature in K. The temperature progressively decreased from an initial value towards zero. The starting temperature was set to such a value that almost all new states are accepted. After a given number of simulation steps the temperature was decreased and the simulation continued. At the end of the simulation, the

temperature limit was zero and accepted only changes that lowered the system energy. Because of long-range dipole interactions and the periodicity of the simulation lattice, Ewald summation for confined geometry was used to determine the energy change.

Mass spectrometry: Mass spectrometry measurements were performed on a Thermo Scientific LCQ Fleet Ion Trap instrument using electrospray (ESI) ionization with helium (5.0 Messer) as a collision gas in the ion trap. The sample was dissolved in acetonitrile (concentration ~100 ng/ml) and introduced through a fused-silica sample tube of 0.100 mm (inner diameter) × 0.19 mm (outer diameter) to the ion source from a Hamilton syringe using infusion at 5.0 μL/min, source voltage 5.87 kV, tube lens voltage -109.94 V, capillary voltage -34.95 V, capillary temperature 275.19 °C, and N_2 (isolated from air in NitroGen N1118LA, Peak Scientific) as a nebulizing sheath gas (flow rate 12.02 p.d.u.). Only negative ions of the respective molecular peaks were detected.

Experimental infrared spectra: The IR spectra of all species were measured in KBr pellets using a Nicolet Nexus 670 FTIR spectrometer at 4000−200 cm^{-1} (1024 scans, 2 cm^{-1} resolution), Thermo Nicolet Corporation, Madison, USA. Typical amounts of the measured sample were 1.0 – 1.3 mg.

3.5 Additional Figures

Electrospray Ionization Mass Spectra of 1,2-$(Me)_2$-9,12-$(HS)_2$-1,2-$C_2B_{10}H_8$

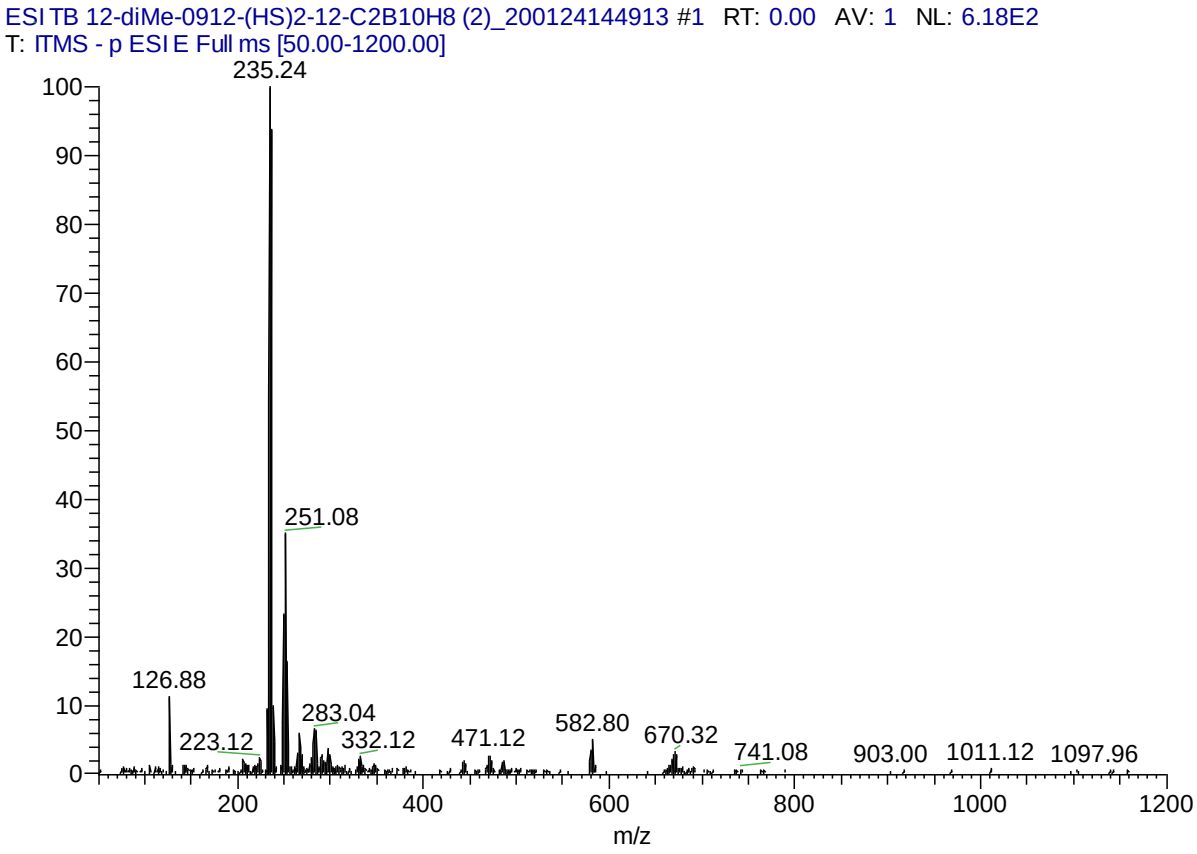

Figure 3.7 Electrospray ionization mass spectra of 1,2-$(Me)_2$-9,12-$(HS)_2$-1,2-$C_2B_{10}H_8$ (Me1,2O9,12)

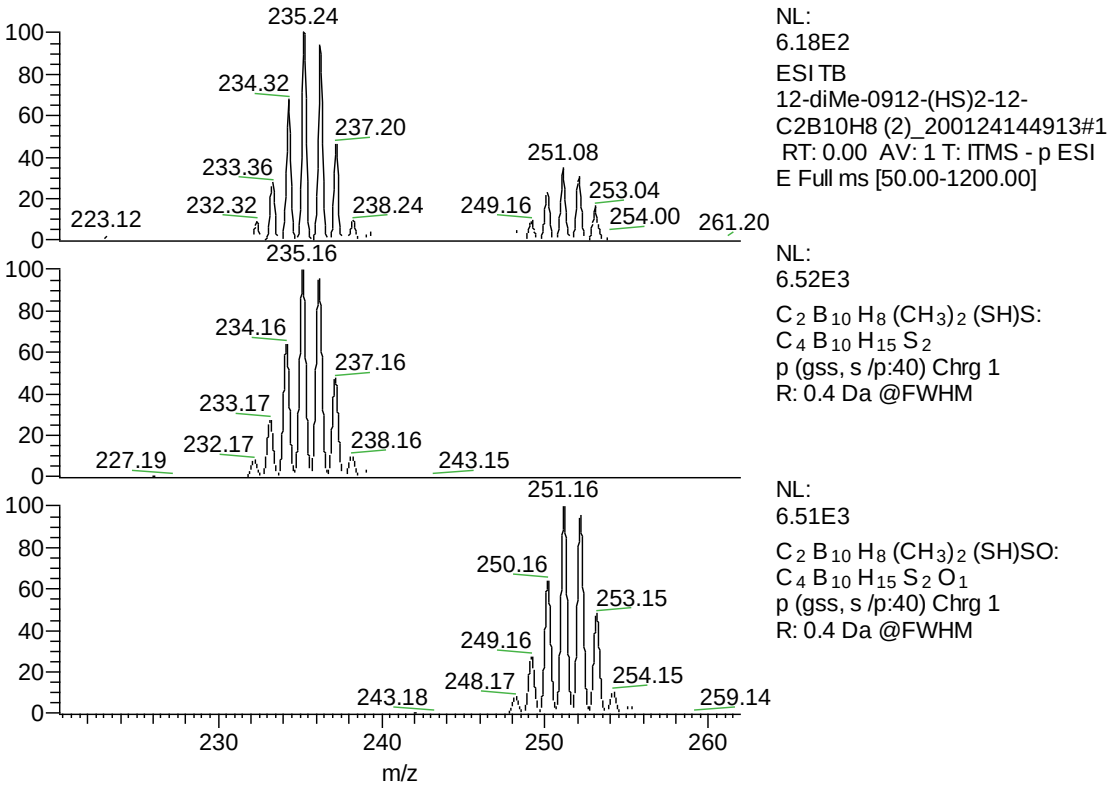

Figure 3.8 (Top) Measured and (bottom) calculated isotopic distribution envelopes for the molecular masses corresponding to 2M-2H+1Na, 2M-H and for 2M-H-2B.

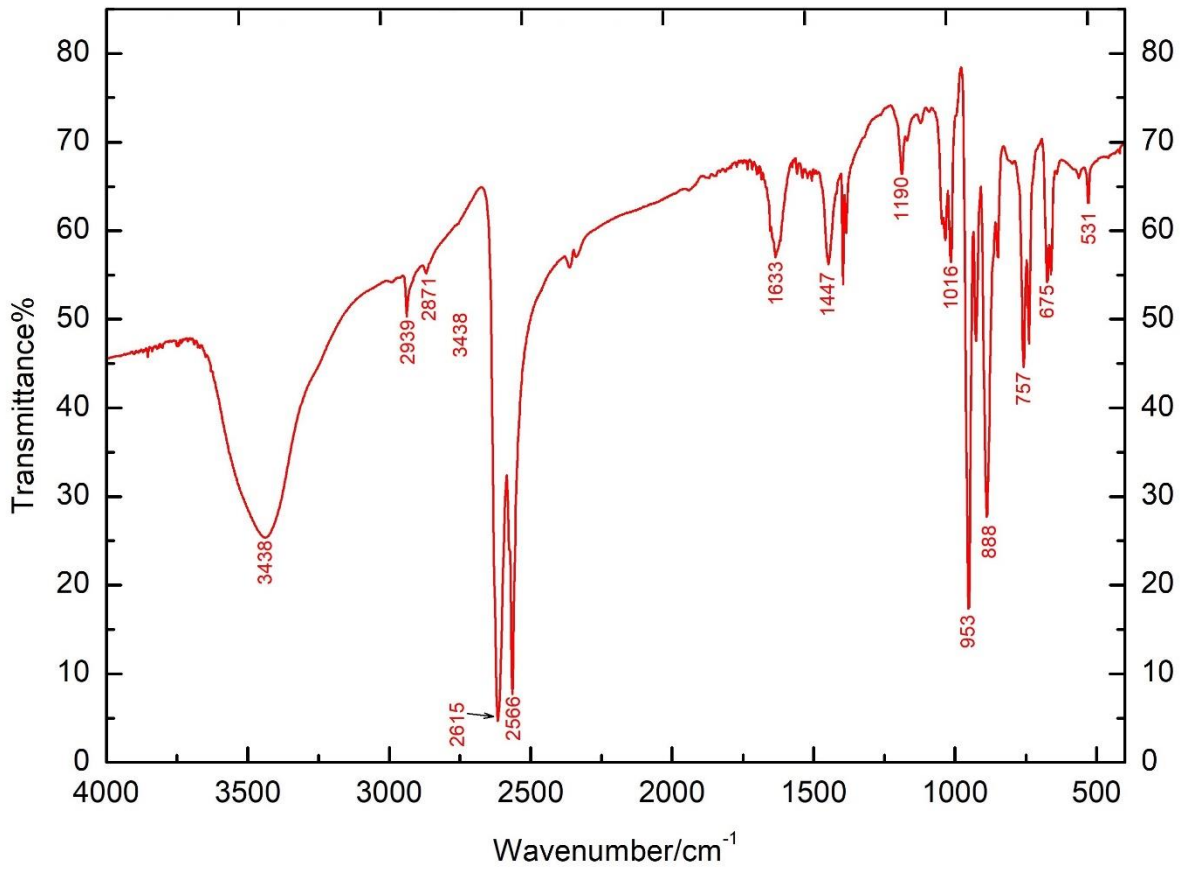

Figure 3.9 The measured overall IR spectrum of 1,2-$(CH_3)_2$-9,12-$(HS)_2$-1,2-$C_2B_{10}H_8$ measured in KBr pellets using a Nicolet Nexus 670 FTIR spectrometer at 4000-200 cm^{-1}.

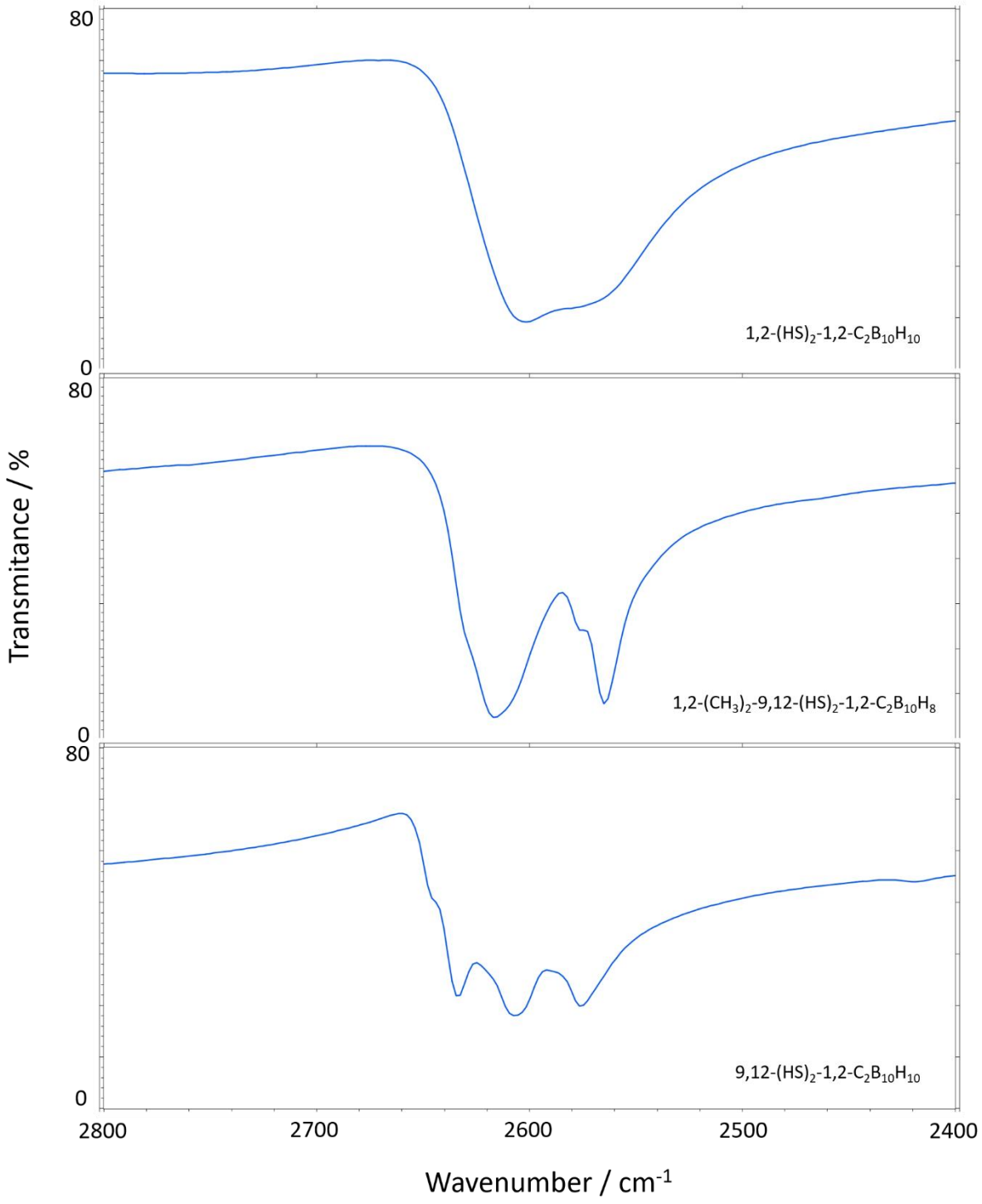

Figure 3.10 Comparison of the νBH stretching vibration regions around 2600 cm^{-1} for all three derivatives measured in KBr pellets using a Nicolet Nexus 670 FTIR spectrometer at 2800-2400 cm^{-1}.

3.6 References

(1) Smith, R. K.; Lewis, P. A.; Weiss, P. S. Patterning Self-Assembled Monolayers. *Prog. Surf. Sci.* **2004**, *75*, 1–68.

(2) Weiss, P. S. Functional Molecules and Assemblies in Controlled Environments: Formation and Measurements. *Acc. Chem. Res.* **2008**, *41*, 1772–1781.

(3) Love, J. C.; Estroff, L. A.; Kriebel, J. K.; Nuzzo, R. G.; Whitesides, G. M. Self-Assembled Monolayers of Thiolates on Metals as a Form of Nanotechnology. *Chem. Rev*. **2005**, *105*, 1103-1169.

(4) Claridge, S. A.; Liao, W. S.; Thomas, J. C.; Zhao, Y.; Cao, H. H.; Cheunkar, S.; Serino, A. C.; Andrews, A. M.; Weiss, P. S. From the Bottom up: Dimensional Control and Characterization in Molecular Monolayers. *Chem. Soc. Rev.* **2013**, *42*, 2725–2745.

(5) Wann, D. A.; Lane, P. D.; Robertson, H. E.; Baše, T.; Hnyk, D. The Gaseous Structure of *closo*-9,12-$(SH)_2$-1,2-$C_2B_{10}H_{10}$, a Modifier of Gold Surfaces, as Determined Using Electron Diffraction and Computational Methods. *J. Chem. Soc. Dalt. Trans.* **2013**, *42*, 12015–12019.

(6) Von Wrochem, F.; Scholz, F.; Gao, D.; Nothofer, H. G.; Yasuda, A.; Wessels, J. M.; Roy, S.; Chen, X.; Michl, J. High-Band-Gap Polycrystalline Monolayers of a 12-Vertex *p*-Carborane on Au(111). *J. Phys. Chem. Lett.* **2010**, *1*, 3471–3477.

(8) Hohman, J. N.; Claridge, S. A.; Kim, M.; Weiss, P. S. Cage Molecules for Self-Assembly. *Mater. Sci. Eng. R Reports* **2010**, *70*, 188–208.

(9) Beall, H.; Muetterties, E. *Boron Hydride Chemistry*; Academic Press: New York, 1975.

(10) Grimes, R. N. *Carboranes*, 3rd ed.; Academic Press: Oxford, 2016.

(11) Woodruff, D. P. The Interface Structure of *n*-Alkylthiolate Self-Assembled Monolayers on Coinage Metal Surfaces. *Phys. Chem. Chem. Phys.* **2008**, *10*, 7211–7221.

(12) Maksymovych, P.; Voznyy, O.; Dougherty, D. B.; Sorescu, D. C.; Yates, J. T. Gold Adatom as a Key Structural Component in Self-Assembled Monolayers of Organosulfur Molecules on Au(111). *Prog. Surf. Sci.* **2010**, *85*, 206–240.

(13) Bürgi, T. Properties of the Gold-Sulphur Interface: From Self-Assembled Monolayers to Clusters. *Nanoscale* **2015**, *7*, 15553–15567.

(14) Vericat, C.; Vela, M. E.; Benitez, G.; Carro, P.; Salvarezza, R. C. Self-Assembled Monolayers of Thiols and Dithiols on Gold: New Challenges for a Well-Known System. *Chem. Soc. Rev.* **2010**, *39*, 1805–1834.

(15) Torres, E.; Blumenau, A. T.; Biedermann, P. U. Steric and Chain Length Effects in the ($\sqrt{3} \times \sqrt{3}$)R30° Structures of Alkanethiol Self-Assembled Monolayers on Au(111). *ChemPhysChem* **2011**, *12*, 999–1009.

(16) Dai, Z.; Ju, H. Effect of Chain Length on the Surface Properties of ω-Carboxy Alkanethiol Self-Assembled Monolayers. *Phys. Chem. Chem. Phys.* **2001**, *3*, 3769–3773.

(17) Hohman, J. N.; Zhang, P.; Morin, E. I.; Han, P.; Kim, M.; Kurland, A. R.; McClanahan, P. D.; Balema, V. P.; Weiss, P. S. Self-Assembly of Carboranethiol Isomers on Au{111}: Intermolecular Interactions Determined by Molecular Dipole Orientations. *ACS Nano* **2009**, *3*, 527–536.

(18) Thomas, J. C.; Goronzy, D. P.; Serino, A. C.; Auluck, H. S.; Irving, O. R.; Jimenez-Izal, E.; Deirmenjian, J. M.; Macháček, J.; Sautet, P.; Alexandrova, A. N.; Baše, T.; Weiss, P. S. Acid-Base Control of Valency within Carboranedithiol Self-Assembled Monolayers: Molecules Do the Can-Can. *ACS Nano* **2018**, *12*, 2211–2221.

(19) Schwartz, J. J.; Mendoza, A. M.; Wattanatorn, N.; Zhao, Y.; Nguyen, V. T.; Spokoyny, A. M.; Mirkin, C. A.; Baše, T.; Weiss, P. S. Surface Dipole Control of Liquid Crystal Alignment. *J. Am. Chem. Soc.* **2016**, *138*, 5957–5967.

(20) Kim, J.; Rim, Y. S.; Liu, Y.; Serino, A. C.; Thomas, J. C.; Chen, H.; Yang, Y.; Weiss, P. S. Interface Control in Organic Electronics Using Mixed Monolayers of Carboranethiol Isomers. *Nano Lett.* **2014**, *14*, 2946–2951.

(21) Thomas, J. C.; Boldog, I.; Auluck, H. S.; Bereciartua, P. J.; Dušek, M.; Macháček, J.; Bastl, Z.; Weiss, P. S.; Baše, T. Self-Assembled *p*-Carborane Analogue of *p*-Mercaptobenzoic Acid on Au{111}. *Chem. Mater.* **2015**, *27*, 5425–5435.

(22) Thomas, J. C.; Goronzy, D. P.; Dragomiretskiy, K.; Zosso, D.; Gilles, J.; Osher, S. J.; Bertozzi, A. L.; Weiss, P. S. Mapping Buried Hydrogen-Bonding Networks. *ACS Nano* **2016**, *10*, 5446–5451.

(23) Goronzy, D. P.; Staněk, J.; Avery, E.; Guo, H.; Bastl, Z.; Dušek, M.; Gallup, N. M.; Gün, S.; Kučeráková, M.; Levandowski, B. J.; Macháček, J.; Šícha, V.; Thomas, J. C.; Yavuz, A.; Houk, K. N.; Danlşman, M. F.; Mete, E.; Alexandrova, A. N.; Baše, T.; Weiss, P. S. Influence of Terminal Carboxyl Groups on the Structure and Reactivity of Functionalized *m*-Carboranethiolate Self-Assembled Monolayers. *Chem. Mater.* **2020**, *32*, 6800–6809.

(24) Baše, T.; Bastl, Z.; Šlouf, M.; Klementova, M.; Jan, S.; Vetushka, A.; Ledinsky, M.; Macha, J.; Carr, M. J.; Londesborough, M. G. S. Gold Micrometer Crystals Modified with Carboranethiol Derivatives. *J. Phys. Chem. C* **2008**, *112*, 14446–14455.

(25) Frohn, J.; Wolf, J. F.; Besocke, K.; Teske, M. Coarse Tip Distance Adjustment and Positioner for a Scanning Tunneling Microscope. *Rev. Sci. Instrum.* **1989**, *60*, 1200–1201.

Chapter 4: Temperature-Dependent Deposition in Carboraneselenolate Self-Assembled Monolayers

4.1 Introduction

Intelligent design of molecular building blocks that compose supramolecular assemblies requires detailed knowledge of the interactions at play within the system that elucidate structure and function of the material. Self-assembled monolayers provide an ideal platform to study how substrate-adsorbate interactions, intermolecular interactions between adsorbates, and the adsorbate-environment interface all play a role in emergent properties in the nanoscale and macroscale.[1–4] The substrate-adsorbate bond serves as a crucial electronic connection of the system.[5,6] This connection is influenced by many factors like orbital hybridization of the anchoring group and backbone, multiple chemically equivalent binding sites present in the substrate and the potential of surface reconstruction to minimize energy.[7–9] All of these factors influence the formation of different surface structures and possible rearrangements which is why it is important to understand each.

Thiol anchoring groups on Au{111} substrates currently represent a large body of research and have attracted great interest over the past few decades. Due to the ease of fabrication and strong Au-S bond, alkanethiols have been an ideal candidate for studies of self-assembly.[1,2,10] However, to encompass a larger variety of chemically suitable combinations, other modes of attachment must be explored such as different chalcogenides. In comparison to *n*-alkanthiolate monolayers, *n*-alkaneselenolate monolayers introduce some interesting new characteristics. Self-assembled monolayers of *n*-alkanethiolates exhibit large domains of hexagonally packed, similarly aligned molecules along with areas of disorder and substrate vacancy island defects.[11,12] Alternatively, *n*-alkaneselenolate monolayers have been reported to display either densely packed distorted hexagonal lattices incommensurate with the underlying Au{111} substrate, or commensurate linear missing-row structures. distinctive moiré patterning, along with a decreased

number of surface defects and domain boundaries observed.[13,14] In addition, differences in conductivity and ease of displacement between *n*-alkanethiol and *n*-alkaneselenol monolayers are also observed.[13] However, due to the large conformational flexibility of the alkane chain, to isolate the contribution of the head group chemistry, it is desired to detach the convoluted variables of the tail group geometry from anchoring group identity.

An ideal comparison of the two anchoring groups is a system that eliminates the effects of different molecules orientations and tilts within the monolayers to compare anchoring group characteristics and properties directly. In a paper published previously in our group by Hohman *et al*., the cage molecule 1-adamantaneselenol (1-ADSe) was used to make this comparison to 1-adamantanethiol (1-AD).[15] Adamantane is a bulky diamondoid cage molecule that consists of 10 carbons with respective hydrogens attached at each of the vertices. Depending on the position that the anchoring group is attached, either by thiolating at a primary (2-adamantanethiol) or tertiary (1-adamantanethiol) carbon, it is possible to create or to eliminate tilt defects based on small changes in molecular structure.[4,16] 1-Adamantanethiol monolayers have been well characterized and it has been shown that the monolayers are predominantly defect free, have weak intermolecular interactions and are geometrically dominated by the symmetry of the large bulky cage projected onto the surface.[3,17,18]

In comparison to the 1-AD monolayers, 1-ADSe monolayers showed some interesting differences. Amongst the differences were the presence of two dynamic site-dependent conductance states and observation of stochastic conductance switching between these high and low states.[15] This observation is in line with the nature of Au-Se bonding being more mobile and highly promiscuous in comparison to its Au-S cousin. The second distinguishing characteristic of these monolayers is the observation that at ambient deposition conditions, these high and low

conductance states are randomly distributed throughout the monolayer, but upon light thermal annealing at 70 °C, the monolayer rearranges into ordered structure of aligned rows of high conductance dimers. This change was attributed to substrate-mediated interactions of the Au-Se bond.

Taking a step further, another class of molecules, carboranes, serve as a different category of rigid cage molecules but add the component of a strong intrinsic dipole. Carboranes are composed of 10 boron vertices and 2 carbon vertices with respective hydrogens that exhibit highly delocalized hexacoordinate bonds arranged in nearly perfect icosahedral symmetry.[19] Depending on the position of the carbon vertices in the cage, the dipole magnitude and direction can be altered. In addition to the ability to tailor the dipole moment, the cage can be externally functionalized with a variety of functionalizations including different anchoring groups such as thiols, selenols or other chalcogenides. In this study, we will provide another example of comparison between thiol and selenol anchoring groups, yet this time, with an added component of strong dipole-dipole interactions.

4.2 Results and Discussion

In this work we assembled and examined two different *m*-carboraneselenol isomer monolayers, 1-HSe-1,7-$C_2B_{10}H_{11}$ (M1Sel) and 9-HSe-1,7-$C_2B_{10}H_{11}$ (M9Sel), on Au{111} substrates. These structures are illustrated in Figure 4.1 in both space filling models and ball and stick models with their respective dipole orientations indicated. Due to the position of the anchoring group in relation to the carbon vertices in the *m*-carboraneselenol cage, the dipole orientation when confined to a substrate is altered. M9Sel exhibits a dipole that lies primarily within the lateral plane of the monolayer with a calculated dipole moment tilted 20° with respect

to the surface normal, whereas the M1Sel isomer exhibits a dipole that is tilted 105° with respect to the surface normal lying primarily in the longitudinal plane.[20]

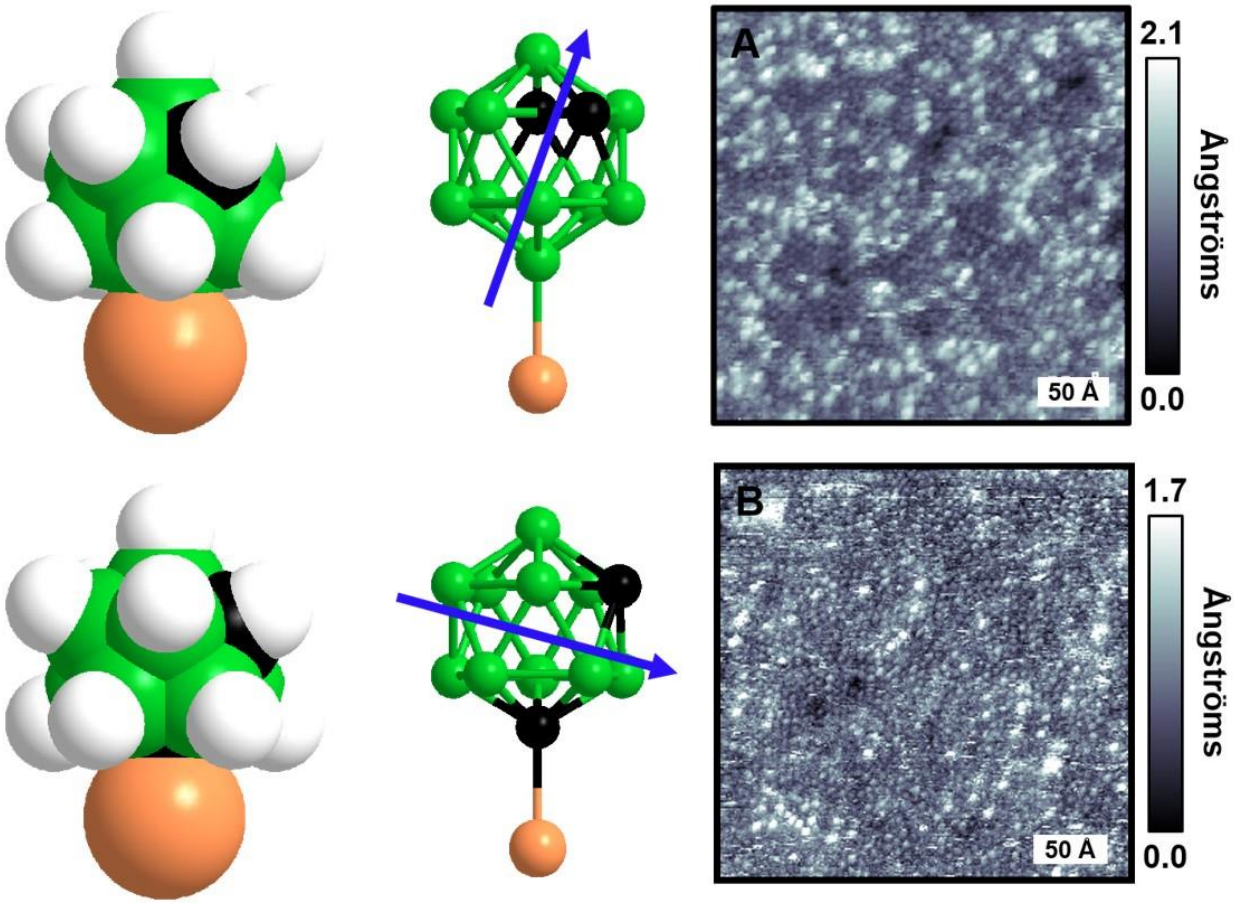

Figure 4.1 (Left) Space-filling models and (Middle) ball and stick models with hydrogens not displayed of (Top) *m*-9-carboraneselenolate (M9Sel) and (Bottom) *m*-1-carboraneselenolate (M1Sel). The central cage is composed of 10 boron atoms (green) and two carbon atoms (black) with hydrogen atoms at the vertices (white) and a selenium atom (orange) for surface attachment. The dipole moment (blue) of the molecules is largely determined by the position of the carbon atoms is the cage. (Right) Scanning tunneling microscopy images of (A) *m*-1-carboraneselenol and (B) *m*-9-carboraneselenol showing self-assembled monolayers composed of a mixture of molecules in a minority high-conductance binding mode and a majority low-conductance binding mode. (V_{sample} = 0.1 V, I_{tunnel} = 100 pA)

The differences between these two isomers have been demonstrated in their respective thiol analogs to cause variance in long range dipole interactions and monolayer stability.[21,22] In addition to the difference in neighboring dipole-dipole interactions, these two isomers have large

dissimilarities in the properties surrounding anchoring group chemistry. The M9Sel isomer has anchoring group attachment to an electron-rich boron vertex, conversely; the M1Sel isomer to the electron-poor C-Se attachment.[19] This charge distribution may play a role in the difference in distribution of the percentage of high and low conductive states between isomers. This is shown in Figure 4.1A,B where scanning tunneling micrographs of M1Sel and M9Sel are displayed. The micrographs of M1Sel show significantly higher surface coverage of the high-conductance state at 32 ± 11% in comparison to the 13 ± 4% of the M9Sel micrographs. The higher conductance state is approximately 1.1 ± 0.1 Å higher in apparent height than the lower conductance state. The prevalence in both selenol isomeric monolayers of the bimodal height distribution is much higher than that of their *m*-carboranthiol counterparts. This characteristic is attributed to differences in the nature of Au-Se bonding despite having the same lattice spacing of 7.4 ± 0.7 Å in comparison to their thiol analogs within error.[22,23]

Another characteristic that differs from the thiol variants is the ability of the selenol to switch binding modes spontaneously on the time scale of several minutes.[15] Figure 4.2 illustrates two sequential images taken a few minutes apart in ambient STM. These images show stochastic switching of species from both low- to high-conductance states and high- to low-conductance states seemingly in a 1:1 ratio. This characteristic highlights the similarities between this system and the observed 1-adamantaneselenol system as both exhibit these dynamic switching kinetics.[15] The differences in conductance states are attributed changes in attachment sites of the substrate.[24–26] Previously, it was proposed that high-conductance states result from a molecule being bound at a three-fold hollow site where low-conductance states are those at the bridge site.[15]

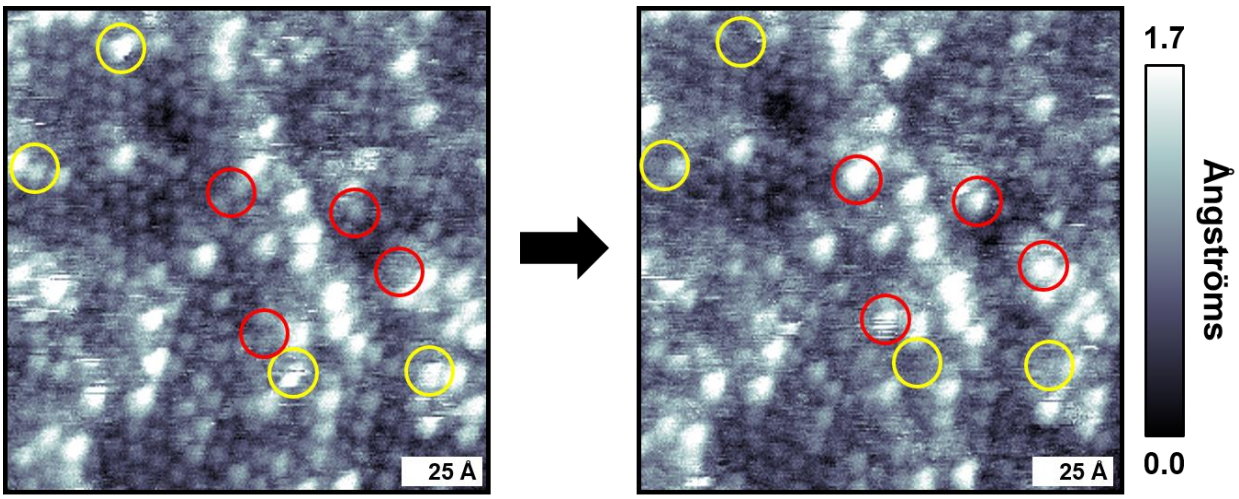

Figure 4.2 Sequential scanning tunneling microscopy images of a *m*-1-carboraneselenolate self-assembled monolayer showing stochastic conductance switching of molecules on the surface. Yellow circles highlight molecules switching from a high to low-conductance binding state and red circles highlight molecules switching from a low to high-conductance binding state. (V_{sample} = 0.1 V, I_t = 80 pA)

The M9Sel and M1Sel monolayers show large similarities in comparison to the behavior of 1-adamadateselenol monolayers. Kinetically favored deposition that results in a dynamic monolayer is consistent between the two systems. In addition to these characteristics, in the 1-adamantaneselenol monolayer and other systems, kinetic favorability can be biased to thermodynamic favorability *via* specific temperature window thermal coercion.[15] In the case of the 1-adamantaneselenol monolayers, it was shown that upon light thermal annealing at 70 °C, the monolayer reordered. It was proposed that the stable and ordered dimer structure that forms likely results from substrate-mediated interactions.[15] Since the *m*-carboraneselenol monolayers already act similar to the 1-adamantaneselenol monolayers we decided to search for the possibility of thermal rearrangement as well.

The 1-adamantaneselenol monolayers only show ordered thermal rearrangement in a small temperature window. Temperatures above the thermal window resulted in monolayer degradation.

As the *m*-carboraneselenol have the added characteristic of dipole-dipole interactions within the monolayer, we set out to find the appropriate temperature window that is applicable to this system. In Figure 4.3, we compare X-ray photoelectron spectra of the M1Sel monolayer after different thermal annealing conditions to help elucidate the effects of annealing temperature.

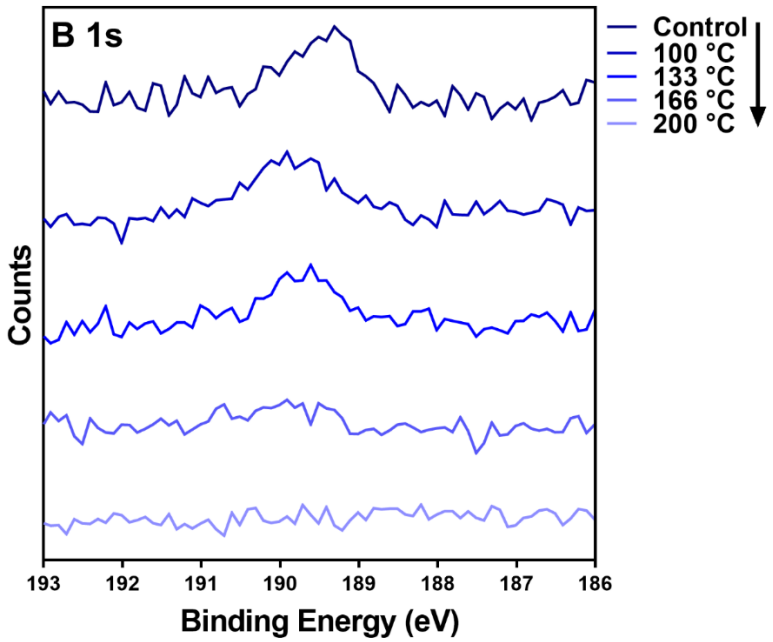

Figure 4.3 X-ray photoelectron spectra showing the B 1s peak for monolayers of 9-HSe-1,7-$C_2B_{10}H_{11}$ (M9Sel) at different annealing conditions to locate the temperature of desorption (N=3). Complete desorption appears to take place between 133 °C and 166 °C as the B 1s peak becomes less apparent.

The B 1s peak is used as a marker for the presence of carborane on the surface. At higher temperatures, this peak becomes increasingly diminished and at 200 °C unmeasurable. From here, we decided to look for the presence of thermal rearrangement right before this temperature. In Figure 4.4, monolayers of M9Sel and M1Sel are imaged after 24 hr thermal annealing at different temperatures.

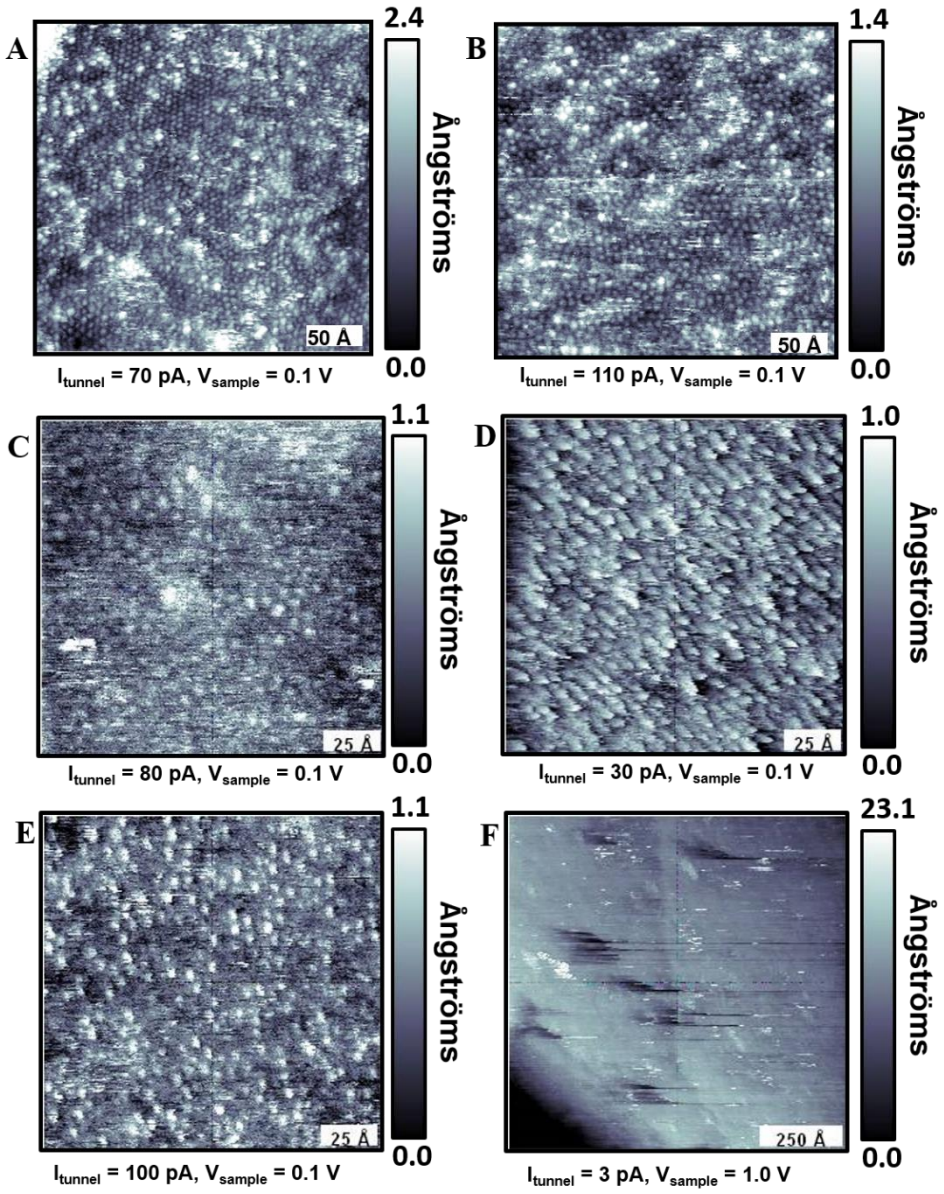

Figure 4.4 (A) Scanning tunneling microscopy image of a *m*-1-carboranselenolate self-assembled monolayer (SAM) after dry-annealing at 70 °C for 24 h (V_{sample} = 0.1 V, I_{tunnel} = 70 pA). (B) Scanning tunneling microscopy image of a *m*-9-carboranselenolate SAM after dry annealing at 78 °C for 120 h (V_{sample} = 0.1 V, I_{tunnel} = 110 pA). (C) Scanning tunneling microscopy image of a *m*-9-carboranselenolate SAM after dry annealing at 100 °C for 24 h (V_{sample} = 0.1 V, I_{tunnel} = 80 pA). (D) Scanning tunneling microscopy image of a *m*-9-carboranselenolate SAM after dry annealing at 120 °C for 24 h (V_{sample} = 0.1 V, I_{tunnel} = 30 pA). (E) Scanning tunneling microscopy image of a *m*-9-carboranselenolate SAM after dry annealing at 130 °C for 24 h (V_{sample} = 0.1 V, I_{tunnel} = 100 pA). (D) Scanning tunneling microscopy image of a *m*-9-carboranselenolate SAM after dry annealing at 165 °C for 24 h (V_{sample} = 1.0 V, I_{tunnel} = 3 pA). Monolayers show order up to 130 °C and appear disordered at 165 °C and higher.

Micrographs of samples with annealing temperatures below 165 °C show intact monolayers with consistent features similar to the monolayers prepared under ambient conditions. Samples that are annealed above 165 °C have monolayers that are unorganized and highly disrupted molecular organization. More samples in the range of 140-165 °C must be analyzed to solidify this observation, but it appears that the added dipole-dipole interactions of M1Sel and M9Sel are strong enough to prevent thermal rearrangement.

4.3 Conclusions and Prospects

Self-assembled monolayers of M1Sel and M9Sel form ordered lattices with parameters consistent with those of their thiol counterparts. However, despite similar physical arrangements, M1Sel and M9Sel monolayers have lattices with varying degrees of bimodal height distribution. Additionally, it was observed that both high- and low-conductance states can stochastically switch back and forth. This observation is consistent with the behavior of 1-admantaneselenol monolayers, which our lab measured previously. Conversely, upon light thermal annealing at temperatures just under the onset of monolayer desorption, there appears to be no substrate-mediated monolayer organization such as the behavior observed in the 1-adamantaneselenol monolayers. This difference is attributed to the addition of dipole-dipole driven interactions that may strengthen the intrinsic stability of the monolayer but more studies must be done to test this hypothesis. M1Sel and M9Sel offer a valid system of comparison for the further exploration of alternative anchoring groups along with offering added insight into B-Se-Au bond versus C-Se-Au bond attachment chemistry.

4.4 Materials and Methods

Scanning tunneling microscopy sample preparation and image analysis: *m*-1-carboraneselenol and *m*-9-carboraneselenol were synthesized as previously described in the literature and stored in a glovebox environment with solutions prepared immediately before use.[27] Samples for imaging were prepared on Au{111}/mica substrates (Agilent Technology, Tempe, AZ), which were hydrogen-flame annealed with 10 passes at a rate of 0.4 Hz prior to SAM formation. Substrates were placed in 1 mM ethanolic solutions for 24 h at room temperature. Ethanol was used as received (Sigma-Aldrich, St. Louis, MO). After deposition, samples where rinsed with neat ethanol and dried under a stream of ultrahigh-purity nitrogen for at least three cycles. Samples were then imaged or sealed in an empty glass vial and dry-annealed at the prescribed temperature and time duration. All STM measurements were performed with a custom-built Besocke-style STM with a platinum/iridium tip (80:20).[28,29] The known lattice of the 1-dodecanethiolate SAMs on Au{111} was used for calibration. The STM image analyses was done using MATLAB (Mathworks, Natick, MA) and Gwyddion (http://gwyddion.net/).

X-ray photoelectron spectroscopy (XPS): Platypus Template-Stripped Gold Chips were used as the substrate for all of the experiments. The Platypus chips were cleaved shortly before use to minimize their exposure to air. For the deposition of M9Se, and M1Se the substrate was immersed in a 96% ethanol solution of the corresponding compound (concentration of 1 mmol · dm^{-3}) for 50 to 70 min and fresh solutions were prepared for each deposition. The chips were then rinsed with 96% ethanol, dried in a stream of argon or nitrogen for three cycles, and stored under inert atmosphere, and subsequently used for further modification or measurements within the next 30 min. Samples were then used or sealed in an empty glass vial and dry-annealed at the prescribed temperature and time duration.

4.5 References

(1) Love, J. C.; Estroff, L. A.; Kriebel, J. K.; Nuzzo, R. G.; Whitesides, G. M. Self-Assembled Monolayers of Thiolates on Metals as a Form of Nanotechnology. *Chem. Rev.* **2005,** *105*, 1103-1170.

(2) Nuzzo, R. G.; Zegarski, B. R.; DuBois, L. H. Fundamental Studies of the Chemisorption of Organosulfur Compounds on Au(111). Implications for Molecular Self-Assembly on Gold Surfaces. *J. Am. Chem. Soc.* **1987**, *109*, 733–740.

(3) Hohman, J. N.; Claridge, S. A.; Kim, M.; Weiss, P. S. Cage Molecules for Self-Assembly. *Mater. Sci. Eng. R Reports* **2010**, *70*, 188–208.

(4) Claridge, S. A.; Liao, W. S.; Thomas, J. C.; Zhao, Y.; Cao, H. H.; Cheunkar, S.; Serino, A. C.; Andrews, A. M.; Weiss, P. S. From the Bottom up: Dimensional Control and Characterization in Molecular Monolayers. *Chem. Soc. Rev.* **2013**, *42*, 2725–2745.

(5) Allara, D. L.; Dunbar, T. D.; Weiss, P. S.; Bumm, L. A.; Cygan, M. T.; Tour, J. M.; Reinerth, W. .; Yao, Y.; Kozaki, M.; Jones, L. I. Evolution of Strategies for Self-Assembly and Hookup of Molecule-Based Devices. *Ann. New York Acad. Sci.* **1998**, *852*, 349–370.

(6) Weiss, P. S.; Bumm, L. A.; Dunbar, T. D.; Burgin, T. P.; Tour, J. M.; Allara, D. . Probing Electronic Properties of Conjugated and Saturated Molecules in Self-Assembled Monolayers. *Ann. N. Y. Acad. Sci.* **2006**, *852*, 145–168.

(7) Häkkinen, H. The Gold-Sulfur Interface at the Nanoscale. *Nat. Chem.* **2012**, *4*, 443–455.

(8) Cossaro, A.; Mazzarello, R.; Rousseau, R.; Casalis, L.; Verdini, A.; Kohlmeyer, A.; Floreano, L.; Scandolo, S.; Morgante, A.; Klein, M. L.; Scoles, G. X-Ray Diffraction and Computation Yield the Structure of Alkanethiols on Gold(111). *Science.* **2008**, *321*, 943–946.

(9) Maksymovych, P.; Voznyy, O.; Dougherty, D. B.; Sorescu, D. C.; Yates, J. T. Gold Adatom as a Key Structural Component in Self-Assembled Monolayers of Organosulfur Molecules on Au(111). *Prog. Surf. Sci.* **2010**, *85*, 206–240..

(10) Vericat, C.; Vela, M. E.; Benitez, G.; Carro, P.; Salvarezza, R. C. Self-Assembled Monolayers of Thiols and Dithiols on Gold: New Challenges for a Well-Known System. *Chem. Soc. Rev.* **2010**, *39*, 1805–1834.

(11) Weiss, P. S. Functional Molecules and Assemblies in Controlled Environments: Formation and Measurements. *Acc. Chem. Res.* **2008**, *41*, 1772–1781.

(12) Poirier, G. E. Characterization of Organosulfur Molecular Monolayers on Au(111) Using Scanning Tunneling Microscopy. *Chem. Rev.* **1997**, *97*, 1117–1127.

(13) Monnell, J. D.; Stapleton, J. J.; Dirk, S. M.; Reinerth, W. A.; Tour, J. M.; Allara, D. L.; Weiss, P. S. Relative Conductances of Alkaneselenolate and Alkanethiolate Monolayers on Au{111}. *J. Phys. Chem. B* **2005**, *109*, 20343–20349.

(14) Monnell, J. D.; Stapleton, J. J.; Jackiw, J. J.; Dunbar, T.; Reinerth, W. A.; Dirk, S. M.; Tour, J. M.; Allara, D. L.; Welss, P. S. Ordered Local Domain Structures of Decaneselenolate and Dodecaneselenolate Monolayers on Au{111}. *J. Phys. Chem. B* **2004**, *108*, 9834–9841.

(15) Hohman, J. N.; Kim, M.; Schüpbach, B.; Kind, M.; Thomas, J. C.; Terfort, A.; Weiss, P. S. Dynamic Double Lattice of 1-Adamantaneselenolate Self-Assembled Monolayers on Au{111}. *J. Am. Chem. Soc.* **2011**, *133*, 19422–19431.

(16) Kim, M. K.; Hohman, J. N.; Morin, E. I.; Daniel, T. A.; Weiss, P. S. Self-Assembled Monolayers of 2-Adamantanethiol on Au{111}: Control of Structure and Displacement. *J. Phys. Chem. A* **2009**, *113*, 3895–3903.

(17) Saavedra, H. M.; Barbu, C. M.; Dameron, A. A.; Mullen, T. J.; Crespi, V. H.; Weiss, P. S. 1-Adamantanethiolate Monolayer Displacement Kinetics Follow a Universal Form. *J. Am. Chem. Soc.* **2007**, *129*, 10741–10746.

(18) Dameron, A. A.; Charles, L. F.; Weiss, P. S. Structures and Displacement of 1-Adamantanethiol Self-Assembled Monolayers on Au{111}. *J. Am. Chem. Soc.* **2005**, *127*, 8697–8704.

(19) Grimes, R. N. *Carboranes*, 3rd ed.; Academic Press: Oxford, 2016.

(20) Schwartz, J. J.; Mendoza, A. M.; Wattanatorn, N.; Zhao, Y.; Nguyen, V. T.; Spokoyny, A. M.; Mirkin, C. A.; Baše, T.; Weiss, P. S. Surface Dipole Control of Liquid Crystal Alignment. *J. Am. Chem. Soc.* **2016**, *138*, 5957–5967.

(21) Thomas, J. C.; Schwartz, J. J.; Hohman, J. N.; Claridge, S. A.; Auluck, H. S.; Serino, A. C.; Spokoyny, A. M.; Tran, G.; Kelly, K. F.; Mirkin, C. A.; Gilles, J.; Osher, O. S. J.; Weiss, P. S.; Al, T. E. T. Defect-Tolerant Aligned Dipoles within Two-Dimensional Plastic Lattices. *ACS Nano* **2015**, *5*, 4734–4742.

(22) Hohman, J. N.; Zhang, P.; Morin, E. I.; Han, P.; Kim, M.; Kurland, A. R.; McClanahan, P. D.; Balema, V. P.; Weiss, P. S. Self-Assembly of Carboranethiol Isomers on Au{111}: Intermolecular Interactions Determined by Molecular Dipole Orientations. *ACS Nano* **2009**, *3*, 527–536.

(23) Thomas, J. C.; Boldog, I.; Auluck, H. S.; Bereciartua, P. J.; Dušek, M.; Macháček, J.; Bastl, Z.; Weiss, P. S.; Baše, T. Self-Assembled p-Carborane Analogue of *p*-Mercaptobenzoic Acid on Au{111}. *Chem. Mater.* **2015**, *27*, 5425–5435.

(24) Moore, A. M.; Dameron, A. A.; Mantooth, B. A.; Smith, R. K.; Fuchs, D. J.; Ciszek, J. W.; Maya, F.; Yao, Y.; Tour, J. M.; Weiss, P. S. Molecular Engineering and Measurements to Test Hypothesized Mechanisms in Single Molecule Conductance Switching. *J. Am. Chem. Soc.* **2006**, *128*, 1959–1967.

(25) Moore, A. M.; Mantooth, B. A.; Donhauser, Z. J.; Maya, F.; Price, D. W.; Yao, Y.; Tour, J. M.; Weiss, P. S. Cross-Step Place-Exchange of Oligo(Phenylene−Ethynylene) Molecules. *Nano Lett.* **2005**, *5*, 2292-2297.

(26) Wang, K.; Zhang, C.; Loy, M. M. T.; Xiao, X. Time-Dependent Tunneling Spectroscopy for Studying Surface Diffusion Confined in Nanostructures. *Phys. Rev. Lett.* **2005**, *94*, 1–4.

(27) Spokoyny, A. M.; MacHan, C. W.; Clingerman, D. J.; Rosen, M. S.; Wiester, M. J.; Kennedy, R. D.; Stern, C. L.; Sarjeant, A. A.; Mirkin, C. A. A Coordination Chemistry Dichotomy for Icosahedral Carborane-Based Ligands. *Nat. Chem.* **2011**, *3*, 590–596.

(28) Frohn, J.; Wolf, J. F.; Besocke, K.; Teske, M. Coarse Tip Distance Adjustment and Positioner for a Scanning Tunneling Microscope. *Rev. Sci. Instrum.* **1989**, *60*, 1200–1201.

(29) Ferris, J. H.; Kushmerick, J. G.; Johnson, J. A.; Yoshikawa Youngquist, M. G.; Kessinger, R. B.; Kingsbury, H. F.; Weiss, P. S. Design, Operation, and Housing of an Ultrastable, Low Temperature, Ultrahigh Vacuum Scanning Tunneling Microscope. *Rev. Sci. Instrum.* **1998**, *69*, 2691–2695.

Chapter 5: Prospects and Future Directions

5.1 Conclusion

Self-assembled monolayers provide an advantageous platform for the controlled exploration of nanoscale properties at 2D interfaces. Investigation and elucidation of the components that result in the emergence of properties observed at the environment/monolayer interface, within the monolayer between adsorbate molecules, and at the monolayer/substrate interface, must be executed from a holistic viewpoint. Due to the synthetic richness in diversity and control, carborane molecules are an ideal scaffold to analyze all three of these interfaces.

Starting from the top down and focusing on the environment/monolayer interface, an array of additional functionalization can be oriented on the carborane antipodal to the anchoring group vertex or in other varying degrees from the surface normal to enable exposition to the environmental interface. As discussed in Chapter 2, examination of a carboranethiol monolayer functionalized in the *meta* position with a carboxylic acid gave rise to many interesting characteristics presented at the environment/monolayer interface. First, it was found that despite being partially buried within the monolayer, the carboxylic acid group demonstrated availability to coordinate with different metal ions at the interface. In some circumstances, ions such as Mg^{2+} and Ba^{2+} coordinated with multiple carboxylic acid groups. In addition to the carborane's availability to coordinate metal ions at the environmental interface, the carboxyl group also showed differences in acid-base character when confined to a two-dimensional lattice within the monolayer in comparison to the free molecule in solution. The increased shift in pK_a was attributed to a combination of a change in dielectric due to the surrounding monolayer, its proximity to the substrate, and intermolecular interactions of the neighboring carboranes.

Taking a step downward and focusing on the forces at play between molecules within the monolayer, we continue our dialogue. Proceeding with the discussion in Chapter 2, due to the extra

steric demands presented by the carboxyl group, the packing density of the monolayer was decreased in comparison to the unfunctionalized carboranethiol. Furthermore, to maximize monolayer packing density, molecular tilt was induced to maximize hydrogen-bonding interactions between the neighboring boron-hydrogen bonds and the carboxyl group, along with increasing the dipole-dipole interaction between molecules. We hypothesize these two strong interactions mitigate the existence of common defects observed in monolayers of other tilted molecules such as dodecanethiol.

Continuing our journey down to the monolayer-substrate interface, we discuss the work described in Chapter 3. The strength of binding and stability of the anchoring group directly affects SAM formation and monolayer packing density. In the previous example, a thiol anchoring group was used for attachment. In Chapter 3, the thiol anchoring group is replaced by a selenol anchoring group to study the difference in adsorption and monolayer properties. While both are chalcogens, a selenium attachment appears to be much more mobile and promiscuous in terms of bonding in comparison to sulfur. This characteristic is demonstrated in the illustration of a dynamic double lattice observed in subsequent scanning tunneling microscopy images. Stochastic switching between high- and low-conductance states supports the idea of higher bonding promiscuity, yet stabilization with high-temperature annealing supports the strength offered by dipole-dipole interactions between neighboring molecules in the monolayers.

An exploration of all three areas is described in Chapter 4 where the elucidation of neighboring interactions of both anchoring groups and varying dipole-dipole interactions is investigated. By adding methyl group labels to one of the carborane isomers, we introduce the ability to map and to probe these interactions. In this way, we change the dipole magnitude and

topographic height in the surface normal direction while keeping anchoring groups and lateral steric demands the same.

5.2 Prospects and Future Directions

5.2.1 Different factors and their effects on surface pK_a

The synthetic diversity accessible through the rich chemistry of the carborane cage allows for many extended possibilities to explore and to isolate different aspects of surface chemistry. Altering surface attachments gives rise to the possibility of anchoring on a diverse array of substrates from metals to semiconductors.[1,2] These alterations may enable new surface properties, a multiplicity of packing densities, and controllable lattice arrangements. Modification of the position of the carbons within the cage enables precise control of dipole direction and magnitude.[3] In addition, functionalization at controlled positions around the cage adds another degree of complexity. By adding different functional groups, such as alkyl, amine, alcohol, ether, halogen, or other attachments, and varying the attachment at electron-poor carbon vertices or electron-rich boron vertices, the desired chemistry can be adjusted to enable specific interactions at the environmental interface, between neighboring adsorbates, or towards the substrate, depending on position.[4]

Acid-base control at the monolayer-environment interface is of particular interest due to its potential applications in biological systems, pH sensors, and changing surface wettability factors.[5–9] The precise synthetic control to functionalize carboranes at different positions, multiple positions, and with diverse omega functionalities provides ample future directions as several fundamental questions remain unanswered.

5.2.2 Position, number, and dilution of carboxyl groups

Building on the work discussed in Chapter 2, moving the carboxylic acid to the *para* or *meta* position has the potential to result in interesting responses in the monolayer. Modulating the position would affect surface pK_a as the acidic functionality becomes increasingly or decreasingly accessible to the environmental interface. Tailoring the effects of desolvation and the dielectric environment along with surface tilt of the molecule anchored to the substrate are variables to be addressed. These could present opportunities to tune the acid-base properties of the monolayer along with varying degrees of hydrophobicity.[10] In addition to the position of the ω-functionality, the stoichiometric number present at the environmental interface could also alter acid-base characteristics. The ability of the carborane cage to be synthesized with several functional groups at different positions results in the ability to increase the stoichiometric ratio of carboxylic acid groups available to the solvent interface. Increasing the density of these functional groups at the interface could additionally have effects on acid-base components and sensing.

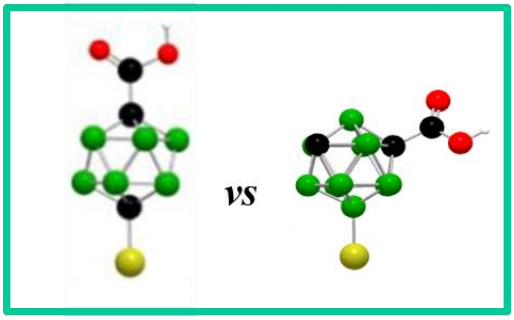

Figure 5.1 Schematic of 1-HS-12-COOH-1,12-$C_2B_{10}H_{10}$ (left) and 1-COOH-9-SH-1,7-$C_2B_{10}H_{10}$ (right) showing the functionalization of the carboxylic acid group at different positions on the carboranethiol cage exposing the acidic group in varying degrees to the environmental interface.

In addition to altering the molecule, surface dilutions have been shown to alter the reactivity of a monolayer. Moldt *et al*. showed that by decreasing the concentration of active

azobenzene molecules in a monolayer by diluting the surface concentration, photo switching between *cis* and *trans* states of the molecule became accessible.[11]

The ability to dilute a monolayer of carboxyl functionalized carboranethiol by having a heterogeneous mixture of the unfunctionalized molecule immobilized on the surface in a 2D array could also give rise to tailoring the acid-base properties of the system. Preliminary data collected from surface dilutions of 1-HS-12-COOH-1,12-$C_2B_{10}H_{10}$ and 1-HS-1,12-$C_2B_{10}H_{10}$ presented in Figure 5.2 suggests that this is a suitable system to be studied for this application.

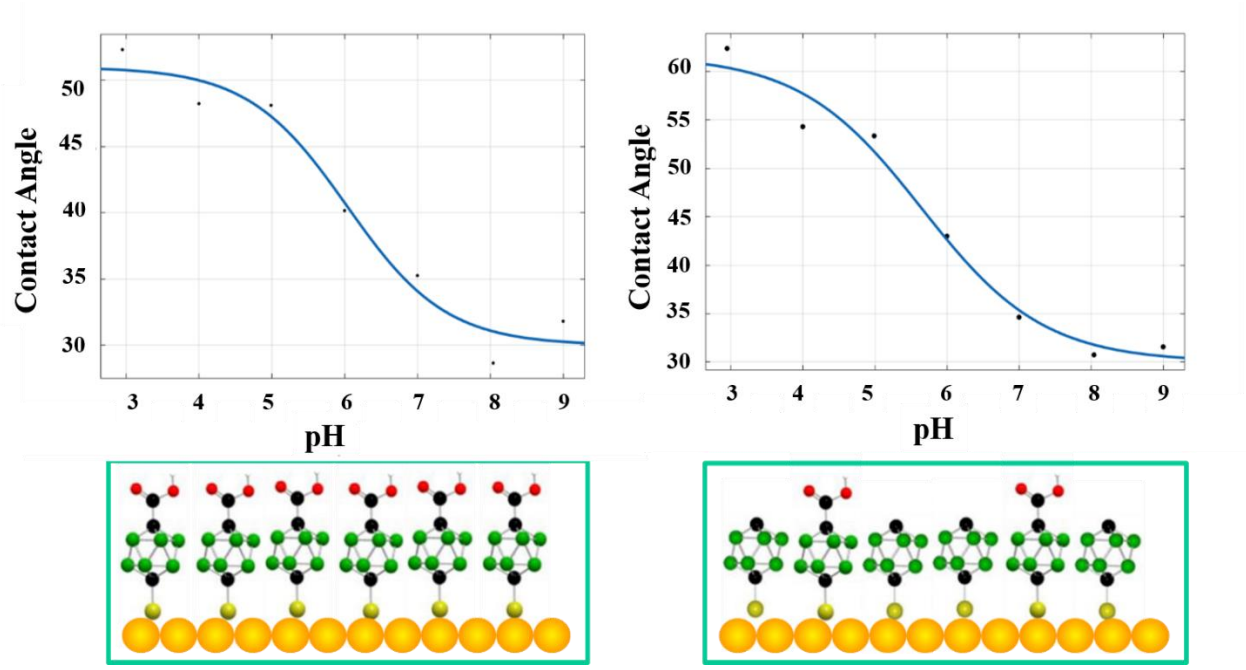

Figure 5.2 Contact angle titration curves of a homogenous 1-HS-12-COOH-1,12-$C_2B_{10}H_{10}$ monolayer on gold (left) and a heterogenous 1-HS-12-COOH-1,12-$C_2B_{10}H_{10}$ and 1-HS-1,12-$C_2B_{10}H_{10}$ (right) monolayer on gold showing surface pK_a measurements of 6.03 and 5.83, respectively.

5.2.3 Surface curvature

In many recent works, modulating surface curvature of functionalized nanoparticles has given rise to tunable chemical and physical properties. Work by Zolbinsky *et al.* demonstrated that surface curvature can have controllable effects on reactivity. Nanoparticles synthesized with 9-(4-mercaptophenyl-ethynyl)-anthracene as ligands showed controlled Diels-Alder reactions when surface curvature decreased but no reaction when increased.[12] Wang *et al.* showed that by altering the diameter of nanoparticles decorated with immobilized ligands of 11-mercaptoundecanoic acid, surface pK_a is controllably manipulated and shifted.[13] Functionalization of carborane/gold nanoparticles has been demonstrated by Cioran and coworkers.[14] Carboxyl-functionalized carboranethiols as ligands anchored on gold nanoparticles could serve as a platform to study effects of surface curvature versus pK_a as the conformational flexibility of longer chain molecules are mitigated being replaced by more rigid and sterically demanding cage molecules. It has been shown that as exposure to solvent increases, neighboring interactions change as surface curvature is varied and due to this finding, carboranes could be of interest for further study of this topic.[13]

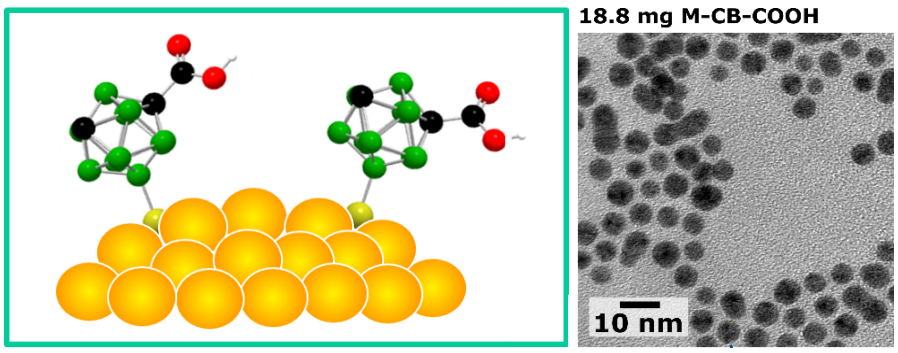

Figure 5.3. Schematic and transmission electron microscope image of 1-COOH-9-SH-1,7-$C_2B_{10}H_{10}$ modified gold nanoparticles.

Preliminary work supports carboxyl-terminated carboranethiol-modified nanoparticles of controlled size using synthetic techniques developed by the Brust group.[14] These functionalized nanoparticles could serve as a platform for further study of factors that alter surface pK_a and other characteristic modifications.

In conclusion, carboranes offer a diverse scaffold to assess many interesting properties fundamental to surface science. Ranging from electronics, surface wettability, device development, and many more, there are many facets that have yet to be explored.

5.3 References

(1) Serino, A. C.; Anderson, M. E.; Saleh, L. M. A.; Dziedzic, R. M.; Mills, H.; Heidenreich, L. K.; Spokoyny, A. M.; Weiss, P. S. Work Function Control of Germanium through Carborane-Carboxylic Acid Surface Passivation. *ACS Appl. Mater. Interfaces* **2017**, *9*, 34592–34596.

(2) Kim, J.; Rim, Y. S.; Liu, Y.; Serino, A. C.; Thomas, J. C.; Chen, H.; Yang, Y.; Weiss, P. S. Interface Control in Organic Electronics Using Mixed Monolayers of Carboranethiol Isomers. *Nano Lett.* **2014**, *14*, 2946–2951.

(3) Schwartz, J. J.; Mendoza, A. M.; Wattanatorn, N.; Zhao, Y.; Nguyen, V. T.; Spokoyny, A. M.; Mirkin, C. A.; Baše, T.; Weiss, P. S. Surface Dipole Control of Liquid Crystal Alignment. *J. Am. Chem. Soc.* **2016**, *138*, 5957–5967.

(4) Bregadze, V. I. Dicarba-*closo*-dodecaboranes $C_2B_{10}H_{12}$ and Their Derivatives. *Chem. Rev.* **1992**, *92*, 209–223.

(5) Harms, M. J.; Castañeda, C. A.; Schlessman, J. L.; Sue, G. R.; Isom, D. G.; Cannon, B. R.; García-Moreno E., B. The pK_a Values of Acidic and Basic Residues Buried at the Same Internal Location in a Protein Are Governed by Different Factors. *J. Mol. Biol.* **2009**, *389*, 34–47.

(6) Isom, D. G.; Castañed, C. A.; Cannon, B. R.; García-Moreno, B. E. Large Shifts in pK_a Values of Lysine Residues Buried inside a Protein. *Proc. Natl. Acad. Sci. U. S. A.* **2011**, *108*, 5260–5265.

(7) Karp, D. A.; Gittis, A. G.; Stahley, M. R.; Fitch, C. A.; Stites, W. E.; García-Moreno E., B. High Apparent Dielectric Constant inside a Protein Reflects Structural Reorganization Coupled to the Ionization of an Internal Asp. *Biophys. J.* **2007**, *92*, 2041–2053.

(8) Gershevitz, O.; Osnis, A.; Sukenik, C. N. Interfacial Chemistry on Carboxylate-Functionalized Monolayer Assemblies. *Isr. J. Chem.* **2005**, *45*, 321–336.

(9) Laibinis, P. E.; Whitesides, G. M. ω-Terminated Alkanethiolate Monolayers on Surfaces of Copper, Silver, and Gold have Similar Wettabilities. *J. Am. Chem. Soc.* **1995**, *114*, 1990–1995.

(10) Burris, S. C.; Zhou, Y.; Maupin, W. A.; Ebelhar, A. J.; Daugherty, M. W. The Effect of Surface Preparation on Apparent Surface pKa's of ω-Mercaptocarboxylic Acid Self-Assembled Monolayers on Polycrystalline Gold. *J. Phys. Chem. C* **2008**, *112*, 6811–6815.

(11) Moldt, T.; Brete, D.; Przyrembel, D.; Das, S.; Goldman, J. R.; Kundu, P. K.; Gahl, C.; Klajn, R.; Weinelt, M. Tailoring the Properties of Surface-Immobilized Azobenzenes by Monolayer Dilution and Surface Curvature. *Langmuir* **2015**, *31*, 1048–1057.

(12) Zdobinsky, T.; Sankar Maiti, P.; Klajn, R. Support Curvature and Conformational Freedom Control Chemical Reactivity of Immobilized Species. *J. Am. Chem. Soc.* **2014**, *136*, 2711–2714.

(13) Wang, D.; Nap, R. J.; Lagzi, I.; Kowalczyk, B.; Han, S.; Grzybowski, B. A.; Szleifer, I. How and Why Nanoparticle's Curvature Regulates the Apparent pK_a of the Coating Ligands. *J. Am. Chem. Soc.* **2011**, *133*, 2192–2197.

(14) Cioran, A. M.; Musteti, A. D.; Teixidor, F.; Krpetić, Ž̂eljka; Prior, I. A.; He, Q.; Kiely, C. J.; Brust, M.; Viñas, C. Mercaptocarborane-Capped Gold Nanoparticles: Electron Pools and Ion Traps with Switchable Hydrophilicity. *J. Am. Chem. Soc.* **2012**, *134*, 212–221.